



CRANFIELD UNIVERSITY  
&  
ROLLS-ROYCE

Engineering Doctorate Thesis  
Sandra Goergen

Cracking Behaviour, Failure Modes and Lifetime  
Analysis of M320 Abradable Compressor Seal Coating

EngD Thesis ;  
Date due: October 4th, 2012



**CRANFIELD UNIVERSITY**

**SCHOOL OF APPLIED SCIENCES**

EngD THESIS

Academic Years 2007-12

Sandra Goergen

Cracking Behaviour, Failure Modes and Lifetime Analysis of M320  
Abradable Compressor Seal Coating

Supervisors: Professor John Nicholls & Professor David Rickerby

October 2012

©Cranfield University 2012. All rights reserved. No part of this publication may be reproduced without the written permission of the copyright owner.



Für meine Großväter:  
Walter Goergen &  
Kurt Naujoks



---

## Abstract

Metco 320 is a  $AlSi - hBN$ -polyester abrasible, used in the high pressure compressor of commercial gas turbines. The material response to cyclic heating and cooling, and the resulting changes in microstructure, as well as their associated failure mechanisms were investigated. It was found that the top surface layer of the abrasible liner degrades over its lifetime. During thermal cycling  $hBN$  is removed from the material's microstructure, which results in the degradation of the abrasible and increased brittleness of the top surface.

Furthermore, material cracking and delamination behaviour during service was successfully reproduced in the laboratory. The cracking and delamination observations made during overhaul, were replicated using cyclic water-quenching, but the spallation of abrasible material did not occur. Investigations into material properties and their influence upon the abrasible failure mechanics revealed, that soft M320 matched the observations made during engine overhauls. It could also be established, that the plasma spray process, grit blasting, surface treatment after deposition and the transient of the substrate affect the abrasible's performance and life-time, when heat cycled.

Some service casings suffer from premature liner loss. These unscheduled overhauls are costly and their number is desired to be reduced, if possible eliminated. In order to control the material failures, the stresses introduced into the abrasible seal during manufacturing need to be reduced, since this is one of main drivers for material cracking and delamination. Furthermore, it was established, that material at the top end of the hardness specification performed better in service. This is due to the fact, that more  $AlSi$  metal matrix is present in the microstructure and the  $hBN$  loss does not affect the material integrity as much as in soft material. 2D and 3D modelling showed temperature and strain profiles evolving during the quenching process. These show the areas of high strain, which are consistent with the crack initiation areas observed during testing.

It can be concluded, that M320 abrasible is a very complex material system, which is influenced by several parameters. This research project highlighted, how sensitive the failure modes are to changes in the material/substrate combination. Recommended is to increase the material hardness towards the upper end of the current specification (70 HR15Y), reduce the stresses in the substrate and the abrasible material by means of annealing stages after grit blasting, and temperature control during plasma spraying. Furthermore, it would be beneficial to reduce the machining of the abrasible's surface after deposition, as well as carrying out further research into the failure modes of abrasibles.

## Acknowledgements

I would like to take this opportunity to thank all the people who helped finishing this research project. Firstly, I would like to profoundly thank my supervisors Professor John Nicholls and Professor David Rickerby for all their help, time, knowledge and support over the last years. I am extremely thankful to Dr. Gyn Brewster and all his support over the years, which helped my understanding and the forthcoming of this project greatly.

For support in producing the samples analysed during this research project, I would like to thank John Gent and Mick Taylor. The work undertaken by Alexander Greatholder as a Rolls-Royce summer intern, was greatly appreciated and referenced in this report. Discussions with Paul Morrell were very helpful in taking this project forward. Furthermore, would like to thank Glen Pattinson for all his knowledge on abrasives, which he shared with me.

All the researchers and technicians from the National High Temperature and Surface Engineering Institute in Cranfield were fantastic whenever I needed help. Christine Chalk and Tracey Roberts who supported the work at the scratch tester and the RFDA. Tim Pryor and Lee Butler, who set up the furnaces in the laboratory and were available to lend a helping hand, whenever new test set-ups needed to be established. Tim Rose, who helped my understanding and assessing of material behaviour. Richard Wellman, who carried out part of the erosion testing.

When things got a little hectic towards the end of the project, James Fowler spent a long time in the preparation lab, polishing samples, which took much pressure off me - thanks a lot for that. A great, big thank you to everyone who supported the research to carry on, whilst I was pregnant and not allowed to enter the labs.

For all their time and knowledge, I would like to thank Christine Kimpton, Andrew Dyer and Xian Wei Liu. A special thank you to Mathew Kershaw, for everything he taught me about XRD before he left. For the support I received from Alex Skordos during the modelling part of this project I am extremely thankful and hope the modelling work will carry on.

I would also like to thank my family and friends without whom this report would not have been possible. First of all, I would like to thank my husband, Mark Craig, who I met here in Cranfield, for all his support and encouragement along the way. I was lucky enough to become pregnant and we now have a wonderful son - Sebastian.

Becoming a mother during the project was not easy and I would like to thank Gemma Blackwell, Lorena Cascant, Ruth Edwards, Katie Gates, Danielle Jordan and Louise Rix,



as well as Cathrine Kilpatrick for their help and support during the first year of Sebastian's life.

A big Thank You to Samantha Davies, who made my time in Derby fantastic, every time I was there - I miss our Wednesday evenings!

Thanks to the Angles & Devils for the craziness that was and is still to come - you are amazing my girls! Berta, Leti, Maria, Nina, Pilar and Sofia.

All the PhD and EngD students that were part of my time at Cranfield - It was great.

Ich möchte mich herzlich bei meiner Familie bedanken, für all die Unterstützung, die sie mir über die Jahre haben zukommen lassen. Meine Mutter Angelika, mein Vater Rüdiger, mein Bruder Gerrit und meine Schwester Saskia, die zwar nicht gleich um die Ecke, aber doch immer da sind. Danke für Alles!

# Contents

<b>Abstract</b>	<b>i</b>
<b>Acknowledgments</b>	<b>ii</b>
<b>Table of Contents</b>	<b>iv</b>
<b>List of Figures</b>	<b>vii</b>
<b>List of Tables</b>	<b>xii</b>
<b>List of Abbreviations</b>	<b>xiii</b>
<b>1 Introduction, Background and Objectives</b>	<b>1</b>
1.1 Introduction . . . . .	1
1.1.1 Overview of Rolls-Royce Abradables . . . . .	2
1.1.2 Rolls-Royce Sealing Strategy . . . . .	5
1.1.3 M320 Process Excellence Work . . . . .	5
1.2 Background to M320 - High Pressure Compressor Abradable Seal . . . . .	6
1.3 Objectives . . . . .	8
<b>2 Research Plan and Experimental Procedures</b>	<b>9</b>
2.1 Research Plan . . . . .	9
2.2 Experimental Procedures . . . . .	12
<b>3 Literature Review</b>	<b>24</b>
3.1 What is an Abradable Seal Coating? . . . . .	25
3.1.1 Abrasion Theory Applicable to a Gas Turbine . . . . .	25
3.1.2 Abradability . . . . .	27
3.1.3 Abradable Seals versus Thermal Barrier Coatings (TBCs) . . . . .	29
3.2 What Kind of Abradable Seal Coatings are used in a Gas Turbine Engine? . . . . .	30
3.2.1 Turbine Seal Coatings . . . . .	31
3.2.2 Compressor Seal Coatings . . . . .	32
3.3 Metco 320 - $AlSi + hBN$ + Polyester Compressor Abradable Seal Coating . . . . .	34
3.4 How is a Compressor Seal Coating manufactured? . . . . .	36
3.4.1 Grit-blasting . . . . .	36

---

3.4.2	Plasma Spraying . . . . .	37
3.5	What are the problems with abradable seals? . . . . .	39
3.5.1	Damage and Wear Phenomena . . . . .	39
3.5.2	Cracking of Abradable Seal Coatings . . . . .	42
3.5.3	Residual Stresses in Thermally Sprayed Coating Systems . . . . .	44
3.5.4	Methods to measure Residual Stresses in Coatings . . . . .	45
3.6	How is the Performance of Abradables Currently Assessed? . . . . .	50
3.6.1	Erosion Testing . . . . .	51
3.6.2	Tensile Testing . . . . .	51
3.6.3	Indentation Testing . . . . .	52
<b>4</b>	<b>Restricted and Classified Rolls-Royce Internal Reports</b>	<b>54</b>
<b>5</b>	<b>Initial Investigation into Metco 320 Material Properties</b>	<b>64</b>
5.1	Methodology . . . . .	64
5.2	Results and Discussion . . . . .	66
5.3	Summary and Conclusion . . . . .	75
<b>6</b>	<b>Cracking Behaviour</b>	<b>77</b>
6.1	Introduction . . . . .	77
6.2	Heat Cycling . . . . .	79
6.2.1	Sample Manufacture . . . . .	81
6.2.2	Crack-Development and Documentation . . . . .	82
6.2.3	Delamination and Material Loss . . . . .	83
6.3	Transient Analysis . . . . .	89
6.4	Crack Driving Parameters . . . . .	96
6.4.1	Grit Blasting . . . . .	96
6.4.2	Plasma Spraying . . . . .	98
6.4.3	Surface Machining . . . . .	99
6.4.4	Abradable Hardness HR15Y . . . . .	103
6.4.5	Precipitation within the Abradable . . . . .	104
<b>7</b>	<b>Material Degradation</b>	<b>111</b>
<b>8</b>	<b>Testing of Abradable Coatings</b>	<b>118</b>
8.1	Introduction . . . . .	118
8.2	Erosion Testing . . . . .	119
8.3	Scratch Testing . . . . .	122
8.4	Indentation Testing . . . . .	126
8.5	Hot Hardness Testing . . . . .	128
<b>9</b>	<b>Residual Stresses</b>	<b>130</b>
9.1	Introduction . . . . .	130

---

9.2	X-Ray Diffraction Analysis . . . . .	130
9.3	Resonance Frequency Damping Analysis . . . . .	132
9.3.1	Theory . . . . .	132
9.3.2	Experimental Analysis . . . . .	133
9.4	Finite Element Modelling . . . . .	135
<b>10</b>	<b>Discussion</b>	<b>139</b>
10.1	Cracking Behaviour . . . . .	141
10.1.1	Grit Blasting . . . . .	141
10.1.2	Plasma Spraying . . . . .	147
10.1.3	Surface Machining . . . . .	148
10.1.4	Abradable Hardness . . . . .	149
10.1.5	Transient Analysis . . . . .	150
10.1.6	Abradable Thickness Variation . . . . .	157
10.2	Material Changes/Degradation . . . . .	158
10.3	Material Testing . . . . .	165
10.3.1	Erosion Testing . . . . .	165
10.3.2	Scratch Testing . . . . .	168
10.3.3	Indentation Testing . . . . .	173
10.3.4	High Temperature Testing . . . . .	175
10.4	Failure Model . . . . .	176
<b>11</b>	<b>Conclusion</b>	<b>185</b>
<b>12</b>	<b>Further Work</b>	<b>188</b>

# List of Figures

1.1	Abradable Research Areas within Rolls-Royce . . . . .	3
1.2	Gas Turbine Engine and specific Abradable Areas . . . . .	4
1.3	Strategy Stages in the Development of Abradable Seals . . . . .	4
1.4	RR Road-map . . . . .	6
1.5	Interaction of Compressor Blades and Abradable Seal during Service .	7
1.6	M320 Microstructure . . . . .	8
2.1	Research Project Work- and Information Flow . . . . .	10
2.2	Sample Generation and Testing Chart for the Research Project . . . . .	10
2.3	Set-up for Compressed Air-cooling of Abradable Samples . . . . .	13
2.4	Set-up for Water-quenching of Abradable Samples . . . . .	14
2.5	Individual Quenching of Abradable Samples . . . . .	14
2.6	Erosion Tester with Backplate, Sample Holders and In-let Valve . . . . .	16
2.7	Scratch Tester with Tungsten-Carbide Ball Indenter . . . . .	17
2.8	Indentation Measurement with Elastic and Plastic Deformation Readings	18
2.9	Hot-hardness Tester with Heating Chamber . . . . .	19
2.10	Resonance Frequency Damping Analysis Machine and Sample Set-up	20
3.1	Schematic Cross Section of an Abradable Seal Coating in Interaction with the Blade . . . . .	26
3.2	Failure Mechanisms of Metco 320 according to Blade Tip Velocity and Incursion Rate . . . . .	27
3.3	Plasma Sprayed Coating with different Microstructure . . . . .	29
3.4	Abradables used in Gas Turbines dependent upon the Environmental Temperature . . . . .	31
3.5	Microstructure of Metco 320 Plasma Sprayed Abradable Seal Coating .	34
3.6	Influence of Mechanical Parameters on the Properties of Metco 320 . .	35
3.7	Rockwell Indentation on the Bond Coat Interface to assess Adhesion .	37
3.8	Theory of the Plasma Spraying Process . . . . .	38
3.9	Theory of the Layering System of Plasma Sprayed Coatings . . . . .	39
3.10	Crack Directions and Growth Preferences . . . . .	43
3.11	Temperature Profile of the Individual Coating Layers Growing during Plasma Spraying . . . . .	44
3.12	Micro-cracking of a Coating during Relaxation . . . . .	45

3.13	Modelling Results of NTSRS in a Plasma Sprayed Abradable . . . . .	47
3.14	Diffraction of X-Rays off the Lattice Structure and measuring Bragg Angle $\lambda$ and Lattice Spacing $d$ . . . . .	48
3.15	Changes in Lattice Spacing due to a Compressive Force ( $F_c$ ) . . . . .	49
3.16	Peak Shifts due to Stresses in a Material measured during XRD Analysis	49
3.17	Tilting of XRD Sample to analyse Multiple Directions of Grain Orientation	50
3.18	Possible Stress Graphs after Analysis of different $\Psi$ . . . . .	50
3.19	Schematic of the Working Mechanism of Tensile Testing Freestanding Abradables . . . . .	52
3.20	Schematic of an Indentation Test for a Pure Plastic and Elastic/Plastic Indent . . . . .	52
3.21	Schematic of an Indentation Scar left on the Surface after Unloading . .	53
4.1	Blade Expansion and Liner Interaction over a Flight Cycle . . . . .	55
4.2	Abradable Failures observed during Service . . . . .	57
4.3	Strain response of the abradable to flight cycles . . . . .	58
5.1	Schematic of the Working Mechanism of the Rig in Rapperswil . . . . .	65
5.2	Microstructures of a Hard and Soft Abradable Coating . . . . .	66
5.3	Erosion Tester along with Sample Holders . . . . .	67
5.4	Erosion scars on the surface of the abradable after $30^\circ$ and $90^\circ$ impact angle . . . . .	67
5.5	Comparison of the Results from the $30^\circ$ & $90^\circ$ Erosion Test . . . . .	68
5.6	Plot of the Erosion Rate as a Function of the Hardness . . . . .	69
5.7	Traces left on the Surface of an Abradable Coatings by the Scratch Tester; showing the Hard Coating on the Left and the Soft Coating on the Right . . . . .	69
5.8	Scratch Damage to a Hard Abradable Seal Coating - Fracturing . . . . .	70
5.9	Scratch Damage to a Soft Abradable Seal Coating - Smearing . . . . .	70
5.10	Weibull Analysis of the measured Erosion Rate Data . . . . .	71
5.11	Weibull Scratch Results of a Hard and a Soft Abradable . . . . .	72
5.12	Results of the ANOVA Analysis of the Data recorded during Abrasion Testing . . . . .	73
5.13	Plotted Mass-loss as a Function of the Abrasion Rate . . . . .	74
5.14	Interaction Phenomena during Abrasion Testing . . . . .	75
6.1	Forces acting upon the Abradable Material during Service . . . . .	78
6.2	Cooling Rates applied to the Material during Air-cooling and Water- quenching . . . . .	80
6.3	Furnace and Bath for Heat Treatment . . . . .	81
6.4	Outside - In Spraying of Abradable Samples . . . . .	82
6.5	Example of Crack Growth of M320 on a $35\text{ mm}$ wide Sample . . . . .	82

6.6	Material Failures due to Heat-Cycling . . . . .	83
6.7	Formation of Two different Material Layers . . . . .	84
6.8	Angling of the Cracks during Growth . . . . .	85
6.9	Confocal Microscope Images of Cracks forming and growing at the Surface . . . . .	86
6.10	Comparing Crack Depth and Width over Number of Cycles for a M320 Abradable by Confocal Microscope . . . . .	87
6.11	Cross Section after Heat Cycling with Mudflat and Delamination Cracks	87
6.12	Crack Propagation through the <i>hBN</i> Phase of the Abradable . . . . .	88
6.13	Set-up for inside-out Spraying of Abradable Material . . . . .	89
6.14	Curvature of the Water-quenching Samples . . . . .	90
6.15	Biot Number for increasing Thicknesses of 316, <i>Ti</i> , <i>Al</i> , <i>Cu</i> . . . . .	91
6.16	Delamination of Abradable from various Substrates . . . . .	92
6.17	Delamination of Abradable from various Substrates . . . . .	92
6.18	Grit-Blasting Procedure and Results . . . . .	96
6.19	Schematic Thermal Cycles of the Substrate during Spraying, depen- dent upon Spray Direction (in/out or out/in Spraying) . . . . .	99
6.20	Ground Samples using a 120 Grit Paper, having failed during Thermal Cycling . . . . .	101
6.21	Profile of a Crack in the Abradable Coating . . . . .	102
6.22	Total Crack Length as a Function of Coating Life, resulting from differ- ent Hardnesses of the Abradable . . . . .	103
6.23	Cracking after 40 Cycles of Water-Quenching . . . . .	104
6.24	Phase Diagram of <i>AlSi</i> Binary System with Emphasis on the Peritectoid	104
6.25	Material Microstructure Before (a) and After (b) Spraying . . . . .	105
6.26	Precipitation Increase and Agglomeration over Time . . . . .	107
6.27	Precipitation Agglomeration at the Bond Coat Interface . . . . .	108
6.28	Degradation of the Material and its Properties . . . . .	109
6.29	Service Cracking and Reproduction in Laboratory . . . . .	110
7.2	Thickness of the $X_1$ -Layer as a Function of the Number of Cycles . . .	111
7.1	Layering Effect observed using the SFEG . . . . .	112
7.3	EDX Maps of the $X_1$ and $X_2$ Interface . . . . .	113
7.4	EDX Results of the $X_1$ and $X_2$ Interface-Mapping, including Element Measurements . . . . .	114
7.5	XRD Scan of an Abradable Chip, cycled for 8 Cycles, from Top and Bottom . . . . .	116
7.6	Service and Laboratory Degradation . . . . .	117
8.1	Layers $X_1$ and $X_2$ visible in the Erosion Scar of water-quenched Samples	122
8.2	Schematic Working of a Scratch-test . . . . .	124

8.3	Subsurface Damage caused during Scratch Testing . . . . .	124
8.4	Damage caused by the Indenter during Scratch Testing . . . . .	125
8.5	Changes of z-Displacement due to Heat Cycling . . . . .	126
8.6	Typical Indentation Graph of Increasing Load and measured Displacement . . . . .	127
8.7	Changes of z-Displacement due to Heat Cycling . . . . .	129
9.1	M320 Comparison <i>hBN</i> -peak and <i>Si</i> -peak . . . . .	131
9.2	M320 Comparison <i>AlSi</i> -peak at $2\Theta=38$ . . . . .	132
9.3	Measured Frequencies in the RFDA . . . . .	134
9.4	Young's Modulus relating to the measured Frequencies between 3000–4000Hz . . . . .	135
9.5	Schematic of the 2D model . . . . .	137
9.6	FEA Modelling of the Water-quenching Process . . . . .	137
10.1	Total Crack Length on Samples with different Grit Blasting Direction . . . . .	142
10.2	Schematic of Surface Stresses and its Effect on the Sample's Deformation . . . . .	143
10.3	Schematic of Plume Size during Grit Blasting in Relation to the Substrate	144
10.4	Beam Theory for the Deflection of the Substrate and the needed Forces	145
10.5	Forces needed to deform a Substrate depending upon its Thickness and Preparation Direction . . . . .	145
10.6	Schematic of Surface Stresses in the Substrate after Grit-Blasting and their relief Mechanisms . . . . .	146
10.7	Crack Initiation on a Polished Abradable . . . . .	149
10.8	Crack Initiation Points according to Stress Distribution . . . . .	150
10.9	Crack Initiation Points in a defective Surface . . . . .	151
10.10	Area of Mudflat- and Edge Cracking as a Function of the Substrate's Thickness . . . . .	153
10.11	Total Crack Length on Substrates of Different Thicknesses and Materials	154
10.12	Crack Growth on a 316 Stainless Steel Substrate . . . . .	155
10.13	Crack Growth on a Titanium Substrate . . . . .	156
10.14	Schematic of the resulting Surface Stresses due to Abradable Thickness Variation . . . . .	158
10.15	Precipitation and Agglomeration of <i>Si</i> in the <i>AlSi</i> matrix . . . . .	160
10.16	$X_1$ -Layer Forming on the Surface, with the $X_2$ -Layer underneath . . . . .	161
10.17	Penetration Depths of varying Beam Intensities . . . . .	162
10.18	XRD Scan of an Abradable Chip: Top ( $X_1$ ) and Bottom ( $X_2$ ) . . . . .	163
10.19	Depletion Profile of a Chromium deprived high temperature alloy . . . . .	164
10.20	Erosion-rate over Time for 30° Erosion Testing . . . . .	167
10.21	Erosion-rate over Time for 90° Erosion Testing . . . . .	168



---

10.22	Scratch Testing Plot of z-displacement for 30 Scratches . . . . .	170
10.23	Cross Section of Scratch Scars before and after Heat Cycling . . . . .	171
10.24	Porous Microstructure of Scratch Tested Samples . . . . .	172
10.25	Surface of an Abradable Sample after Scratch and Indentation Testing .	172
10.26	Scratching Subsurface Damage as a Function of $X_1$ -Layer Thickness .	173
10.27	Plastic Deformation as a Function of the Number of Cycles, showing Cyclic Nature of Indentation Performance . . . . .	174
10.28	Temperature Profile of an Engine and Material Response . . . . .	177
10.29	Schematic of Crack Initiation and Growth . . . . .	177
10.30	Schematic of Samples for Laboratory Testing and Casing Geometry . .	178
10.31	Lifetime Model of a M320 Abradable Seal Coating . . . . .	178
10.32	Initial Drop of the Sample into the Water Quenching Bath . . . . .	180
10.33	650ms after the Drop into Water . . . . .	181
10.34	1.2s after the Drop into Water . . . . .	182
10.35	3.5s after the Drop into Water . . . . .	183
10.36	5s after the Drop into Water . . . . .	184

# List of Tables

2.1	Work-packages . . . . .	11
3.1	Overview of the Metco Materials and their Composition . . . . .	28
4.1	Current Abradable Seal Coatings used by Rolls-Royce . . . . .	62
4.2	Metal Matrix and Dislocator Material . . . . .	63
6.1	Sample Selection provided from Production . . . . .	79
6.2	Cooling Rates recorded for Air-cooling and Water-quenching . . . . .	79
6.3	Material Data for the Substrate Materials . . . . .	91
6.4	Crack Growth for M320 Abradable Samples with 3 mm Top Coat on 316- Stainless Steel Substrates . . . . .	93
6.5	Crack Growth for M320 Abradable Samples with 3 mm Top Coat on Ti- Substrates . . . . .	94
6.6	Crack Patterns for M320 Abradable Samples with 3 mm Top Coat and Varying Substrate Thickness . . . . .	95
6.7	Stresses in the Substrate after Grit-Blasting . . . . .	97
6.8	Influence of Grit-blasting Direction upon Cracking Behaviour . . . . .	98
6.9	Crack Development on Polished Surfaces . . . . .	100
6.10	Precipitation and Agglomeration data . . . . .	108
7.1	Peak Intensities of $X_1$ and $X_2$ Layer . . . . .	115
8.1	Erosion Rates [ $g/kg$ ] of Aged Samples Eroded at $30^\circ$ . . . . .	120
8.2	Erosion Rates [ $g/kg$ ] of Aged Samples Eroded at $90^\circ$ . . . . .	121
8.3	Results of Indentation Testing with a 50N Load . . . . .	128
9.1	Material Data used for the Modelling Stage . . . . .	136
10.1	Overview of Sample tested for Cracking and Delamination . . . . .	152
10.2	Biot Numbers of Al and Cu Substrates . . . . .	156
10.3	Biot Numbers of thin Stainless Steel Samples . . . . .	157
10.4	Penetration Depths for EDX Analysis . . . . .	162
10.5	Erosion Testing Experiments . . . . .	168
10.6	RFDA Results of Heat Cycled Material . . . . .	175

## List of Abbreviations

Abbreviation	Description
sfc	Specific fuel consumption
M320	Metco 320 <i>AlSi</i> – <i>hBN</i> -polyester Abradable Seal Coating
<i>AlSi</i>	Aluminium Silicon
<i>hBN</i>	hexagonal Boron Nitrite
HR15Y	Hardness Rockwell 15mm Ball Indenter
LPC	Low Pressure Combustor
IPC	Intermediate Pressure Combustor
HPC	High Pressure Combustor
HVOF	High Velocity Oxygen Fuel Process
RR	Rolls-Royce
TST-L	Turbine Surface Technology Ltd
FEA	Finite Element Analysis
OM	Optical Microscope
SFEG-SEM	Scanning Field Emission Gun - Scanning Electron Microscope
EDX	Energy Dispersive X-Ray Analysis
CM	Confocal Microscope
XRD	X-Ray Diffraction
RFDA	Resonance Frequency Damping Analysis
<i>NO<sub>x</sub></i>	Nitrogen Gases
TBC	Thermal Barrier Coating
BC	Bond coat
TGO	Thermally Grown Oxide
TC	Top coat
APS	Air Plasma Spraying
CS	Combustion Flame Spraying
TET	Turbine Entry Temperature
<i>cBN</i>	cubic Boron Nitride
RT	Room Temperature
<i>Ti</i>	Titanium Element No. 22

316	316 Stainless Steel
<i>Al</i>	Aluminium Element No. 13
<i>Cu</i>	Copper Element No. 29
<i>Ni</i>	Nickel Element No. 28
<i>Ar</i>	Argon Element No. 18
<i>H<sub>2</sub></i>	Hydrogen - inert gas
CET [ $\alpha$ ]	Coefficient of Thermal expansion - sign $\alpha$
d-spacing	Vertical displacement during scratch and indentation testing
$\Psi$	Tilting angle of the XRD stage
$\Theta$	XRD diffraction angle
UTS	Ultimate Tensile Strength
<i>E</i>	Young's Modulus
<i>h</i>	Convection coefficient
<i>k</i>	Thermal conductivity
v	Vertical grit blasting preparation
h	Horizontal grit blasting preparation
$\Delta\alpha\Delta T$	Thermal expansion mismatch
$\sigma_f$	Fracture Stress

## Chapter 1

# Introduction, Background and Objectives

### 1.1 Introduction

The performance of a gas turbine is subject to the airflow in the engine, which influences the specific fuel consumption (sfc). To improve the gas flow through the engine, over-blade leakage needs to be reduced. The clearance gap, which is installed between the blade tips and the housing is sealed with an abradable material. This abradable seal needs to be erosion resistant, not to wear off in the gas stream and be abradable to let the blades cut a path into the liner. It needs to be oxidation and corrosion resistant and easy to replace, when worn out.

In 1980 Bill and Ludwig [1], reported that the effect of possible blade damage during interaction with an abradable seal results in an increase of up to 10% in fuel consumption and the resulting over blade leakage can lead to up to 17% loss of engine power. Improving the abrasion process and maintaining the integrity of the blade, whilst ensuring sealing performance helps to reduce these additional costs.

Metco 320 is used as an abradable seal in the high pressure stages of gas turbine compressors. The material is used in temperatures between  $350 \rightarrow 450^{\circ}\text{C}$ , where  $450^{\circ}\text{C}$  represents the upper temperature limit of Metco 320. The abradable coating is made of three components: *AlSi* as the metal matrix to provide corrosion and oxidation resistance; hexagonal boron-nitride (*hBN*) as a dislocator to provide abradability and *polyester*, which is burned out after spraying to introduce porosity into the coating [2].

Metco 320 is sprayed to a hardness (HR15Y) of  $45 \rightarrow 70$ . Softer coatings contain more dislocator phase and they experience higher hardness reductions in service compared

to coatings at the higher end of the hardness scale. Due to the burn out of the polyester phase, the absorption capacity of the cutting force is reduced.

Inter-particle integrity and strength vary with the coating microstructure and hardness. The benefits of Metco 320 are a better corrosion resistance using *hBN* as a dislocator than the aluminium graphite abrasives. It shows a good erosion resistance and little blade tip wear or material pick-up [3].

When put into service, the material on the abrasion surface is subject to densification and the gradual reduction of the pore structure. Densification of the abrasible due to compression from the blade results in work-hardening of the abrasible seal. During the abrasion process the metal matrix is separated from the dislocator phase and the pores in the abrasible seal fill up with sliding material [4, 5]

The grain size of Metco 320 abrasible seals is characteristically about  $40\ \mu\text{m}$ , whereas the typical depth per pass are typically about  $0.003 - 5\ \mu\text{m}$  in service. This says that the typical blade passing over the surface is touching the outer edges of the grains, rather abrading them off completely. The cutting process is characterised by the rate of movement of the blade into the material, as well as the blade velocity [6]

When attempting to model the abrasion process, material features that have to be included into the model are the low yield stress in tension, the non-equal yield stress in compression as well as the distribution of stresses and strains through the coating [5]

It has been found that the corner radius of the cutting device has a major effect on the cutting force ratio [7]. Furthermore it has been discovered that a cutting corner radius of approximately  $0.05 \rightarrow 0.1\ \text{mm}$  is closest to the real conditions in the engine.

Research showed that only about 0.1% of the heat is taken by the debris, therefore heat gets absorbed by the seal material. Areas of work-hardening, due to the heating and cooling, were found to be the top  $0.1\ \text{mm}$  of the densified material [8, 9, 10, 11]

### 1.1.1 Overview of Rolls-Royce Abradables

Throughout the engine different materials and application methods are used for abrasible seals, dependent upon the temperature range the coating has to work in. In the fan section Aluminium Honeycombs and Graphite Filled Epoxy Pastes (EPWA) are used, which withstand temperatures of up to  $100^\circ\text{C}$  and allow the fan blades to cut through their

structure.

In the compressor M601 (LPC , Temp < 325°C), M320 (IPC , Temp < 480°C) and M314 (HPC , Temp < 800°C) are used. After the combustion chamber, in the turbine section of the engine, Honeycombs filled with *NiAl* are used for shrouded sections and CoNiCrAlY by HVOF for unshrouded sections. All these abrasives are subject to further research and in the future will either be improved or replaced.

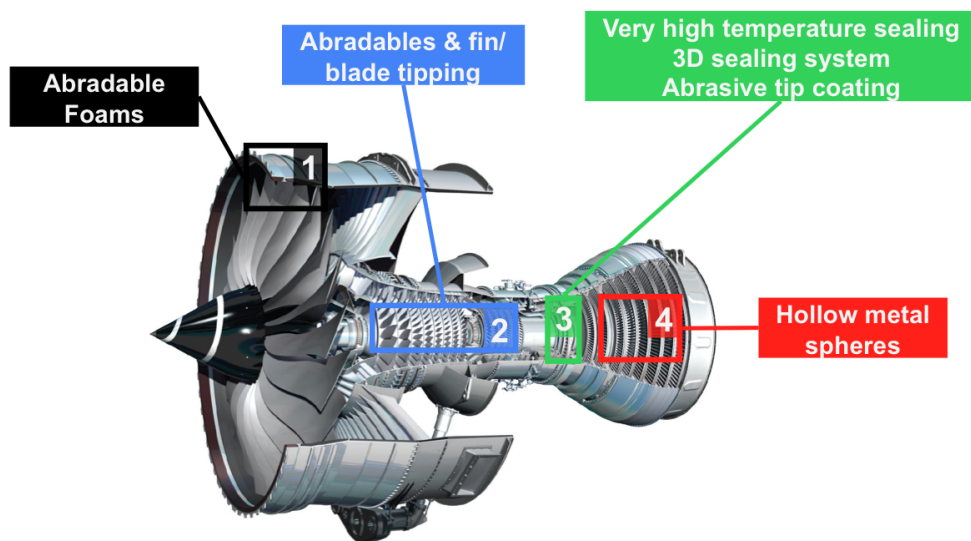


Figure 1.1: Abradable Research Areas within Rolls-Royce

The long term goals of the Rolls-Royce sealing strategy, with its vision of materials to be used, are shown in Figure 1.1. In order to improve sealing and material performance, Rolls-Royce supports research projects in all the areas shown in the figure above. Currently, research is carried out throughout the entire range of seal coating used in an engine. Figure 1.2 lists the current areas under investigation, as well as the sites within the company responsible for this technology.

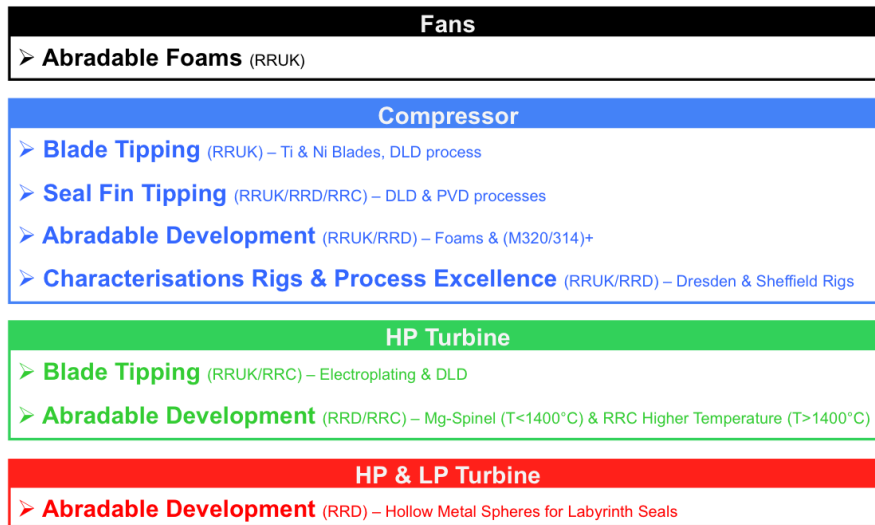


Figure 1.2: Gas Turbine Engine and specific Abradable Areas

This doctorate programme links in with the ongoing research strategy within Rolls-Royce and is part of the characterisation and process excellence work, which can be seen in the bottom bar in Figure 1.3. Highlighted in the green box is the annual report, reviewing the methods and expected results from this research.

### Compressor Sealing Programmes

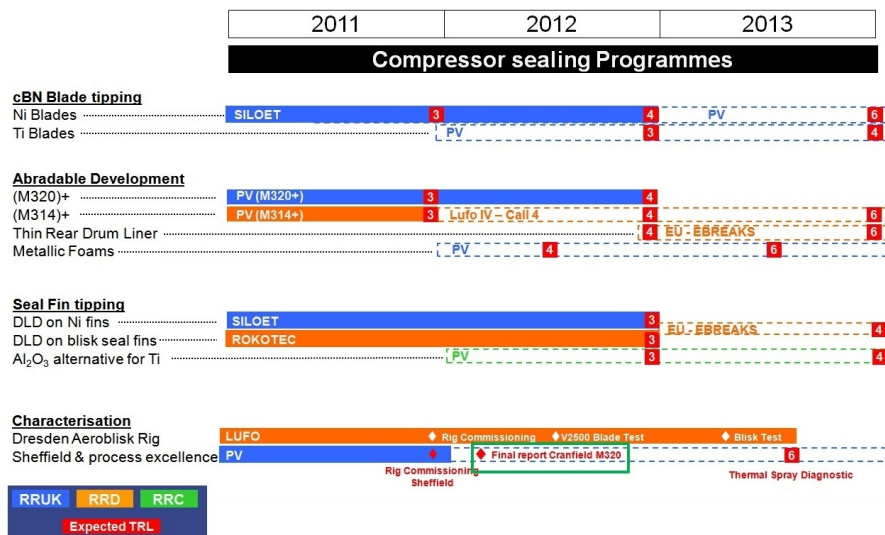


Figure 1.3: Strategy Stages in the Development of Abradable Seals



### 1.1.2 Rolls-Royce Sealing Strategy

Sealing strategies are put into place in order to deal with the current issues arising in service or future product requirements. These are of different nature, depending upon the material in use. Metco 320 (M320) is difficult to spray and expensive due to the *hBN* used as a dislocator. During service the material cracks and delaminates and causes engine stalls. Metco 314 (M314) hardens over time and therefore is responsible for blade tip abrasion and cracking. Sherritt Gordon erodes rapidly and needs refurbishing before the planned overhaul interval.

In Rolls-Royce's vision for the future, metallic foams with a metallic filler may be used in the fan area, followed by an *Al*-Graphite abradable for the entire compressor section. For the unshrouded turbine stages, *Mg*-Spinel/TBT 429 is under development, along with a newly designed high temperature abradable and an improved *SiC/Cr* blade tip coating.

The requirements a new compressor seal coating should meet have been established and are listed below:

- Good abrasability with minimum heat generation during rub while being resistant against corrosion and erosion
- Cost reduction
- High temperature capability
- Height of 2 → 15 *mm*
- Closed cell size < 1 *mm*
- Reduced or equal cost to relative to honeycomb
- Direct replacement of existing honeycombs

### 1.1.3 M320 Process Excellence Work

In Figure 1.4, the layout of the Rolls-Royce process excellence and material development plan is outlined. This research project occupies a box further to the right, describing the cracking mechanisms and residual stresses within the coating (See Figure 2.2 on page 10). The process capability box refers to work which is currently undertaken at TST-L, whereas the right box list studies and testing work to be undertaken by outside companies and in universities.

### SM320/D2223 Process Excellence and Material Development

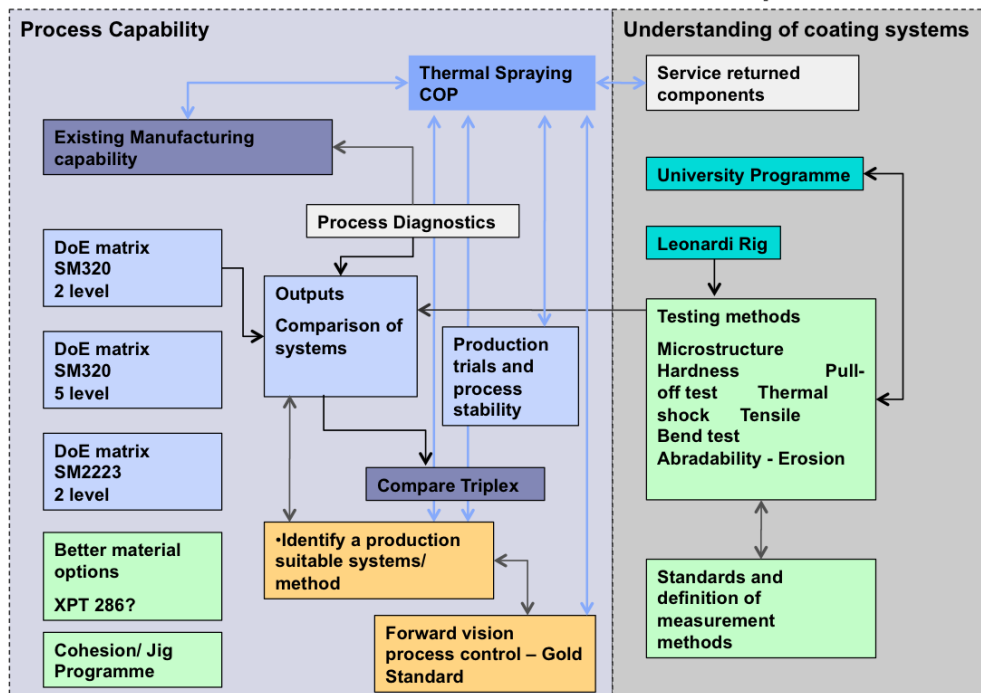


Figure 1.4: RR Road-map

To increase the understanding of abrasible sealing systems and their failure modes, work from different areas within Rolls-Royce has to be combined. It is vital to understand the mechanisms of abrasible failure, to know what each material is capable of delivering in service and how the manufacturing process influences performance. The entire working behaviour of the material system needs to be understood in order to act before any material fails in the engine.

It has been recognised that room temperature testing is not sufficient to describe materials working at elevated temperatures in the engine. At temperature the abrasible softens and changes its properties, which can only be analysed when heat treated and tested at temperatures similar to the working environment.

## 1.2 Background to M320 - High Pressure Compressor Abradable Seal

During service, the interaction between the blade and the casing causes the abrasion failure of the seal material. Figure 1.5 shows the cold stage of a gas turbine, with no interaction between blade and abrasible (a), as well as the initial abrasion of the seal

taking place during service. With increasing temperature, the blades expand and make contact with the abradable (b), followed by further blade expansion and the abrasion of the seal coating (c). Once the engine cools down, the blades shrink, leaving behind a rub path, which can be seen in the abradable (d).

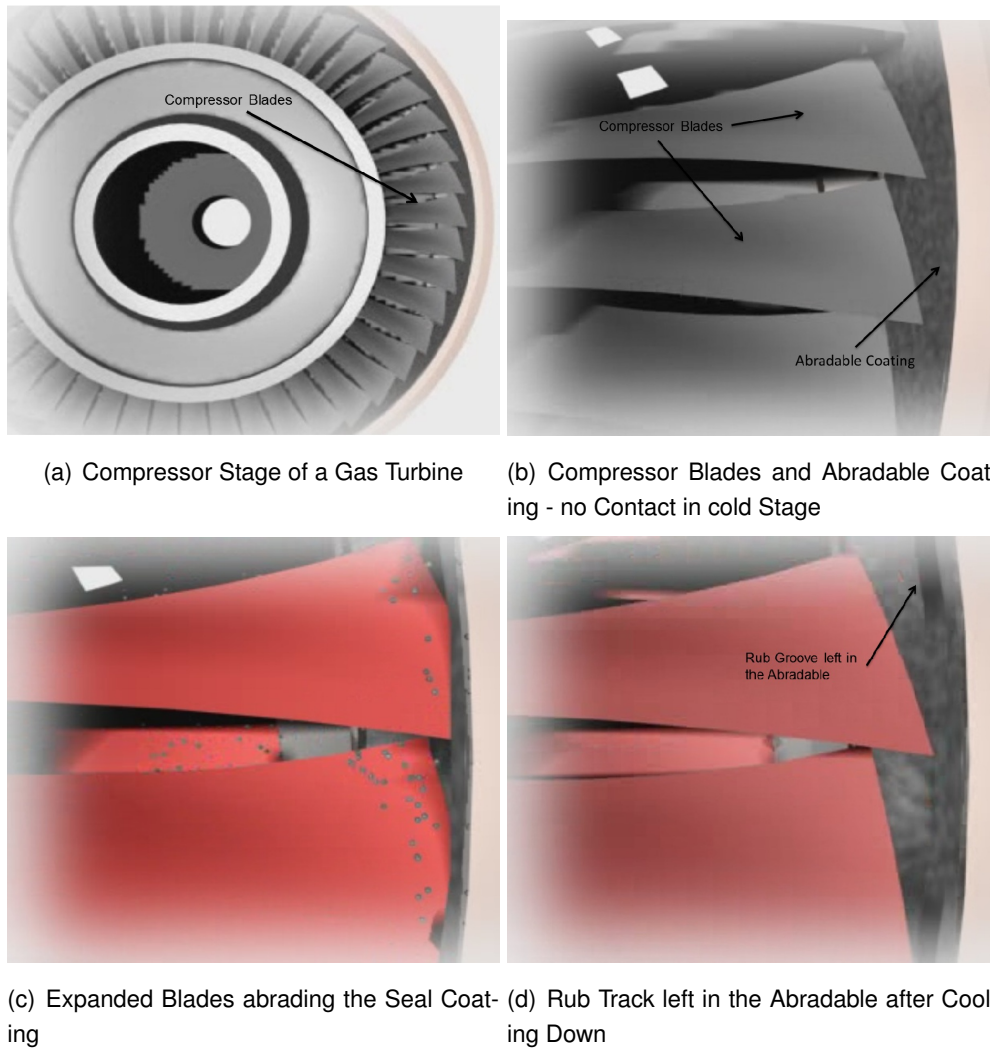


Figure 1.5: Interaction of Compressor Blades and Abradable Seal during Service

It is recognised that some M320 compressor coatings fail prematurely in service due to cracking, spallation and delamination. This results in a loss of efficiency because of poor sealing and potential stalling or surging of the engine. Identifying major crack drivers and failure modes will help understand the failure process and generate a material's database upon which key performance parameters can be identified and taken into consideration when spraying an abradable liner.

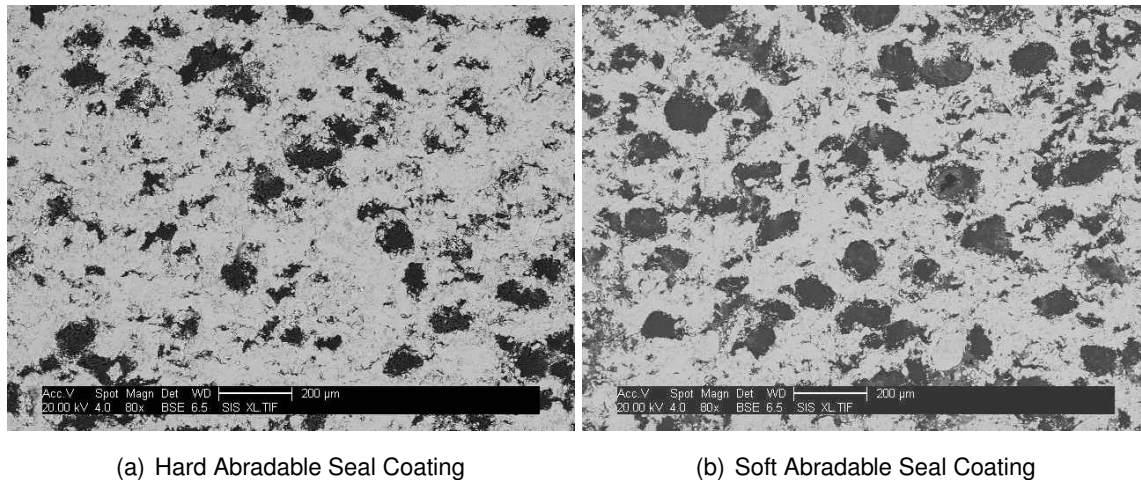


Figure 1.6: M320 Microstructure

The development of measures and test methods for the shopfloor in order to ensure manufacturing produces material which performs consistently and identify quality issues is required. Along with mechanical testing methods, Finite Element Analysis (FEA) will be used to generate stress models for the abradable seal and casing system to support component lifing. It is known that a mismatch in thermal expansion coefficients leads to stresses building up along the interface which promotes cracking and delamination.

### 1.3 Objectives

Having identified the problems with M320 as a material system, the objectives for this thesis were outlined as:

1. Identify the main parameters that control (define) the cracking behaviour of M320,
2. Establish a testing method for the shopfloor to assess abradable coating performance,
3. Asses how ageing influences the abradable's properties,
4. Develop a FEA model for M320 cracking / delamination,
5. Create a M320 failure model.

## **Chapter 2**

# **Research Plan and Experimental Procedures**

### **2.1 Research Plan**

The desired properties of an abradable seal can be identified from published data, either confidential Rolls-Royce data, or data in the open literature. Abradable samples were sprayed at TST-L with performance evaluation carried out at Cranfield University and Rolls-Royce plc. in Derby. Linking the microstructural changes in the material to the changes in mechanical properties was the most important step towards creating a model for abradable coatings (see Figure 2.1).

In order to achieve the creation of a FEA model, the generation of material properties/performance data and test procedures/sequences had to be thoroughly organised and documented. In figure 2.2 the used test procedures are listed, along with the knowledge which was gained during testing and sample analysis.

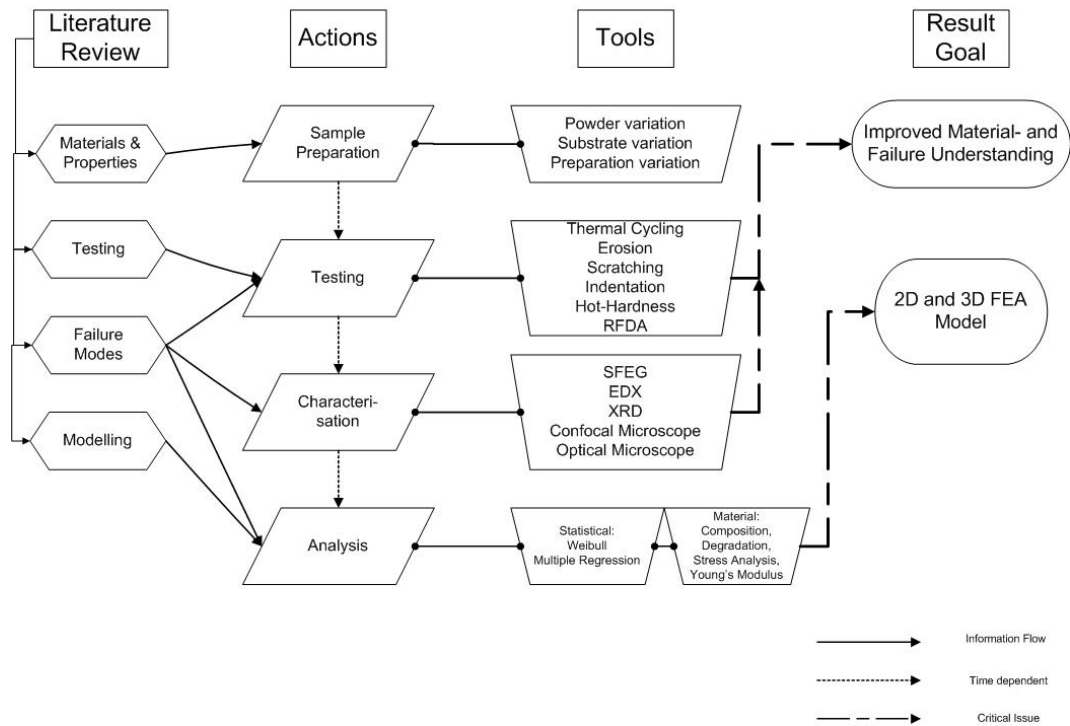


Figure 2.1: Research Project Work- and Information Flow

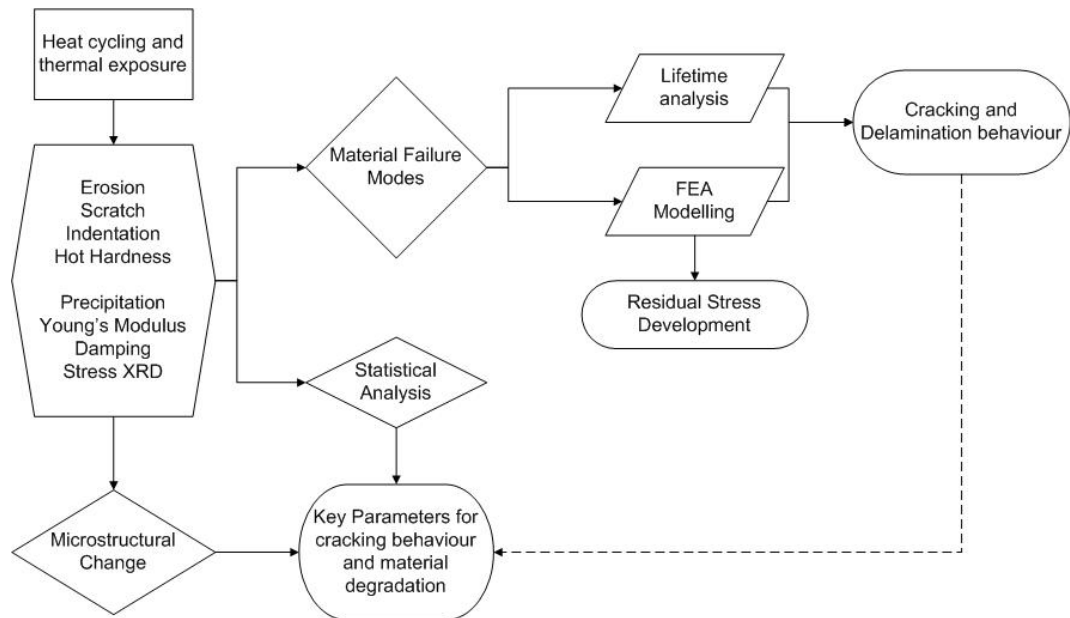


Figure 2.2: Sample Generation and Testing Chart for the Research Project

## Identified Work-packages

Testing and characterising the abradable sample supplied by TST-L was organised into different work-packages which flow together on different levels in order to serve the overall goal of this research project which was: identifying the main crack parameters and developing a failure model for the material's performance in service.

Table 2.1: Work-packages

Work Package	Name	Input	Output
Cracking Analysis see Chapter 6			
I	Failure Analysis	Thermal Cycling	Crack and Delamination Failure
II	Grit Blasting	Horizontal and Vertical Grit Blasted Samples	Crack length as a function of cycles
III	Transient Analysis	Varying Substrate Thicknesses	Differences in mode and time to failure
Material Testing see Chapter 8			
IV	Erosion	Different Hardnesses and Aged Material	Erosion Rate as a function of time/age
V	Scratching	Cycled Samples	Assessment of material degeneration
VI	Hardness	Aged & Cycled Samples	HR15Y as a Function of age
VII	Indentation	Cycled Samples	Assessment of Material Degradation
VIII	Precipitation	Aged & Cycled samples	Precipitation and Agglomeration as a Function of time
IX	Hot Hardness	Aged Samples	Hardness as a Function of Time and Temperature
X	Abrasion	Aged & Cycled Samples	Cutting Performance as a Function of Age
Residual Stresses see Chapter 9			
XII	X-Ray Diffraction	Cycled Samples	Residual Stresses as a Function of Age
XII	RFDA	Cycled Samples	Young's Modulus and Damping as a function of Age and Temperature
XIII	Modelling	Parameters obtained during testing	2D/3D FEA Model

## **2.2 Experimental Procedures**

The open literature on abradable seal coatings is very limited due to confidentiality from aero-engine companies and the leading research institutes. Research is carried out for specific applications in gas turbines and in order to gain a competitive advantage, which means companies prefer not to disclose their investigations and findings.

In order to assess the cracking behaviour and material changes within the abradable liner, thermal aging studies were carried out, focusing on material performance and microstructural changes to the seal coating. Initially heat cycling was pursued in an automated cycling furnace, which cooled the samples using compressed air, directed at the material through adjustable nozzles. This set-up was changed to a standard heating furnace and water-quenching bath after the first test run with 3 samples, as the air-cooling took too long (750 cycles) to introduce cracking into the material, when cooled using an air blast.

To evaluate the degradation in material performance over its lifetime, heat cycled material was investigated by assessing its erosion resistance, scratch and indentation performance. The samples were analysed under the Optical Microscope (OM), Scanning Field Emission Gun - Scanning Electron Microscope (SFESEM) - including Energy Dispersive analysis of X-rays (EDX) - and Confocal Microscope (CM) to assess the microstructural changes in the material as a function of time at temperature.

Stress measurement were carried out using X-Ray Diffraction (XRD) and the damping and Young's Modulus were assessed using Resonance Frequency and Damping Analysis (RFDA). These properties were also looked at as a function of the material's age, to see whether degradation affected those characteristics.

Finite Element Analysis (FEA) was used to model the behaviour of the abradable samples in order to see whether the observations in the laboratory could be predicted by computer simulation.

### **Heat Cycling - Air Cooling**

Heat Cycling (air cooling) was carried out firstly in a bespoke test apparatus at Cranfield University, using compressed air cooling nozzles to cool the sample. Three samples could be placed into the machine by making a wire-basket to hold the material. Compressed air-nozzles, situated at the lower end of the drop cylinder, projected compressed air onto the surface of the sample. Figure 2.3 shows the compressed air-cooling set-up at Cranfield University.



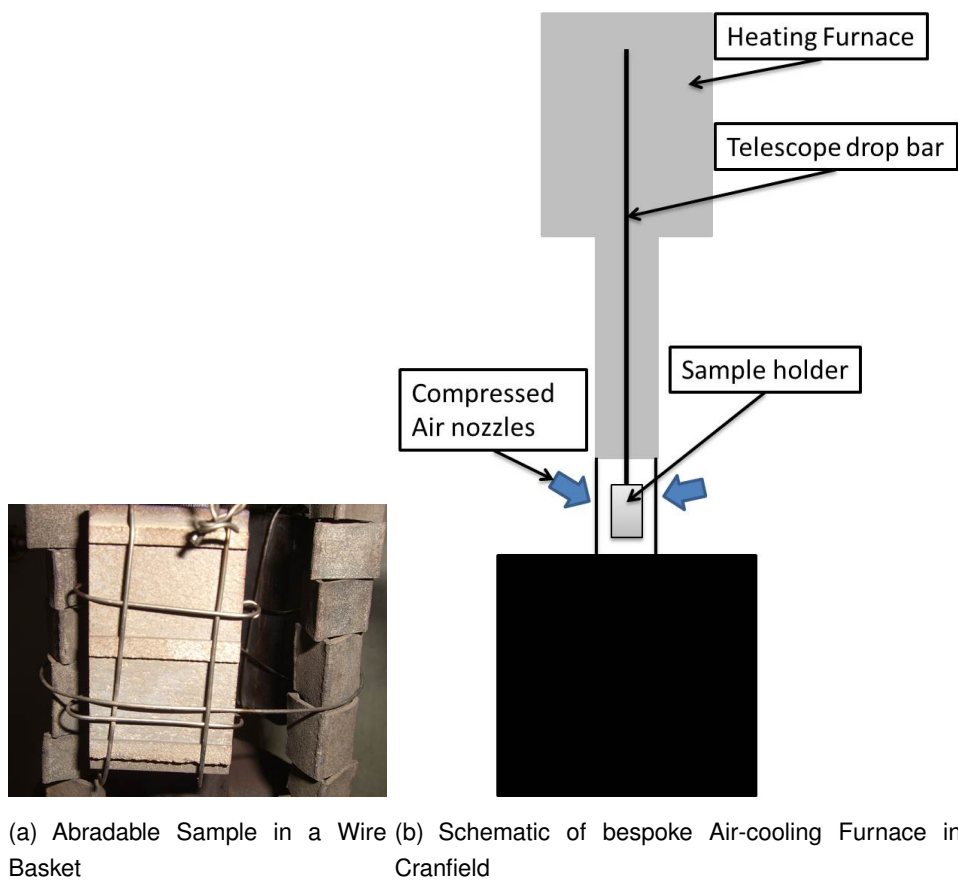


Figure 2.3: Set-up for Compressed Air-cooling of Abradable Samples

Three samples were loaded into the machine and heat cycling was carried out at  $450^{\circ}\text{C}$  for  $90\text{ min}$  with subsequent  $5\text{ min}$  of compressed air cooling. Every  $50\text{ cycles}$  the samples were removed from the machine and investigated for cracking of the abradable.

### Heat Cycling - Water-quenching

An Elite Thermal Spray Ltd. heating furnace - HT/50/SS/500/DIG - was used to heat the samples to  $450^{\circ}\text{C}$  for  $90\text{ min}$  and a water-quenching bath ensured cooling rates of up to  $110\text{ K/s}$ . Figure 2.4 shows the Air-oven used for the water-quenching process and the samples in the furnace.

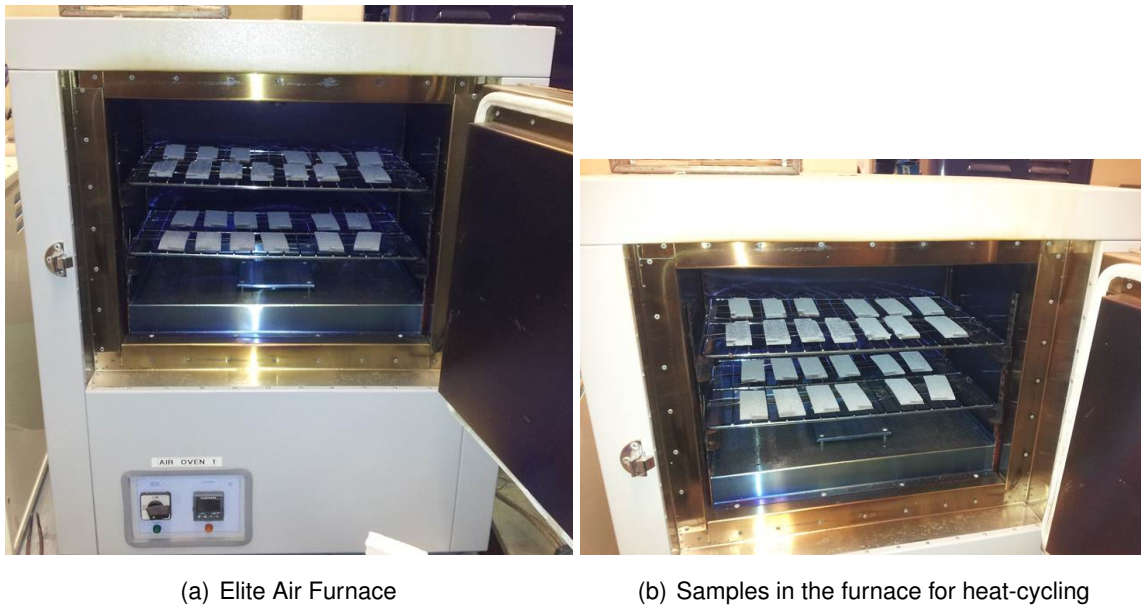


Figure 2.4: Set-up for Water-quenching of Abradable Samples

Once the samples had been in the furnace for  $90 \text{ min}$ , they were removed individually, using tongs, and placed into the sieve of the water-quenching bath. Figure 2.5 shows a sample being held with tongs and the water-quenching bath used at Cranfield University.

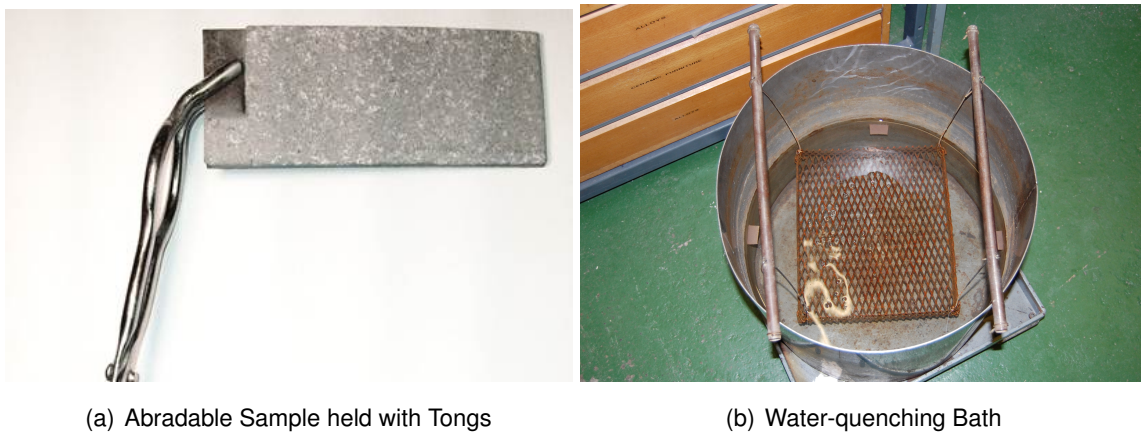


Figure 2.5: Individual Quenching of Abradable Samples

After water-quenching the samples needed to be dried completely before they could be placed into the furnace again. This is due to the fact that the expanding water in the microstructure could break the seal material and introduce damage into the coating. After each cycle the samples were dried in a baking furnace at  $80^\circ$  for  $45 \text{ min}$  and then placed into the Elite air-furnace for the next heat cycle. For further details of the heat-cycling process see Section 6.

## Erosion Testing

was carried out at Cranfield University, using a bespoke machine, which provided a steady gas flow with a pressure of 6 bar. Initial tests were carried out using *SiO*-sand as a erodent with a particle size of 76 – 212  $\mu\text{m}$  and a feeding rate of 4 g/s, resulting in particle speeds of 80 – 120 m/s. Since fine *SiO*-sand was classed hazardous, alumina was used as an erodent. The  $\text{Al}_2\text{O}_3$  particles had a size range of 95 → 120  $\mu\text{m}$  which accelerated to 85 → 110 m/s in the 6 bar gas stream. A feeding rate of 4 g/s was used for  $\text{Al}_2\text{O}_3$  erosion testing.

Samples could be adjusted to give an impact angle of 30° or 90° in the machine, with the possibility of testing 6 samples within one set-up. In figure 2.6 the sample holder, as well as the erosion machine can be seen. The sample holder with stages for 30° and 90° testing is fixed to the back plate of the test machine. The screws used to clamp the samples to the holders can be seen in the picture.

After each run, the samples were taken out of the machine and weighed. By plotting the mass loss over the weight of erodent used, the erosion rate could be calculated. These results can be found in Section 8.2.

In order to ensure the samples were placed into the same position, the position of the screw was marked on each sample when they were first adjusted on the stage. This way, an impact on the same spot could be carried out during every run.

The gas pressure was generated in a pressure vessel and the directed towards the samples. On its way towards the back plate and the adjusted samples, the air passed the in-let valve, where the erodent particles were injected into the gas stream. Due to the fine nature of the erosion particles, an extractor was placed over the back end of the machine during testing, in order to suck away the exiting particles.

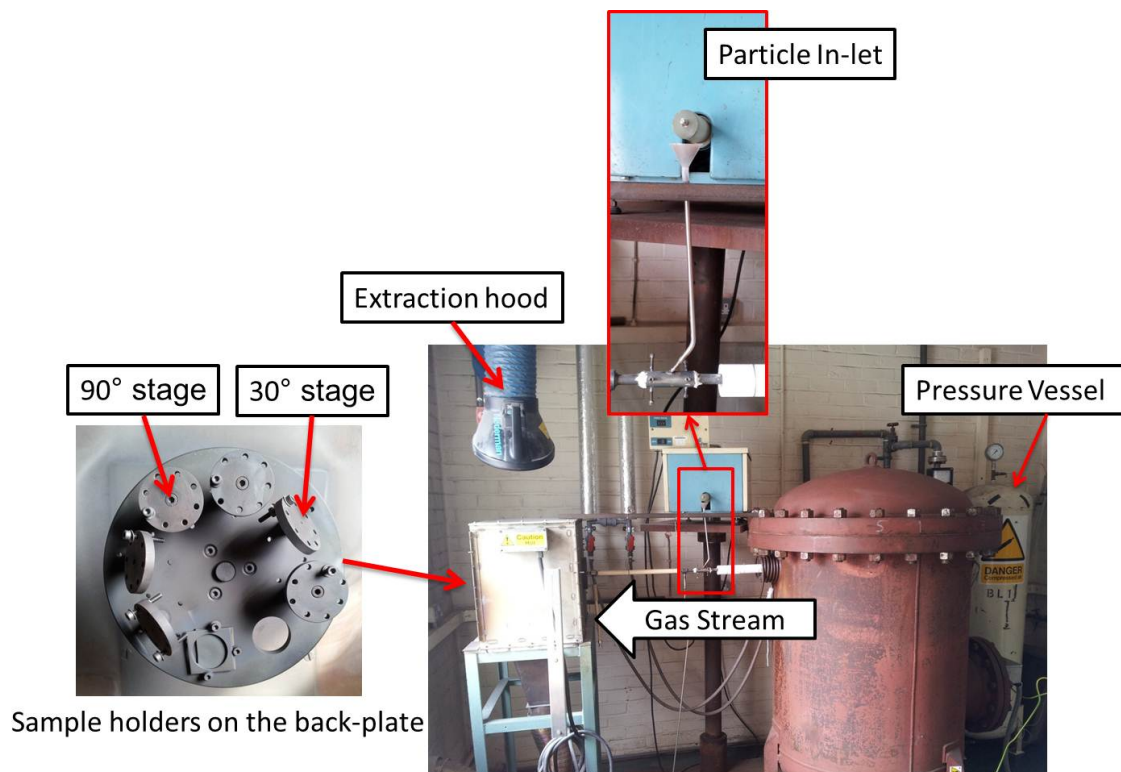


Figure 2.6: Erosion Tester with Backplate, Sample Holders and In-let Valve

### Scratch Testing

was carried out on a Teer Coating Ltd. machine, Model ST 3001. A spherical tungsten carbide indenter with a  $5\text{ mm}$  ball was used for the tests. The tip of the ball was given as  $200\ \mu\text{m}$ . The samples were adjusted in the machine by horizontally clamping them with the screws provided and afterwards the arm with the indenter was lowered onto the surface of the material and the test was performed by the table sliding under the tungsten carbide ball. The tests were carried out with a  $20\text{ N}$  load and a scratch length of  $10\text{ mm}$  for 30 passes with the indenter. The tester recorded acoustic emission, friction and z-displacement; where the displacement was used as an indication for the material performance. The machine, with the table for samples and the loading arm, as well as a close up on the indenter, are shown in Figure 2.7.

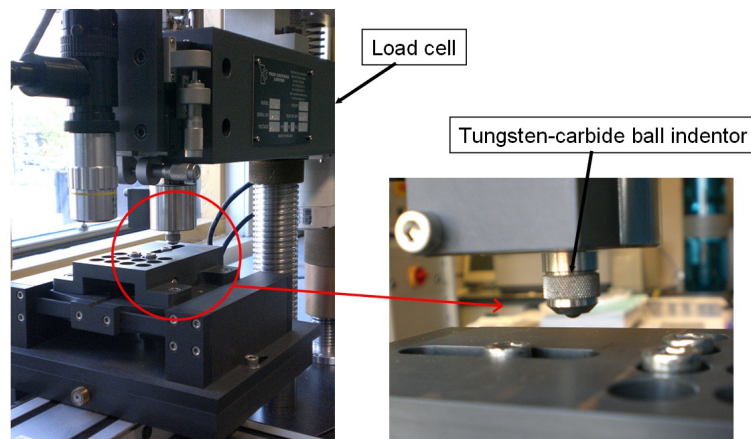


Figure 2.7: Scratch Tester with Tungsten-Carbide Ball Indenter

Results of the scratch testing investigation is provided in section 8.3.

### Indentation Testing

Ball indentation testing used the same machine as the scratching described previously, but in this case no movement of the sample was applied, resulting in a single point of indentation. A loads of  $20\text{ N}$  was used to indent the material and produce a loading and an unloading curve measuring the vertical displacement. From these, elastic and plastic work of the material could be calculated. A loading curve can be see in Figure 2.8, with the elastic and plastic deformations indicated. Please see section 8.4 for indentation results.

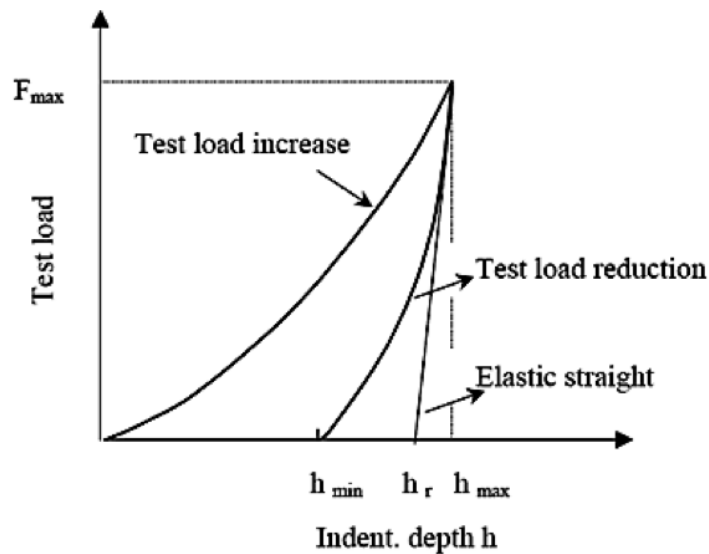


Figure 2.8: Indentation Measurement with Elastic and Plastic Deformation Readings [12]

### Hot Hardness Testing

Hot hardness testing was carried out using a machine manufactured by AE - The Associated Engineering Group, Cawston House, Rugby, Warwickshire. The individual parts were resourced from Carl Zeiss Jena (Microscope), Ernst Leitz GmbH (Objective Lenses), Eurotherm Ltd. (Furnace), L.M. Van Moppes and Sons (Indenter) and Wesley Coe Ltd. (Seals).

A sample of maximum  $10 \times 10\text{mm}$  was loaded into the heating chamber of the machine (see Figure 2.9). The sample was surrounded by heating elements, which could reach temperatures of up to  $900^\circ\text{C}$ . The indenter is adjusted above the sample using the two wheels in the front of the machine for movement into the X- and Y-direction. High adjustments are not possible, hence the sample needs a gentle polish to ensure an even surface for the test procedure.

The chamber is heated up to temperature and 3 – 7 indentations were to be placed onto the surface of the sample. Due to the failure of a thermal couple, only one test sequence at  $250^\circ\text{C}$  could be carried out.

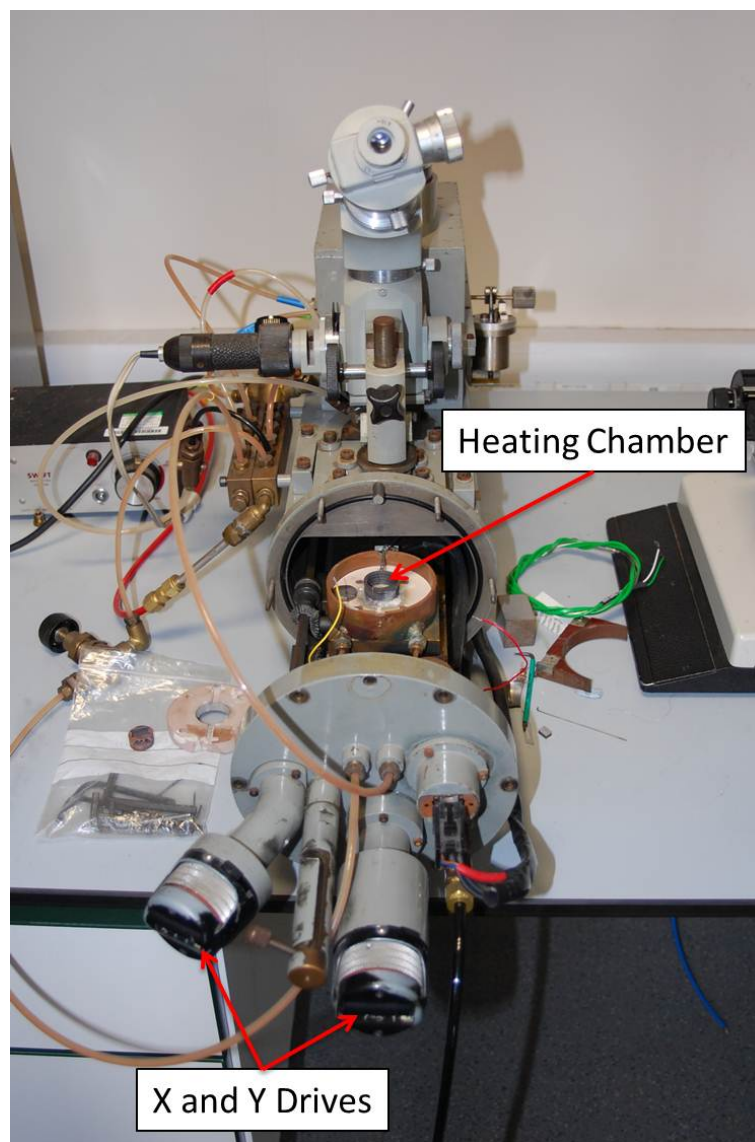


Figure 2.9: Hot-hardness Tester with Heating Chamber

### XRD - Phase Identification

XRD was used to identify elements in the material in the top  $50 \mu m$  surface layers. A Siemens D5000 X-Ray Diffractometer was used to analyse the material and identify  $AlSi$ ,  $hBN$  and  $Si$  phases in the abrasible structure. Measurements were carried out from  $10 - 90^\circ$  with a continuous movement, a step size of  $0.02$  and a step time of  $1 s$ .

## XRD - Residual Stress Measurements

A Siemens D500/501 high angle X-Ray Diffractometer was used to carry out stress measurements. An  $AlSi$  peak was identified at  $2\Theta = 138 - 139$ , which was used for the stress analysis. A scan from  $2\Theta = 136 - 142$ , with a continuous movement, a step size of 0.01, a time step of 8 s and 11 angles of  $\Psi$  was carried out for each stress analysis. The stage was stationary and the spray direction of the abradable top coat was in line with the X-ray source and detector. Data for the stress analysis can be found in section 9.2.

## RFDA

Resonance Frequency Damping Analysis was used to measure the damping capacity and Young's modulus as a function of temperature. An IMCE - Integrated Material Control Engineering - RFDA HTVP 1250 was used to carry out the testing and temperature profile of  $2^{\circ}C/min$  heating, a 10 min hold and  $1^{\circ}C/min$  cooling was used.

The free-standing abradable samples were weighed and measured for length, width and thickness. To achieve best results, the sample has to be as square as possible, due to the vibration of the material. The vibration waves travel through the material, bouncing off the edges and traveling back through the sample. Should the sample be irregular in shape, the recordings would be faulty, due to the mis-readings of 'returning' waves.

The frequencies of the waves traveling through the material and their damping were recorded and plotted against the temperature. The set-up of the machine and the sample to be tested can be seen in figure 2.10.

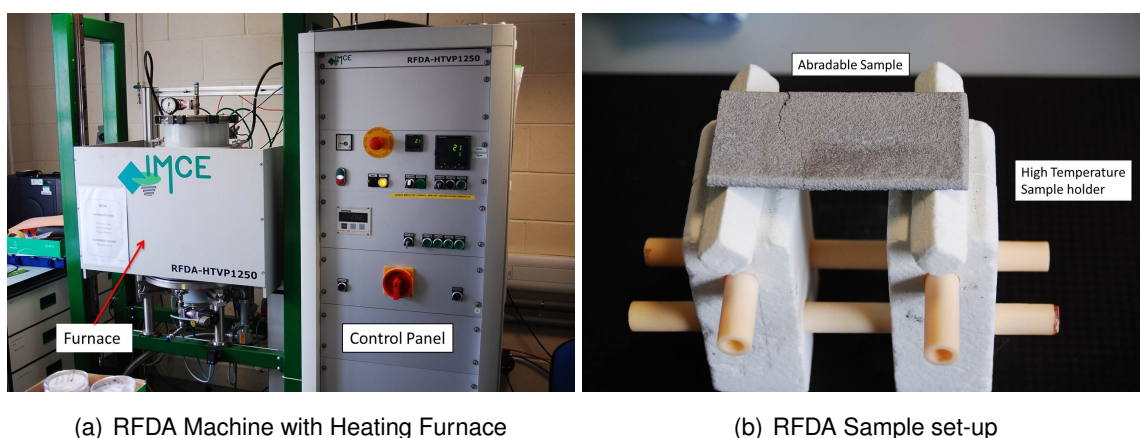


Figure 2.10: Resonance Frequency Damping Analysis Machine and Sample Set-up



The sample was hit by the stylus every 5 *min* and the vibration frequencies and damping capacity was recorded.

The recorded frequencies could be converted into the Young's modulus of the tested material, following the equation:

$$E = 0.9465 * \left(\frac{m * f_f^2}{b}\right) * \left(\frac{L^3}{t^3}\right) * T_1$$

The frequency recordings and calculated Young's Moduli are documented in section 9.3.

## Sample Preparation

For sample analysis under the microscopes, abradable samples had to be mounted and polished, which was carried out in the material's laboratory at Cranfield University, as well as Rolls-Royce Derby. The specimen were sectioned and vacuum mounted, using Struers EpoFix resin and hardener. To ensure there was no air in the porous material, the mixture of resin and hardener was placed into a Townson and Mercer vacuum oven and evacuated for 90 *s*. The evacuation was repeated 3 times to ensure elimination of any trapped air in the mounting mixture. Afterwards, the evacuated resin-hardener mix was poured into the containers with the samples. With the samples being in place, the evacuation process was repeated, this time for 120 *s*, again 3 times. The containers with the samples and mounting resin were removed from the vacuum oven and left to cure over night.

After 24 *h* the resin had set and polishing could be carried out, using Struer's automated Motopol polishing machine. Ensuring the sample holder rotated counter-clockwise and the samples were adjusted in the holder, ensuring compressive grinding and polishing. 6 – 8 samples were polished at any one time and a pressure of 4 *kN* was applied per sample. For 2x2 *min*, the samples were ground with 120, 240, 1200 and 2500 grit paper (each stage was repeated twice, so 2x2 *min*, before moving to the next grit size).

After the grinding, polishing was carried out using the same polishing machine. A 6  $\mu\text{m}$  polish for 5 *min*, followed by a final 0.05  $\mu\text{m}$  Silicate polish for 5 *min* concluded to sample preparation process.

## Optical Microscope

Optical microscopes were used to see how the microstructure changes over the material's exposure to heat and subsequent quenching. Two different optical microscopes were used to investigate the samples. Firstly, a Nikon Opiphot with a magnification range of  $2.5 \rightarrow 40$  and secondly, a Nikon Eclipse ME600 with a magnification range of  $5 \rightarrow 50$ , both situated in the metallurgy laboratory at Cranfield University. It was chosen to use two different microscopes, due to the fact that the Nikon Optihop was capable of magnifying the material by only  $2.5x$ , which provided great overview of the material, whereas the higher magnification of  $50x$  on the Nikon Eclipse, was useful when investigating the precipitation agglomeration.

Cross sections, previously ground and polished as described above, were used to assess the material- and microstructural changes due to heat cycling and water-quenching.

## Confocal Microscope

The confocal microscope enables the measurement of surface topography, using a laser to scan the material and produce surface maps. An Olympus Lext with a Stable Table TS150, an Olympus OLS3000 Laser and Olympus MM6-ASPS Photography software was used for this analysis. This equipment is available at Cranfield University in the metallurgy laboratory.

The 3D surface imaging of the confocal microscope is possible due to laser reflection off the surface, which is converted into a topography picture. Crack initiation and widening was documented using the confocal microscope and the results of the investigation can be found on page 84.

## SFEG-SEM & EDX

Scanning Field Emission Gun - Scanning Electron Microscopy (SFEG-SEM) and Energy-dispersive X-ray spectroscopy (EDX) was carried out using a Philips XL30 SFEG, to look at the material's elementary composition, as well as microstructural features. The machine is situated in the microscope of the water-sciences building suite at Cranfield University. Beam intensities between  $5 - 25 \text{ kV}$  were used to investigate the material, with magnifications of  $80 \rightarrow 4000x$ . Backscattered electron were used to analyse the material composition and generate EDX maps.

**FEA**

Finite Element Analysis (FEA) was carried out using PATRAN / Marc 2008 software, to simulate the rapid quenching of an abrasible coating on a 316 stainless steel substrates. Documented material data were used for the stainless steel substrate and those for the abrasible were calculated from bulk data or using data generated in the laboratory. All data and results are presented in Section 9.4.

## Chapter 3

# Literature Review

The performance of gas turbine engines is important for today's airline companies. Improving the efficiency of an engine reduces the specific fuel consumption (sfc) and thereby reduces the fuel expenses, as well as  $NO_x$ -Emissions [13, 14]. Therefore the interest of the industry into improving the performance and lifetime of the aero engine's material is given.

When introducing new materials into a gas turbine, it has to be ensured, that those can withstand the increased compressor delivery temperature and the increased turbine entry temperature. But the performance of the sfc of an engine is dependent upon the thermal, as well as the propulsive efficiency.

During service and with increased gas temperatures, the parts within an engine expand [6, 15]. Due to this expansion, a clearance gap between the blade tip and the casing has to be installed during manufacturing. This gap is sealed with an abradable seal coating. Should the gap remain then the air can flow over the blade tip during service. The engine loses pressure and therefore performance. The loss of pressure due to over-tip leakage increases linear to the clearance gap [7]. Misalignment of the rotor blades, start-ups, stops, vibrations and thermal, as well as centrifugal effects influence the rotation and therefore the cutting path through the seal coating.

For good clearance control a material which combines the contradicting material properties for erosion resistance and abrasibility has to be created [4]. These material properties are most important when developing a new seal coating [16]. Additionally, the coating has to withstand the environmental influence of the gas turbine, as well as delivering abrasibility without damaging the blade [17].

### 3.1 What is an Abradable Seal Coating?

Current abradable seal research is based on five important areas of the working environment, blade tip material and geometry, blade tip speed, incursion rate and life expectation of the coating [2]. The gas passing through the engine varies, depending upon the location of the engine. It could be run at hot dusty location, like a desert, or a moist and salty environment, when close to the sea. No matter, where an engine is run, the seal coating has to perform to the same standard.

A material seal was found to improve clearance control, and decrease the blade tip - casing clearance, much better than any mechanical means could; and also corrects the clearance should the casing be deformed and lateral movement is present [15]. The abradable seal is required to close the gap between the blade tip and the casing path without damaging the blade during the interaction [17].

A coating on the casing may also supply protection against hot corrosion and oxidation from the working environment [18]. The porous material reduces the surface temperature of the casing material and thereby protects the casing against oxidation and corrosion [19].

Summarising, an abradable seal coating is a material which closes the clearance gap, to prevent over blade leakage; it is resistant to erosion from the hot gas and the contaminant particles entering the engine; it is abradable, when interacting with the blade tip and it acts as a thermal barrier to protect the casing material from thermally induced damage.

#### 3.1.1 Abrasion Theory Applicable to a Gas Turbine

The theory of abrasion with respect to turbine service must account for the blade being able to expand during service and encroach upon the abradable coating; where it first slides over the surface and whilst continuing to extend, starts to rub away sealing material. The dislocator phase of the coating is designed to shear easily and release metal splats through contact with the blade. The debris created is released behind the blade since the speed of the interaction is too high for chips to form [15, 20] (see Figure 3.1).

Material transfer to the blade is supposedly minimised by using a high blade tip speed and high incursion rate which results in wear debris being generated. The discharged material is not harmful to the following stages of the compressor and burns out in the

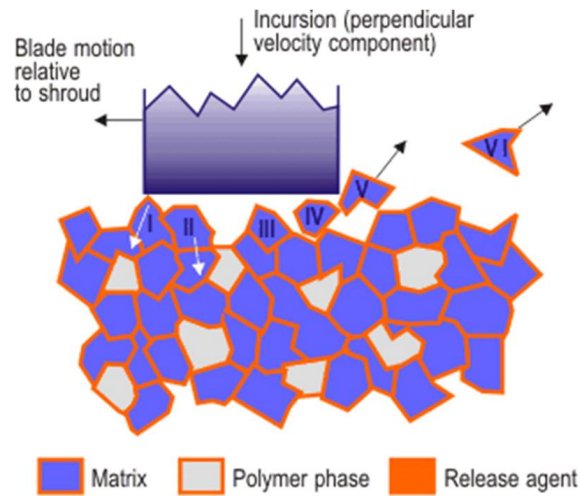


Figure 3.1: Schematic Cross Section of an Abradable Seal Coating in Interaction with the Blade [20]

combustor. An abradable with lower hardness produces smaller debris [6] but is also more susceptible to erosion from foreign objects streaming into the engine.

In the engine the pores and voids within the abradable liner act to transfer the energy of the rubbing process into the metal matrix [21]. Instead of shearing and releasing, the material is dragged into sharp angles due to large plastic deformation of the surface layer. The deformation of the material roughens the surface layers [8] and creates a harder surface for subsequent blade/abradable interaction. The surface hardens as a result of the metal matrix being separated from the dislocator phase and the pores in the abradable seal fill up with sliding debris material [4].

The frictional heating during metallic transfer of material from and to the blade leads to densification and thermal cracking of the abradable liner [8]. The grain sizes of Metco 320 abradable seals are characteristically about  $40 \mu m$ , whereas the typical depth per blade pass is typically about  $0.003 - 5 \mu m$  in service. Tests at the abradable facility in Baden, Switzerland, were carried out with blade tip speeds between  $200 \rightarrow 410 m/s$  and an incursion rate between  $2 \rightarrow 2000 \mu m/s$ . The blade tip speed is the velocity of the rotating blade tips once the engine runs and the incursion rate characterise the expansion of the blades, due to temperature and centrifugal forces, into the seal material.

The cutting process is characterised by the movement of the blade into the material, as well as the blade velocity [22]. It has previously been shown, that Metco 320 fails due to different mechanisms depending upon the incursion rate and blade tip velocity. Figure 3.2 summarises the failure mechanisms for different tip speeds and incursion rates [23].

Metco 320 wear map	200 m/sec	250 m/sec	300 m/sec	360 m/sec	419 m/sec
1 $\mu\text{m}/\text{sec}$	Rubbing Blade pick up due to adhesive transfer Creep Gramophone formation Very high temperatures			Rubbing Blade wear Gramophone formation Very high temperatures	
50 $\mu\text{m}/\text{sec}$					
100 $\mu\text{m}/\text{sec}$	Some adhesive transfer Gramophone formation	Micro-rupture Some gramophone formation			
200 $\mu\text{m}/\text{sec}$	Micro-rupture No Blade pick up or wear No Gramophone formation Densification due to high incursion rates				
500 $\mu\text{m}/\text{sec}$					
1000 $\mu\text{m}/\text{sec}$					
2000 $\mu\text{m}/\text{sec}$					

Figure 3.2: Failure Mechanisms of Metco 320 according to Blade Tip Velocity and Incursion Rate [23]

Due to the characteristics of the abradable surface, the contact area between the blade tip and the seal is only a small fraction of the blade tip area [24]. This decreased contact area increases abradability and therefore the balance of abradability and erosion resistance [25].

### 3.1.2 Abradability

The abrasion mechanism for Metco 307 (M307), observed by Maozhong [4], shows that Ni-particles are dragged into sharp angles along the sliding direction. The resulting lips of the coating work-harden over time and break off.

The abrasion process introduces large particle deformation, the metal matrix separates and the pores disappear, leaving behind a surface behaving more like a bulk material. The wear behaviour can be split into two different mechanisms, that of adhesive and abrasive wear.

Adhesive wear is more severe than abrasive wear and it also increases with increasing test load. Of course, the wear mechanisms will vary for different coatings. The material removed with the blade tip is the key to sealing performance [6]. If polyester is used as a dislocator, then the heat treatment will burn it off and produce voids. These help to absorb the cutting force during blade interaction [13]. The defined key parameters for abradability are: particle size, chemistry, hardness and deposition efficiency.

In addition to these key parameters, environmental and material related factors influence the performance of the abrasible coating. The most important performance drivers are: thermal expansion & grain size, thermal conductivity, particle to particle cohesive strength, volume percentage porosity, oxidation level & distribution and oxidation properties [26].

In order to characterise an abrasible material, the temperature capabilities are important to measure. The parameters listed above have to be considered and optimised, when creating a new abrasible seal coating, but to distinguish and rank different materials the performance under service conditions is most important [27].

As the material has to work in environments at elevated temperatures, thermal capabilities are essential. Furthermore, the composition and the particle distribution are vital for the coating's performance [16]. It was found [21], that *AlSi - hBN* delivers better abrasible properties than *NiCrAl - bentonite*, due to the properties of the metal matrix and the solid lubricant.

The pores on the surface of the coating act as crack initiators and therefore are responsible for the separation of the grains from one another. Thus, the structure of the coating is weakened by the porosity and abrasibility is promoted [28].

During this blade and seal interaction, the blade modulus is higher than the seal modulus. On the rubbing surface the pores are reduced and the modulus changes gradually over the duration of the rubbing process. The resulting compression of the coating leads to densification and a reduction of the number and size of the pores.

Table 3.1 lists the main abrasible seal materials which are currently in use in the compressor stages of Rolls-Royce gas turbines.

Table 3.1: Overview of the Metco Materials and their Composition

Material	Metal-Matrix	Metal-Matrix	Dislocator	Additive	max. Temp.
Metco 307	75%Ni		25%Gr		480°C
Metco 310	57%Al	8%Si	35%Gr		480°C
Metco 313	40%Al	5.5%Si	45.5%Gr	9%org. - b.	415°C
Metco 601	60%Al/Si - alloy			40%Polye.	325°C
Metco 314	79%Ni4Cr4Al		21%Bentonite		815°C
Metco 320	80%Al/Si		20%hBN		480°C
Sherrit Gordon	75%Ni		25%Gr		450°C

Gr - Graphite, Polye. - Polyester, org.-b. - Organic Binder



### 3.1.3 Abradable Seals versus Thermal Barrier Coatings (TBCs)

As stated in the name, TBCs (with internal air cooling) are used to protect parts of the engine from high temperatures, as well as corrosion and oxidation. Indeed, some thermal barrier coatings have been used as high temperature abrasives, particularly plasma sprayed  $ZrO_2 - 8wt\% Y_2O_3$  [29]. Due to the nature and the materials used for TBCs, manufacturing and testing can be compared to abrasives, as long as microstructural differences and expectations towards the seal coating are taken into consideration.

Both coatings can be manufactured, using plasma spraying (see section 3.4.2), which means the process and materials used can be compared. Looking at the resulting coating and its microstructure, reveals very different images depending on TBCs or seal coating (see Figure 3.3).

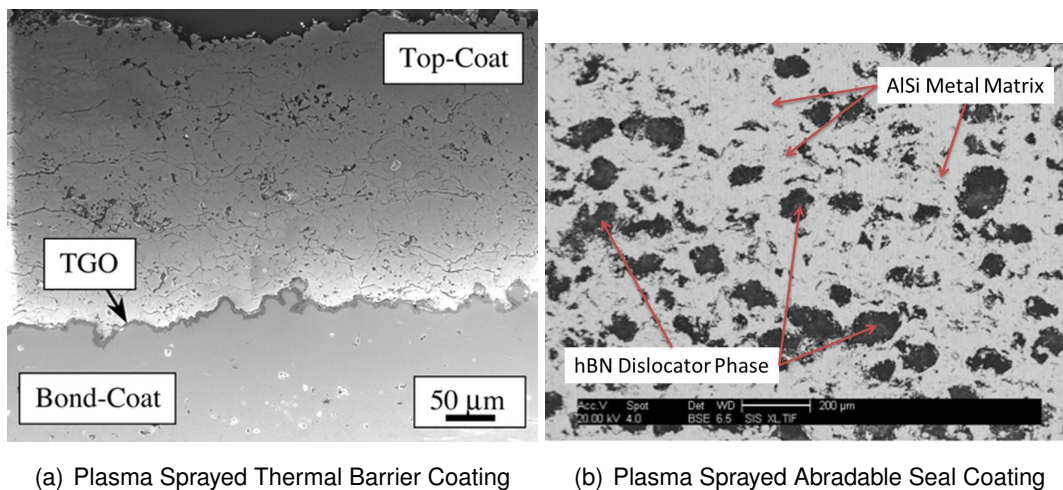


Figure 3.3: Plasma Sprayed Coating with different Microstructure

Furthermore, both coatings are subject to engine environments and erosion, corrosion and oxidation attack. The testing methods developed for TBCs can be applied to seals as well, but the results of those tests are not comparable due to the differences in microstructure.

Failure mechanisms observed in TBCs also occur in abrasives, which indicates that the material response to the working environment is similar even though microstructures vary. This also suggests that failure modes and models can be compared - again bearing in mind that material properties play a big part in modelling.

## 3.2 What Kind of Abradable Seal Coatings are used in a Gas Turbine Engine?

Different possibilities of applying protective coatings to engine parts are available. Plasma spraying and high velocity oxygen fuel processes are both used for applying abradable seals. In both processes semi-molten particles adhere to a metal substrate and each other as the layers build up, which will protect the surface for a longer life.

McIntyre [30] described the High Velocity Oxygen Fuel Process (HVOF) in which thermal energy is produced by fuel and oxygen burning. In this process kinetic energy is dominant over the use of thermal energy, which results in the flight velocity and high speed impact being enough to ensure the plastic deformation of the powder particles upon impact, allowing them to interlock.

In plasma spraying an electric arc contained in a nozzle is used to dissociate and ionise the inert gas passing through it forming a plasma. A second gas controls the ionised gas stream, which directs the gas flow towards the substrate, keeping the ionised gas contained within a funnel [31]. This increases the temperature of the carrier gas and therefore alters the melting capacity of the plasma. When the powder is injected into the gas stream, it accelerates towards the substrate, becomes partially molten and the particles flatten upon impact on the surface [32].

Abradable seals are usually applied using either Air Plasma Spraying (APS) or Combustion Flame Spraying (CS). The difference between CS and APS is the transportation of the material from the feedstock to the substrate material. In CS the powder for the coating is fed into a hydrogen flame and the molten material is then accelerated towards the substrate, using a thermal spraying gun. In APS the particles of the powder are fed into an inert, ionised gas, which transports the powder towards the parts to be coated [33]. The differences in the resulting coatings between these two methods are mainly the resulting porosity, some oxidation and the stability of the process [34].

An abradable flash document by Sulzer Metco [3] states that different materials are used in different stages of the engine, dependent upon their temperature capabilities (see Figure 3.4). The *AlSi* based abradable research in this study is highlighted and will be discussed in more detail in section 3.3.

Other fabrication methods for abradable coatings are casting and diffusion bonding / brazing. During the casting process, polymer based abradables are cured in an oven. Limitations for this method are the size of the oven and the precise work that is needed to apply the coating to the requested area [2]. In diffusion bonding and brazing honeycombs and

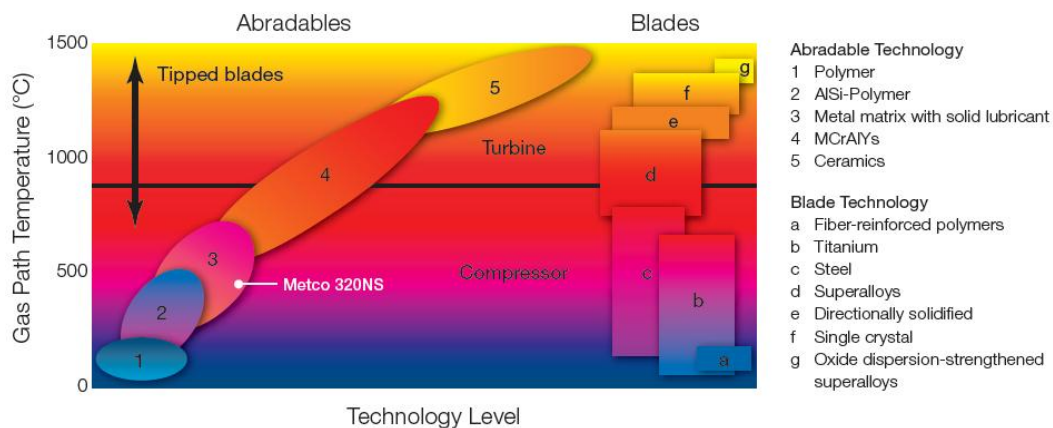


Figure 3.4: Abradables used in Gas Turbines dependent upon the Environmental Temperature [3]

felt-metals are fitted to the designated area with the help of a furnace heat treatment.

### 3.2.1 Turbine Seal Coatings

Abradable seal coatings in the turbine section need to withstand higher temperatures than those in the compressor section. With a turbine entry temperature (TET) of about 2000 K ceramic coatings are most likely to survive the harsh working environment of the turbine section. Bardi et.al. [35] investigated  $CoNiCrAlY / Al_2O_3$  which was applied using APS, alongside  $NiCrAlY /$  graphite produced via laser cladding. The ceramic filler in the metal matrix is supposed to promote brittleness of the material and thereby abrasability. Top coats with medium to high porosity show good abrasability against  $cBN$ -tipped blades.

Sporer et. al. [29] tested  $MCrAlY$ -type abrasables in comparison to  $ZrO_2$ -based materials and found that the ceramic coating reduces the maximum metal temperature by 20% as well as a 34% reduction in thermal misalignment. Furthermore, ceramic abrasables were shown to reduce the area within the coating, where yield strength was exceeded.

These results encouraged the research of alternative ceramic materials, which can be used as seal coating in the turbine. Dysprosium-oxide ( $Dy_2O_3$ ) stabilised zirconia exhibited a good cyclic life, with no material loss after 100 engine cycles and a 1.8% increase in power-output, as well as 1.3% improvement in overall engine efficiency [29].

Another material system subject to research is Zirconia-24%Magnesia [36], which provides good temperature stability and low hardness which promotes abrasion. Applying the coating using plasma spraying results in a dense material and thereby high erosion

resistance, but low abrasability. The lower spraying velocities of combustion spraying promote higher levels of porosity, but the cohesion of the resulting coating is insufficient for this application.

Research shows that the addition of fine alumina powder during combustion spraying improves the melting of the coating material and introduces a fine dispersed aluminum-oxide phase in the coating. The abrasable seal produced shows improved performance in lab-tests up to  $1000^{\circ}C$ .

Another material used to seal the turbine section of the engine is a honeycomb structure. The blade interaction with a honeycomb abrasable requires the blades to have cutter teeth on their tips to deform the walls of the individual cells during the abrasion process [37]. The honeycomb structure is made of either Hastelloy X or Haynes 214, which survive temperatures of  $950^{\circ}$  and  $1200^{\circ}$ , respectively. The tight labyrinth mesh reduces the performance degradation and maintains a good clearance [15].

The oxidation problems of Haynes 214 resulted in efforts to introduce  $FeAlCr$ -alloy as an alternative material, which has the advantage of a self-healing oxide-layer. Hollow sphere and fibre structures are also subject to research as future abrasable seals in the turbine section. The lifetime of hollow spheres is expected to be improved compared to honeycombs due to reduced heat transfer possible, whereas the abrasion capabilities and sealing properties of the fibre structure is believed to be superior [37].

### 3.2.2 Compressor Seal Coatings

The thermal spraying process can be used to apply porous coatings with the help of a polymer phase which is burned out by applying a post spraying heat treatment. This polymer, or binder burn out, causes pores in the microstructure and aids the abrasion process. Different types of material can be applied by this process [2], achieving individual properties and temperature capabilities for example:

- Aluminium + Polymer
  - usable in the temperature range from room-temperature (RT) up to  $320^{\circ}C$ ,
  - no layering occurs during deposition,
  - can be used for  $Ti$ -blades, but when applied incorrectly blade wear can occur,
  - age hardening occurs at room temperature and the hardness can go up by 10 pts (on the Rockwell Scale).

- Aluminium + filler
  - coatings can operate above  $320^{\circ}\text{C}$  and pure *AlSi* abrasives can operate up to  $400^{\circ}\text{C}$ ,
  - with a solid-lubricant as filler the coating can operate up to  $450^{\circ}\text{C} - 490^{\circ}\text{C}$ ,
  - *AlSi - BN* is found to be similar to *AlSi*-graphite, whereas *Al*-graphite coatings can be subject to local debonding,
  - the downside, both *BN* and graphite modified aluminium based abrasives are stiffer than the polymer modified abrasives, which promotes micro-rupture.
- *Ni*-based flame spraying
  - *Ni - 25%* graphite, commonly used in jet engines, can be used up to  $650^{\circ}\text{C}$  for short-term exposures,
  - the coating has to have a hardness (HR15Y) of about 50, which leads to a low erosion resistance, but using this coating in the final compressor stages helps prevent *Ti*-fires.
- *CoNiCrAlY -BN - Polymer*
  - good oxidation and corrosion resistance up to  $950^{\circ}\text{C}$ ,
  - can not be deposited by APS and does not transfer to the blade,
  - thermal expansion similar to most of the casing materials, with a  $850^{\circ}\text{C}$  oxidation temperature of the *BN*,
  - can operate over the complete compressor temperature range and with most blade materials

New technologies now allow the continuous monitoring of the application process, the analysis of the interaction of process parameters and the final coating quality allows for ever improving service performance. It was found, that a linear influence of argon flow, current and hydrogen flow upon the quality of the seal coat exists [32].

An ideal seal coating would be created, when all the particles impacted the substrate completely molten and flattened upon impact. But the particle size of the injected powder varies and therefore the smaller particles move faster than the bigger ones. The higher speed of the small particles causes a decreasing heating capacity of the material [38].

A wide variety of particles sizes results in a porous coating, whereas cooler spraying temperatures create denser areas [32]. Higher temperatures, of the gas stream, can lead to increased hardness because the temperature affects the lay-down rate of the particles.

### 3.3 Metco 320 - $AlSi$ + $hBN$ + Polyester Compressor Abradable Seal Coating

Metco 320 is used as an abradable seal in the high pressure stages of a gas turbine compressors. The material is used at temperatures between  $350 \rightarrow 450^\circ C$ , where  $450^\circ C$  represents the upper temperature limit of Metco 320. The abradable is made of three components:  $AlSi$  as the metal matrix to provide corrosion and oxidation resistance; hexagonal boron-nitride ( $hBN$ ) as a dislocator to provide abradability and polyester, which is burned out after spraying to introduce porosity into the coating. The microstructure of the sprayed material can be seen in Figure 3.5.

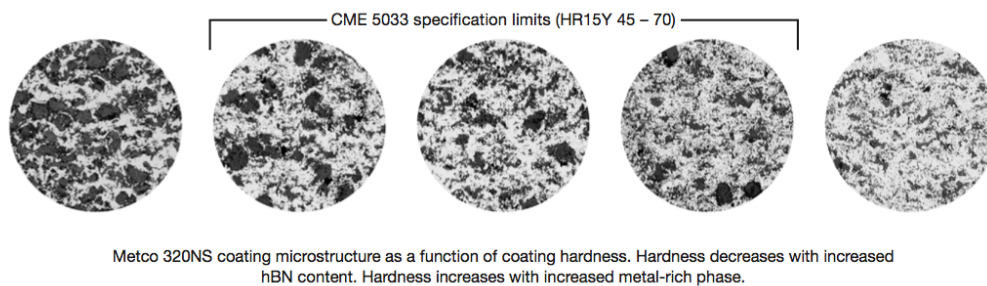


Figure 3.5: Microstructure of Metco 320 Plasma Sprayed Abradable Seal Coating [3]

The benefits of Metco 320 are better corrosion resistance of the  $AlSi + hBN$  material than the aluminum graphite abradables. It shows a good erosion resistance and little blade tip wear or material pick-up within the hardness range of the specification [3], enabling the compressor to run at  $450^\circ C$  because of the good microstructural integrity. The microstructure has a close correlation with the hardness, which can be adjusted during the spraying process.

Metco 320 powder, produced by Sulzer Metco, is sprayed to a hardness of HR15Y  $45 \rightarrow 70$ . Using an F4 plasma spray gun, the coating hardness can easily be adjusted by changing the primary gas flow. Primary gas flow influences the hardness of the coating during spraying therefore a reduction of the primary gas flow increases the hardness of the coating. The flame intensity, regulated by the primary gas, is directly proportional to coating hardness. Higher primary gas flow, means hotter flame which results in a harder coating. The particle velocity is inversely proportional to the hardness [3].

The coating's hardness is dependent upon the amount of dislocator in the material. Softer coatings contain more dislocator phase and experience higher hardness reduction in service, compared to harder coatings. Softer coatings also show poorer erosion

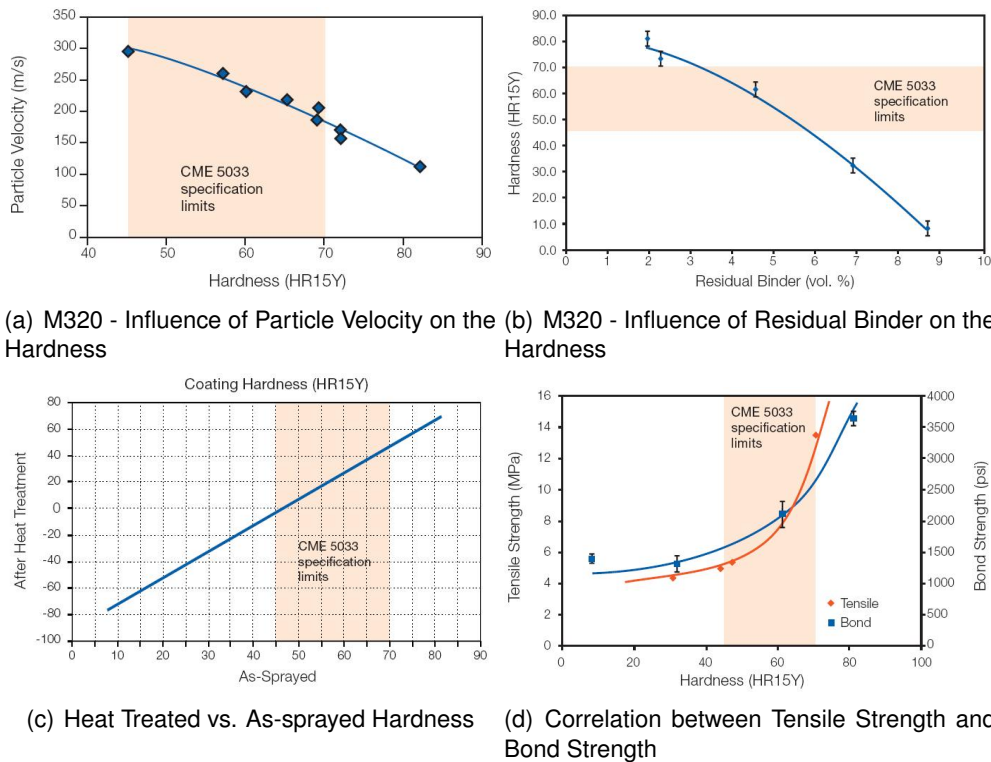


Figure 3.6: Influence of Mechanical Parameters on the Properties of Metco 320 [3]

resistance and lower bond strength than harder sprayed coatings. Inter-particle integrity and strength vary with the coating microstructure and hardness. Material property data, measured by Sulzer are shown in Figure 3.6 [3].

Heat generated during the cutting process is proportional to the rubbing velocity and the incursion rate. Using a *Ti*-blade in interaction with an *AlSi-hBN* coating, the blade modulus is higher than the coating throughout the duration of the test. Plastic deformation is introduced into the seal, whereas the blade reveals little or no wear. At the rubbing surface the pores are gradually reduced in size and number and ultimately eliminated. Densification of the abrasible, due to compression from the blade, results in work-hardening of the abrasible seal. The reduction in pores and the increase in hardness indicates that the yield stress of the seal material was exceeded [5] resulting in local cold work.

## 3.4 How is a Compressor Seal Coating manufactured?

### 3.4.1 Grit-blasting

The adhesion of coatings to the substrate is of vital importance to the lifetime of the material. For thin, dense coatings scratch testing is used regularly to assess the adhesion strength of the top coat [39]. Rough surfaces, after grit blasting, are known to increase adhesion between the substrate and abrasives. Unfortunately, the final result can depend upon the operator skill, as the blasting process can result in left-overs and residues on the surface of the substrate which may weaken the adherence of the top coat [40]. Furthermore the treated, roughened surface is prone to oxidise quickly, which also affects adhesion. It was found that Young's Modulus and surface roughness may be correlated [40] associated with changes in the material properties during grit blasting.

Material removal happens due to either micro-cutting or indentation, dependent upon the angle of attack. The treated surface increases in hardness due to work-hardening from the grit-blasting particles, whereas the subsurface layers are not affected [41]. Surface roughness, as well as residual stresses and subsurface hardness change with grit-size, blasting pressure and angle. Residual stresses reduce the adhesion and subsequently influence the performance of the coating. Experiments were carried out [42] in order to investigate the influence of grit-blasting stresses upon the coatings lifetime. It was found that post-blasting heat treatment did release some of the stresses which had built up, but could not eliminate them entirely. Further investigations into the stresses resulting from the grit-blasting treatment [43] showed that, the rougher the surface, the higher the stresses at the interface.

During manufacturing, the interaction between grit blasting particle pressure and grit-blasting distance are most important for the thermal cycling performance of the grit blasted part. Indentation testing at the bond coat showed that rough surfaces increase the adhesion until  $R_a = 5\mu m$  of surface roughness after grit blasting, for a *CoNiCrAlY* bond coating with a  $0.3mm$  thick  $ZrO_2$  top coat.

An average hardness, measured between substrate and coating, was defined [42]. This hardness described the onset of a crack, when indenting at the substrate - coating interface. The length of the crack resulting from hardness testing is measured ( $a_c$ ). Increasing substrate hardness leads to a decrease in  $a_c$ , indicating a delayed onset of cracking during indentation (see Figure 3.7). Grit blasting influences the hardness of the top surface, where the coating adheres, therefore, influences the crack initiation during indentation.

Research on surface roughness, depending on grit-blasting angle, showed the mecha-



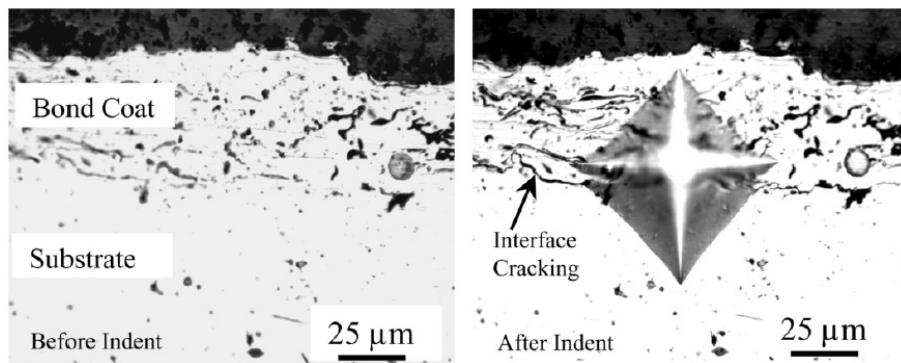


Figure 3.7: Rockwell Indentation on the Bond Coat Interface to assess Adhesion [42]

nism of surface treatment changes but the roughness achieved is constant. However, at blasting-angles of about  $75^\circ$  hook shapes start to form, which further increase coating adhesion [44].

To improve adhesion due to grit-blasting, the angle and grit-properties along with blasting time are important. In addition to that, the cooling after spraying should be very slow in order for residual stresses not to built up [45]. As a general rule, higher pressures and shorter grit-blasting times are preferred over lower pressure and longer times [40].

### 3.4.2 Plasma Spraying

The preferred application process used to generate an abradable compressor seal coating is plasma spraying. Plasma sprayed coatings are suitable for big engine parts with simple, flat surfaces, because the coating can only be applied if the surface area can be reached with the plasma gun (line of sight). Complex little parts would not get covered appropriately due to hidden areas and covered surfaces [14].

Figure 3.8 shows the plasma spraying process, which uses argon as the inert gas to surround the plasma jet. Any hydrogen introduced into the gun is ionised via an arc, which accelerates a mixture of  $Ar$  and  $H_2$  towards the substrate. By inserting the particles into the  $Ar$  and  $H_2$  flow, the powder melts and then impacts on the surface of the substrate, where they flatten and solidify [47].

The resulting coating follows the layering process described in Figure 3.9. The different sized particles melt to different degrees. Upon impact, the varying stages of solidification leave different traces in the coating's microstructure. The solid particles continue to exist in the coating as solid hard spots, whereas the partially or completely molten particles

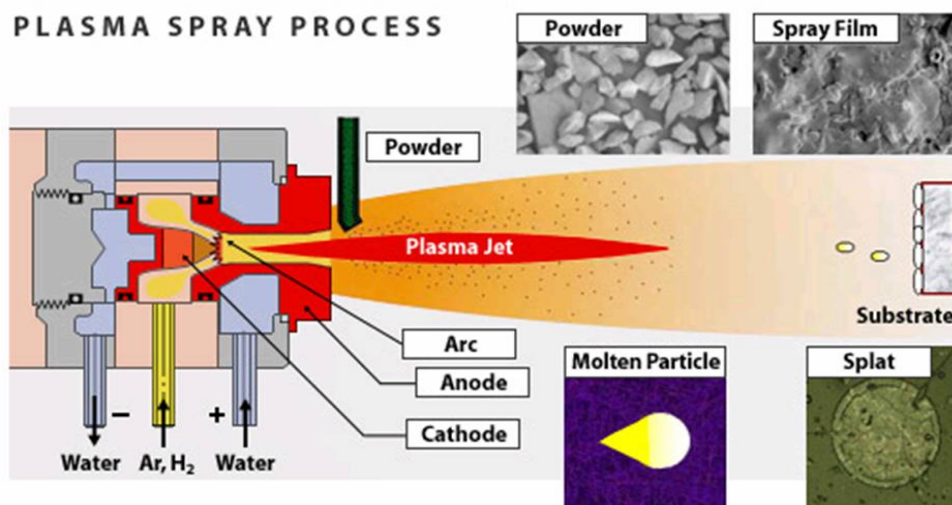


Figure 3.8: Theory of the Plasma Spraying Process [46]

flatten on the surface [38, 48]. The actual coating microstructure will be discussed in more detail in chapter 4.

New technologies now allow the monitoring of the application process, the analysis of the interaction of spray parameters and how this affects the final coating quality. It has been found, that a linear influence of argon flow, current and hydrogen flow upon the coating quality exists [32]. Moreover, coating properties, such as porosity, structure, strength and adhesion, as well as thickness and surface quality, may be controlled with the spray settings; namely, the velocity of the particles, injection of the powder into the plasma stream, velocity of the second gas and the temperature of the substrate, whilst spraying [31].

An ideal coating would be created, should all the particles impacting the substrate be completely molten and flatten upon impact. But, as the particle size of the injected powder varies, therefore, the smaller particles move faster than the bigger ones. The higher speed of the small particles causes a decreased time of heating for the powder and can result in a potentially less molten state [48]. A big variation in particle sizes results in a porous coating [32] due to the differences in solidity and flattening of the particles upon impact. Higher temperatures of the gas stream can lead to increased hardness because the temperature affects the lay-down rate of the particles.

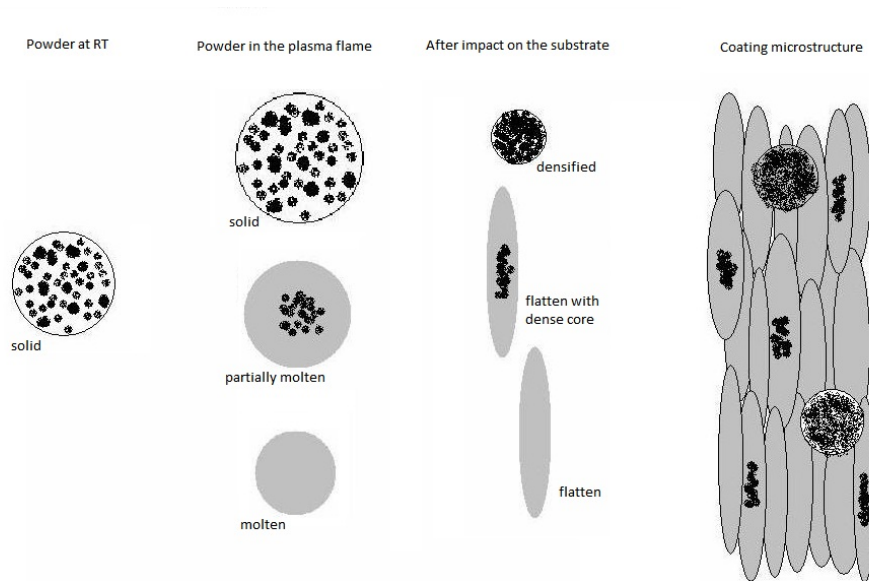


Figure 3.9: Theory of the Layering System of Plasma Sprayed Coatings

## 3.5 What are the problems with abradable seals?

### 3.5.1 Damage and Wear Phenomena

Abradable seals are designed to progressively fail in service. Their purpose is to abrade easily and to not damage the blades or the following stage of the gas turbine. Most important parameters for the coating design are [13]:

- Particle size of the powder, grain size in the coating
- composition, hardness,
- as sprayed compared to heat treated material,
- deposit efficiency, thermal expansion, thermal conductivity,
- particle to particle cohesive strength, volume percentage porosity,
- oxidation levels.

The erosive wear in abradable seals is mainly micro-cutting and gramophone grooving (due to plastic deformation); but high porosity may promote brittle behaviour. Higher hardness, higher porosity and more non-metal phase results in shorter and flatter traces of micro-cutting and ploughing [49]. The possibility of observing cutting in the material is

very unlikely because the leading edge of the blades can not be manufactured that sharp. Even if the tool to make a blade with a good cutting edge existed and was applied, the edge would be machined off during the interaction of the blade and the coating [50].

The heat conducted by the material of the abradable seal coating has been proposed to be carried away by the debris, but research showed that only about 0.1% of the heat is removed by the debris. The temperature generated by the contact promotes subsurface cracking and possible material removal with the blade [9]. High local temperatures indicate where the coating is strongest; as the friction increases, pick up can occur and poor abrasability results [51]. Thus, hot spots indicated areas of intense thermal activity, resulting in melting and densification of the material. Those areas are more likely to crack and promote cracks into the subsurface layers [10]. Areas of work-hardening were found to be up to  $0.1\text{mm}$  of the densified material [11, 52].

Cutting is the most desired form of blade and seal interaction and preferred over adhesion or melting, due to the damage resulting from the transfer processes in these latter cases. During the cutting process, the material affected by the cut, shows very little or no deformation at all. When the surface particles are strained extensive material flow may be witnessed and smearing is observed. Other failure mechanisms of abradable seals can be 'plucking' due to casing vibration or rotor frequencies influencing the wear process, as well as chipping following an insufficient bonding with the substrate [53].

Adhesive transfer depends upon the different layers of the coating and their behaviour during heating. If non-metallic particles are covered by a compact surface, then the created heat causes densification. A thick and hard surface layer can form and frictional heat may then cause material transfer to the blade [8]. Ball-on-disc tests showed that M601 and M313 compressor seal coatings (see Table 3.1) are unlikely to adhere to the blade during interaction [54]. Should the seal material melt under the heat created, then new, complex chemical compositions may be generated. The melting and rapid solidification results in the formation of thick and hard areas, which promotes cracking of the seal. The molten and solidified material further increases the risk of blade wear and pick-up [8].

Of these described interaction phenomena, cutting is most desired but unlikely to occur due to previously explained geometric reasons. Following that, the most likely interaction mechanism is crushing, so the material requires a low compressive strength and very little tendency to densify or smear [50].

The properties of the abradable seal are crucial for the over-all performance of the engine. Different parameters like blade velocity, incursion rate and the thermo-mechanical properties of the materials influence the seals in service, once the blade and the seal interact [5]. The abrasability of the coating can be measured by the worn sliding volume.

The work put into the abradable during a flight cycle, is used entirely to deform and break the sealing material. Heat is conducted into the blade and the seal material and is carried away by the debris. The heat load of the materials can be determined with the help of differential equations which are a function of time [9]. During start up and stop, enough force and friction is created to cause critical damage to the seal coating. Tests have been carried out to evaluate the performance of the seal during such blade interaction [22]. It was found that for an abradable alloy  $AlSi(72\%) - BN(20\%) - \text{organic binder}(8\%)$  in interaction with a  $Ti$ -blade, the material transfer can be minimised by a high linear speed and incursion velocity. During the blade interaction with the seal coating, the frictional heat created, reaches  $500^{\circ}C - 1170^{\circ}C$  and is proportional to the transverse force [7]. In the tests carried out, it was established that the radius of the cutting edge of the blade influences the evolution of these forces. An increasing radius leads to an increase of the frictional forces created during the rubbing process.

**Blade Pick-up** is only seen at low incursion rates and blade tip speeds, when in contact with  $Al$ -based abradables. During the cutting process the blade causes localized deformation which results in high frictional forces. Smearing of the surface leads to higher frictional forces, needed for the blade to remove seal material. Higher forces are associated with a higher friction coefficient, which leads to an associated increase in temperature. Increasing heat can soften or melt the material, which in turn forms adhesive tears or balls during the rub, sticking to the blade. Such pick-up on the blade result in grooving of the abradable seal. The brittle to ductile behaviour is temperature and stress rate dependent. Key parameters for pickup are: the melting/softening temperature of the coating, compared to the blade material, friction coefficient and the translation to frictional heating, as well as surface roughness and particle size.

**Blade Wear** occurs at temperatures high enough for  $Ti$  to deform plastically and usually at incursion rates lower than  $1 \mu m/s$ . Blade wear is characterised by cracking in the blade tip and the subsequent tearing and breaking of the material. The process of blade tip wear can be minimised if not eliminated, if the blade modulus is higher than the abradable modulus throughout the duration of the test [5]. Softening and smearing increases the frictional heating, which in turn increases the blade material loss. Key parameters for blade wear behaviour are: Young's modulus and yield stress of the abradable at high temperatures and available slip systems in  $Ti$  and sufficient local temperature to provide the activation energies for this deformation [2].

**Macro Rupture** is only seen at high incursion rate and high tip speeds, in contact with

*Ni*-based coatings. Once high stresses associated with the cutting process are introduced into the material the seal fractures at the weakest point. The crack propagates through the weak dislocator phase and the material loss occurs due to brittle fracture. The incursion and abrasion process is so quick that even soft materials fail in a brittle manner. Key parameters for macro rupture are: fracture toughness of the material at elevated temperatures, Young's modulus and Yield stress of the abradable at high temperatures and the level and size distribution of weak phase and porosity in the metal matrix (see also Section 3.5.2), in effect defining the defect distribution.

### 3.5.2 Cracking of Abradable Seal Coatings

The occurrence of residual stresses and the cracking of abradable seals during heat cycling are intrinsically tied to each other, due to the fact that the abradable is restricted in movement by the substrate. The built up of residual stresses, either directly after spraying or in service, peaks at pores and hard spots and in turn leads to cracking of the material [55, 56].

Due to the extreme working environment and the big and fast changes in temperature, the coating materials, as well as the bond coat and casing have to expand and shrink during service. Different materials, with individual compositions and coefficients of expansion, are subject to the same temperature changes and need to expand within their own ranges which makes the contact zones prime areas for stresses to build up and cracks to start [57, 58].

Plasma spraying is used to deposit the abradable seal material onto the substrate, layer by layer. With each layer of coating deposited, the particles solidify and form a new surface for the next cover. This built up promotes residual stresses within the individual layers of the seal, but very little stresses through the thickness of the seal coating. The described stress distribution results in intersplat cracking in directions  $x_1$  and  $x_3$ , but intrasplat cracking in direction  $x_2$  (see Figure 3.10). Intrasplat cracking is described as the microcracks within the grains, resulting from rapid cooling and solidification during the spraying process [59].

Guo et. al. [60] found that the crack density within a plasma sprayed coating is dependent upon the substrate temperature during deposition. The higher the substrate temperature when the abradable is manufactured, the higher the crack density (number of microcracks in a set volume) in the material. Seals sprayed at high temperatures reveal good intersplat bonding and are therefore less prone to separation as a result of crack growth.

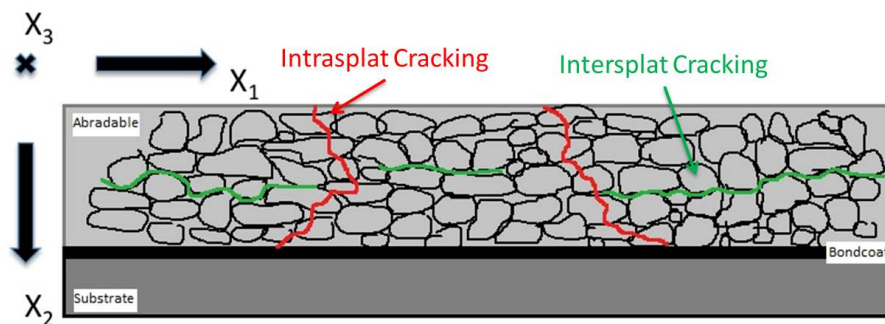


Figure 3.10: Crack Directions and Growth Preferences [59]

Furthermore, the influence of pores has been evaluated, with pores between  $0.02 - 1 \mu\text{m}$  being helpful in the prevention of crack propagation [60]. The segmentation cracks may meet pores in the microstructure which can pin them. The cracks cannot grow past the obstacle without the generation of more stresses to overcome the pores and re-initiate sharp cracks on the other side of the pores.

A study of thermal cyclic heat treatment has been carried out by Fu et. al. [61]. Layered coatings were heat treated and analysed for crack initiation and propagation. Grading of the material introduces gradual microstructural and compositional changes into the abradable seal which improves the thermal expansion mismatch between the different films. It was found that more layers are increasingly thermal shock resistant, which is understandable due to the coefficient of thermal expansion changing more slowly, giving better chances for the stresses to be absorbed/relieved.

Three different types of thermal cracking failure have been identified by Schlichting et. al. [62], which either run within the top coat (cohesive failure of the material), along the bond coat /thermally grown oxide interface (adhesive failure of the material) or a network of vertical and horizontal cracks within the coating material resulting in coating loss.

These vertical and horizontal components of stresses in a multi-layered coating have been calculated [63], not for an abradable system but for a TBC. The system analysed by Evans and co-workers [63] was an APS TBC with stresses in the thermally grown oxide (TGO) and the top coat (TC). The effect such stresses have upon the system and crack initiation showed that the vertical stress has a great influence on the tensile stresses generated in the material and the peak stresses increase with the cyclic lifetime. The energy release rate was calculated for those areas, starting to open or debond. For the TBC analysed in [63] a maximum was found in the areas where the TGO and the TC came apart.

### 3.5.3 Residual Stresses in Thermally Sprayed Coating Systems

Stresses within a material that has been deposited by plasma spraying are generated in two stages. The first one is referred to as solidification and describes the quenching stresses which occur during cooling from spraying temperature ( $T_{Sp}$ ) to the substrate temperature ( $T_{Su}$ ) [64]. The layering and associated temperature profile can be seen in Figure 3.11. The second stage is due to rapid cooling (cooling rate of  $10^6 \text{ K s}^{-1}$ ) and is the process mostly mentioned in connection with the build up of residual stresses [65]. Thermal stresses are generated during this stage, where the material cools from  $T_{Su}$  to room temperature.

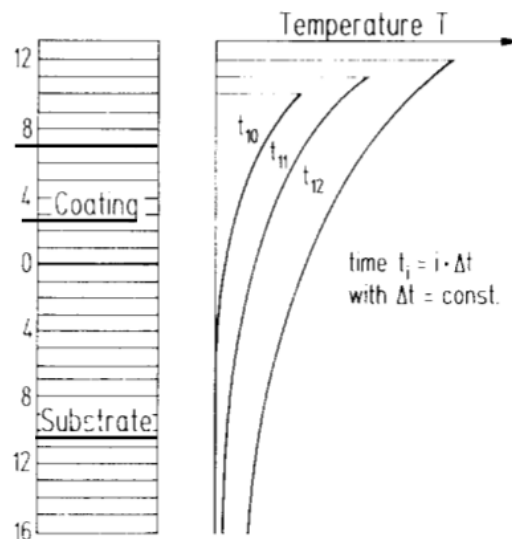


Figure 3.11: Temperature Profile of the Individual Layers Growing during Plasma Spraying [66]

The tensile stresses due to spraying can grow to several GPa [62, 67] through the thickness of the seal depending upon the material. Backplate heating or a post deposition treatment may be used to influence the stress development in the seal and possibly eliminate them entirely [68]. A heat treatment after spraying and slow cooling reduces the intra-layer stresses and therefore the likelihood of cracking and delamination.

In a plasma sprayed  $ZrO_2$ -TBC, the stresses are tensile in the first layers of a thin coating, but with increasing thickness they change to compressive stresses on the top surface [69]. The tensile stresses induce microcracking (see figure 3.12 [70]) and due to the mis-matching coefficient of thermal expansion (CTE) the cracks will continue to



grow. Research [71] shows that the energy release rate for small cracks, is high in the midsection of the TBC, but the maximum value for long cracks is near the bond coat. This explains the delamination of the coating just above the bond coat, within the TBC, as observed for many thermally sprayed systems.

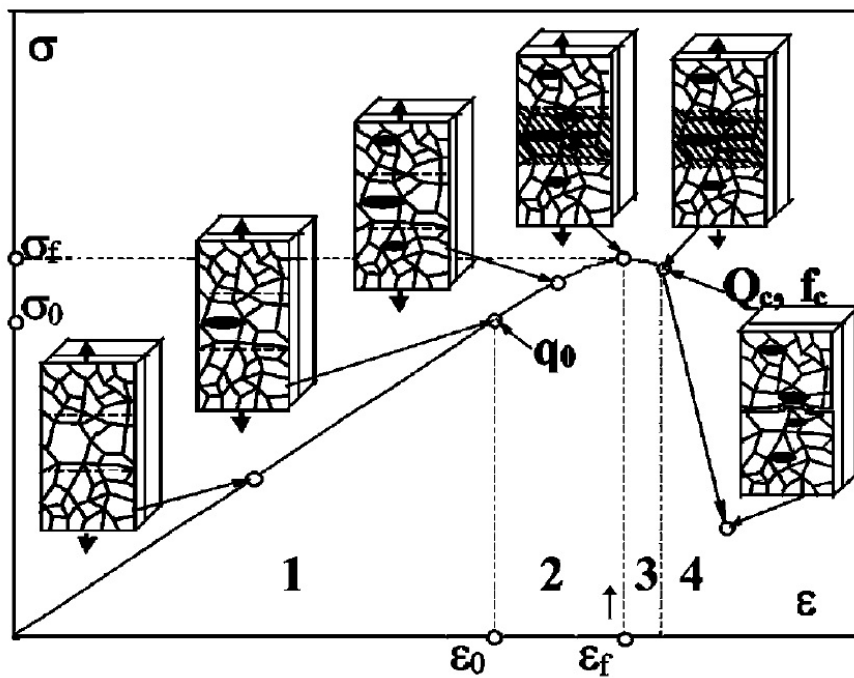


Figure 3.12: Micro-cracking of a Coating during Relaxation [70]

TBCs which were not stress relieved before being put into service reveal a quick accumulation of residual stresses in the TGO/TC interface over the first few cycles of their lifetime [72]. Mechanical loading of the coating - like thermal cycling - leads to delamination cracking within the TBC [73]. After the first increase of the stress level the material starts cracking and the residual stresses decrease. Stresses are reduced not only due to the cracking of the liner, but also because of creep relaxation and sintering processes, in both the ceramic and bondcoat/substrate system.

### 3.5.4 Methods to measure Residual Stresses in Coatings

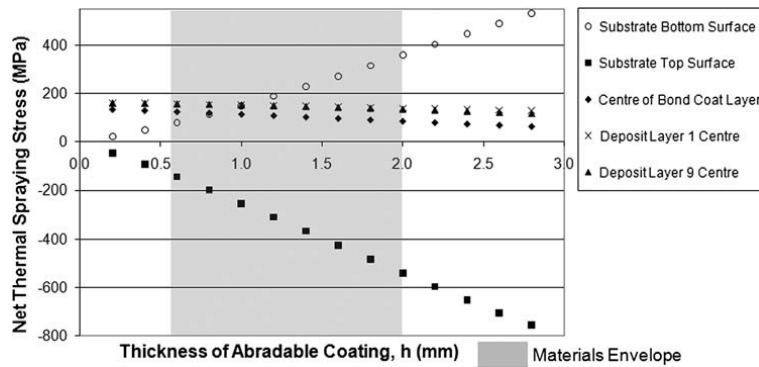
Methods to measure residual stresses in coatings are a subject of current and past research. Much of this work until now has focused on thermal barrier coatings. The most promising technique to measure stresses in a coating is X-Ray Diffraction (XRD). Portinha et. al [74] used XRD to assess the changes of stresses within a  $ZrO_2$ -based ceramic TBC topcoat and found that thermal cycling reduced the compressive stresses more efficiently

than annealing. Furthermore, scattering of the X-Ray beam by small pores resulted in a broadening of the diffraction peak. As an overall observation it can be said that a decrease in porosity increases the residual stresses in the ceramic of a TBC [74].

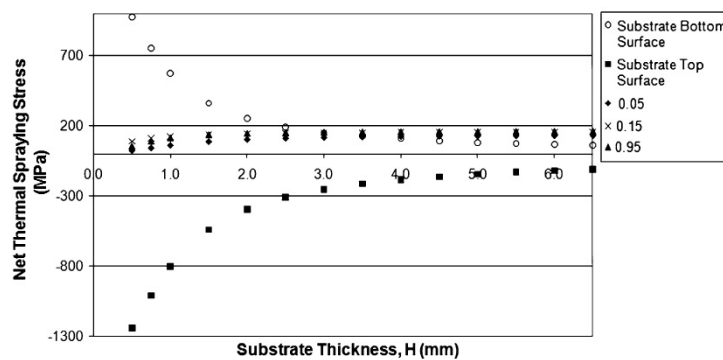
Testing abradable seals, using XRD, shows that the lattice spacing increases during heat treatment [75]. For an  $AlSi$  abradable, the  $Si$  precipitates out of the supersaturated  $AlSi$  matrix and agglomerates during further cycling. The size of the  $Si$  precipitates influences the strain recovery of the of the top coat. In order to reduce the strain on the  $Al$ -lattice, the amount of  $Si$  can be reduced and the resulting stresses decrease.

Attempts have been made to model the stresses in layered coatings [76] and following from that in abradables [47]. It was suggested that the hot splats heat the substrate and the resulting stresses depend upon the CET of the individual materials. If  $\alpha_C > \alpha_S$ , then tensile stresses form; should  $\alpha_C < \alpha_S$ , then compressive stresses form. Thus, residual stresses in the coating can be controlled via substrate heating and cooling [65].

Johnston et. al. [47] proposed a variable called Net Thermal Spray Residual Stresses (NTSRS) during their modelling activities of plasma sprayed seal coatings. They showed that decreasing the deposition stresses in the coating resulted in a reduction of the NTSRS. Their modelling results and the influence of substrate thickness, as well as abradable thickness upon the stress state can be seen in figures 3.13 a and b.



(a) Influence of Abradable Thickness upon Stress State



(b) Influence of Substrate Thickness upon Stress State

Figure 3.13: Modelling Results of NTSRS in a Plasma Sprayed Abradable [47]

### X-Ray Diffraction Theory

Using X-Ray Diffraction, a sample of the material is subject to an intense X-ray beam, which is reflected off the lattice structure of the solid structure. The reflected beam is captured in an X-Ray detector, where its angle and intensity is recorded. Figure 3.14 shows the working mechanisms and how the lattice spacing and Bragg angle can be measured.

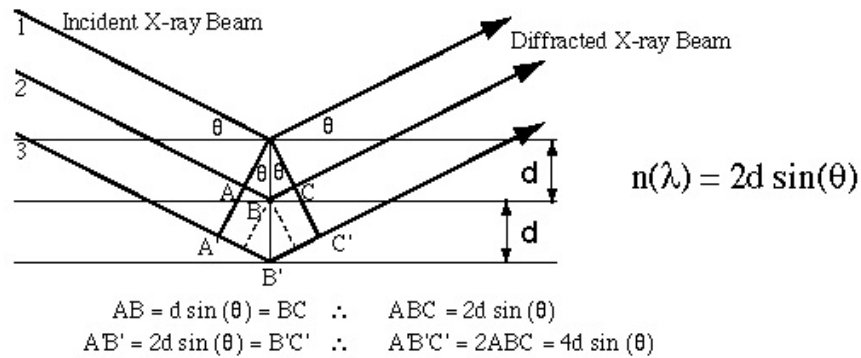


Figure 3.14: Diffraction of X-Rays off the Lattice Structure and measuring Bragg Angle  $\lambda$  and Lattice Spacing  $d$

In order to measure residual stresses and change of stress states in the material's surface, X-Ray diffraction can be used. Any material has its individual peaks, when investigated with XRD and these patterns change depending upon the stress state of the surface. X-rays can penetrate a sample to a depth of approximately  $50 \mu\text{m}$  and variations in lattice spacing can be traced [77].

Macro-stresses - which extend over large distances - result in a shift of the peak away from its initial  $d$ -spacing. Micro-stresses - which result from imperfections in the crystal lattice - show in a broadening of the peak [78].

Any surface treatment applied to a component results in stresses being introduced into the material. These are the stresses recorded when analysed with XRD. Subsurface stresses vary a great deal from the surface parameters, especially if the surface was machined. During service it is mostly the subsurface stresses which initiate failure and influence a component's lifetime [79].

In XRD stress measurements, one peak of the material is analysed at several different angles of  $\Psi$ . A potential preference in crystal growth or change in lattice spacing due to stresses can be recorded due to the changes in the stage angle. To achieve greatest precision, when using XRD as a tool for stress measurement, a peak of high intensity and at high a diffraction angle as possible has to be chosen.

If a material is under stress, the lattice spacing changes, which is indicated in Figure 3.15.

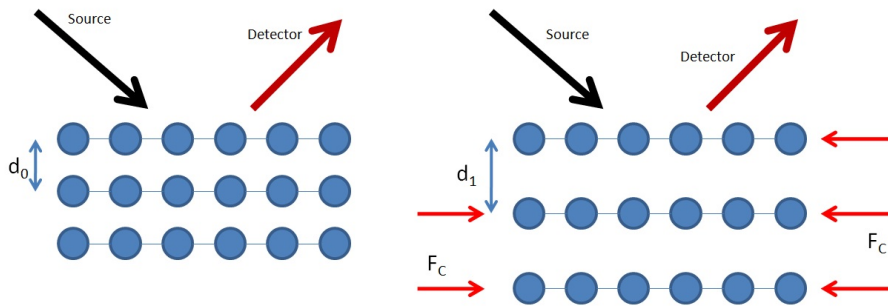


Figure 3.15: Changes in Lattice Spacing due to a Compressive Force ( $F_c$ )

Figure 3.16 shows the shift of a peak due to stresses in the lattice. The initial atom spacing  $d_0$  is plotted in the centre of the graph. If the sample is subject to increased stresses, the peak shift with tension ( $d_2$ ) or compression ( $d_1$ ).

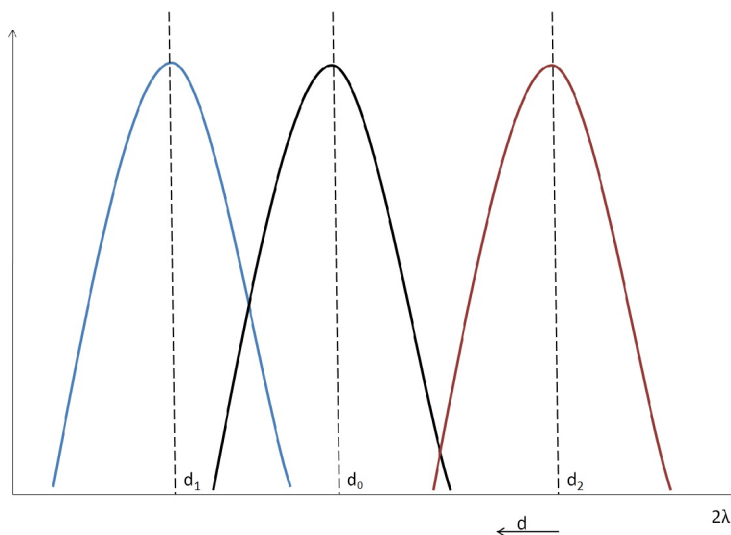


Figure 3.16: Peak Shifts due to Stresses in a Material measured during XRD Analysis

For greatest precision in a stress measurement of a sample, the highest  $2\theta$  peak has to be identified for further analysis. To cover multiple directions of grain orientation, the sample is tilted into different angles of  $\Psi$  and for each  $\Psi$  angle the identified peak of  $2\theta$  is scanned. Tilting the sample into different angles, means tilting the stage of the diffractometer, as the sample is fixed to it. The stage range for the D500 diffractometer at Cranfield University is between  $-4 \rightarrow 101^\circ$ . Figure 3.17 shows how the orientation of the lattice needs to be brought into position for the X-ray to analyse it.

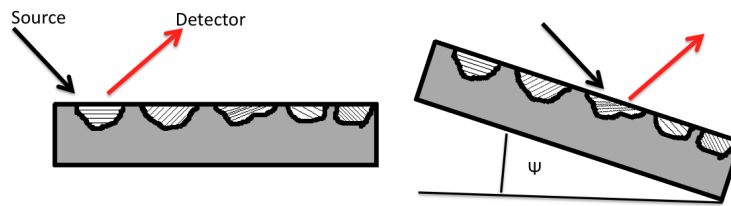


Figure 3.17: Tilting of XRD Sample to analyse Multiple Directions of Grain Orientation

Depending upon the precision of the results needed, the sample is tilted into 3 → 15 different angles and the peak scan initiated. From the resulting patterns a stress profile can be plotted, which indicates normal, shear and potentially a stress gradient in the surface of the sample.

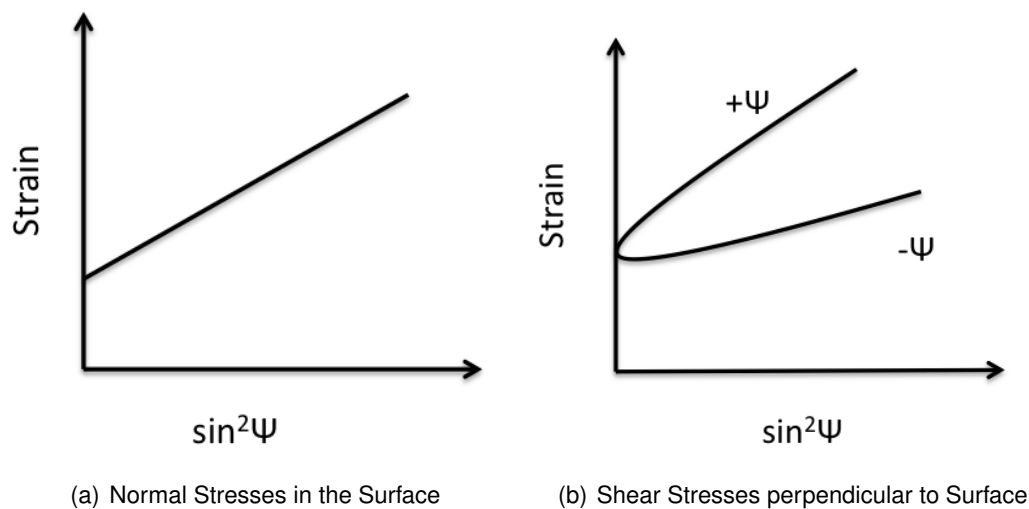


Figure 3.18: Possible Stress Graphs after Analysis of different  $\psi$

### 3.6 How is the Performance of Abradables Currently Assessed?

The extensive testing of abradable seals provides the opportunity to produce wear mechanism maps for each material. They help to model the performance of abradable seal coatings to withstand service conditions [8]. In experiments which have been carried out, it was found, that material was transferred to the blade from the seal and then back to the seal. The temperatures during rubbing can reach up to  $1300K$ , depending on the materials being rubbed together.

### 3.6.1 Erosion Testing

Different wear mechanisms are reported depending on whether there is interaction with the blade or not. During the seal material wear with the blade tip, cutting, smearing, adhesive transfer, crushing and melting can occur. Without blade interaction, erosion, corrosion, thermal stresses and high-temperature oxidation can damage the abradable seal in a high-temperature environment [8, 80].

Erosion testing and the influence of the particles and the impact angle on the seal coating performance have been evaluated for different coating compositions. The tested materials were, Metco 307, 310, 313 and 601 (see Table 3.1). The samples were tested in a vacuum chamber of  $1.3 - 6.5 Pa$ , with a feeding rate of abrasive particles of  $16 g * s^{-1}$ , for 1 h and an impact angle of  $30^\circ$ ,  $60^\circ$  and  $90^\circ$ , with a mean particle velocity of  $30 - 70 m * s^{-1}$ , which results in an impact speed of  $20 - 80 m * s^{-1}$ . From these experiments, it can be said, that the erosion rate does not directly relate to erosion time, impact angle, erosion speed and the kind and size of the erosion particles [49]. However, these supposed independences of the erosion parameters upon the erosion process were proven wrong during this research project (see Section 8.2).

However, the erosion rate is related to the characteristics of the coating, its form and microstructure. Mass loss from the coating surface only occurs, when the impact strain reaches a critical value. After initiation of the erosion process, the erosion rate stabilised [4].

### 3.6.2 Tensile Testing

In order to measure the tensile strength of a fragile abradable coating a method had to be developed to assess the coating without the influence of the substrate. Johnston et. al. [81] devised a method of spraying into a ceramic mould, which can withstand the temperatures during the application process but is dissolvable in water to release the sample after manufacturing (see Figure 3.19).

Different abradables (M320, M314, M314+BN) were tested with the method presented and it was found that *AlSi - hBN* has a much higher UTS than *NiCrAl-Bentonite-BN* or *NiCrAl-Bentonite* [82]. These results differ from those measured by Ma et. al. [83], who attempted to analyse Young's modulus, microhardness and UTS via bend testing of abradable liners with the substrate still attached. Ni-graphite came out with highest values for the named properties, followed by Al-graphite and AlSi-Polyester.

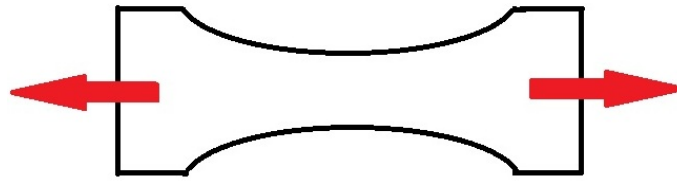


Figure 3.19: Schematic of the Working Mechanism of Tensile Testing Freestanding Abradables [81]

### 3.6.3 Indentation Testing

Indentation, or more specific, micro indentation describes the investigation of the surface of a material, using an indenter. The indenter tip can be of different geometric shapes but most commonly cone or ball indenters are used. Venkateswarlu et. al. [84] used ball indentation to assess the properties of cast material and was able to establish its validity for material property measurements. The advantage of ball indentation lies in the non destructive analysis of the sample, which contrasts the use of tensile testing.

The test records a loading and unloading curve, which enables the calculation of the material's stiffness  $S$ , reduced Young's Modulus  $E_r$ , hardness  $H$  [85, 86, 87] and plasticity index  $PI$  [88].

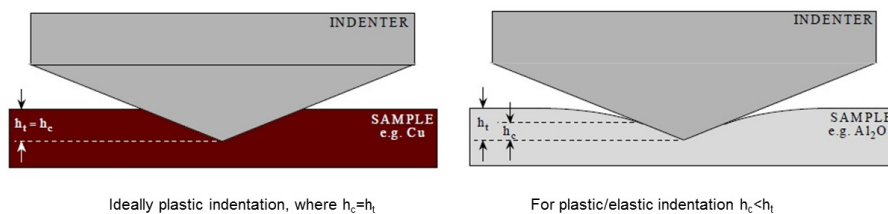


Figure 3.20: Schematic of an Indentation Test for a Pure Plastic and Elastic/Plastic Indent [89]

Figure 3.20 shows the material responses to an indentation test, depending upon elasticity of the specimen. Plastic deformation leaves behind a scar in the surface, whereas the elastic part recovers. Copper shows what a purely plastic deformation scar after testing. Alumina on the other hand reveals elastic recovery and therefore, the final indent depth is not equivalent to the maximum depth during testing.



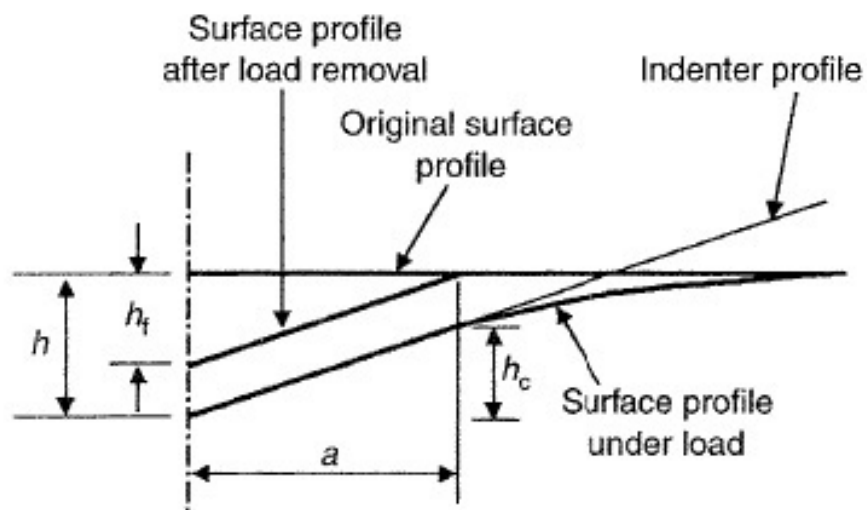


Figure 3.21: Schematic of an Indentation Scar left on the Surface after Unloading [90]

In order to analyse the material properties, different geometric characteristics are needed from the test scar. Figure 3.21 shows values required for further analysis. The total indent depth  $h$ , indent depth after unloading  $h_f$ , contact depth  $h_c$  and radius of the circle of contact  $a$ .

Efforts have been made to assess material changes with increasing temperature, as plastic deformation and elastic recovery change with increasing temperature. [88] showed, that with increasing temperature, decreasing hardness and increasing Plasticity Index ( $PI$ ) could be observed. The optimum combination of hot hardness and toughness/plasticity varies with the requirements towards the material and the nature of its working environment.

Also materials change their properties during heating and potentially do not fully recover during cooling down. This might happen due to microstructural or chemical changes during the hot phase [91]. The dependency of indentation results upon material properties were investigated [92] and simulated using finite element modelling. It was established, that it is possible to assess residual stresses, Young's modulus, yield strength and strain hardening from indentation testing.

## Chapter 4

# Restricted and Classified Rolls-Royce Internal Reports

M320 is used extensively in the HPC of large civil, longhaul aircraft engines. Their designed lifetime is in excess of 4000 cycles and many engines reach this service interval. Some however fail prematurely and cause engine failure by doing so. These unplanned service overhauls are expensive and reducing their number would be beneficial to both, manufacturer and airline company.

Failure reports stated lifetimes as low as 10,936h or 2,213cycles and failure investigation showed a softening of the material [93, 94]. Furthermore, a less controlled particle size and distribution of the *hBN*-phase was documented. The thermal cracking behaviour of M320 in service has been shown to be dependent upon the initial thickness of the abradable seal. During manufacturing the material is deposited to a thickness of up to 6 mm and then machined down to 3 – 4.5 mm (depending upon the application stage), where 3 mm represents the application guideline for M320 abradable material.

Research showed that surface hardness measurement of the coating is not an indicator of material toughness [95] due to the degradation of the surface during cycling, which results in planes of weakness [96] within the top coat. Though the same hardness was found along the abradable liner during servicing, differences in chip sizes have been documented, which are an indicator of the cohesive strength of the material. Thus, suggesting a weaker or more defective material along the leading edge of the casing, compared to the trailing edge.

Within Rolls-Royce, abradable failures are classed into two different categories, *Class – 1* and *Class – 2*, where *Class – 1* are functional failures such as blade wear, gramophone grooving or coating loss and *Class – 2* are more serious structural failures, such as cracking, spallation and delamination, which can lead to engine stalls [97]. Service experience

showed that rub conditions during engine runs may lead to melting and material transfer to the blade.

Furthermore, the incursion rates during service result in different failure mechanisms depending upon the speed the abradable is removed with, as well as the incursion rate. An example of the different stages of a flight cycle and the potential interaction between blade and abradable is shown in figure 4.1 [98].

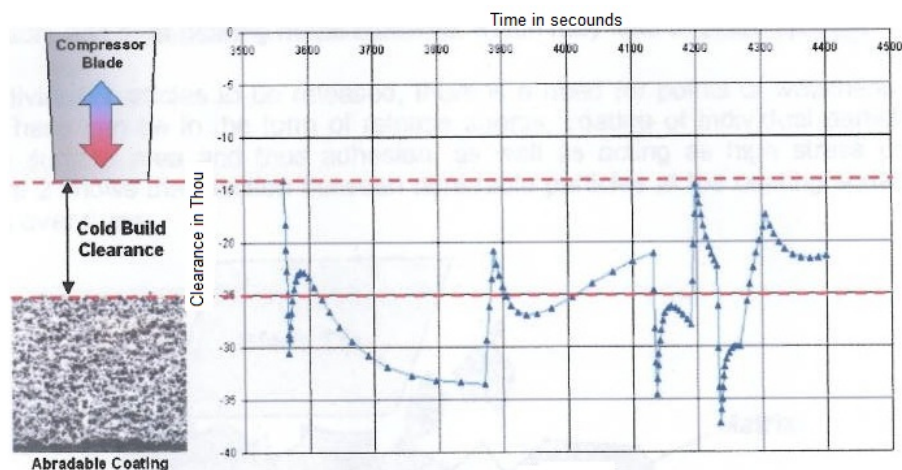


Figure 4.1: Blade Expansion and Liner Interaction over a Flight Cycle [98]

The blade is shown in the top left corner of the picture and the abradable's surface is indicated below. The clearance, which is incorporated into the engine during manufacturing is given as the cold build clearance. The graph describes the expansion of the blades and when they cut into the seal coating. Once a certain depth is cut into the abradable, this will be the new surface level, even if the blade shrinks again. So the lowest spot on the y axis is the new clearance.

## Experiences with Abradable Coatings

This doctorate programme was introduced in order to continue the work on abradable coating systems, previously researched by Noel Hopkins [80]. His research provided Rolls-Royce with valuable insights into the key performance drivers for the spraying process, used to deposit abradable coatings.

Further, the possibility of freestanding abradable samples was explored and implemented as a testing method for material properties [80, 81]. In the first attempts, a dissolvable mould was used to generate the samples; later on the mould was improved into

a reusable rubber mould [81].

In extensive testing programmes different material-blade combinations have been investigated and the occurring failure mechanism for most material was shown to be ductile rather than brittle. These results proved Karl Schmid's abrasability model [20] to be accurate only for some interactions. The blade tip - abrasable system described by Schmid is appropriate for brittle failure and not applicable for ductile interaction.

Since this original research programme finished in 2007 [80], more work has been done to assess abrasable behaviour and failure mechanisms for Rolls-Royce sealing systems. Under investigation are the current seal materials used in the compressor; namely M601, M313, M314, M320 and Sherritt Gordon. All the materials listed have advantages and disadvantages concerning lifetime and performance in service.

M601 is used in compressor stages up to  $400^{\circ}\text{C}$  and cuts well, but the produced debris can cause blockages of the cooling system in the high pressure turbine (HPT). M313 performs well but can not be used with  $Ti$  blades due to a high risk of  $Ti$  fire. M314 has a significantly reduced lifetime due to the susceptibility to aqueous corrosion. M320 was developed and taken into service in order to overcome the other material's shortcomings. Service data on the  $AlSi - hBN$  abrasable now shows degradation due to cracking and delamination of the top coat as a dominant failure mechanism [99].

Experience with abrasable seals show that the fragile material fails in different ways depend on engine locations, type and operation. Erosion, corrosion, cracking and spallation are the modes most observed (see Figure 4.2). Failure modes and microstructural, as well as material reasons for non-performance are listed in Tables 4.1 and 4.2.

At some M320 failure interfaces a black powder was found during overhaul, which was identified as oxidised abrasable material. It is currently thought that when delamination interfaces rub against each other they produce the abrasable powder [100]. Oxidation is expected to be a result of such delamination failure starting along the edges of the liner. The strain in the material is expected to increase along the edges, which are prone to start delaminating, enabling the oxidation attack.

Further to the possibilities of oxygen attacking the aluminium, cracks initiate on the surface of the abrasable, growing towards the substrate [101], opening up during further cycling. It is generally believed, for small cracks, to be performance enhancing due to the stresses in the material being relieved. Small cracks do not open as much area for corrosion or oxidation attack as deep long crack do and therefore these are favoured during service.

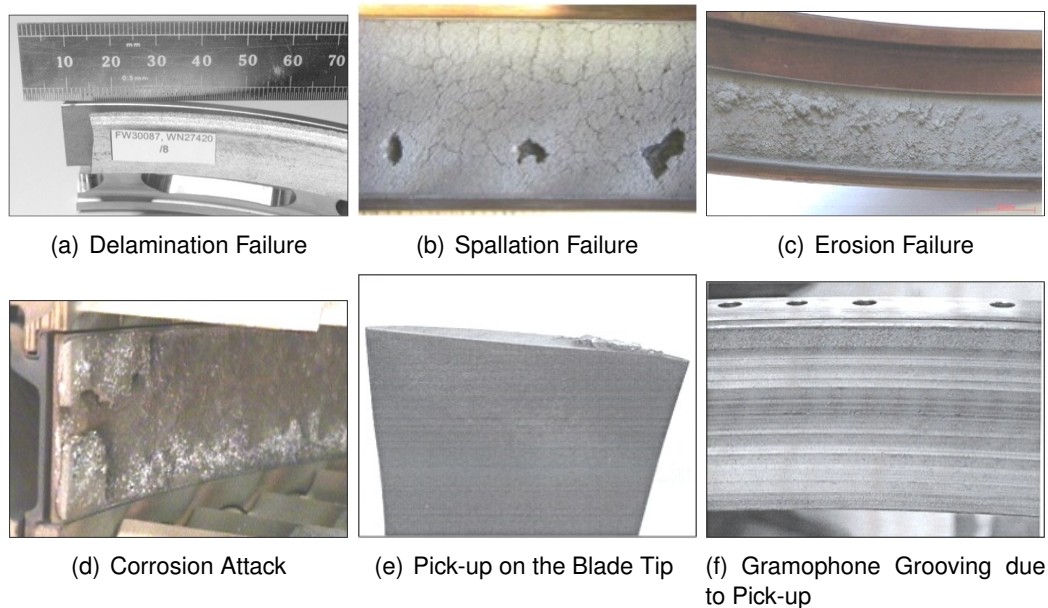


Figure 4.2: Abradable Failures observed during Service

### Metco 320

Metco 320 was developed to replace pure  $AlSi$ -polyester abrasives, which are only suitable for temperatures up to  $350^{\circ}C$  and over-heat during service. The addition of fillers into the metal matrix provided the material system with easily shearing systems to aid particle release during blade interaction. This reduced the occurrence of local hot spots and the associated large plastic deformation of the  $AlSi$  matrix, which resulted in a smoother cut across the abradable surface.

The amount of hexagonal Boron-Nitride ( $hBN$ ) in the abradable system is critical for its cohesive strength and abrasibility. More  $hBN$  results in more slip planes and therefore more particle release during blade interaction due to less inter-particle cohesion. Less  $hBN$  strengthens the coating, but reduces its abrasibility [102].

### Ageing Studies and Precipitation Characteristics

Experiments to assess the precipitation characteristics of M320 were carried out, looking at the effect of time and temperature upon the abradable seal material [103]. Subjecting the sprayed material to elevated temperatures initiates the precipitation of  $Si$  out of the  $AlSi$  matrix. With increasing time at temperature, the precipitates agglomerate, even if

more  $Si$  is still coming out of the matrix. Once the excess  $Si$  has precipitated out of the metal matrix, the agglomeration is just a reduction in overall energy within the material system due to Ostwald ripening [104] and not a further increase in the amount of  $Si$  precipitated.

Due to the flight cycles affecting the plasma sprayed abrasible material (see Figure 4.3), an investigation into the influence of abrasible thickness upon the cracking and delamination behaviour of M320 was initiated. It showed that a thickness of  $2\text{ mm}$  of abrasible reveal an optimum life cycle, when heat cycled. For this abrasible, samples of different thicknesses were heat-cycled and air cooled and their delamination and cracking were assessed during cycling [105].

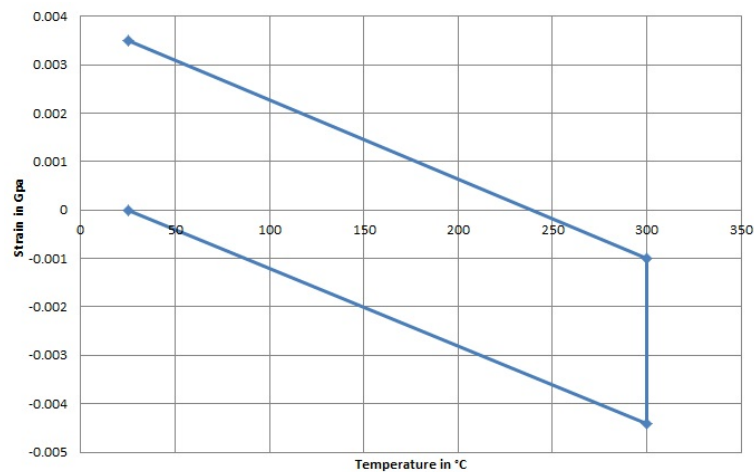


Figure 4.3: Strain response of the abrasible to flight cycles [106]

Further tests were carried out using a scratch tester, scratching the abrasible surface with constant and increasing loads, either uni- or bi-directional. It was intended to find a correlation between erosion performance and friction measurements during scratching. For hard coatings this was possible, but soft abrasibles could not be matched using these two tests, which disqualified scratching as a valid testing method for abrasible liners [107].

During aging trials on  $Al$ -abrasibles it was found that an increases spray distance during manufacturing increased the aged strength of the material [108]. The porous material was perceived as pre-cracked and brittle for this testing project.

## **International Abradable Projects**

### **Sealcoat**

The Sealcoat project was a 48 months research study of abrasives used in a high pressure compressor [109]. The overall goal of the project was to gain more understanding of the abrasion process and develop a new coating family, as well as a FEA model to feed data into the material generation process. Ideally, a constant feedback loop between modelling and material research could be implemented. The modelling objectives were defined as:

- to develop a fundamental model for abrasion seal coatings
- to fully validate the model using OEM and project test data
- to develop a predictive simulation package for abrasion as a design tool for future applications

Along with the modelling route, the material research aimed to:

- develop a novel manufacturing route for a new family of three phase abrasion powders
- optimise coatings using these powders against a range of ranking tests
- fully test optimised coatings and tapes applied to prototype components

Over the duration of the project, the Lermps ellipse generator and the Lermps abrasion test simulator were developed at UTBM (Université de Technologie Belfort Montbéliard - Lermps is the surface engineering department). This FEA code is still the most up to date software to predict abrasion of a coating. It predicted that small amounts of unclad particles in the coating reduce the mechanical properties significantly, which has been observed during testing as well.

The ellipse generator takes a picture of the abrasion's cross section and fits ellipses around/into the individual particles of the microstructure. This simplified interaction model between the ellipses is analysed using the abrasion simulator, delivering deformation, abrasion and strain data for the particles. This method currently supports 2D testing, but is under investigation for 3D modelling as well [109].

In order to assess blade wear problems a bilinear elastic-plastic law has been developed, which showed good correlation to the blade wear measured during test runs. Finally, a new family of coating powder was developed, which may be applied using plasma spraying or flame spraying [109].

The aim of establishing a relationship between the stress-state in the microstructure and the macroscopic material behaviour could not be fulfilled. As it turned out, the existing data were not useful for investigation of the stress-state dependence upon the microstructure. For this reason new ways of testing had to be found in order to establish detailed physical and mechanical material properties first [109].

## MACE

MACE was a 4-year investigation into the cutting mechanisms and coating development for abradable seals in a gas turbine compressor [110]. The research into new coatings was driven by abradability, erosion and mechanical integrity performance of the abradable. To achieve an optimum material response during service, the metal matrix of the seal should be softer than the *TiAl6V4* blades against which it rubs and exhibit a coefficient of thermal expansion similar to the casing material.

To extend test data, two different matrix and dislocator materials were chosen: 316 stainless steel and *Ni20Cr* were investigated for suitability as metal matrix; and mica, as well as *hBN*, was considered for the dislocator phase. It was found that the matrix alloy has a dominant influence upon the coating performance. Also that the reduction of mica in the microstructure, from 20%  $\rightarrow$  15%, resulted in an improved erosion resistance but no change in blade wear.

Furthermore, testing revealed a good temperature resistance for *Ni20Cr* but a hardness greater than that of *TiAl6V4* blades, which resulted in notable blade wear. 316 stainless steel showed high sensitivity to heat treatment and work-hardened during rubbing [110].

As part of the project, modelling of M314 and M320 was carried out, using FEA of the micro contact between the blade and the abradable. The model confirmed what testing showed in the laboratory; a strong link between abradability and cutting behaviour, dominated by plastic deformation and material transfer to and from the blade [110].

Erosion testing showed a dependency of the performance upon the material's hardness. At a 90° impact angle during erosion testing and medium to high hardness of the abradable, brittle failure was documented. Softer material was more susceptible to cutting, therefore showing increasing ductility [111].

Incursion testing provided a better understanding of what can be perceived as good cutting: 'This is, where the level of stress applied to the abradable by the blade tip is high



enough that plastic deformation is minimal and brittle fracture of the abradable occurs, resulting in energy dissipation by the generation of two new surfaces', rather than plastic work [23].

For *Al*-abradables it was found that low incursion rates enabled the material to respond with some plastic deformation within available slip systems, as the energy release rate is low enough for slipping to occur rather than brittle fracture. Higher incursion rates lead to increased stress and strain energy being transferred into the abradable and once the energy for fracture is exceeded, material removal by cutting is observed [23, 98, 111, 112].

Table 4.1: Current Abradable Seal Coatings used by Rolls-Royce [97]

Abradable	Advantages	Limitations
XPT 264 - Al/Si, hBN, Polyester	Relative tough system, not prone to spallation or delamination	Polyester will limit max. operating temp.
M304 - Al/Si, Bronze		Copper tends to align and oxidise in layers resulting in laminar delamination;
M605 - Al/Si, Bronze, Polyester		Copper tends to align and oxidise in layers resulting in laminar delamination; Polyester will limit max. operating temp.
M601 - Al/Si, Polyester	Easy to Spray; Relatively low cost; Powder is a simple blend; can be used with Ti Blades	Al may corrode with extended exposure to atmosphere; Prone to adhesive transfer; Max. operating temp. $350^{\circ}\text{C}$ ; Released Material may clog up turbine cooling holes; Released material may burn in the combustor - possible surge
M320 - Al/Si, hBN, Polyester	Operating temp. $450^{\circ}\text{C}$ ; Corrosion resistance	Generally weak structure - prone to stress induced cracking; Prone to adhesive transfer; Difficult to spray due to friable dislocator phase; Microstructure difficult to interpret; High cost due to requirement of large hBN agglomerates; Released material may clog up turbine cooling holes; Released material may burn in combustor - possible surge; Material hardness sensitive to lay-down method
M314 - Ni/Cr/Al, Bentonite	Tough coating, resistant to cracking, spallation and erosion	Coating too abrasive for use with Ti blades
Sherritt Gordon - Ni/Graphite	$\alpha$ similar to that of substrate, reduces cyclic thermal stresses	Prone to erosion, cracking and spallation; Combustion sprayed - close monitoring of gas flow; May cause blade tip wear
M313 - AlSi, Graphite	Relatively tough abradable seal	Prone to corrosion, spallation and swelling; Released material may clog up turbine cooling holes; Released material may burn in combustor - possible surge

Table 4.2: Metal Matrix and Dislocator Material [97]

Metal Matrix	Advantages	Limitations
Al/Si	Little damage to blades under high incursion; Relative low cost; Easy to spray	Max. operating temp. limited to $450^{\circ}\text{C}$ ; Will smear and pick up on blades under low incursion; Suffers from galvanic corrosion in humid conditions; Inherently weak material - may crack in service; Material will harden due to sintering and densification; Released material may adhere to/ clog up turbine cooling holes; Released material may burn in combustor - possible surge
Ni	Resistant to corrosion; high operating temp; unlikely to pick-up on blade tips; Addition of Cr, Al, Y alloying elements appear to improve inherent toughness	May cause damage to blade under high incursion rates; Requires significant dislocator phase, such as porosity - no plasma spraying option; Combustion spraying required; Requires high amount of dislocator phase - very disjointed and weak structure
Dislocator Phase	Advantages	Limitations
Porosity	Free; None reactive; Infinite availability	Cannot be directly incorporated into plasma spraying; No additional lubrication during cutting
Polyester	Works well with Al; May offer a degree of crack suspension	Limits temp. capability to $350^{\circ}\text{C}$ - oxidises otherwise; Supply tightly controlled - no possible price reductions
hBN	Inert compound; High temp. capability ( $850^{\circ}\text{C}$ )	High cost; Difficult to form large agglomerates; Friable structure easily damaged by plasma; Ultimate coating structural integrity may be compromised by incorporating fractured hBN particles; Low density compared to metal matrix - requires binder phase during plasma spraying
Graphite	Good abrasability experience with knife seals in lubricated sealing applications; Slightly abrasive nature of graphite may suppress adhesive transfer of aluminium to blade	Sets up galvanic cell corrosion in Al-system; Energy absorption may limit resistance to erosion
Bronze		Copper tends to oxidise in layers resulting in laminar delamination of the coating

## Chapter 5

# Initial Investigation into Metco 320 Material Properties

Erosion and Scratch testing has been used to assess the material properties of M320 abrasion resistant seal coating. Samples were taken from production and tested at Cranfield University in an attempt to characterise their properties.

The erosion rate has been shown to be related to the characteristics of the abrasion resistant coating, its composition, microstructure and hardness, but not to the thickness the abrasion resistant is sprayed to [7, 49].

During scratch testing, densification occurs ahead of the indenter due to compression of the soft material contained in the microstructure. Higher yield stress and elastic modulus confine the possibilities of the material to deform and compress and therefore the coating's performance during scratch testing.

### 5.1 Methodology

Selected Metco 320 samples from production were erosion tested at two different angles of attack, which resulted in two different modes of failure. Material suffering a 30° impact was more likely to fail due to smearing of the surface layers, caused by the impacting erodent. Those samples subject to a 90° erosion angle were most likely to show brittle fracture as their main failure mechanism.

4 g/min of particles were fired at the surface of the coating, with an acceleration distance between the sand inlet and the point of impact of 1 m in length. The particle size of the erosion sand was 76 – 212 μm and the impact speed varied between 80 – 120

$m/s$ , dependent upon the particle size. The samples were subjected to erosion for an increasing length of time, starting at one minute; continuing with 2, 5, 10 and 15 minutes, resulting in an overall erosion time of 33 minutes.

The scratch tester used at Cranfield University uses a  $5\text{ mm}$  tungsten carbide ball as an indenter and scratches over the coating's surface with constant load, measuring the displacement in z-direction, the friction and the acoustic emission. In the tests a constant load of  $10\text{ N}$  was used for a scratch length of  $10\text{ mm}$ , repeating the unidirectional scratches 10 times over the same tested region.

The abrasability rig, located in Rapperswil, Switzerland, was used to abrade test samples, during the research project undertaken by Noel Hopkins [80]. The samples were  $40\text{ mm}$  wide and  $120\text{ mm}$  long, with a curvature radius of  $270\text{ mm}$  to simulate the impact and abrasion processes happening in the engine. The impact produced on the abradable's surface during abrasion testing can be compared to engine conditions, since it was shown by Legrand et. al. [113], that the rub contact is not continuous during operation.

The blades used for the tests were  $15\text{ mm}$  wide, so two tracks could be cut into each sample of the abradable seal. For each test a new blade had to be used and some tests may reveal completely different failure mechanisms, depending upon test parameters. A schematic drawing of the rig in Rapperswil can be seen in Figure 5.1.

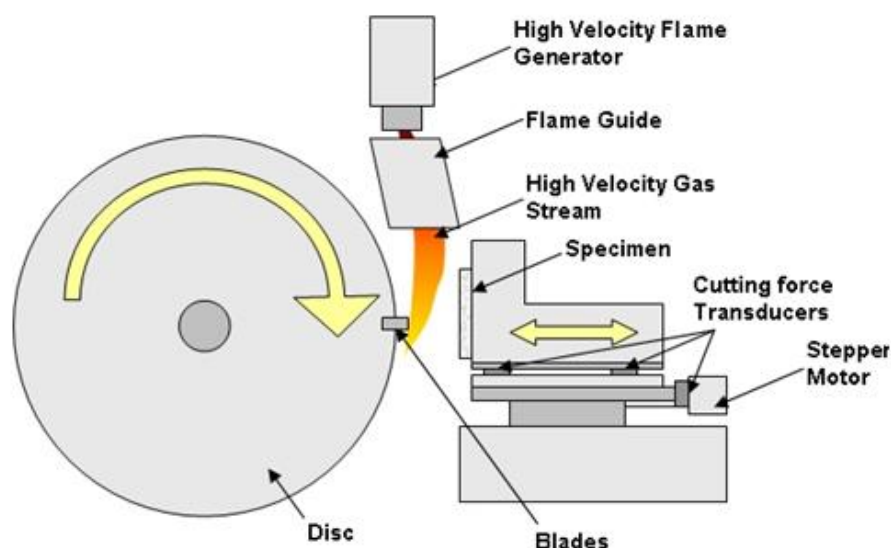
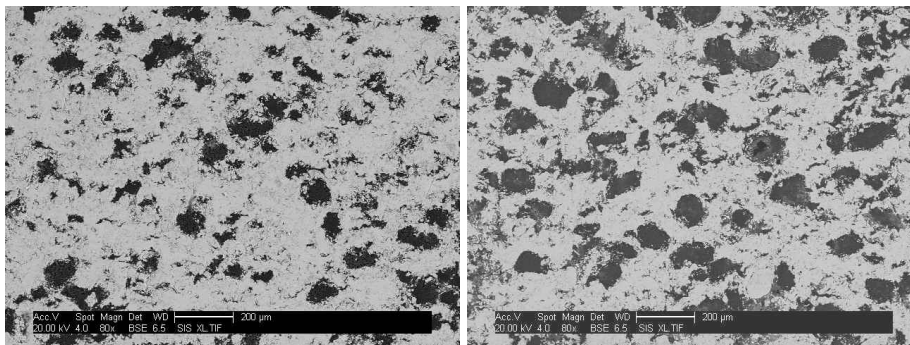


Figure 5.1: Schematic of the Working Mechanism of the Rig in Rapperswil

The polyester within the coating will burn out during the abrasion test and therefore the damping capacity of the material will reduce. The polyester and its mechanical properties are thought to help absorb the cutting force [13, 16, 114, 115]. For further analysis, the abraded seal samples were investigated under the optical, as well as electron microscope.

## 5.2 Results and Discussion

In Figures 5.2 a & b the differences in porosity and the amount of *hBN* between these coatings can clearly be seen. The more dislocator present in the deposited material, the softer the coating. The lighter areas of material in Figure 5.2a are the *AlSi* phase, whereas the darker spots represent the *hBN* phase. Comparing the amount of *hBN* spots in the hard coating to the soft coating, it is clearly visible, that more dislocator was deposited in the coating in Figure 5.2b.



(a) Hard coating - HR15Y 72 + / - 2

(b) Soft coating - HR15Y 57 + / - 3

Figure 5.2: Microstructures of a Hard and Soft Abradable Coating

## Erosion Testing

Two different angles of erosion attack were tested, which left individual scars on the surface of the coating. In Figure 5.3 the set-up of the erosion tester can be seen. The two different sample stages, enabling 30° and 90° testing, are adjusted to the back plate.

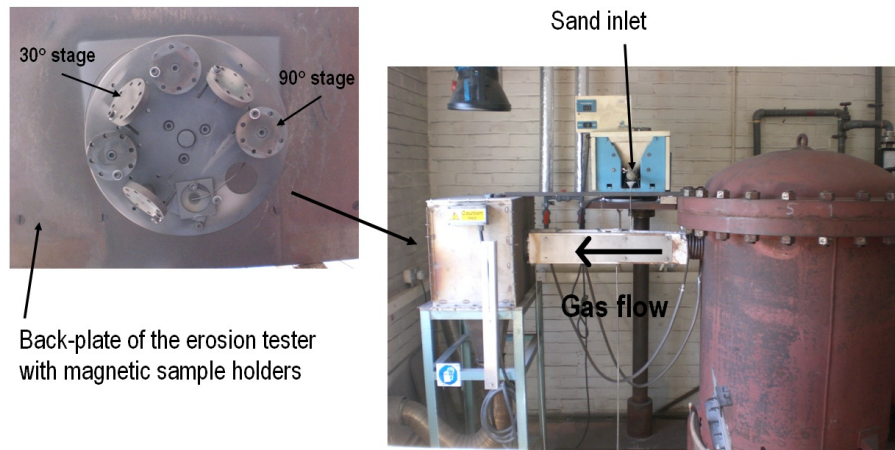


Figure 5.3: Erosion Tester along with Sample Holders

In Figure 5.4 samples of the impact angles  $30^\circ$  and  $90^\circ$  are shown. The red circles indicate the shape of the eroded area on the samples.

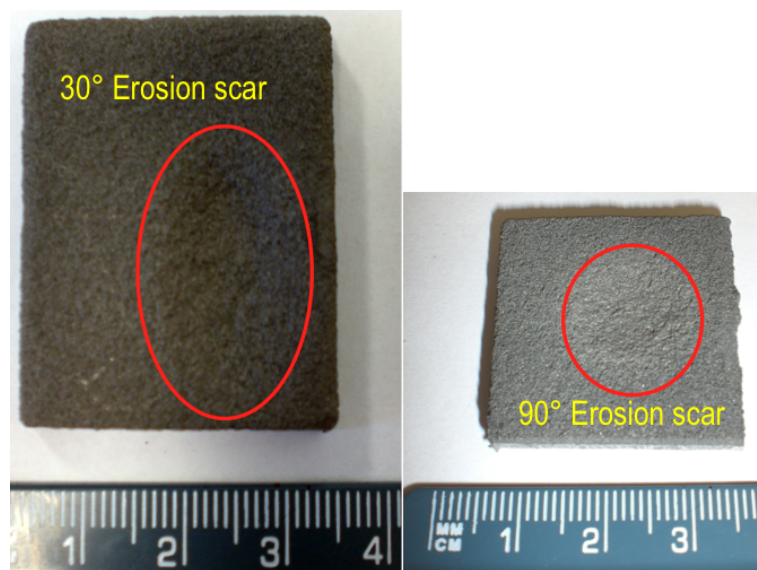
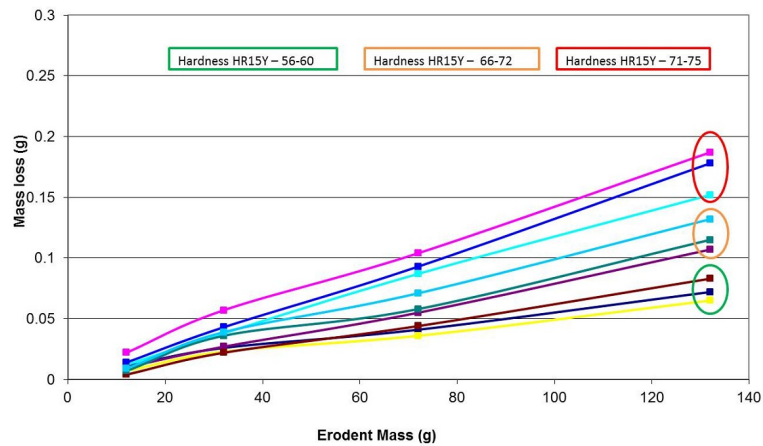
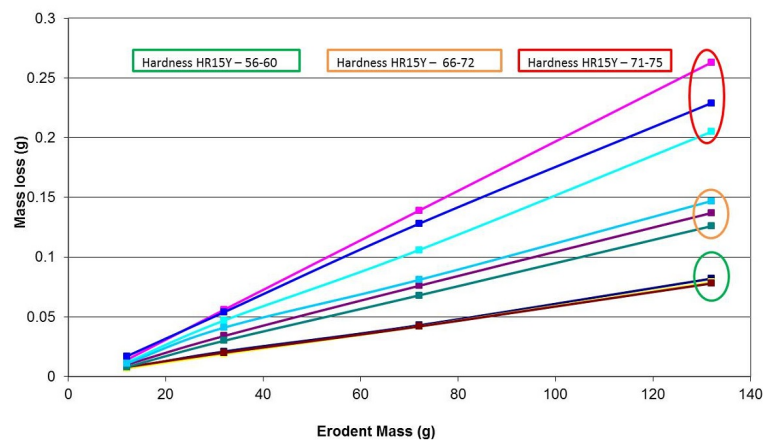


Figure 5.4: Erosion scars on the surface of the abrasible after  $30^\circ$  and  $90^\circ$  impact angle

Comparing the results of the  $30^\circ$  erosion test to the  $90^\circ$  tests, shows the difference in the damage to the surface layers. The dominant brittle fracture of the surface layers protects the deeper particles from deformation and compaction. The samples tested at  $30^\circ$  showed more smearing and plastic deformation, when analysed under the optical microscope.



(a) Results of the 30° Erosion Tests



(b) Results of the 90° Erosion Tests

Figure 5.5: Comparison of the Results from the 30°&amp;90° Erosion Test

Figure 5.5(a) and (b) show the results of the erosion testing in graphs. Material erosion rates are usually reported as mass loss per mass of eroding particles, thus giving a dimensionless measure of material removal, generally quoted as  $g/kg$ . The erosion rate is then the slope of the linear region on these curves.

Looking at the plots of the mass loss over the mass of erodent, which was used, three different groups can be identified. These are indicated with the help of the red circles included in Figure 5.5. The samples representing each group, are the same for the 90° and the 30° erosion tests, suggesting that the difference in behaviour reflects a change in material properties for each group of abrasives.

As mentioned earlier, the erosion rate would appear to be dependent upon the hardness of the coating. The harder coatings, containing less dislocator, erode less than the supposedly softer coatings with more dislocator. In Figure 5.6 the spread of the material loss is plotted against the hardness. The formerly indicated groups can be identified



within this plot whether eroded at 30° or 90° impact angle

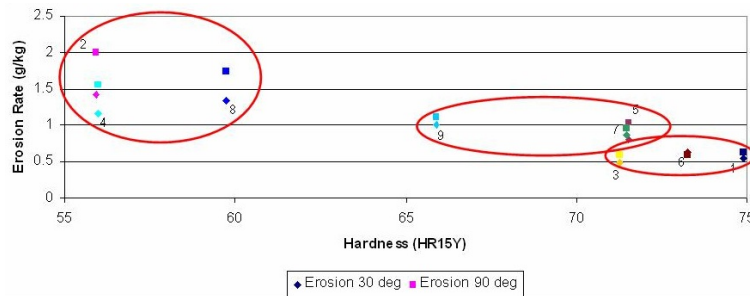


Figure 5.6: Plot of the Erosion Rate as a Function of the Hardness

## Scratch Testing

Scratch testing at Cranfield University with a load of 20 N and a scratch length of 10 mm was carried out on hard and soft M320 samples. The scratch trace on the soft coating is about twice the width of the trace on the hard coating. The indenter ball can compress the softer coating more, resulting in a wider track.

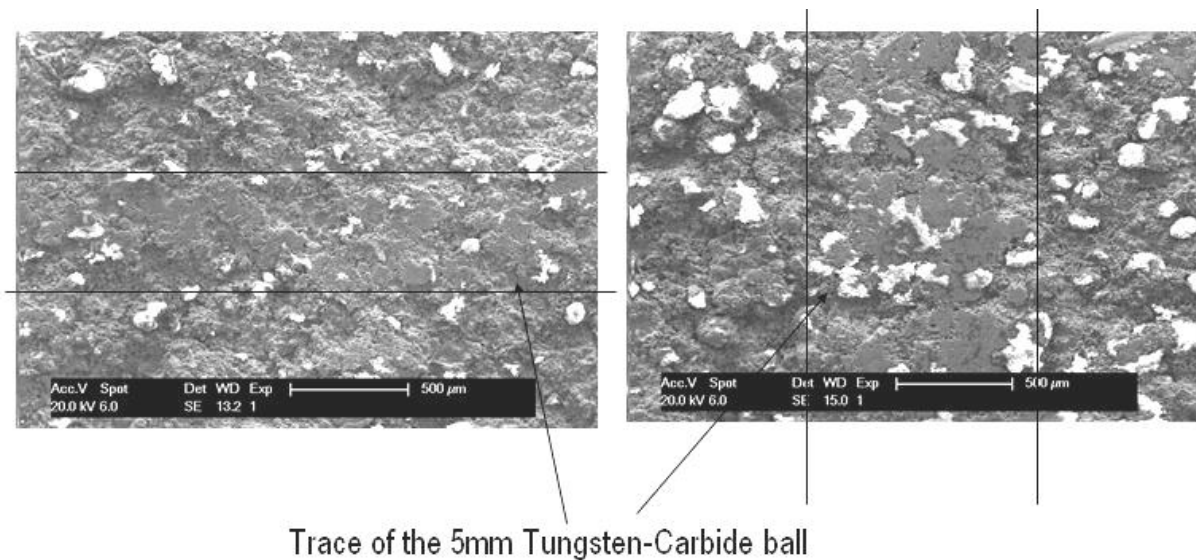


Figure 5.7: Traces left on the Surface of an Abradable Coatings by the Scratch Tester; showing the Hard Coating on the Left and the Soft Coating on the Right

The pictures in Figure 5.8 and 5.9 show the scratch samples when examined under the Scanning Field Emission Gun (FEG-SEM). The hard coatings reveal a cutting of the surface and some brittle fracture of the particles. The soft samples show smearing of the

material over the surface and grooving of the particles.

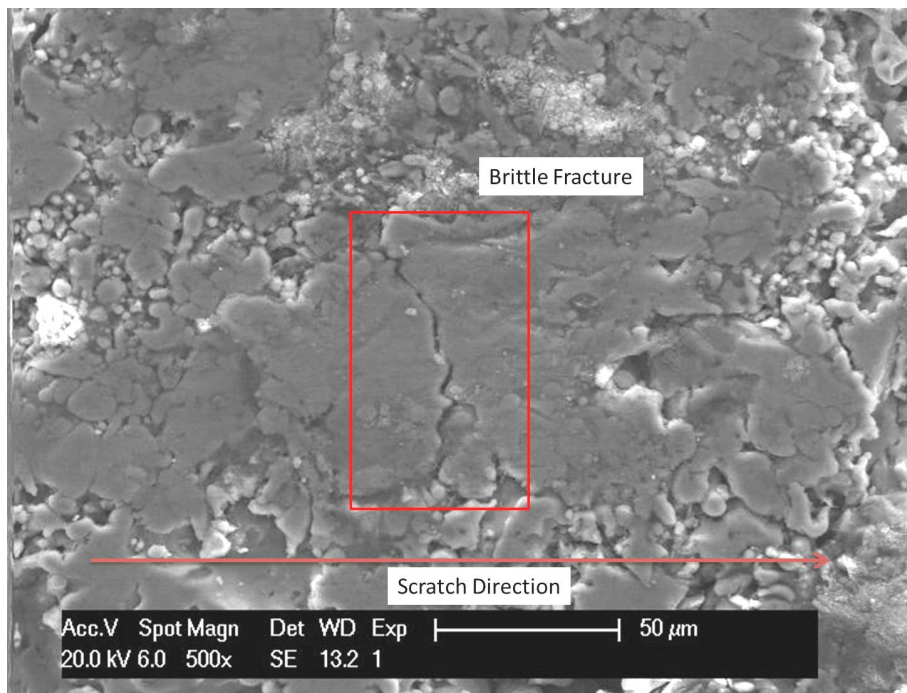


Figure 5.8: Scratch Damage to a Hard Abradable Seal Coating - Fracturing

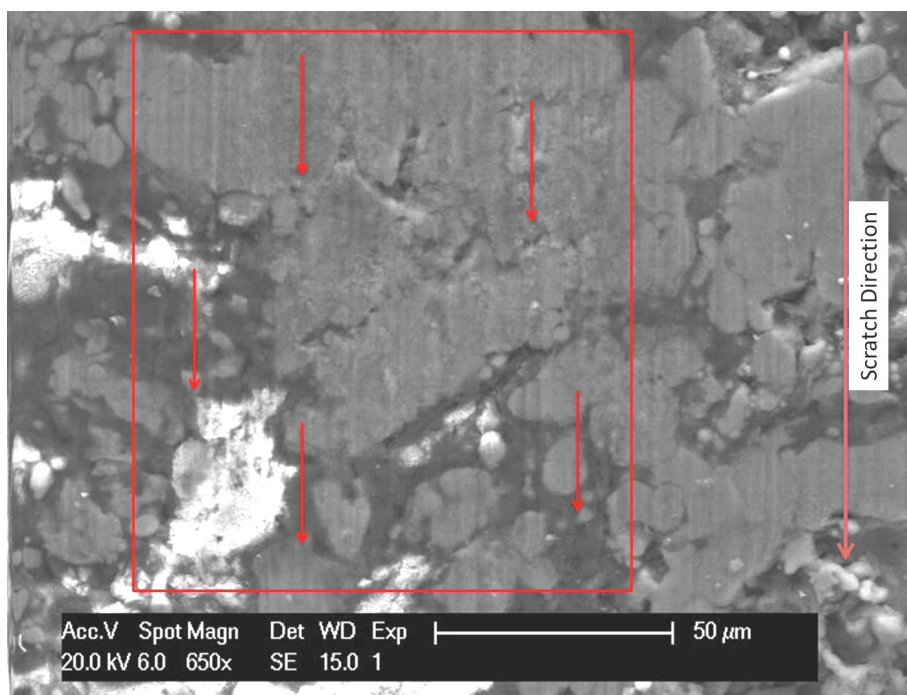


Figure 5.9: Scratch Damage to a Soft Abradable Seal Coating - Smearing

The softer coating material can be compacted more easily. This is due to the amount

of dislocator present in the microstructure. This compression of the soft coatings can be reproduced using scratch testing. Conversely the harder coatings show brittle fracture rather than compression and compaction.

## Statistic Analysis of the Erosion and Scratch Data

Analysing the erosion data at 30° and 90° using Weibull statistics shows that this model describes well the erosion damage of abrasible coatings in both tests conducted. The calculated  $\bar{R}^2$  for the two different tests are around 0.92 and 0.95, indicating a high degree of correlation between the experimental data and the Weibull statistical model.

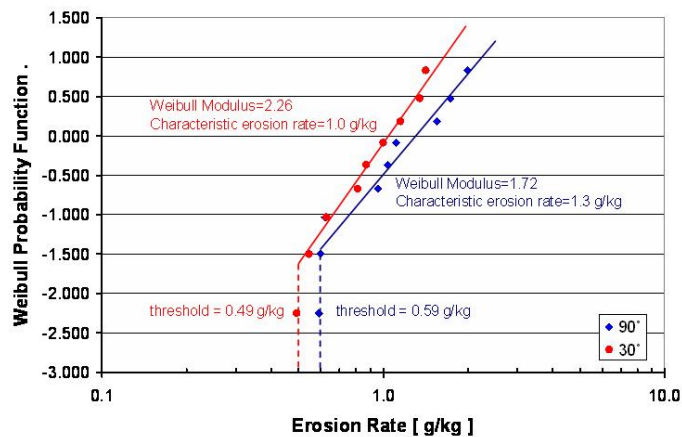


Figure 5.10: Weibull Analysis of the measured Erosion Rate Data

This model is plotted in Figure 5.10 and predicts the likelihood of damage at a given erosion rate. The graph shows that for either of the two test conditions a threshold of a minimum erosion rate is evident. No matter how much material of erodent is fired at the sample, a minimum rate of seal material removal will always be observed under the impact conditions used in this test. The threshold removal rate was  $0.49 \text{ g/kg}$  at a 30° impact angle and  $0.59 \text{ g/kg}$  at a 90° impact angle, whereas the characteristic erosion rate at these two impact angles were respectively  $1 \text{ g/kg}$  and  $1.3 \text{ g/kg}$ . Local maximum erosion rate may exceed  $1.5 \text{ g/kg}$  and  $2.0 \text{ g/kg}$  respectively. It is suggested that the threshold rates reflect the erosion behaviour of a 'hard' abrasible, with little dislocator present and the increase in erosion observed reflects softening due to added dislocator.

Thus, a similar analysis was carried out for the samples following the scratch testing. For each scratch a set of data was recorded and the degree of damage was evaluated for a scratch of  $10 \text{ mm}$  length.

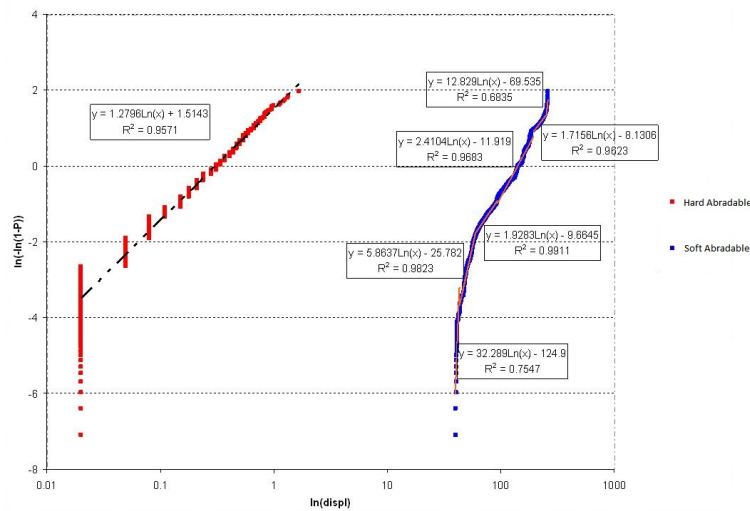


Figure 5.11: Weibull Scratch Results of a Hard and a Soft Abradable

Figure 5.11 plots this data for a series of hard and soft coatings. The plot shows that the samples behave differently during the test which reveals different patterns of material removal for the two coating types.

The harder coating shows less indentation and a two parameter Weibull curve after the 10 repeat scratches. The soft coating reveals a deeper indentation and multiple failure modes, which can be seen in the change in the slope. A threshold depth of damage is also observed. Multiple failure modes were identified for the hard coatings. Thus, this plot shows the possibilities to characterise coating failure using Weibull statistics. Depending on the mode of failure one may be able to identify this in the Weibull curve, but this will not always be the case, depending how different failure mechanisms interact.

Where the curve intersects with the x-axis, the characteristic scratch depth ( $\eta$ ) can be identified. This reveals a characteristic indentation depth for the hard material of  $\eta_H = 0.31 \mu m$  and  $\eta_S = 141.82 \mu m$  for the soft material. Thus, coating hardness, more specifically the microstructure and dislocator content is a most significant factor in determining material removal.

Further to these tests, M320 samples were abrasion tested and the recorded data were analysed using ANOVA statistics. During the evaluation, it was found that collinearity existed between some of the chosen exploratory variables. Therefore, rotations per minute (related to blade tip velocity) and volts (related to temperature during testing) were excluded, leaving blade tip velocity, incursion rate, time, cut per pass, temperature, tangential and axial force as exploratory variables.

Further investigations, and the inclusion of blade material loss and blade pick-up, led to the results shown in Figure 5.12. The analysis delivered an  $\bar{R}^2$  of 0.75 and an F-statistics of 24.73, which implies that the chosen variables are viable to describe the dataset given. Next to the blade material loss and heavy blade pick up ( $< 10 \text{ mg}$ ), the temperature and the blade tip velocity are statistically significant parameters defining the abradable material loss.

Regression Statistics									
Multiple R	0.89								
R Square	0.79								
Adjusted R Square	0.75								
Standard Error	250.65								
Observations	32.00								
ANOVA									
	df	SS	MS	F	Significance F				
Regression	4.00	6214636.27	1553659.07	24.73	0.00				
Residual	27.00	1696235.61	62823.54						
Total	31.00	7910871.88							
	Coefficients	Standard Error	t Stat	P-value	Lower 95%	Upper 95%	Lower 95.0%	Upper 95.0%	
Intercept	1926.11	458.74	4.20	0.00	984.86	2867.36	984.86	2867.36	
X Variable 1	-2.37	0.66	-3.56	0.00	-3.73	-1.00	-3.73	-1.00	
X Variable 2	-4.53	0.64	-7.11	0.00	-5.84	-3.23	-5.84	-3.23	
X Variable 3	7.65	1.20	6.35	0.00	5.17	10.12	5.17	10.12	
X Variable 4	2912.05	309.87	9.40	0.00	2276.26	3547.84	2276.26	3547.84	
	X1 - Blade Tip Velocity		X3 - Weight difference of the blade						
	X2 - Temperature		X4 - Heavy Blade Pick-Up						

Figure 5.12: Results of the ANOVA Analysis of the Data recorded during Abrasion Testing

It is important to notice the t-statistics resulting from the analysis to describe the relevance of individual variables in the equation. The  $|t_{crit}|$ , given from a table according to the degrees of freedom of the system, has to be smaller than the calculated  $|t_{stat}|$ . The  $|t_{crit}|$  for a 95% confidence level with 30 degrees of freedom is given with 2.042.

The data used to generate the statistical models was taken from work carried out by Noel Hopkins in his doctoral thesis from 2007 [80]. Prior to the statistical analysis of the given dataset, efforts were made to describe the numbers with a numerical model. Excel was used to plot the data points into graphs and develop a possible equation. A dimensionless variable named Abrasion Rate was introduced to describe the data set.

$$\text{Abrasion - Rate} = \frac{\text{Blade-tip-velocity}}{\text{Incurision-rate}}$$

In the Figure 5.13 a plot of mass loss of the abradable seal over the abrasion rate can be seen. A trendline was calculated for the change in mass for the blade as well as the abradable material; both are indicated with the lines through the respective data points.

The approximation of the dataset to a 3<sup>rd</sup> degree Polynomial looks promising. The initial cluster of point at the lower abrasion rate has a slight tendency towards a reduced mass loss. Tests with very high abrasion rates show a very rapidly changing mass loss with decreasing abrasion rate from 2500 *mg* → 25 *mg*.

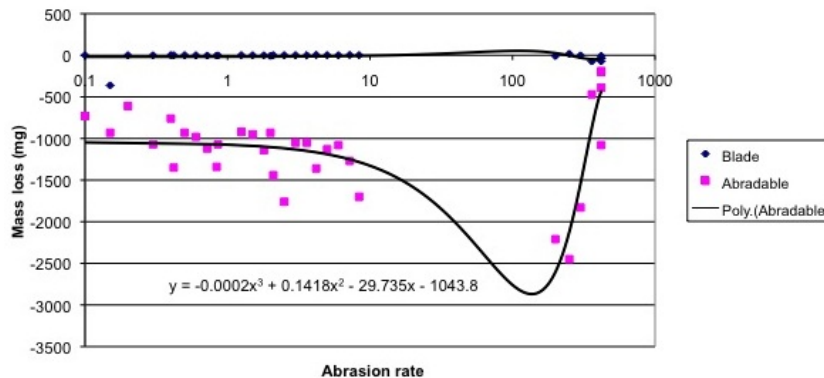


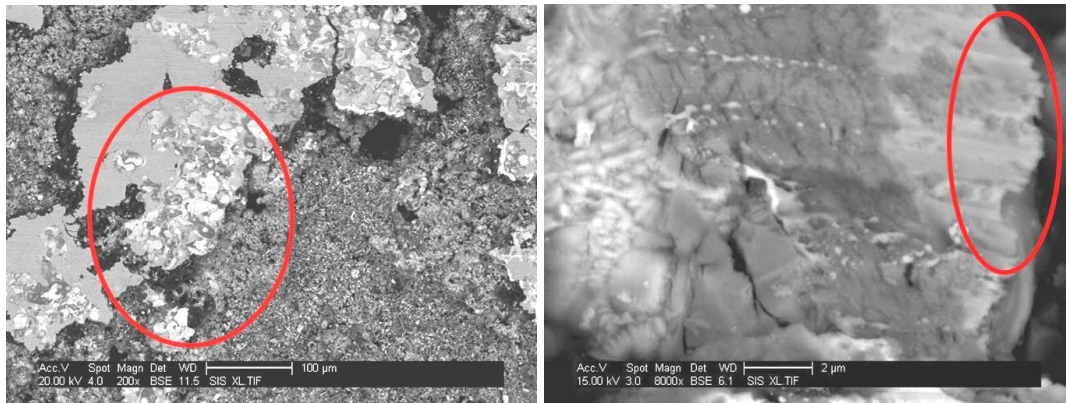
Figure 5.13: Plotted Mass-loss as a Function of the Abrasion Rate

So far attempts to find a relationship between the temperature and the blade weight loss, looking at the possibility for blade pick-up depending on higher temperatures resulted in no connection between these two variables.

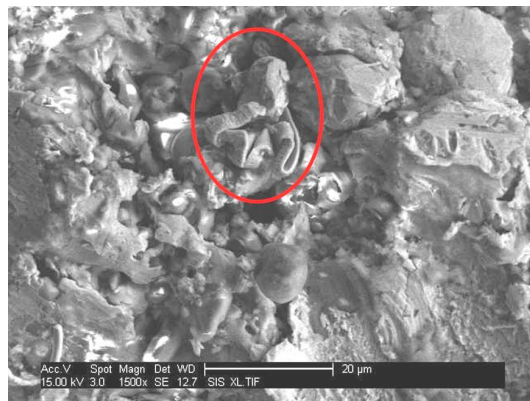
## Abrasion Testing

The failure modes observed under the microscope were variable and could be characterised as cutting, smearing and chip formation. Of the documented failure modes, cutting would be most preferred, but most likely is crushing, due to the limited edge radius of the blade.

Figure 5.14 shows the abrasion modes found using the electron microscope (Scanning Field Emission Gun - SFEG). In the red circles the damage caused during the interaction with the blade can be seen.



(a) Traces of Cutting through the Abradable during Testing (b) Traces of Smearing of the Abradable during Testing



(c) Chip left on the Surface after Abrasion Process

Figure 5.14: Interaction Phenomena during Abrasion Testing

### 5.3 Summary and Conclusion

- Erosion testing was found to generate very reliable and reproducible information on material loss from the various abradable coatings evaluated. A linear relationship between the erodent used and the material loss over the time was found. Soft coatings erode more than hard coatings and the mechanism of failure changes according to the impact angle.
- Microstructural analysis of the material after testing showed that the softer coatings show more severe erosion damage than the harder coatings. Softer coatings showed smearing on the surface layers and compaction of the porosity introduced through polymer and dislocator additions.

- The current lack of understanding of abradable seals coating performance creates the need to generate mechanical test data, and particularly measurement of the coatings repeatability in performance. The data created so far have been investigated with statistical measurements in mind.
- The influence of test parameters on cutting behaviour has been investigated. It was found that the temperature during the test, the blade tip speed and the blade pick up were statistically significant to describe the abrasion process.
- Investigations into the failure modes during the abrasion process revealed changing characteristics of the wear scar, relating to different failure modes.
- Cutting and smearing wear could be observed in the rub path of abrasion samples.



## Chapter 6

# Cracking Behaviour

### 6.1 Introduction

Pores in the abradable coating microstructure act like pre-cracks, where the metal matrix is separated by either voids or hBN particles. This non-continuous body has weak adhesion and fails along the pores [49] and hBN areas. Heating of the coating introduces inelastic deformation to the surface which leads to tensile deformation of the abradable's surface [116]

The Jethete casing material has a thermal expansion coefficient of  $9.8 * 10^{-6} m/K$ ; Jethete is the material used for casings in high pressure compressors. The bondcoat shows  $10.5 * 10^{-6} m/K$  and the M320 top coat expands at  $26 * 10^{-6} m/K$ . Due to the mismatch in thermal expansion, the coating cracks during thermal cycling in service, expanding a lot quicker than the substrate during start-up and contracting more rapidly when cooling down (see Figure 6.1). During heating up, the seal coat is in compression and slowly releases those stresses via creep relaxing during the cruise period. When the engine reduces temperature, the abradable shrinks and goes into tension, which can be seen in the dip below the x-axis on the graph.

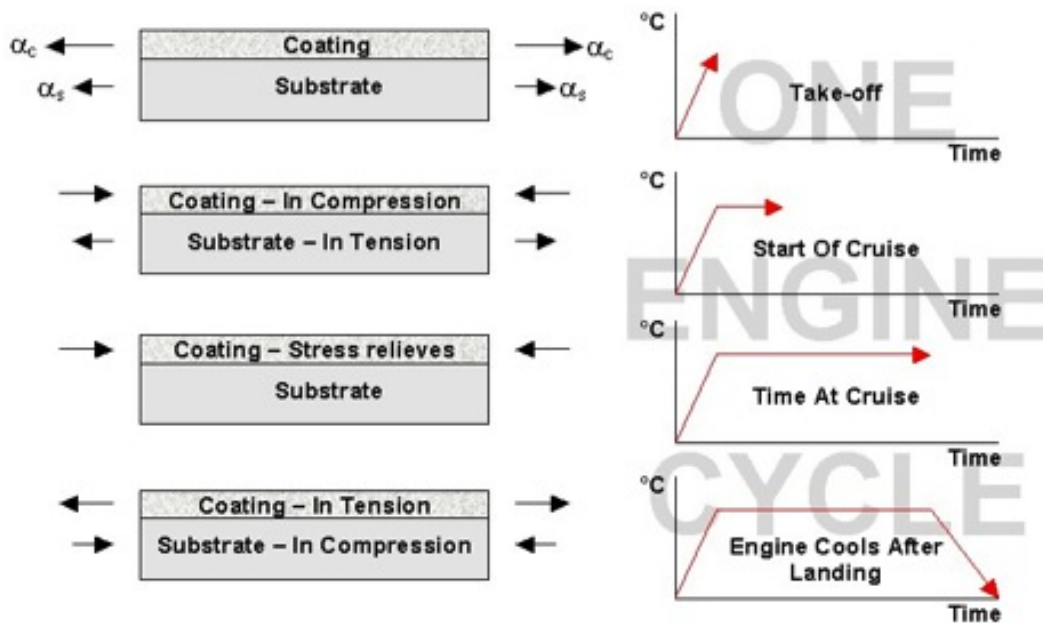


Figure 6.1: Forces acting upon the Abradable Material during Service

The reproduction of service failure modes in the laboratory has attempted in the laboratory for over 20 years, but neither mudflat cracking, nor spallation were achieved. In order to evaluate the cracking of an abradable seal coating, samples were water-quenched; and the influence of coating thickness, surface topology, thickness of the substrate, as well as preparation of the substrate and spray-direction upon the cracking behaviour was investigated.

Since water-quenching of abradable seals had never been done before, the cracking mechanisms, as well as the material degradation had to be monitored closely. The aim was to reproduce mudflat cracking as it was observed during service and microstructural changes happening in the material (mudflat cracking is the formation of islands on the coating's surface due to crack opening (see Table 6.6)).

Table 6.1 shows the sample geometries provided by Rolls-Royce, which were used for the beginning of the heat cycling study. Sets 1 – 4 were readily available as soon as the project started and set 5 was produced 6 months after the project had started.

Table 6.1: Sample Selection provided from Production

Set	Substrate			Abradable
	Length	Width	Thickness	Thickness
1	60	30	3	3
2	100	45	5	3
3	80	30	3	3
4	50	20	2.5	2.5
5	100	35	3	3

## 6.2 Heat Cycling

In order to generate service related cracking within the laboratory, M320 samples of set 1-4 (see Table 6.1) were heat cycled. At first, samples were cycled in an oven with air-cooling nozzles to cool the materials using compressed air. This took about 750 cycles (90 *min* at 450°C and 3 *min* in cooling air per cycle) for the material to initiate cracking on a micro scale. This type of heating and cooling would be representable of conditions in a gas turbine engine.

Due to the time-scale of this test and the limitation in furnace capacity (max. 3 samples could be cycled at once), the experimental stage was modified to allow water-quenching of the material after heating. In order to establish the cooling rates applied to the abrasible top coat, an infrared thermometer was used to measure surface temperatures during compressed air cooling, as well as water-quenching. The measurements taken are listed in Table 6.2.

Table 6.2: Cooling Rates recorded for Air-cooling and Water-quenching

Air Cooling		Water-quenching	
Secounds	Temperature	Secounds	Temperature
0	450	0	450
10	352	3	76
20	291	6	52
30	248	9	37
45	192	12	29
60	149	15	24
75	110	18	22
90	89		
120	58		
150	40		
180	35		

The difference in cooling rate achieved can be seen from the graph in Figure 6.2. It was

thought that even though higher cooling rates are applied to the material, the cracking will still be comparable to that happening in the engine. This was supported by observation made during testing, where micro-cracking after 2 water-quenching cycles was comparable to those cracks observed after 750 air cooling cycles.

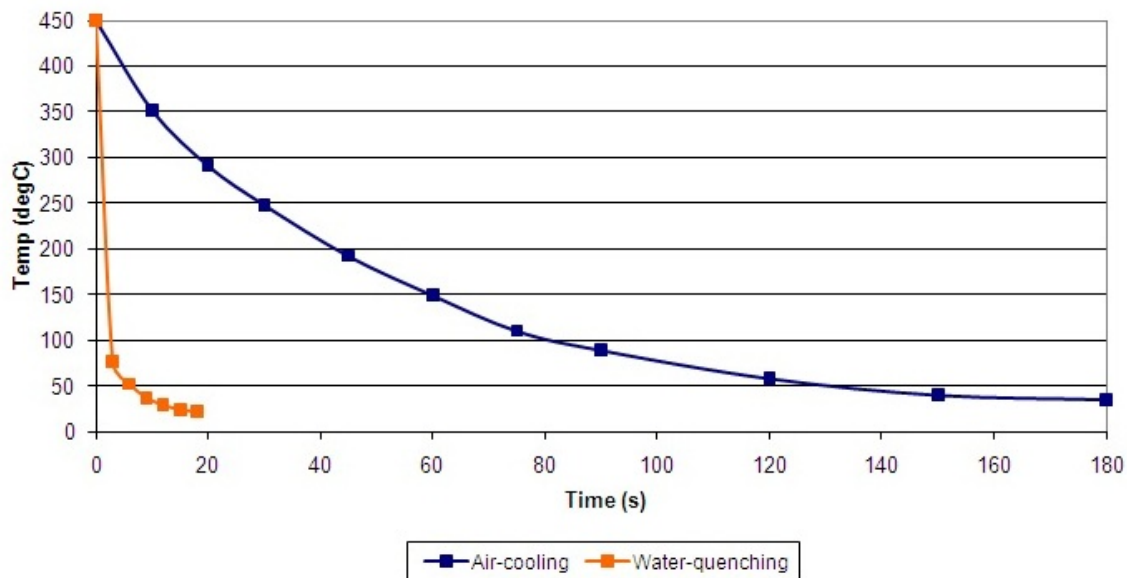


Figure 6.2: Cooling Rates applied to the Material during Air-cooling and Water-quenching

For the water-quenching set up the specimen were heated for 90 *min* at 450°C and then taken out individually any placed into a quenching bath. Holding the samples with tongs, they had to be swiveled through the bath at first because a layer of steam is formed on top of the surface. The movement in the water ensured an even cooling rate because the steam layer could not build up and insulate parts of the coating during the cooling cycle.

To evaluate the cracking mechanisms occurring during service, a new furnace was installed, more suitable for the testing below 500°C. Two trays were available inside the furnace (see Figure 6.3a), so up to 28 samples could be tested at the same time. The quenching bath, including the sieve to rest the samples on, is shown in Figure 6.3b.

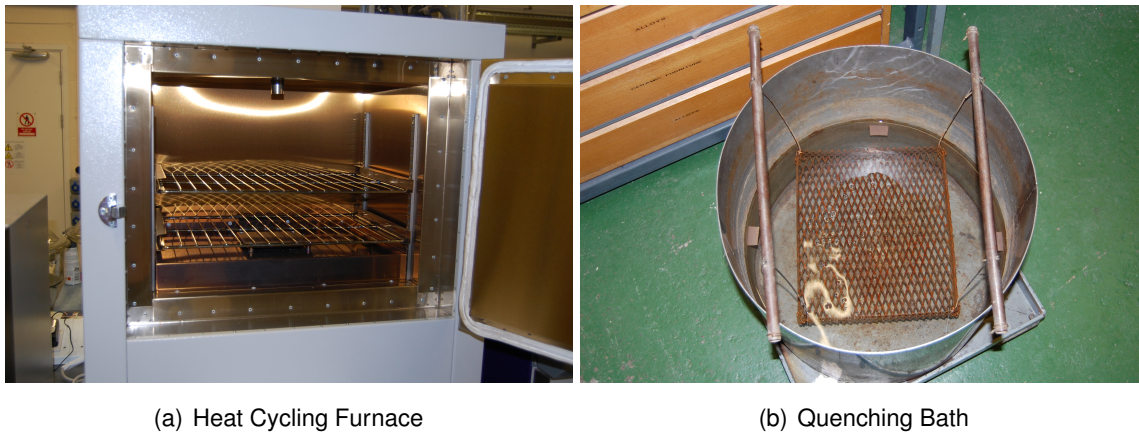


Figure 6.3: Furnace and Bath for Heat Treatment

After the *90 min* at temperature and the subsequent water quench, a *15 min* drying period at  $80^{\circ}\text{C}$  ensured that the material was completely dry, before the samples were heated again. This was important as enclosed water would evaporate almost immediately and the gas expansion could destroy the coating, should the samples be placed into  $450^{\circ}\text{C}$  whilst still wet.

### 6.2.1 Sample Manufacture

Further samples were produced (set 5 in Table 6.1), in order to intensify the research on M320 abradable cracking behaviour. Stainless steel substrates of  $100 \times 35 \times 3 \text{ mm}$  were grit blasted, bond-coated and finally the abradable top coat was applied. Figure 6.4 shows the plasma spraying process and the adjustment of the substrates in the machine.

Each substrate was individually clamped into a holder and a total of 16 samples could be held in the spray-booth during any one spray run. The stage rotated and the plasma spray gun was in a fixed position pointing at the stage. During deposition, the spray gun moved in a vertical direction, whilst the stage rotated, ensuring material deposition onto the entire substrate's surface.

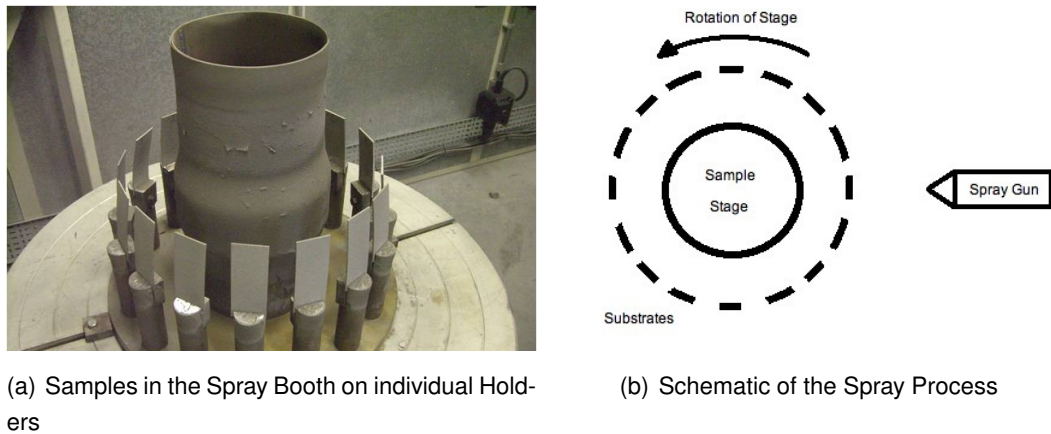


Figure 6.4: Outside - In Spraying of Abradable Samples

Two spray runs were carried out, resulting in 32 samples for testing at Cranfield University. These samples were heat cycled and their erosion resistance, scratch development and indentation performance was tested.

### 6.2.2 Crack-Development and Documentation

Cyclic heat treatment of abradable samples introduced cracking into the material. Cracks developed on the surface and grew downwards towards the substrate. Figure 6.5a shows a magnified image of a sample after 7 cycles. The onset of cracking can be seen on the bottom edge, indicated by the arrow. The following pictures document the very same area through the material's lifetime. First an increasing number of cracks can be seen, which then slowly grow into a network.

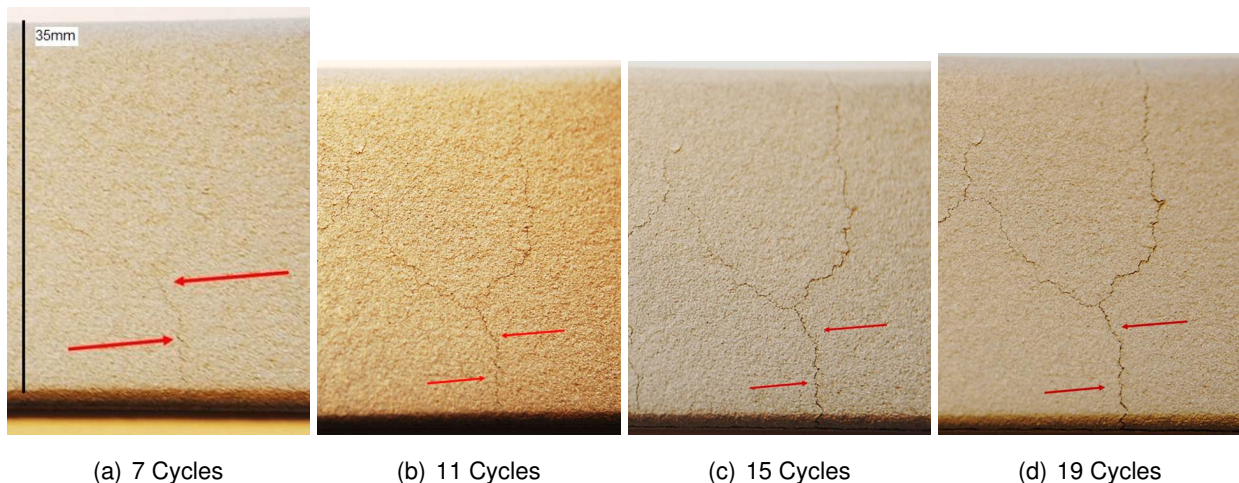


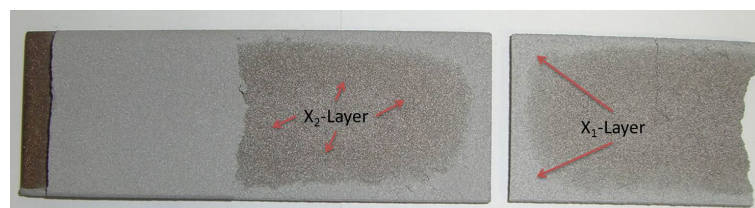
Figure 6.5: Example of Crack Growth of M320 on a 35 mm wide Sample

### 6.2.3 Delamination and Material Loss

Along with the observed cracking of the abrasible's surface, delamination was documented as an ongoing failure mechanism (see Figure 6.6a). Some of the samples cracked and delaminated until the stresses in the system were lower than the Yield Stress and therefore, remained in that position for the rest of heat cycling. Other samples delaminated and came off the substrate in chunks, leaving behind the bond coat surface (see Figure 6.6b).



(a) Delamination of the Abradable during Heat-Cycling



(b) Material Loss due to Delamination

Figure 6.6: Material Failures due to Heat-Cycling

Looking at the failed material, the formation of a lighter surface layer ( $X_1$ ), and a darker bottom layer ( $X_2$ ) was observed for all the samples subjected to heat-cycling. Figure 6.7 shows the different layers after the abrasible had failed due to delamination.

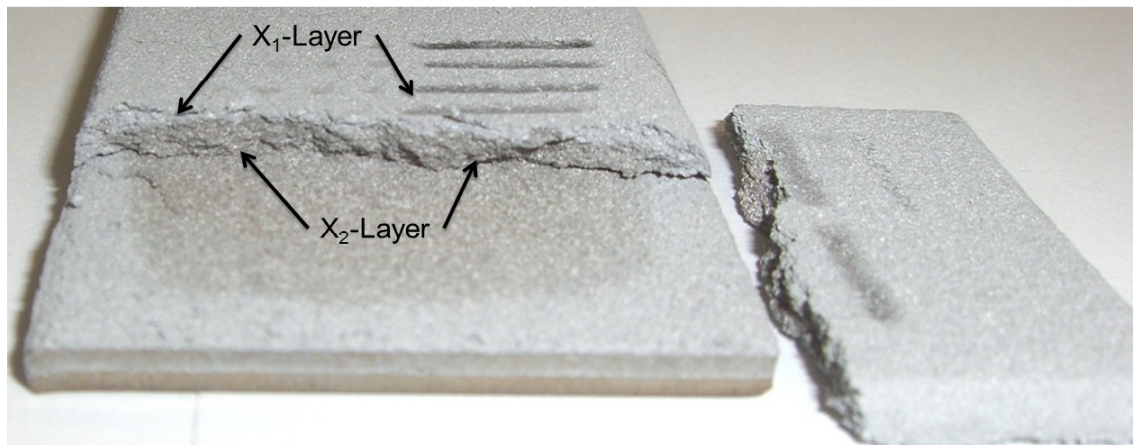


Figure 6.7: Formation of Two different Material Layers

### Confocal Microscopy of Crack Depth

A Confocal Microscope was used to analyse the depth of cracks opening on the surface of the abradable seal material. A laser scanned over the surface, measuring the response from the surface topography. The laser was adjusted above the sample and can only read straight down. It formed a  $90^\circ$  angle between the beam and the surface of the coating. Therefore, only cracks perfectly perpendicular to the surface could be measured. As soon as the fracture of the seal coating angled off (see Figure 6.8), it could not be tracked by the confocal microscope.



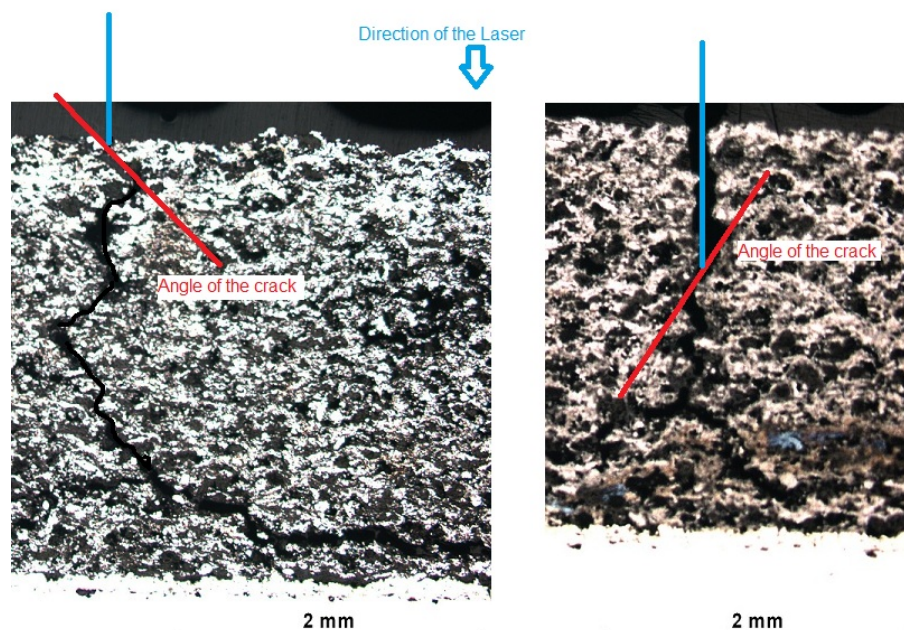


Figure 6.8: Angling of the Cracks during Growth

It was, however, possible to track the initial crack growth and later on the crack widening of the material. In Figures 6.9, M320 is imaged during different stages in the cyclic life. The first picture shows that cracking had not begun after 3 cycles; only the rough surface of the material after spraying can be seen. Due to the roughness it was difficult to distinguish between surface topography and crack initiation. Figure 6.9b captures the onset of a crack after 6 cycles of water-quenching.

In Figures 6.9 c & d the crack can be distinguished from the surface and due to the different magnifications of the pictures it can be seen that the crack widens between cycles 9 and 20.

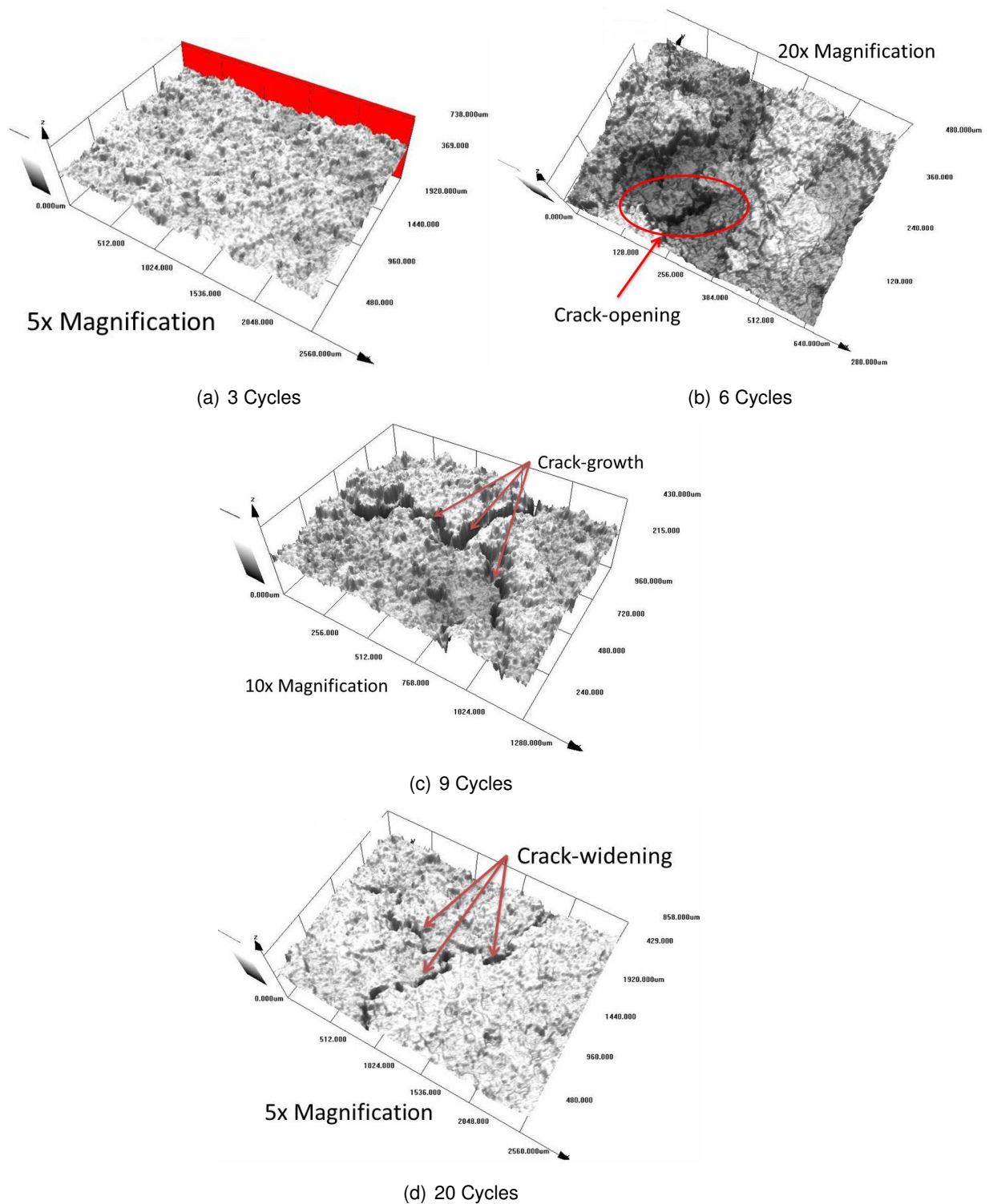


Figure 6.9: Confocal Microscope Images of Cracks forming and growing at the Surface

Plotting the measured crack depth and width against the number of cycles can be seen in Figure 6.10. The width of the cracks continues to grow over the material's lifetime, whereas the depth measurements level out at higher cycles. This could be due to the fact that the cracks do not grow perpendicular to the surface. Depth measurements can not

be traced continuously, but the widening of the crack can.

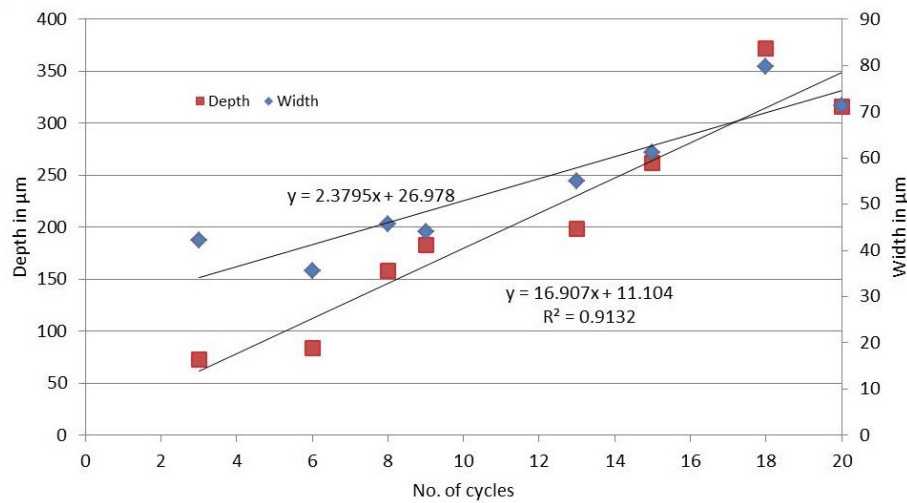


Figure 6.10: Comparing Crack Depth and Width over Number of Cycles for a M320 Abradable by Confocal Microscope

### Optical Microscope

Using the optical microscope the crack path can be analysed due to the different colouring of the phases within the material. It can be seen that the crack finds its way through the hexagonal Boron Nitride phase during propagation. The cracks grow towards the substrate and angle their way through the abradable liner until they reach the area just above the bond coat, where delamination may have started already. There, the mudflat cracks grow into delamination cracks and cause the coating to spall (see Figure 6.11).

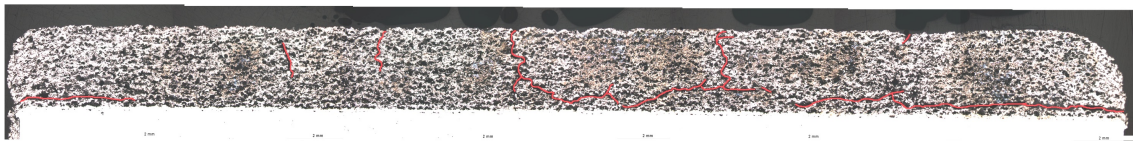


Figure 6.11: Cross Section after Heat Cycling with Mudflat and Delamination Cracks

### Scanning Field Emission Gun - Scanning Electron Microscopy - SFEG-SEM

For further detail of the crack growth the samples were analysed using the SFEG-SEM. Cracks could be seen and their path was traceable along *hBN*-rich planes. In Figure 6.12 the opening of the crack-path follows bigger areas of the dislocator and makes its way through them, in order to keep growing, finding its way to the next *hBN* particle.

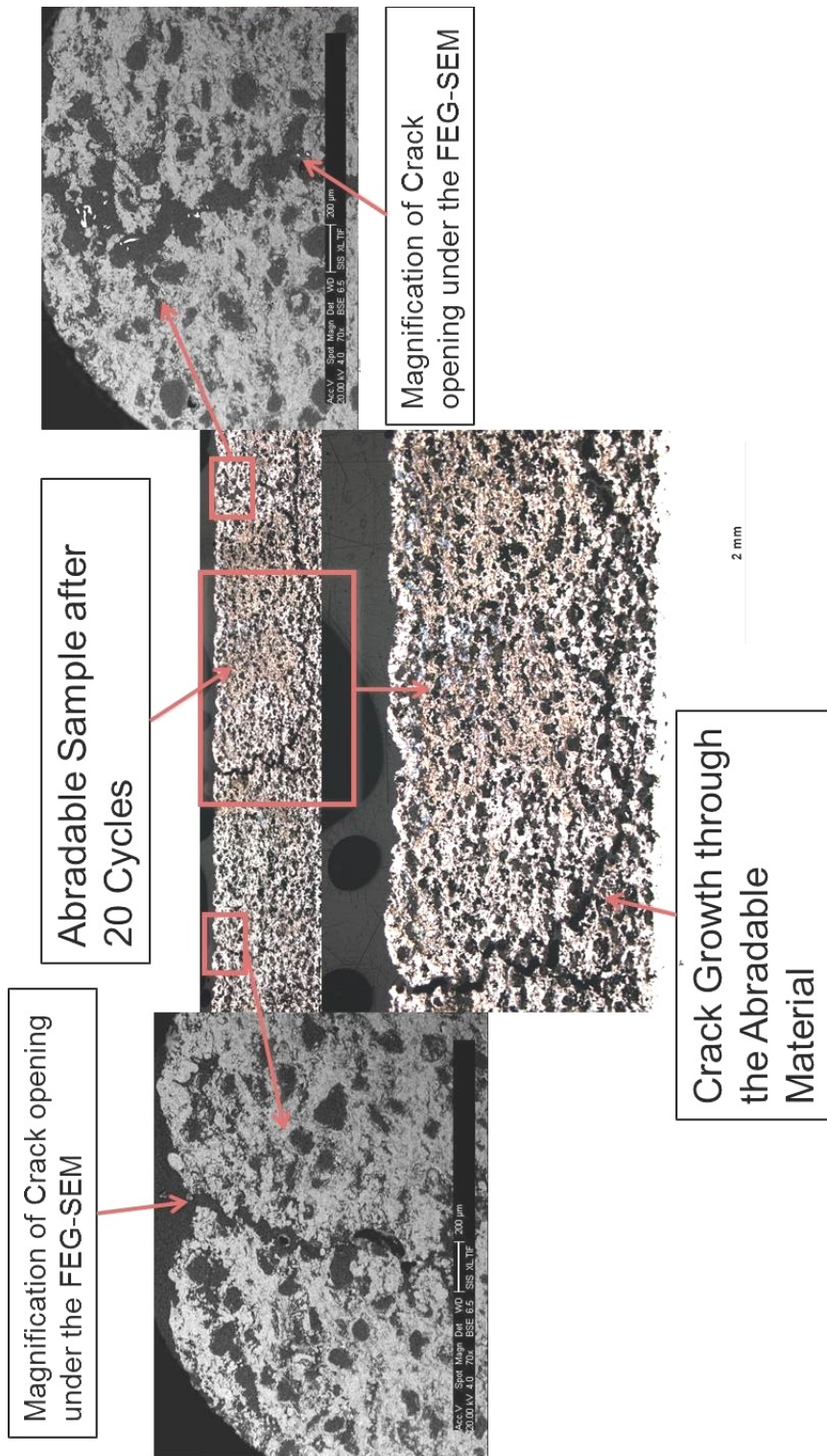


Figure 6.12: Crack Propagation through the *hBN* Phase of the Abradable

### 6.3 Transient Analysis

Looking at the failure modes of samples evaluated concerning their cracking behaviour, it was found that increased crack growth could be observed on thicker substrates. For all samples heat cycled in a preliminary assessment, crack initiation at the surface started around the 4th cycle and from that point onward started growing across the surface and towards the substrate. Due to the fact that the selection of samples initially provided included substrates of varying geometries (see Table 6.1 on page 79), it became clear, that the transient of the material influenced the failure mode of the top coat. // The transient describes the thermal properties of the substrate, when exposed to a sudden temperature change. In this case, different materials were water-quenched from  $450^{\circ}\text{C}$  to room temperature. The transient describes how quickly the samples lose their stored heat over the surface area and convection properties of the quenching-medium.

To see the influence the substrate thickness had upon the cracking of the abrasible, stainless steel samples, measuring  $100\times 40$  with a thickness of 0.5, 1, 1.5, 2, 2.5 and 3 mm, were manufactured. After grit-blasting, the 0.5 and 1 mm substrates were excluded due to intense deformation, which would have been impossible to place into the spray booth.

The 1.5 – 3 mm samples were bond coated and then placed into the spray booth for the application of the top coat. To simulate conditions during spraying of a compressor casing, it was chosen to clamp the samples into an empty casing for the deposition of the abrasible top coat. Figure 6.13 shows the new lay out of the deposition process.

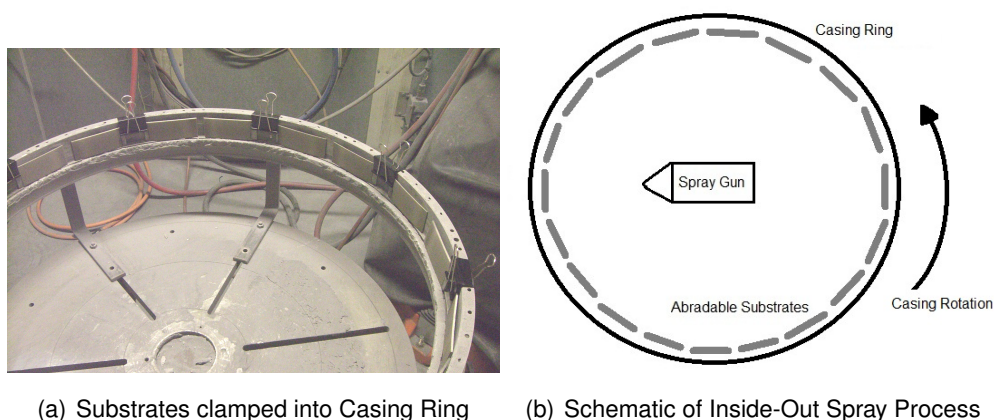


Figure 6.13: Set-up for inside-out Spraying of Abradable Material

During thermal cycling the samples cracked and bend, which can be seen in Table 6.6 on page 95. It became clear during testing that thinner substrates bent during thermal cycling, whilst the abrasible on thick substrates showed more cracking. The stresses within the top coat were sufficiently high to produce a concave bending (see Schematic

in Figure 6.14) of the samples sitting on substrates with a thickness of 1.5 mm, which indicated tensile stresses developed in the coating. With increasing thickness the curvature of the sample reduces and the crack patterns produced during cycling change from local crack initiation to crack initiation and growth.

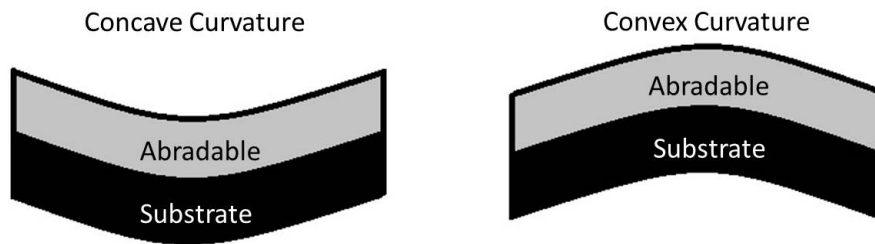


Figure 6.14: Curvature of the Water-quenching Samples

Unlike previous samples, delamination was never a dominant failure mechanism for the samples measuring 100 x 40 mm. The mudflat cracking network, which formed on the surface, was distinct for each sample geometry. It was evident that the thinner the substrate the more irregular the pattern of the mudflat cracks. No proper network of cracks formed, but rather a collection of crack initiation sites that progressively grew together. The thicker the substrate, the more regularity could be seen in the crack network pattern forming on the surface. The cracks initiated at the edges and at the centre of the surface and grew over time, connecting and building up a distinct system of bigger mudflats on the outside, surrounding smaller mudflats in the centre.

Following on from these results, the research into the substrate influence was taken further, by looking into different materials that could be used as substrates. New substrates were procured, grit blasted and sprayed; again, clamping them into an empty casing. To justify the chosen material and geometry their transient properties were calculated, using the help of the Biot Number. The Biot Number is a dimensionless measure of the temperature drop in a solid, relative to the temperature difference between its surface and the surrounding fluid [117]. It is calculated via:

$$Bi = \frac{hL_c}{k},$$

where  $L_c$ -characteristic length (calculated as  $Volume/Area$ ),  $h$ -film coefficient associated with convection heat transfer through the thermal boundary ( $h = \frac{dQ}{AdT}$ ) and  $k$ -thermal conductivity of the solid.

Figure 6.15 shows the results of the transient analysis of substrate materials 316, Ti, Al and Cu. In order to compare failure modes, 316 and Ti substrates were designed to

be 3, 4, 5 and 6 mm thick, whereas *Al* and *Cu* was chosen to measure 5, 6, 7 and 8 mm in thickness.

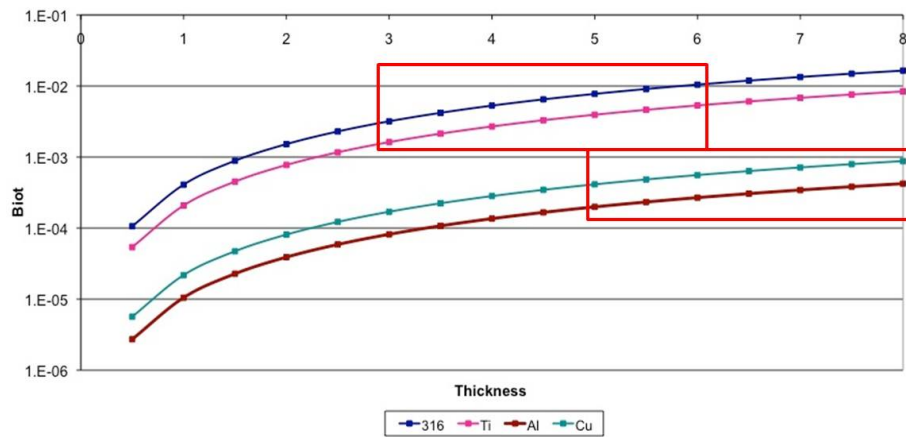


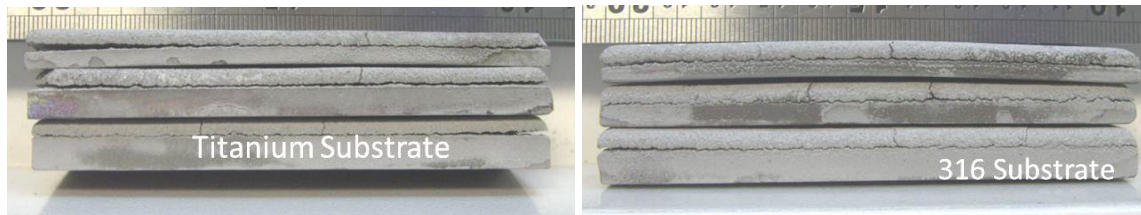
Figure 6.15: Biot Number for increasing Thicknesses of 316, *Ti*, *Al*, *Cu*

This way 316 and *Ti* could be compared for transient properties and their resulting cracking. Similarly, *Al* and *Cu* could be compared concerning their failure mode. Furthermore, in all sets the thickness of 5 and 6 mm was incorporated to see how the substrate thickness influenced the cracking, depending upon the material. The material data for the substrate materials used for the transient analysis are listed in Table 6.3.

Table 6.3: Material Data for the Substrate Materials

Material	Young's Modulus [GPa]	Thermal conductivity [W/m * K]	Thermal expansion [ $\mu\text{m}/\text{m} * K$ ]
316 Stainless Steel [316]	200	19	16
Titanium [ <i>Ti</i> ]	105	22	9
Copper [ <i>Cu</i> ]	117	390	16
Aluminium [ <i>Al</i> ]	69	250	22

Intense thermal cycling of the samples resulted in concave bending (see Figure 6.17) and cracking (see Figure 6.16) of the top coat, dependent upon substrate material. Also, the observations made on the initial stainless steel samples, namely bending, crack initiation and growth, could be confirmed. Therefore, the change in cracking behaviour could be linked to the transient properties of the substrate material.

(a) *Ti*-Substrates of 3, 4 and 5 mm Thickness

(b) 316-Substrates of 3, 4 and 5 mm Thickness

Figure 6.16: Delamination of Abradable from various Substrates

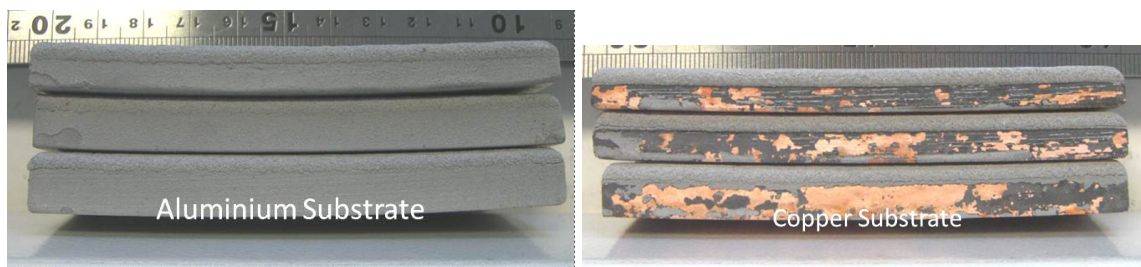
(a) *Al*-Substrates of 5, 6 and 7 mm Thickness(b) *Cu*-Substrates of 5, 6 and 7 mm Thickness

Figure 6.17: Delamination of Abradable from various Substrates

Tables 6.4 and 6.5 shows the cracking behaviour and resulting crack-patterns of M320 deposited onto *Ti*- and 316-Substrates.

Table



Table 6.4: Crack Growth for M320 Abradable Samples with 3 mm Top Coat on 316-Stainless Steel Substrates

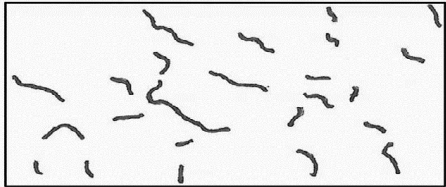
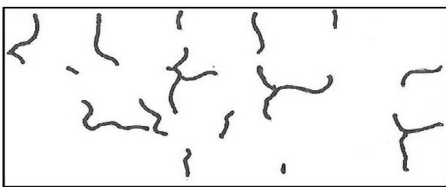
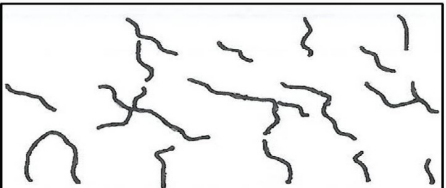
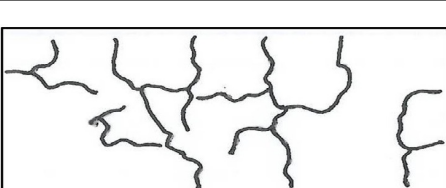
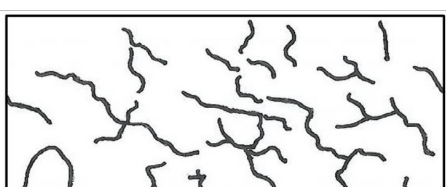
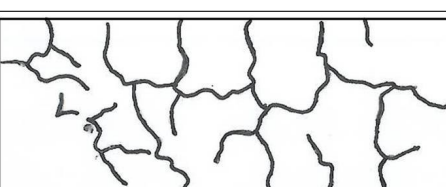
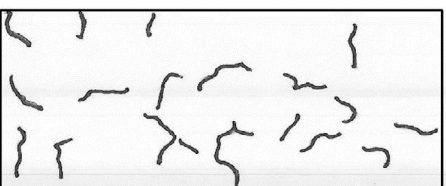
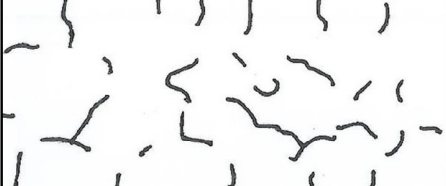
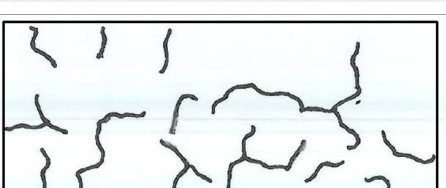
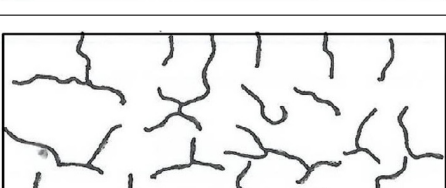
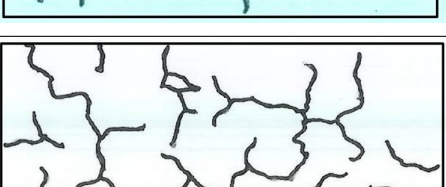
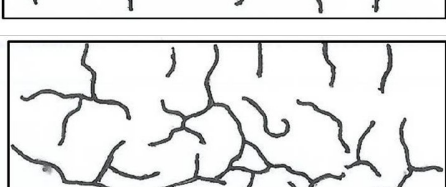
No. of Cycles	3 mm Substrate	4 mm Substrate
5		
10		
15		
	5 mm Substrate	5 mm Substrate
5		
10		
15		

Table 6.5: Crack Growth for M320 Abradable Samples with 3 mm Top Coat on Ti-Substrates

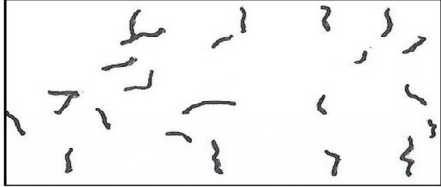
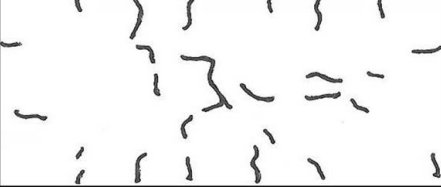
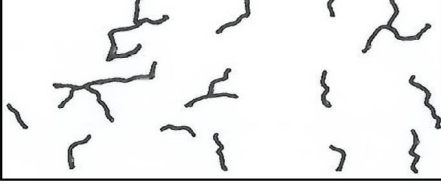
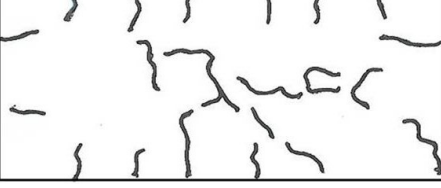
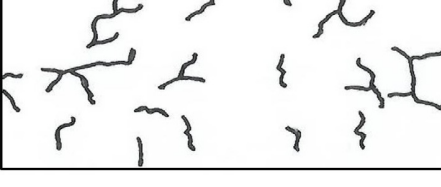
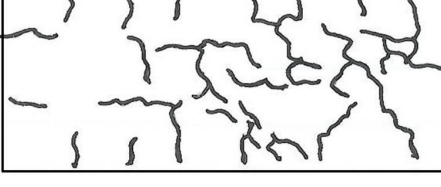
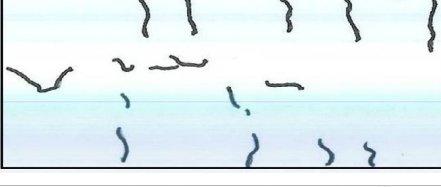
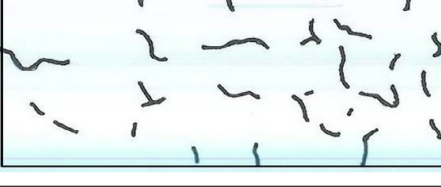

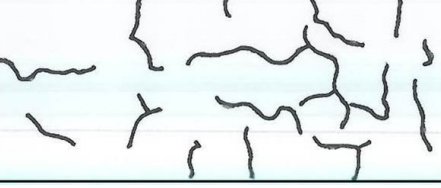

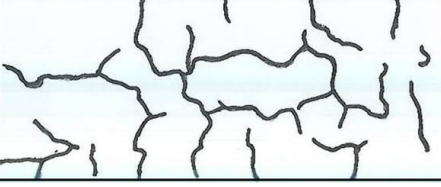
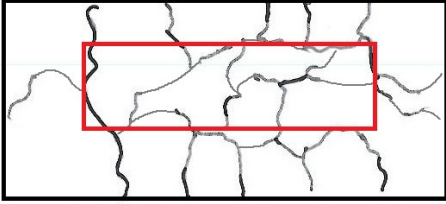
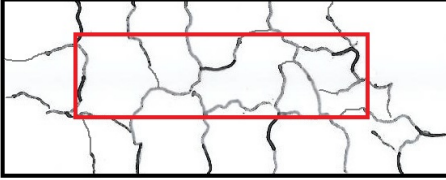

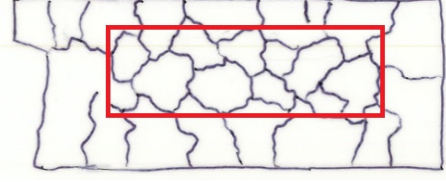
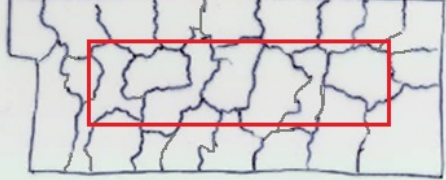
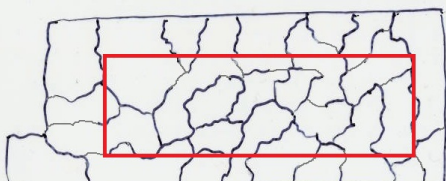
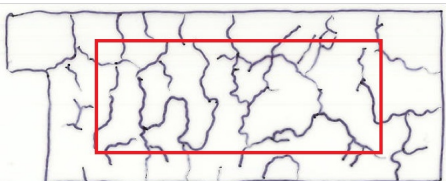
No. of Cycles	3 mm Substrate	4 mm Substrate
5		
10		
15		
	5 mm Substrate	5 mm Substrate
5		
10		
15		

Table 6.6: Crack Patterns for M320 Abradable Samples with 3 mm Top Coat and Varying Substrate Thickness

Thickness	Pattern	Mudflat Area in $mm^2$	Edge Area in $mm^2$
6		960	3040
5		1150	2850
4		1180	2820
3		1125	2775
2.5		1550	2450
2		1785	2215
1.5		1825	2175

The material deposited onto a substrate of 3 mm thickness revealed more crack growth

and therefore a more defined network of deeper cracks with an increased size of mudflats. The top coat did not delaminate and the samples remained intact throughout testing.

## 6.4 Crack Driving Parameters

### 6.4.1 Grit Blasting

As a trial to assess the grit blasting influence upon the stresses in the substrate, 1 mm and 1.5 mm stainless steel plates of 100x40 mm were grit blasted along the short axis (vertical - v) and along the long axis (horizontal - h) respectively. Figure 6.18 shows a schematic of the grit-blasting process (a) and the effects upon the substrate (b).



(a) Schematic of Horizontal and Vertical Grit-Blasting

(b) Deflection of 1 and 1.5mm Substrates after Grit-Blasting

Figure 6.18: Grit-Blasting Procedure and Results

In order to calculate the stresses generated in the substrate, the curvatures of the plates after grit blasting were measured and the bending radius calculated via:

$$\left(\frac{l}{2}\right)^2 = h * (2R - h) \quad [118],$$

where  $R$  - radius,  $h$  - height of the arc the substrate presents when placed onto a flat surface and  $l$  - length of the sample.

Using elastic beam theory, the stress in the material can be calculated with:

$$\sigma_{surf/bend} = \frac{Et}{2R} \quad [118],$$

where  $E$  - elastic modulus of the substrate material and  $t$  - thickness of the substrate. The results and the decrease in measurable stresses with increase in substrate thickness is shown in Table 6.7. The vertically treated material shows higher stresses and a slower decline of stresses, compared to horizontal grit blasting.

Table 6.7: Stresses in the Substrate after Grit-Blasting

Substrate Thickness in mm	Grit-Blasting Direction	Stresses in MPa
1	vertical	34
1.5	vertical	30
1	horizontal	18
1.5	horizontal	4

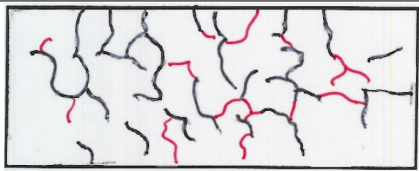
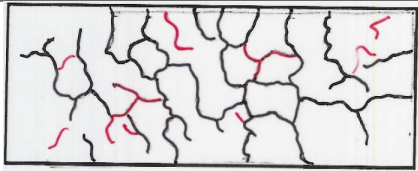
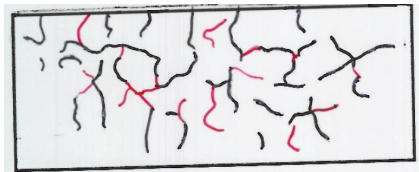
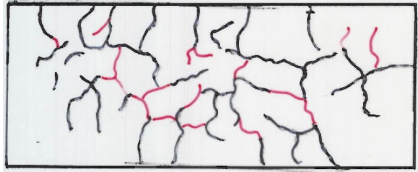
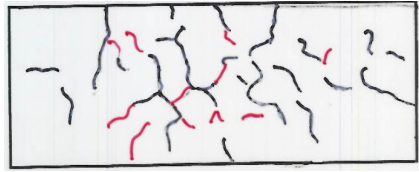
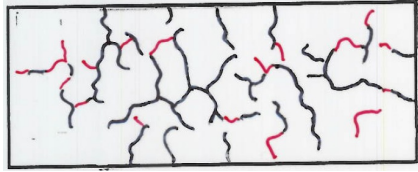
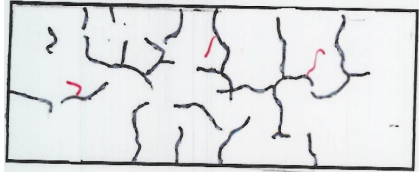
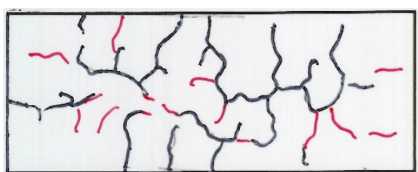
Even though the degree of bending declines with increase in substrate thickness, the grit blasting process affects the material surface and following that the stress state of the sample. The surface, which is later bond coated and plasma sprayed with an abradable top coat stores the stresses applied during grit-blasting and stress relieves during thermal cycling. To show the effects of grit blasting upon the cracking behaviour, experiments with different substrate thickness and grit-blasting direction were carried out.

2.5 and 3 mm stainless steel substrates were grit blasted either vertically or horizontally. Afterwards a bond-coat and abradable top coat were applied. The differences in stresses introduced into the surface varied drastically and the resulting crack pattern and the overall crack area can be traced back to the grit blasting treatment.

After the initial similarities in crack growth, the samples grit blasted parallel to the long edge (horizontally) cracked to a total crack length of around 200 – 250 mm, whereas the samples prepared parallel to the short edge (vertical) continue to increase their crack propagation to a length of 380 – 430 mm with number of cycles.

These results show that even though the samples do not bend after grit blasting, still a layer of an increased stress state is induced into the material surface. The thickness of the sample prevents the whole substrate from bending, but the surface stresses influence the cracking behaviour of the top coat.

Table 6.8: Influence of Grit-blasting Direction upon Cracking Behaviour

	15 – 19cycles	19 – 36cycles
2.5 vertical		
3 vertical		
2.5 horizontal		
3 horizontal		

The measured crack areas for the different thicknesses and grit-blasting directions can be traced on the sample's surfaces. Representative of the tested specimen, Table 6.8 shows the growth of the crack pattern of the top coat during cycling. The increase in cracking is indicated in red, whereas the black lines show the network previously present on the surface.

#### 6.4.2 Plasma Spraying

During plasma spraying the substrate goes through thermal cycles due to the rotating movement of the sample stage. The heat cycles the material is subjected to depend upon the spraying process and sample positioning. During spraying from the outside inwards the samples are held individually and can cool down appreciably due to the lack of a back plate insulation.

Should the substrates be clamped to a casing ring, then the spraying direction is from the inside outwards, the thermal cycle is reduced because the substrate is thermally insulated by the casing and therefore not able to cool as much.

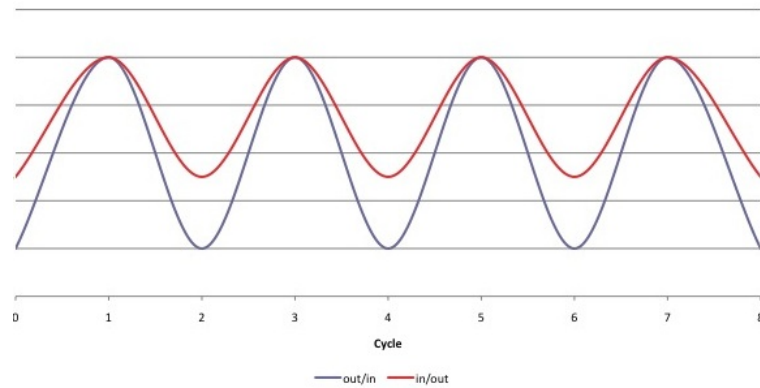


Figure 6.19: Schematic Thermal Cycles of the Substrate during Spraying, dependent upon Spray Direction (in/out or out/in Spraying)

With each pass of the samples (adjusted in a rotating casing) along the plasma gun, a new layer is deposited, which solidifies quickly and shrinks during cooling. The splats adhere to the previously deposited surface and cool down, whilst held in place by the solidified layers underneath. Stress in each layer build up due to the restricted shrinkage of the deposited powder particles.

With each layer being deposited, new stresses form, all being kept within one layer of deposition. This leads to stresses throughout a material layer, but no stresses forming through the thickness, as explained by Asghari et. al. [59] and shown in Figure 3.10 on page 43.

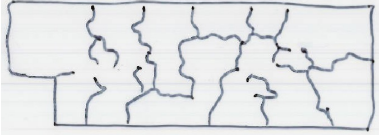
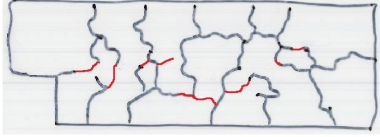

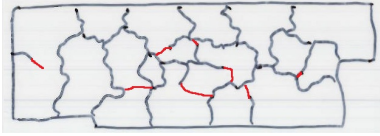
### 6.4.3 Surface Machining

Plasma Spraying leaves behind a very rough surface of the top coat, which is machined in order to smoothen the abrasible after cooling. Comparing as-sprayed, gently ground and abrasively machined seal coatings shows an influence of the surface treatment upon the failure observed during testing.

As-sprayed material has an open pore structure within which the abrasible can extend during heating and shrink during cooling, allowing stresses to be absorbed in the microstructure. Gentle polishing takes off the unevenness of the sprayed surface but leaves enough porosity for the top coat to absorb initial stresses building up during cycling.

The more violent the abrasible is machined back after spraying, the more stresses are introduced into the material during preparation, before the actual exposure to a working environment. It was thought, that more machining meant more densification and an ever

Table 6.9: Crack Development on Polished Surfaces

Surface Polish	Cracks after 29 cycles	Cracks after 36 cycles	Lifetimes
120			7 – 36 cycles
240			25 – 44 cycles

decreasing amount of open porosity in the material surface and the once 'flexible' material hardens and compacts, resulting in an almost dense top coat. During testing no evidence of surface compaction was found, even though abradable material was machined down from 3 mm to 1 mm.

Heat cycling the ground samples resulted in premature delamination of the samples. This indicated higher stresses in the material after machining, which reduced material's cyclic life. The cracks resulting from water-quenching increased in width and depth at an increased pace, followed by the loss of the abradable liner.

The harsher treated top coat (120 grit polishing paper was used) showed less cracking on the surface throughout the test period (see Table 6.9), but on all samples the abradable delaminated within 36 cycles. The smoother treated abradable showed more intense cracking on the surface, but only 30% of the samples failed due to delamination during testing.



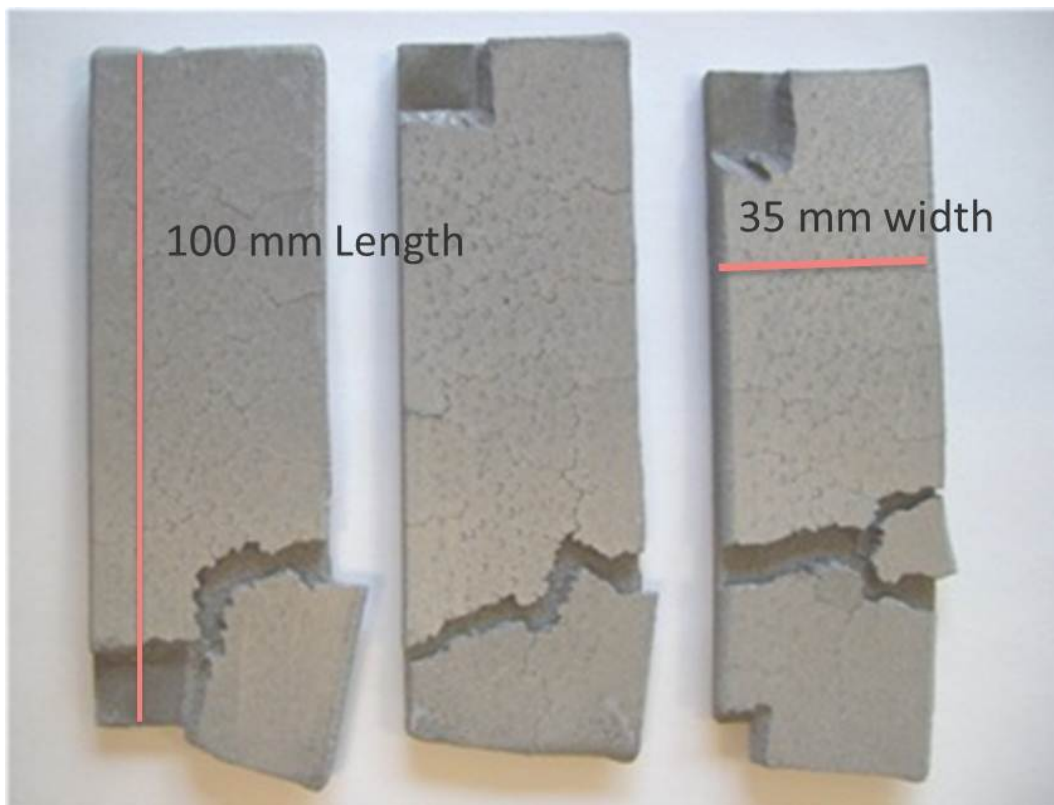


Figure 6.20: Ground Samples using a 120 Grit Paper, having failed during Thermal Cycling

Figure 6.20 shows the samples, which were ground with a 120 grit paper and their failure during heat cycling. All samples delaminated prematurely, within 7 – 15 water quenching cycles. The material lasted up to 40 cycles unpolished and 25 cycles when ground with a 240 grit paper.

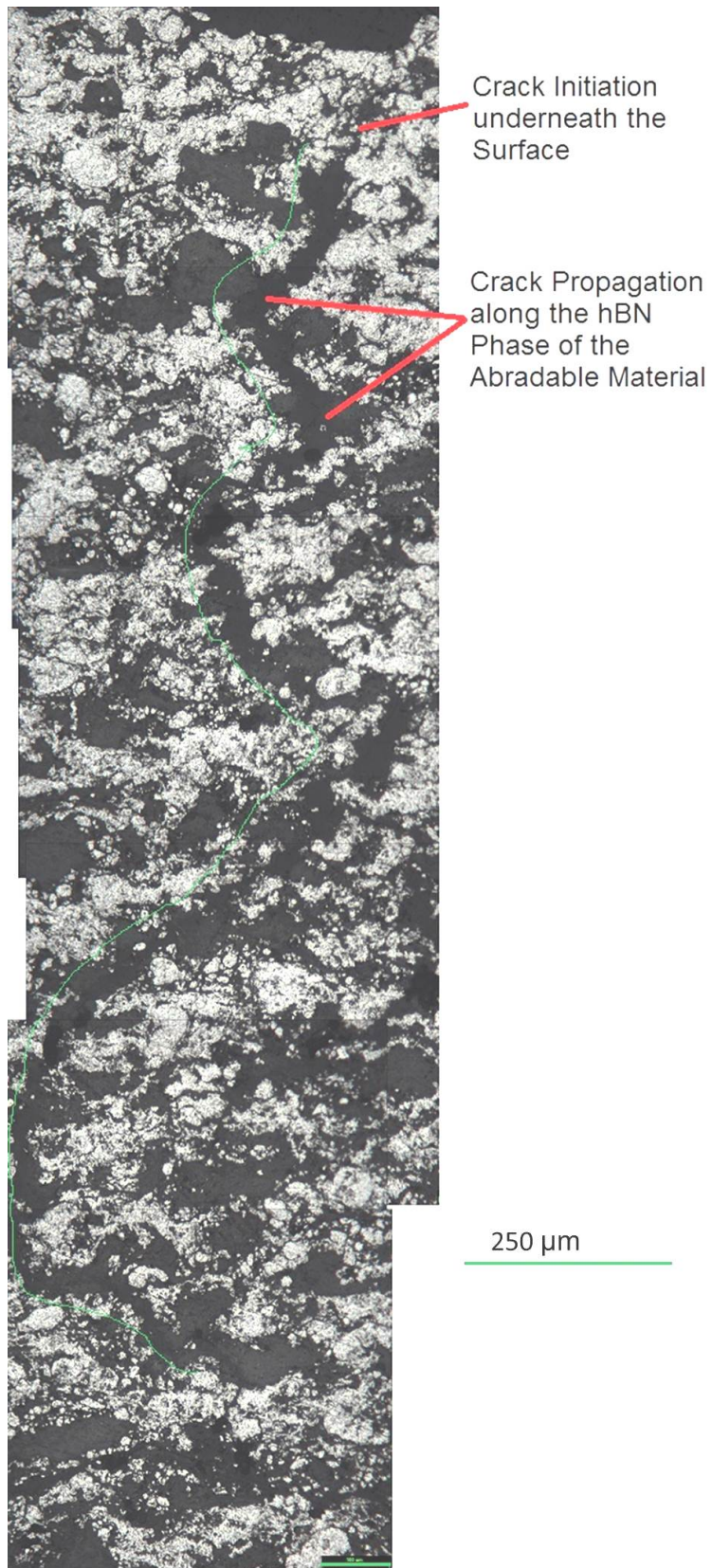


Figure 6.21: Profile of a Crack in the Abradable Coating

Figure 6.21 shows the propagation of a crack through the microstructure of the abradable top coat. This crack, however, did not initiate on the surface, but just below and grew towards the substrate. The surface of the sample was machined with a 240 grit paper, which allowed for crack initiation in subsurface layers.

#### 6.4.4 Abradable Hardness HR15Y

Material of soft (HR15Y of 40) and hard (HR15Y of 70) M320 was sprayed on to  $35 \times 100 \times 3$  mm substrates and heat cycled. The abradable was sprayed to a thickness of 3 mm and it was observed that the soft material cracks with a very fine pattern and with a mudflat-size much smaller than the hard coating. The cracking on the soft material is similar to that on the service return parts, which are brought back to Rolls-Royce following premature failure at overhaul. This suggests that the softer material does not perform as well in service as the harder sprayed coating.

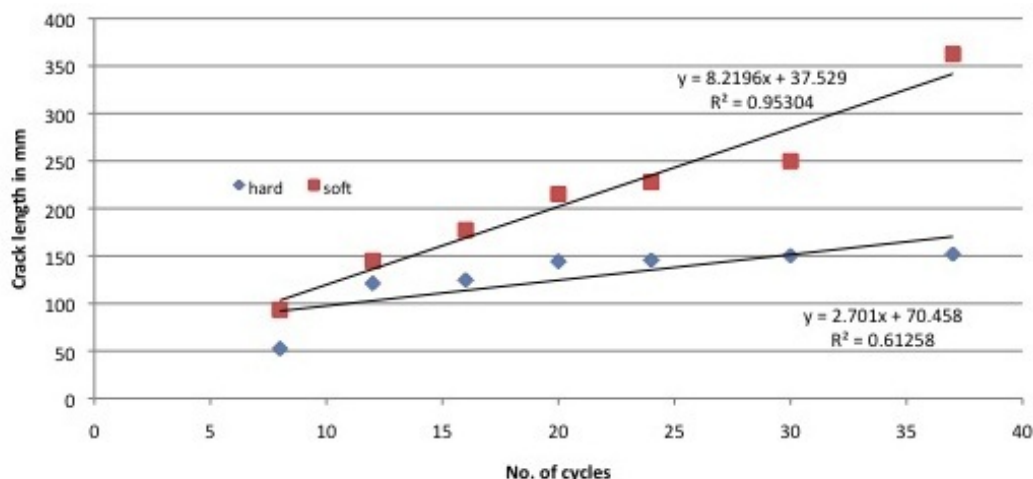
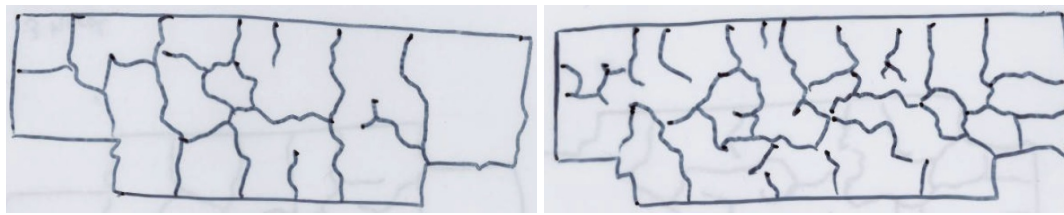


Figure 6.22: Total Crack Length as a Function of Coating Life, resulting from different Hardnesses of the Abradable

The differences in crack length previously observed can be seen in the pattern emerging on the material's surface as well. Figure 6.23 shows the cracks of a soft and a hard M320 abradable liner after 40 cycles of water-quenching.

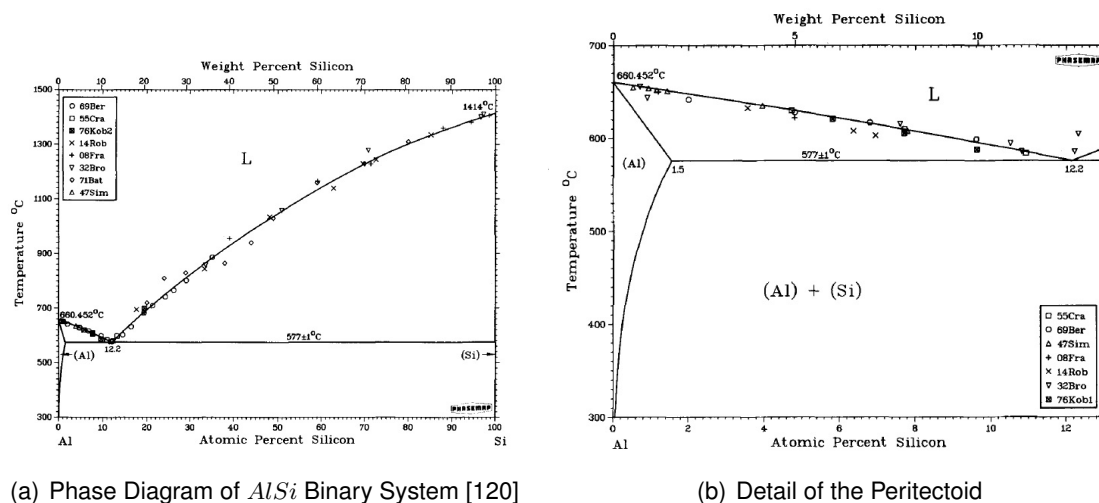


(a) Crack Pattern on a Hard Abradable - HR15Y (b) Crack Pattern on a Soft Abradable - HR15Y 70

Figure 6.23: Cracking after 40 Cycles of Water-Quenching

### 6.4.5 Precipitation within the Abradable

During shock cooling of the binary  $AlSi$  material system it is possible to supersaturate the  $Al$ -matrix with  $Si$ , due to the higher solubility of  $Si$  in liquid  $Al$  than in the solid phase. The quicker the mixture is cooled, the less  $Si$  can be diffused out of the  $Al$ -matrix before the material solidifies [119].



(a) Phase Diagram of  $AlSi$  Binary System [120]

(b) Detail of the Peritectoid

Figure 6.24: Phase Diagram of  $AlSi$  Binary System with Emphasis on the Peritectoid [120]

Figure 6.24 shows the phase diagram of the  $AlSi$  system used as the metal matrix material in M320. The powder, used to deposit the  $AlSi - hBN$  abradable seal contains a mixture of approximately  $Al_{12}wt\%Si$ , which is a percentage well above the solubility of  $Si$  in the  $Al$ -matrix.

Temperatures in excess of  $700^{\circ}C$  during plasma spraying allow for a formation of a homogeneous  $AlSi$  liquid. The cooling rate during deposition is steep, such that much of the  $Si$  remains in the  $Al$ -matrix, even in a solid state. This condition is metastable following

the rapid cooling, and precipitation of the *Si* phase out of the *Al*-matrix begins almost immediately. Heat cycling enables precipitation at an increased pace.

As-sprayed material shows a mix of microstructures, looking at the *AlSi* metal matrix. Some areas were completely molten during plasma spraying and were deposited as *Si*-exaggerated *Al12%Si*. Other areas show the very same dendritic structure of *AlSi*, which was a previous characteristic of the powder particles. Figure 6.25 shows an *AlSi* powder particle (a) and the cross section an *AlSi – hBN* abrasable (b). The preserved dendritic structure can be seen in the cross section.

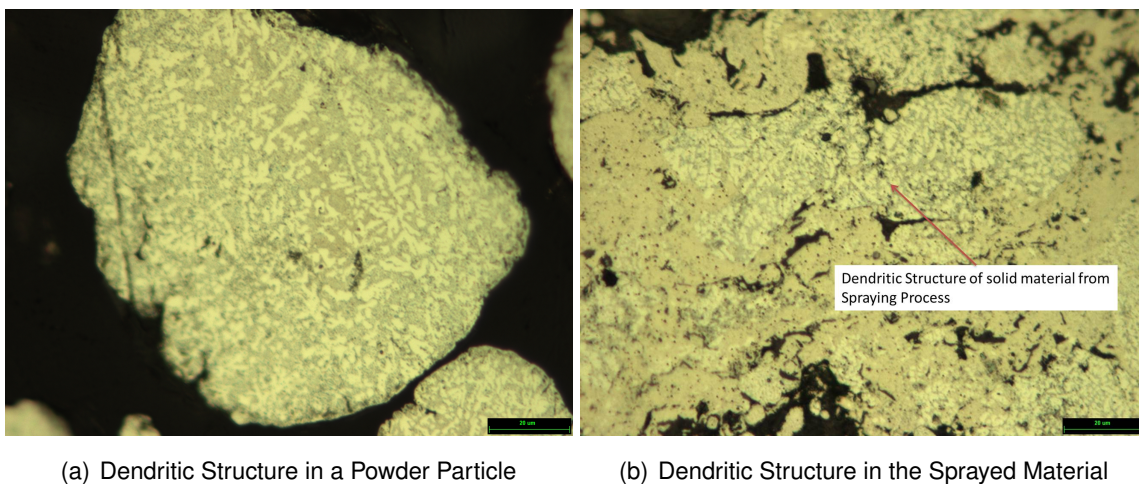


Figure 6.25: Material Microstructure Before (a) and After (b) Spraying

A metastable phase of equilibrium is envisaged for the *Al*-matrix, which can hold about 2% of *Si* at room-temperature. Precipitation starts with the formation of small nuclei, where local atomic conditions allow for *Si*-atoms to diffuse and form a new, more stable, phase. After the formation of the initial nuclei, the larger *Si*-agglomerates are able to grow further. This is based on the energy balance between the nucleus and its surrounding. Every further increase in size of the *Si*-precipitation has to incorporate a reduction in net-energy of the material system. For already large nucleation areas, further growth is always linked to a reduction in surface energy of the phase [121].

Precipitation can occur at room-temperature as well as elevated temperatures for these *AlSi* alloys. The diffusion processes during room-temperature precipitation leads to areas of increased stresses, which are linked to an increase in hardness and yield strength of the material. If the abrasable is taken to its operating temperature of  $450^{\circ}\text{C}$ , the material softens and precipitation can happen quicker and without further stress development. The resulting two-phase material is still harder than the original micro-structure [122].

### Experiments to assess the Precipitation Processes in the Abradable

M320 abradable liner samples were held in an oven at  $450^{\circ}\text{C}$  for different lengths of time. The heat treatment was chosen due to the maximum working temperature of the M320. Once heat treatment had started,  $\text{Si}$  precipitated out of the  $\text{Al}$  matrix. The number of  $\text{Si}$  precipitation areas increased over time in the furnace at the beginning and was replaced by precipitate agglomeration, once all the excess  $\text{Si}$  had come out of the  $\text{Al}$ -matrix. The  $\text{Si}$  rich regions which formed throughout the  $\text{AlSi}$  phase can be seen in Figure 6.26. The blueish spots in the material show where the  $\text{Si}$  is precipitating out of the  $\text{Al}$  matrix.

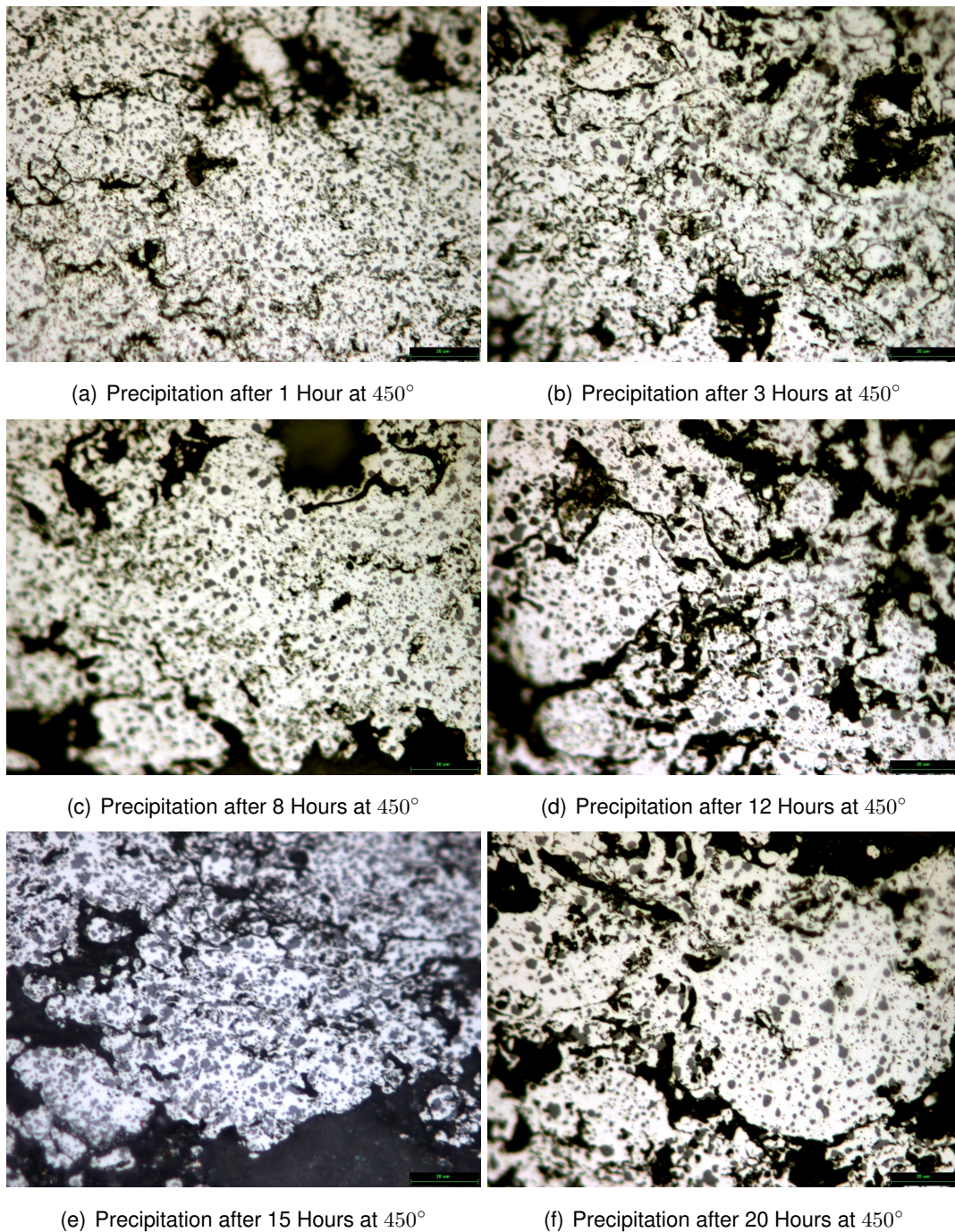


Figure 6.26: Precipitation Increase and Agglomeration over Time

After only one hour of ageing the microstructure changed completely; the dendrite/eutectoid structure had normalized and the first  $Si$  precipitates had started to form. As ageing continued, coarsening of these  $Si$ -precipitates was observed, which peaked after 20 hours. The agglomeration of the  $Si$  started, whilst precipitation was still happening, and carried on, after the  $AlSi$  matrix had stabilised.

Table 6.10 lists the area fraction of the  $Si$ -precipitates with in the metal matrix, as well as the precipitation size over time. The area fraction is defined as 'Area  $Si$  / Area  $AlSi$ ' and is a dimensionless number. The average precipitation size is measured in  $\mu m^2$ , since only 2-dimensional pictures of a cross section can be analysed.

Table 6.10: Precipitation and Agglomeration data

No. of Cycles	Average area fraction	No. of Cycles	Average Precipitation Size	Hours at Temp.	Average Area Fraction
3	0.298	1	1.041	5	0.394
6	0.299	3	1.857	10	0.438
8	0.349	8	2.571	25	0.455
9	0.353	12	3.143	50	0.473
13	0.401	15	3.175		
15	0.412	20	3.365		
18	0.430	30	4.063		
20	0.483				

It was noticed, that the development of the interface between the abrasible coating and the bond coat differed from the rest of the abrasible microstructure.  $Si$  precipitates grew bigger at the boundary layer, than throughout the rest of the material (see Figure 6.27). Evidence for this growth started after around five hours at  $450^{\circ}C$ .

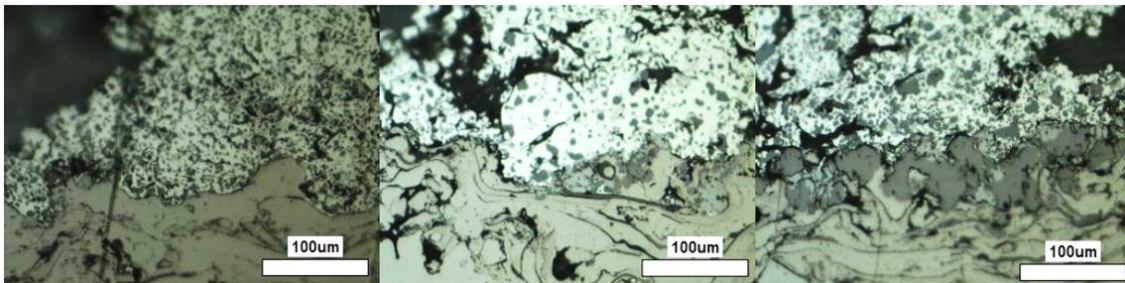


Figure 6.27: Precipitation Agglomeration at the Bond Coat Interface [123]

Investigating the hardness development of M320 over time, the changes in the microstructure have to be taken into account. Precipitation will increase the hardness, since two stable phases are harder than one unstable solid solution. Similarly the binder burn-out



will have an effect on the hardness of Metco 320. Figure 6.28 gives a visual representation of how the different types of behaviour might combine to produce the observed behaviour.

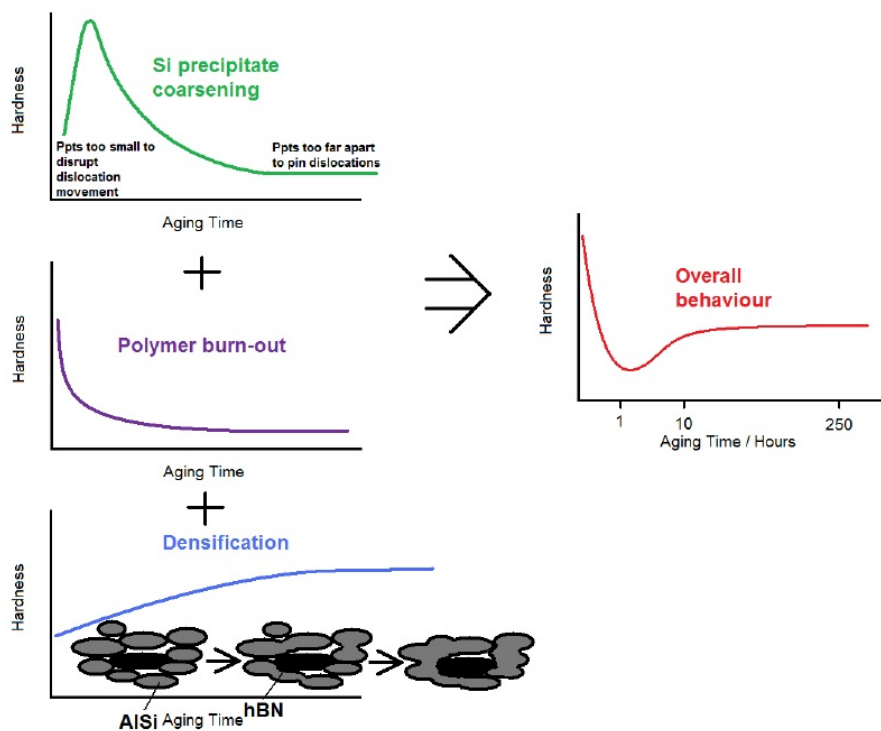


Figure 6.28: Degradation of the Material and its Properties [123]

The initial drop of the hardness curve can be associated with polymer binder burning out of the microstructure, leaving vacancies and porosity behind. Over time, the precipitation hardening results in an increase of the abradable hardness and a climb in the curve can be detected.

## Conclusion

Concluding from the cracking investigation, it can be said that the cracking observed on service return parts could be reproduced in the laboratory for the first time. Those service returns analysed over the duration of this project cracked in a very fine manner, with small mudflats on the surface. Figure 6.29 shows the service cracking documented and the reproduction in the Laboratory using water-quenching.



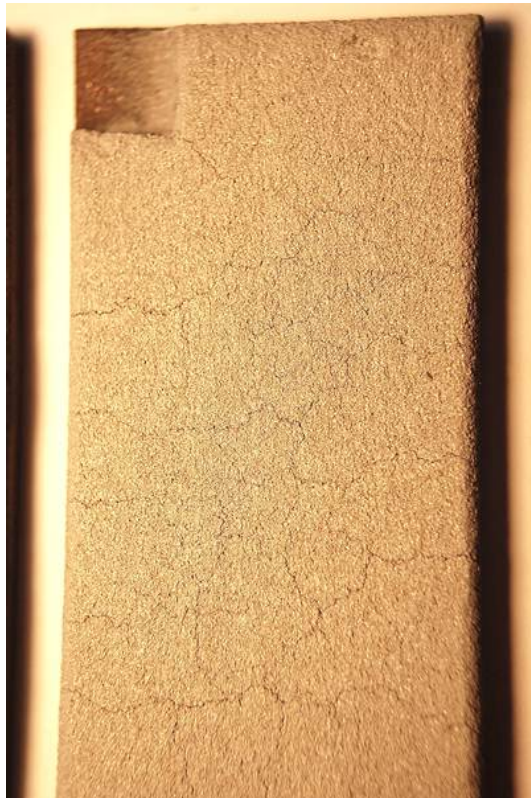
(a) Service Failure - Mudflat Cracking and Spallation



(b) Service Failure - Mudflat Cracking and Delamination



(c) Mudflat Cracking on a Test sample in the Laboratory



(d) Fine Mudflat Cracking on an Abradable Sample

Figure 6.29: Service Cracking and Reproduction in Laboratory

## Chapter 7

# Material Degradation

During water-quenching of M320 abrasible samples, the formation of a lighter layer on the surface was observed. This layer grew over time and could be seen in all the samples. In order to characterise the changes happening, samples were cut and mounted, to investigate them using the SFEG. Figures 7.1 a and b, show the microstructure of the material after cycling and the  $X_1$ -layer forming on the surface.

The progression of the growth of the  $X_1$  layer was investigated by cutting and polishing samples of different ages. From the cross section of the material, the thickness of  $X_1$  could be measured and it was possible to establish, that the layer grows mostly at the beginning. With increasing age, the penetration in depth slows down, as can be seen in Figure 7.2.

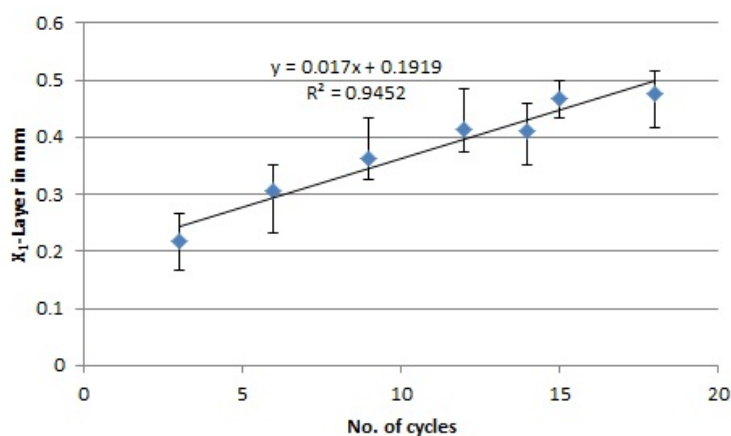
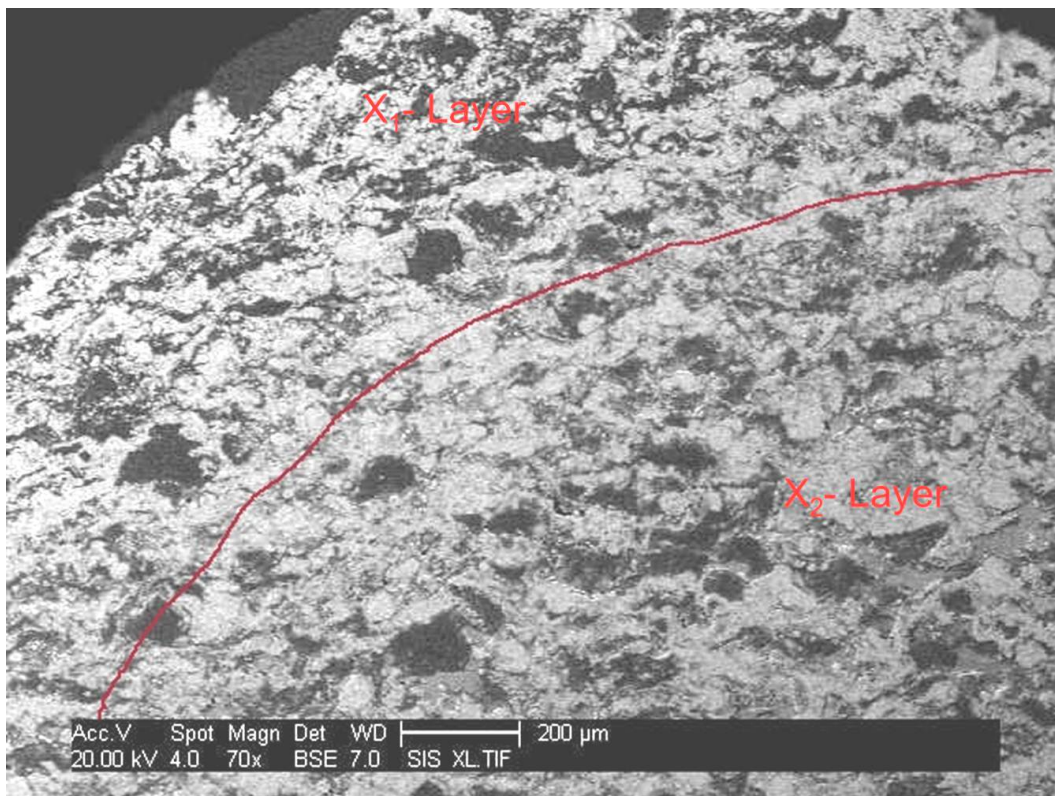
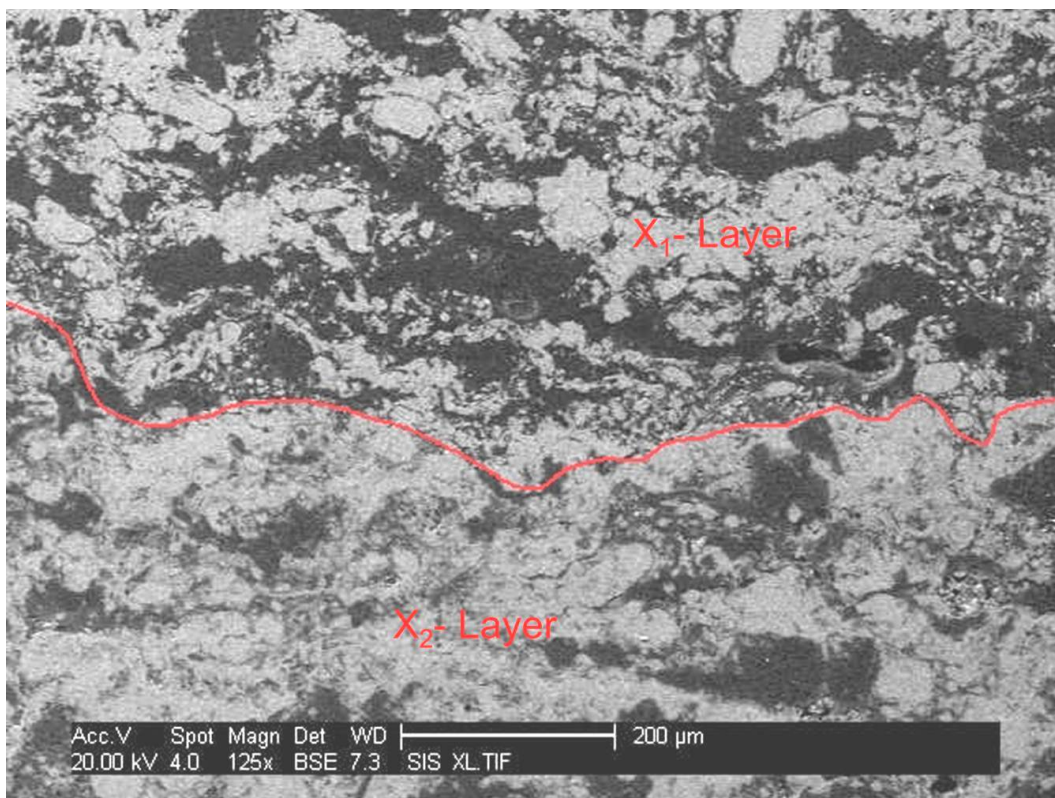


Figure 7.2: Thickness of the  $X_1$ -Layer as a Function of the Number of Cycles

In order to see, what caused the difference in material appearance, EDX maps were produced (see Figure 7.3), focusing on the two individual layer  $X_1$  and  $X_2$ . Even though



(a) Sintering of the Top Coat along Edge of the Sample



(b) Sintering of the Abradable Microstructure

Figure 7.1: Layering Effect observed using the SFEG

the difference in microstructure can be seen when looking at the sample cross section by eye, the element mapping did not reveal any variations between layer  $X_1$  and  $X_2$ .

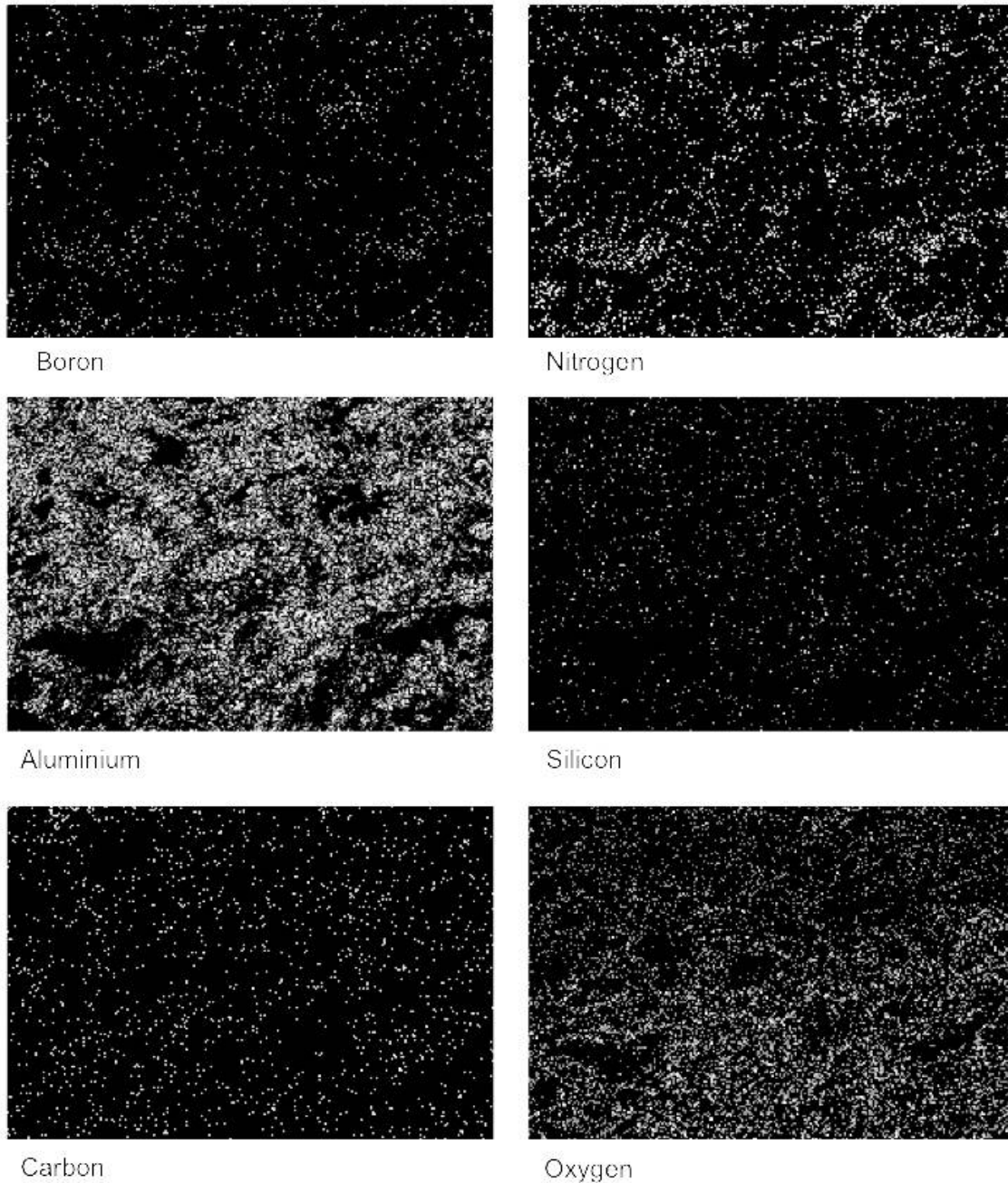


Figure 7.3: EDX Maps of the  $X_1$  and  $X_2$  Interface

Figure 7.4 shows the analysis of the interface, using EDX. The white spots on the pictures indicate the detection of the material named below. It can be seen, that aluminium is dominant in the microstructure. All the other materials were not detected to the degree they are present according to the material composition. Also, no difference in composition of the  $X_1$  and  $X_2$  microstructure could be detected.

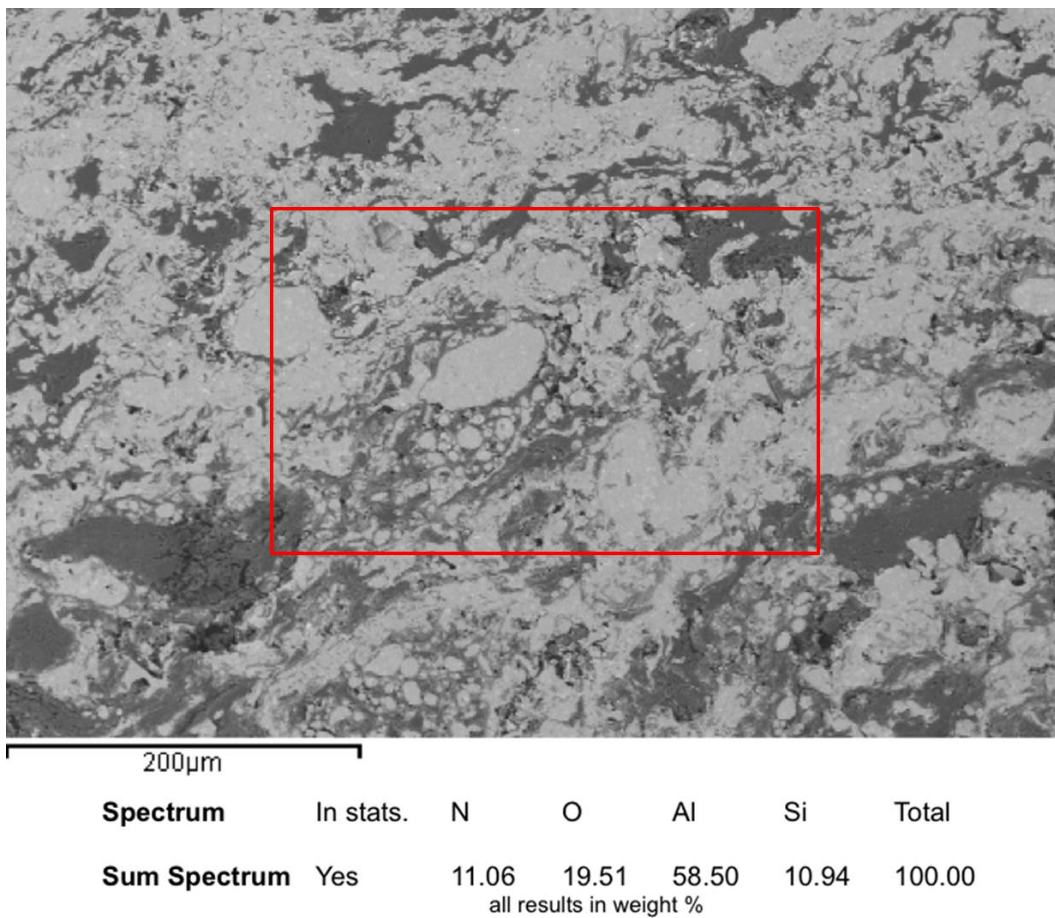


Figure 7.4: EDX Results of the  $X_1$  and  $X_2$  Interface-Mapping, including Element Measurements

Further investigations into the degradation of the abradable and the formation of the  $X_1$ -layer focused upon the analysis of the chipped off material using the XRD. Scans over the entire available  $2\theta$  range were conducted and analysed towards differences in material readings.

Samples of 8, 12 and 25 cycles of age were analysed using the XRD and changes in counts per second for each material peak were measured (see Table 7.1).

Table 7.1: Peak Intensities of  $X_1$  and  $X_2$  Layer

Sample	Main $AlSi$ peak	Main $hBN$ peak
8cyc $X_1$	3100	800
8cyc $X_2$	1900	1750
12cyc $X_1$	3600	1000
12cyc $X_2$	1750	1450
25cyc $X_1$	3350	1750
25cyc $X_2$	2250	2300

Figure 7.5 on page 116 shows the result of the XRD analysis of both sides of the abradable top coat, using delaminated material. The scan lines for the different samples are offset (by 1200 Cps) to emphasise the intensity of the overlapping peaks. From those scans, the amount of  $hBN$  and  $AlSi$  in the material can be assessed from the intensity of individual peaks. For all the samples analysed, the  $AlSi$  peak was more intense for the  $X_1$  layer, indicating more  $AlSi$  in the surface layer when compared to  $X_2$ .  $hBN$  readings are higher for the bottom layer  $X_2$  when compared to  $X_1$ , showing more dislocator phase in the  $X_2$  layer.

There are no additional peaks when comparing the  $X_1$  to the  $X_2$  scan, which eliminates the potential of the formation of an additional phase in the structure. Also, oxidation would have been picked up, should the top surface oxidise during heat cycling. All the peaks in the scan are accounted for by either  $hBN$  or  $AlSi$ .

## Conclusion

Concluding from the degradation analysis, it can be said that water-quenching introduces the same material microstructure, as it was documented on service return parts. The  $hBN$  deprived state of the  $X_1$  layer can be compared to the microstructure of the analysed service samples. Figure 7.6 shows the degradation of service material compared to test samples. The service material can be compared to the  $X_1$  layer forming on the surface of the laboratory samples.

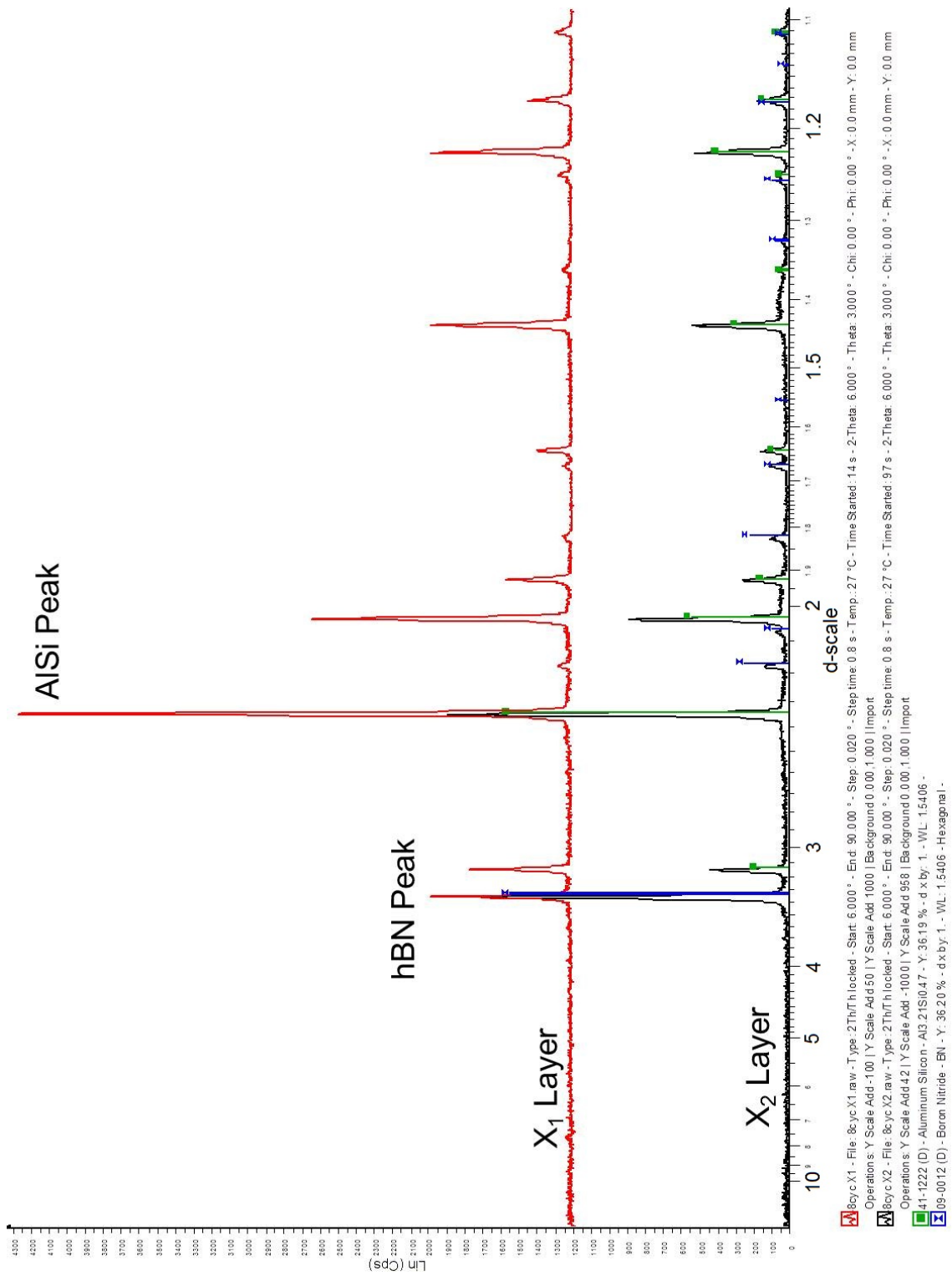
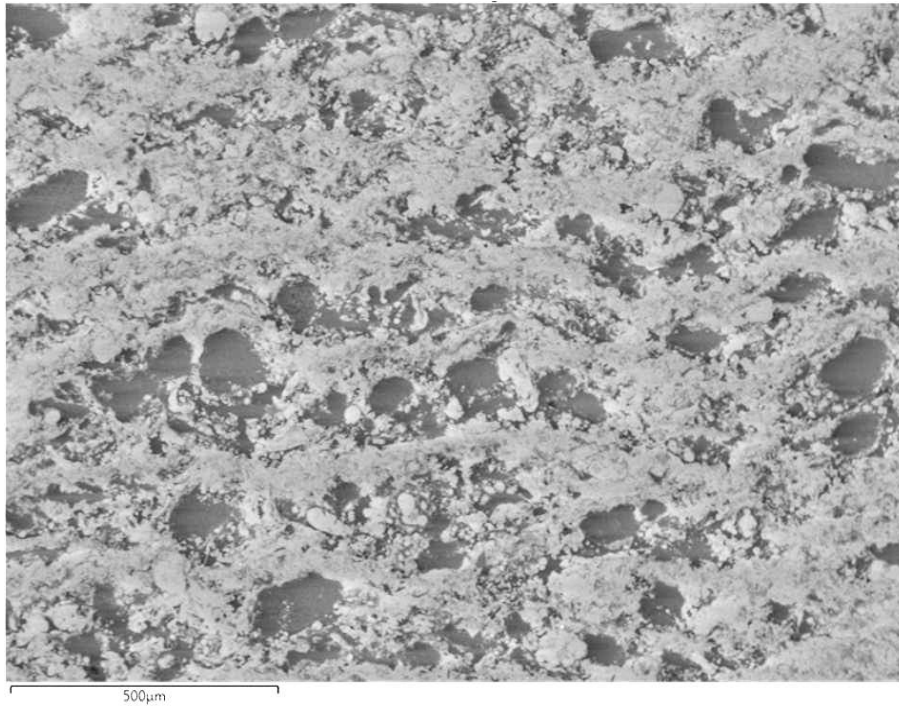
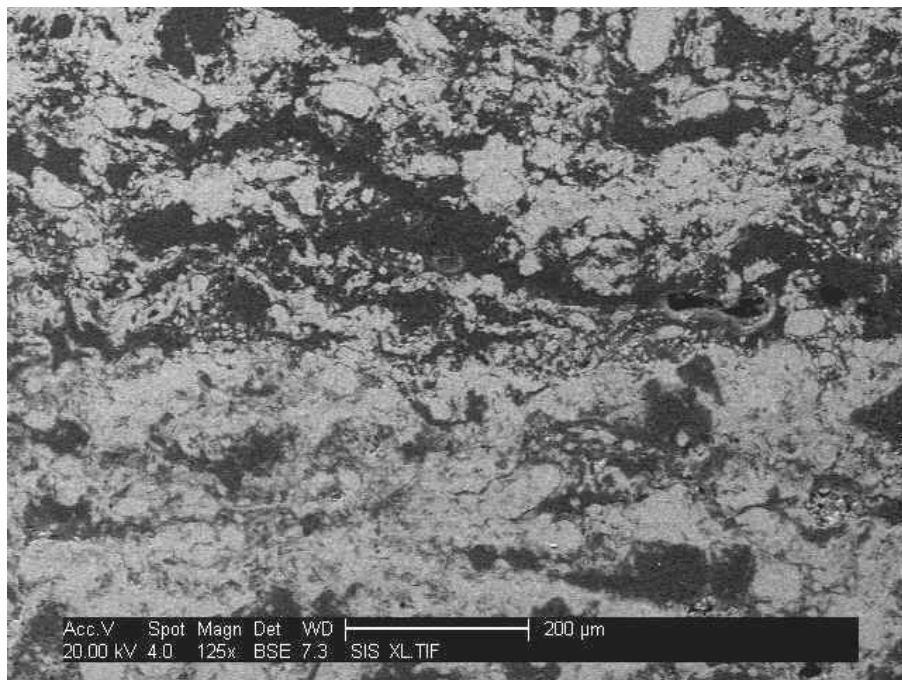


Figure 7.5: XRD Scan of an Abradable Chip, cycled for 8 Cycles, from Top and Bottom





(a) Service Sample - Cross Section



(b) Laboratory Sample - Cross Section

Figure 7.6: Service and Laboratory Degradation

## Chapter 8

# Testing of Abradable Coatings

### 8.1 Introduction

The friable nature of abradables makes them subject to abrasion, erosion and corrosion attack throughout the component's life. Particles like sand, dust and debris enter the gas stream and due to the velocities these particles attain, impact the abradable and erode material away from the leading edge of the casing.

In salty and moist areas, corrosion can attack the *AlSi* material at the surface and work its way down through the abradable coating towards the casing. This results in spallation of the top coat due to reduced bond strength.

The most likely cause of material failure is due to abrasion from the blades. Abradables are designed to fail once contact with the blade is made, enabling them to cut a path into the top coat, without damaging the blade tips. The debris produced is supposed to burn up in the following stages of the engine without causing problems downstream.

Ideally, a smooth pathway is cut into the abradable and no damage to the blades occurs after interaction. Unfortunately, blade pick up, gramophone grooving, top coat hardening and degradation are observed during service.

The working environments described and failure mechanisms need to be tested and understood in order to improve Metco 320 as a material system. Therefore, erosion testing, scratching testing, ball indentation testing, residual stress testing and Young's modulus analysis was carried out on as sprayed, cycled and aged material.

## 8.2 Erosion Testing

The relationship between erosion mass loss and erosion time is linear, with a maximum erosion rate at an impact angle of  $60^\circ$ . According to [49] the erosion rate is not related to the impact angle, the kind or size of the particles, both of which have been proven wrong in these current studies. Experiments carried out in Cranfield throughout this research showed a dependency of the erosion rate upon impact angle and particle kind.

Research by Sutter et. al. [7], which was confirmed during this project, showed that the erosion rate is also related to the characteristics of the abradable coating, its composition, microstructure and hardness, but not to the thickness. Erosion testing was carried out on test samples previously manufactured at Rolls-Royce and a linear relationship between the erodent mass fired at the sample and the mass loss of the abradable was established for as-sprayed material. Furthermore, it has been shown for aged material, that the initial erosion rate is very high and drops over the duration of the test (see Section 10.3.1 on page 165).

### Methodology

In order to test abradable material and its erosion resistance, samples of at least  $30 \times 40$  mm, with 3 mm abradable were fitted onto the individual  $30^\circ$  or  $90^\circ$  sample holders ensuring that the impact falls entirely within the sample. The substrates of the samples were magnetic, which enabled the use of magnets to fit the specimen to the erosion stage.

$Al_2O_3$  was used as an erodent, since health and safety warnings were issued about using silica sand, which had been used in previous tests (see Chapter 5). The grain size of this erodent varied between  $95 \rightarrow 120 \mu m$  and was accelerated to  $85 \rightarrow 110 m/s$  with a particle feed of  $4 g/min$ .

Experiments were carried out on thermally cycled samples, ranging from 3 cycles, and the onset of cracking, to 33 cycles and part of the sample had actually delaminated from the substrate and come off.

### Results and Analysis

Samples of different ages were tested and the influence of heat-cycling upon the erosion behaviour of M320 was evaluated. In 1 → 3 min intervals the samples were eroded and subsequently weighed to track the mass loss of the top coat. Following that, the erosion rate can be calculated for each stage of the test performed.

$$Erosion - rate = \frac{Mass-loss(g)}{Mass-erodent(kg)}$$

Looking at the data collected during testing, it became clear that there were differences between 30° and 90° erosion impact, as well as the material’s age. The older the material, the higher the initial erosion-rate in each of the tests. The data obtained during erosion testing are listed in Tables 8.1 and 8.2.

Material under a 30° impact angle shows a decline of the erosion rate at about twice the rate of the 90° erosion. As previous work confirmed, the failure modes of the two impact angles are different and prohibit a direct comparison of the results. What can be said though, is that the smearing and sliding of the erosion particles across the surface in 30° testing stops the erosion attack better than brittle fracture which was observed for 90° testing.

Table 8.1: Erosion Rates [g/kg] of Aged Samples Eroded at 30°

		Number of Cycles									
		3	7	11	14	15	17	18	21	25	33
Erosion Time in min	1	8.8925	10.2025	10.565	10.28	8.405	11.2775	10.655	11.0975	13.7425	11.4575
	2	8.20125	7.14125	7.55	7.74125	7.00125	10.7525	8.62	7.03	9.125	9.9475
	3	8.20125	7.14125	7.55	7.74125	7.00125	6.9525	7.6225	5.8225	7.225	10.05
	4	6.7155	5.094	4.96125	5.42	5.08125	4.57375	5.6675	5.03625	6.165	5.8375
	5	6.7155	5.094	4.96125	5.42	5.08125	4.57375	5.6675	5.03625	6.165	5.8375
	6	6.7155	5.094	4.22125	4.46375	4.6675	4.86375	5.4275	4.36375	5.65375	5.32625
	7	6.7155	5.094	4.22125	4.46375	4.6675	4.86375	5.4275	4.36375	5.65375	5.32625
	8	6.7155	5.094	4.1375	4.32	4.1125					
	9	5.9225	4.27625								
	10	5.9225	4.27625								

Erosion testing is an important tool to assess the performance of abradable seal coatings during service. Extensive testing of as-sprayed, as well as heat cycled material revealed that the ageing process affects the erosion resistance of the top coat. Room temperature testing of 3 mm M320 topcoat samples, as-sprayed and heat cycled, resulted in two different failure modes for the chosen angles of attack. Testing showed, that heat cycling introduced material degradation over time, which was resulted in a growing, lighter surface layer (X<sub>1</sub>). Once this layer is eroded away, a darker bottom layer (X<sub>2</sub>) can be seen

Table 8.2: Erosion Rates [ $g/kg$ ] of Aged Samples Eroded at  $90^\circ$ 

		Number of Cycles									
		3	7	11	14	15	17	18	21	25	33
Erosion Time in min	1	7.6775	8.5425	8.7375	8.9825	8.305	8.3	9.6975	8.8675	9.2975	9.32
	2	7.74	5.98625	6.425	6.7275	7.03125	6.35	7.1375	6.65	7.955	9.055
	3	7.74	5.98625	6.425	6.7275	7.03125	6.35	7.1375	6.65	7.1875	8.4875
	4	6.2555	5.436	6.40875	6.37375	7.09	6.7725	8.3325	7.165	7.1875	8.4875
	5	6.2555	5.436	6.40875	6.37375	7.09	6.7725	8.3325	7.165	7.1875	8.4875
	6	6.2555	5.436	5.55375	5.73625	7.4825	6.285	8.2875	6.7425	6.30125	7.075
	7	6.2555	5.436	5.55375	5.73625	7.4825	6.285	8.2875	6.7425	6.30125	7.075
	8	6.2555	5.436	5.5475	5.7225	7.7525					
	9	5.7125	5.765								
	10	5.7125	5.765								

in the center of the erosion scar (see Figure 8.1).

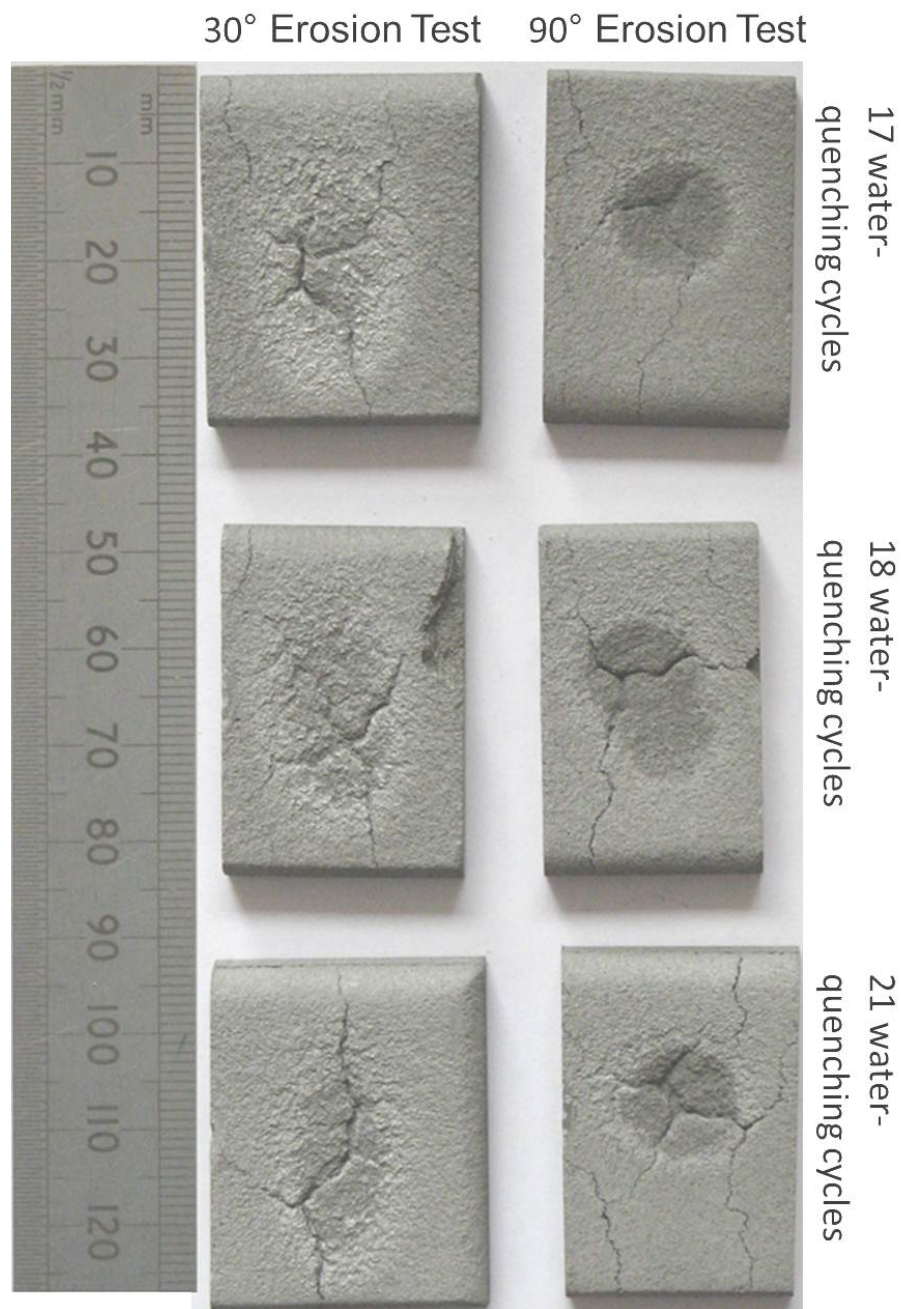


Figure 8.1: Layers  $X_1$  and  $X_2$  visible in the Erosion Scar of water-quenched Samples

### 8.3 Scratch Testing

Ma, X. [83] investigated the behaviour of Metco 313 coatings during scratch testing. The tests were carried out with an increasing load of  $100 \text{ N/min}$  and scratches of different length were applied to the surface of the sample. The results showed that densification occurred ahead of the indenter due to compression of the soft material contained in

the material's microstructure. 'Progressive abrasability hardness (PAH)', 'specific energy' [124] or 'specific grooving energy' [125] are all terms used to describe the work done per unit volume of material abraded. Work done describes the point product of the force used and the measured z-displacement.

When the scratch length and indentation depth increases, more work has to be done; energy is needed to remove the increasing material which needs to be abraded. Higher yield stress and elastic modulus impart the greatest constraining effect by the material surrounding it, and this adds to the degree of densification beneath the indenter [83].

In order to test abradable seals during service, a method of assessing the material's properties has to be developed. For the test to be useful on the shopfloor the machines or appliances needed to carry out the test have to be easy to use. Furthermore, it would be advantageous for the test apparatus, or the tip of the machine, to fit onto a boroscope, as this would ensure the usability of the test method even if the engine is not taken apart.

It has been shown that cyclic heat treatment caused the top coat to degenerate and crack. The aim of scratch testing abradable M320 samples is to prove the decay of the material's properties and performance over time and cycles. Along with the material deterioration the validity of scratch testing as a servicing tool was assessed.

## Methodology

Figure 8.2 shows the process of one single scratch over a sample's surface. Due to the indentation caused by loading the indenter onto the specimen, plastic deformation occurs underneath the tungsten-carbide tip. The motion of the indenter scratches the tip over the surface of the sample, causing damage to the abradable. This damage is dominated by plastic deformation ahead of the indenter, resulting in material compression underneath and material loss to the sides of the motion. Abradable samples were tested with a fixed 20 *N* load, which is loaded at the beginning of the test and kept constant for the 10 *mm* scratch scar. Vertical displacement, friction coefficient and acoustic emission were recorded every 0.05 *s* of the test.

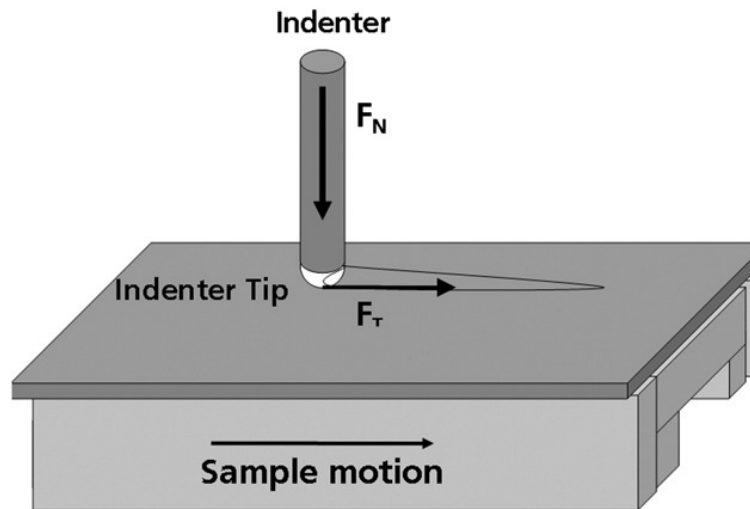


Figure 8.2: Schematic Working of a Scratch-test

## Results and Analysis

The damage caused during scratch testing can be seen in Figure 8.3. The layer of compressed material on the surface is the result of plastic deformation and compression during scratching.

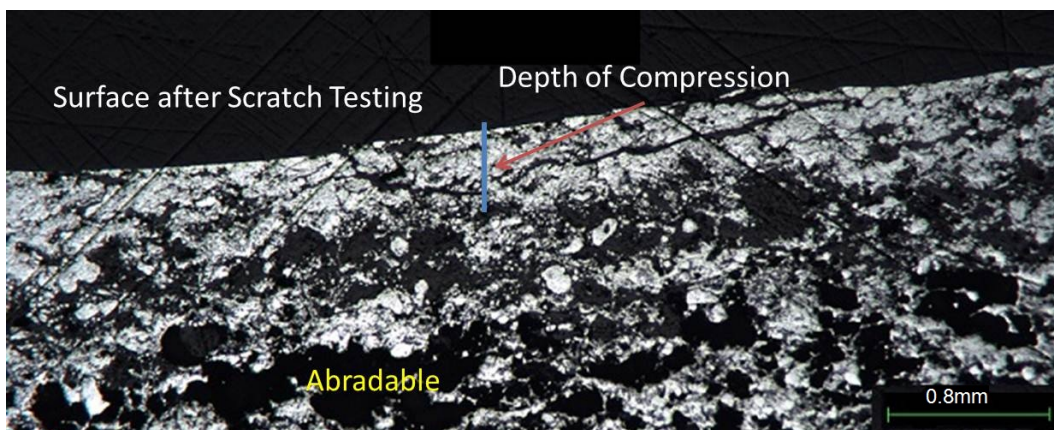


Figure 8.3: Subsurface Damage caused during Scratch Testing



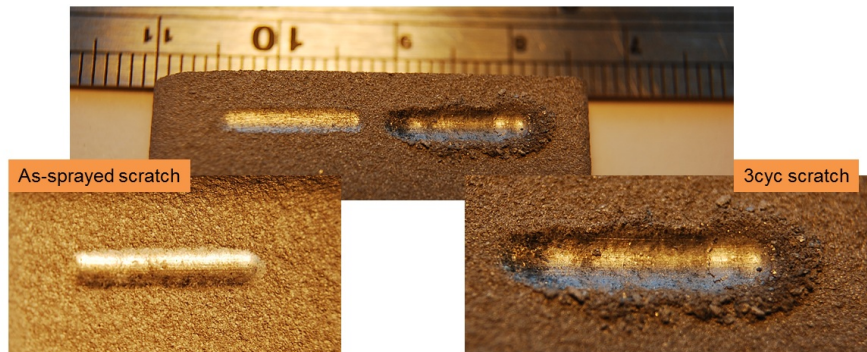


Figure 8.4: Damage caused by the Indenter during Scratch Testing

As an initial characterisation and ranking tool the scratch tester was used to introduce controlled damage into the material. The vertical displacement data recorded were plotted over the number of passes (see Figure 8.5 on page 126). Some of the passes within one test, recorded increased measurements for the vertical displacement, peaking out from the rest. The number of peaks decreased over the lifetime of the abradable material, with the peaks reducing with increasing age of the sample. The last measurements taken for heat cycled material showed no more peak displacements and within 2 – 3 water-quenching cycles after this reading, the material failed due to delamination.

Figure 8.5 shows how the material's performance can be tracked during scratch testing. Every 3 cycles of water-quenching, the samples were scratched 30 times over their surface, which can be seen in the individual figures.

It was found that with increasing age the number of peak scratches decreased, until they disappeared and soon after that the top coat delaminated. Peak displacements are those lines indicating a higher z-displacement throughout the entire scratch, when compared to the rest of the scratches.

It could be established that the as-sprayed condition showed most peaks and just before the material failed, the peaks had disappeared. It was observed that the peaks decreased over the material's life time and therefore indicated the stage of the material's life. Some samples showed variability in their peak count, but ultimately failure occurred and the peaks had disappeared.

In an abradable material, it is possible to hit very hard areas (metal-matrix structure), as well as very soft areas (pores and hBN-phase). These different components of the coating give different readings for the measured z-displacement, during a given scratch test.

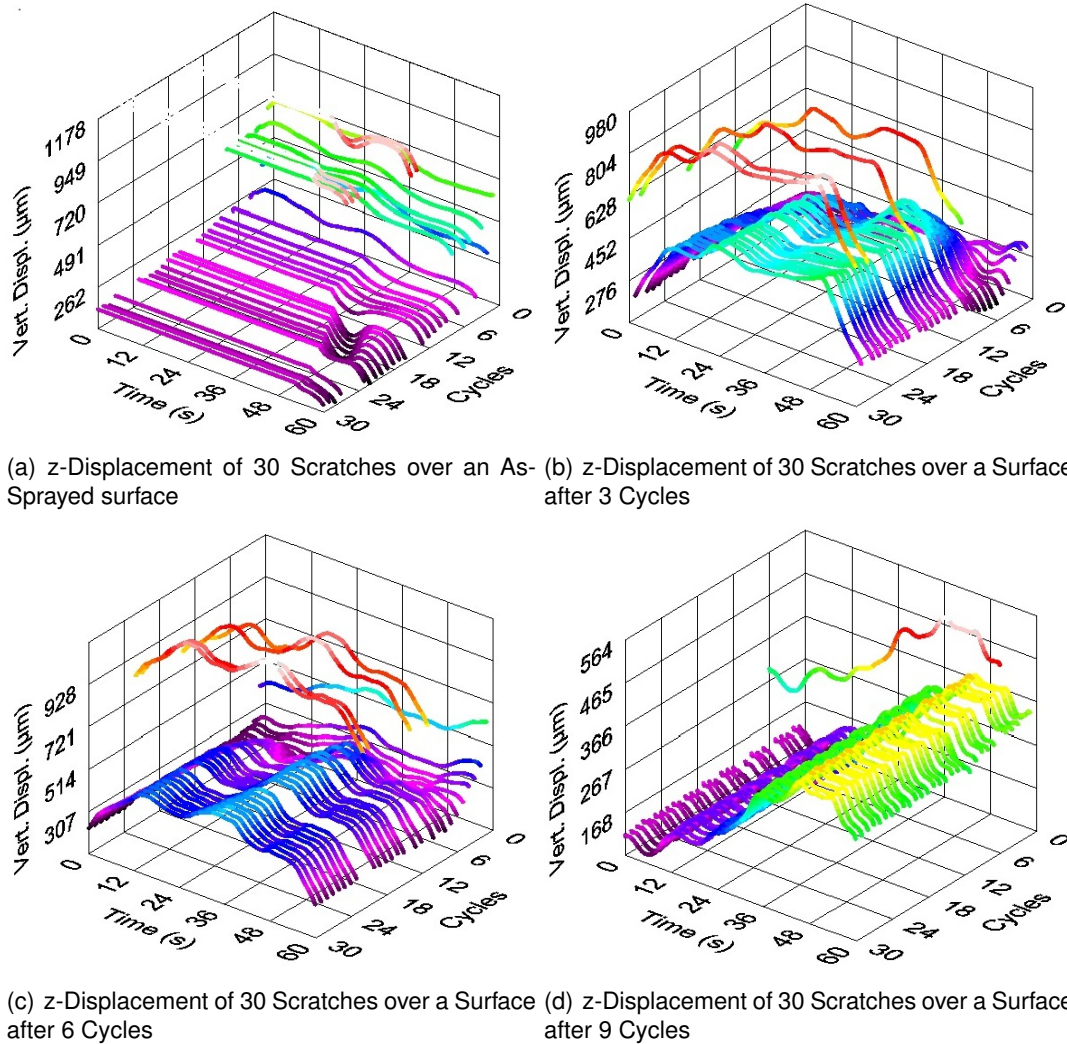


Figure 8.5: Changes of z-Displacement due to Heat Cycling

Within the 30 passes of the test, increased readings for all the points can be observed, indicating a bigger volume of material removal. Almost as though the smaller z-displacement readings were passes, which introduced damage into the liner and then the fractured and broken material was removed in subsequent passes.

## 8.4 Indentation Testing

Indentation testing was investigated concerning its suitability as a material assessment tool for manufacturing and overhaul sites. Indentation with small loads (up to 20  $N$ ) causes a small scar on the surface, which has a diameter of about 200  $\mu m$ . Two sample sets (I & II), from different spray-runs, were heat cycled and indented, in order to evaluate

the traceability of the material's degradation.

## Methodology

During indentation testing the elastic recovery and plastic deformation of the top coat under a given load can be assessed. Upon loading the displacement of the indenter is recorded and plotted over the load. Figure 8.6 shows the loading (lower slope) and unloading (upper slope) of a M320 sample to a load of 20 *N*.

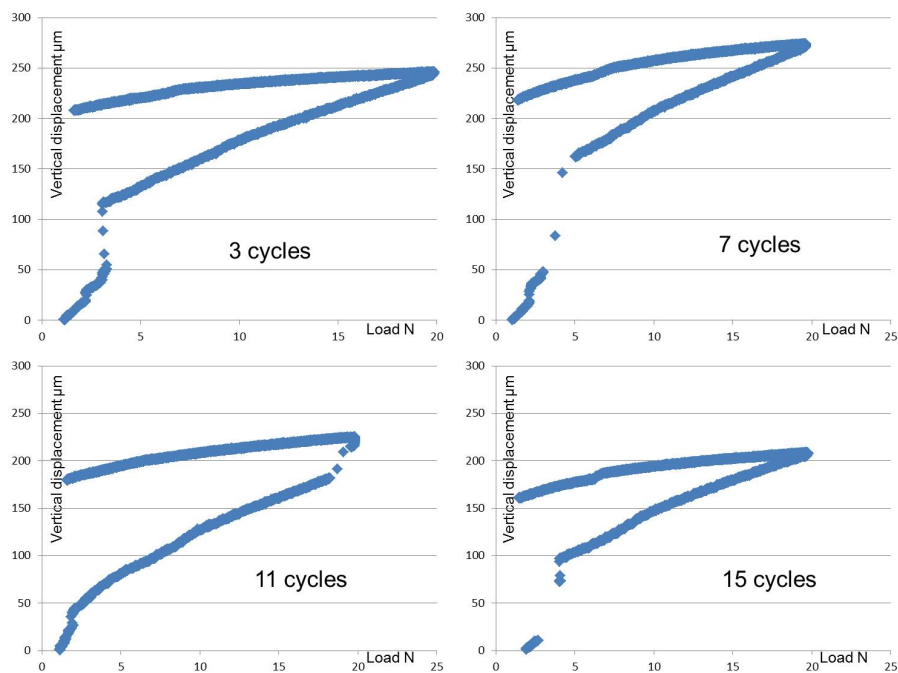


Figure 8.6: Typical Indentation Graph of Increasing Load and measured Displacement

## Results and Analysis

Table 8.3 lists the measured plastic deformation results of two sets of indentation testing. The elastic recovery of the material is around 90  $\mu\text{m}$  throughout its lifetime, whereas the plastic deformation changes and appears to form two loops, indicating a cyclic nature of the material response to the testing.

Usually the first cracking of the top coat can be observed around 3 cycles, which indicates a built up stresses in the material until that point, with a decrease in stress level after the material has cracked. Further cycling causes an increase in stress state, followed by further crack opening and the relieving of stresses. With stress relieve advancing,

the material's plastic deformation correspondingly increases, compared to earlier higher stress levels.

The built up of stresses is caused by the material deformation, which makes an indent on the surface harder, when compared to an unstressed surface. Therefore, indentation of a stressed surface leads to plastic deformation later, than indentation of a stress relieved material. This way, the second peak in plastic deformation can be explained with a built up of stresses in the top coat after the initial cracking. Ongoing cycling causes the top coat to continue to creep at high temperatures and stresses increase when quenched. These stresses need to be relieved by further cracking of the material, meaning that plastic deformation increases again, associated with the raising stress level in the material.

Table 8.3: Results of Indentation Testing with a 50N Load

Set I		Set II	
Cycle	Plastic Deformation in $\mu m$	Cycle	Plastic Deformation in $\mu m$
3	370	0	155
7	220	3	252
11	200	6	200
14	110	8	160
15	190	9	115
17	320	13	150
18	250	16	190
21	100	18	205
25	100	20	125
33	280		

## 8.5 Hot Hardness Testing

Hot hardness testing was carried out in order to investigate the response of the abradable to elevated temperatures. The material softens during service, but it is currently not known to which degree the softening happens and how it affects the material performance.

A testing series for abradable material was drafted out and indents at room temperature, 250, 300, 350, 400, 420 and 450°C were designed to be carried out. Figure 8.7a shows an indent at room temperature. The width of the indent is 260 $\mu m$  and the surface cracking due to the indentation can be seen on the left to the indent.

Testing at 250°C left indents on the surface of 640  $\mu m$ , 660  $\mu m$  and 700  $\mu m$  width. These can be seen in figure 8.7b. The indent size of almost 3 times the size of room tempera-

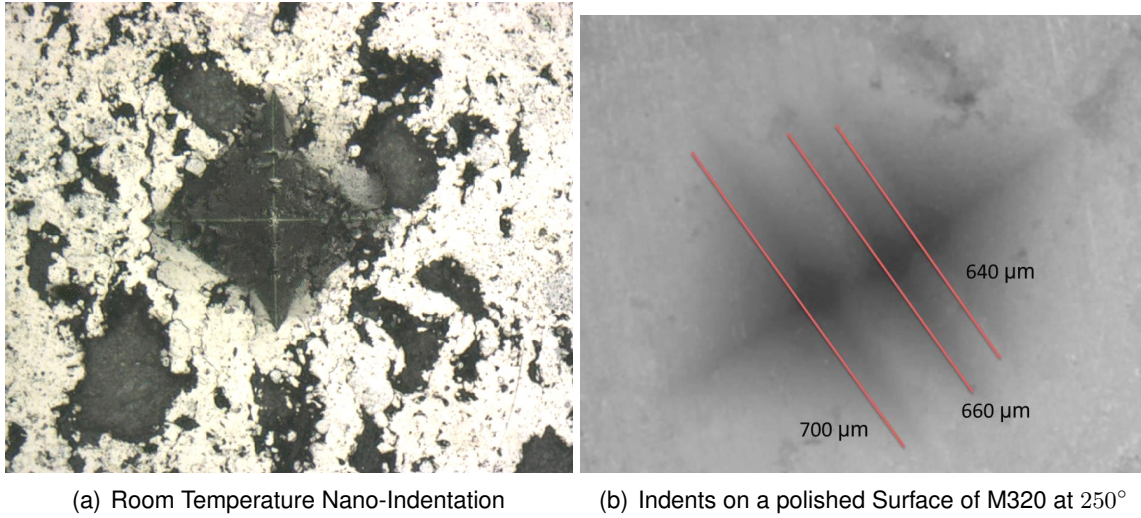


Figure 8.7: Changes of z-Displacement due to Heat Cycling

ture testing results from the material softening during heat exposure.

A full testing plan for hot hardness testing for temperature from room temperature up to 450°C was drafted out for as sprayed and heat cycled material. Unfortunately the machine broke after the 250°C tests were finished and no further measurements could be conducted.

## Chapter 9

# Residual Stresses

### 9.1 Introduction

X-Ray Diffraction Analysis (XRD) is often used to analyse materials for their phase composition. X-Rays impact the flat surface of the material and penetrate it to a depth of up to  $50 \mu\text{m}$ . The diffracted X-rays from the lattice structure are picked up by a detector and depending upon the wavelength of the registered beams, phases can be assigned to the material.

Next to determination of composition, XRD can be used to measure stresses in the material. A detailed explanation of stress measurements with XRD is given in section 3.5.4. In order to get most accurate stress measurements from the analysis, an intense  $AlSi$  peak at a high angle has to be found. This is due to the reflected  $K\alpha_1$  and  $K\alpha_2$  overlap at lower angles which are hard to separate. At high angles of XRD analysis the peaks can be distinguished and the counts per second readings are more accurate. This is due to the fact that at high angles the  $K\alpha_1$  and  $K\alpha_2$  peaks separate, whereas at lower angles they overlap and give inaccurate counts per second readings.

### 9.2 X-Ray Diffraction Analysis

#### Peak Shifting Measurement

The heat cycled, as well as a powder and an as-sprayed sample were analysed using X-Ray Diffraction. Looking at the main peaks of the pattern, it shows the difference in lattice spacing between the powder, the as sprayed and heat cycled material. In figure 9.1 the main  $hBN$  peak (left), as well as the main  $Si$  peak (right) can be seen. The  $Si$  peak only appears after heat treatment and is an indication of the precipitation of the  $Si$

out of the *Al* matrix. The *hBN* peak is very low in the powder, which can be explained by the *hBN* being encapsulated by the *AlSi* matrix material. Once the material is sprayed, the *hBN* content can be pick up by XRD. When heat treated the *hBN* content decreases (see Chapter 7) and therefore the intensity of its peaks decreases.

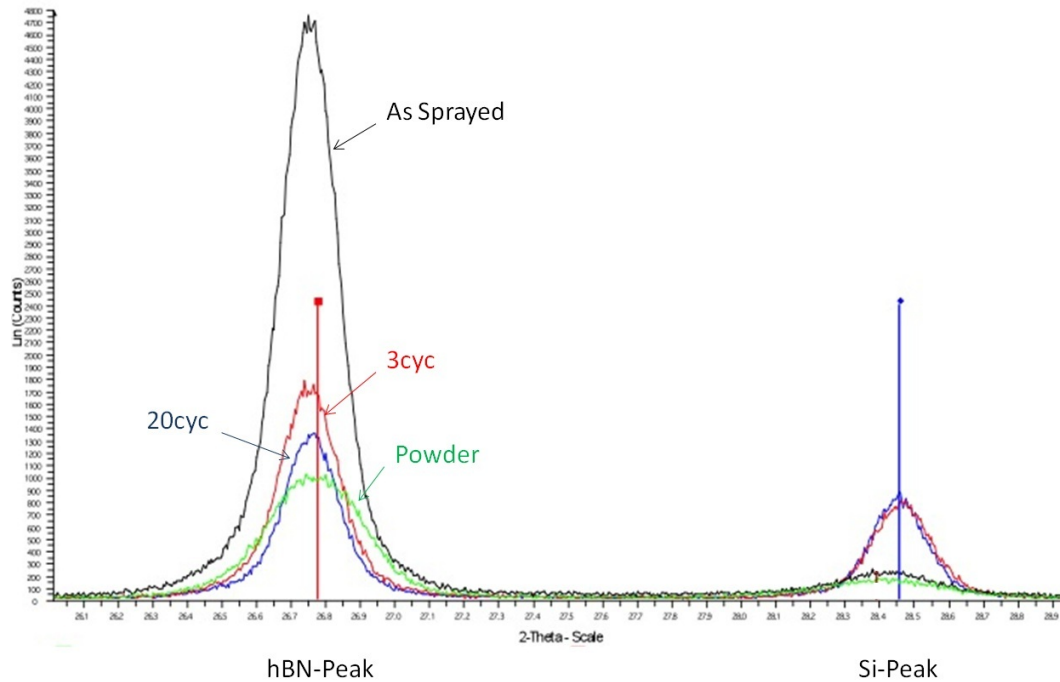


Figure 9.1: M320 Comparison *hBN*-peak and *Si*-peak

Figure 9.2 shows the main *AlSi* peaks of the material. The green lines indicate the pattern of the powder; those are lower in intensity than the as sprayed and heat treated material. It can be seen that the peaks shift once the material was subject to cyclic heating. The heat treated samples show slightly higher d-spacings between their atoms, indicating a reduction of the tensile stresses in the material's top surface of  $50 \mu\text{m}$ .

It can also be seen that once the initial heat treatment has introduced a shift in the peaks, all further aged samples show a similar pattern as seen for the first cycled material. This shift in peaks between the powder, as-sprayed and heat cycled can be explained by the *Si* precipitation out of the *AlSi* metal matrix. The formation of a stable 2-phase material reduces the intra-granular strain fields, resulting a sharpening of the XRD trace and a shift towards the original *AlSi* peak.

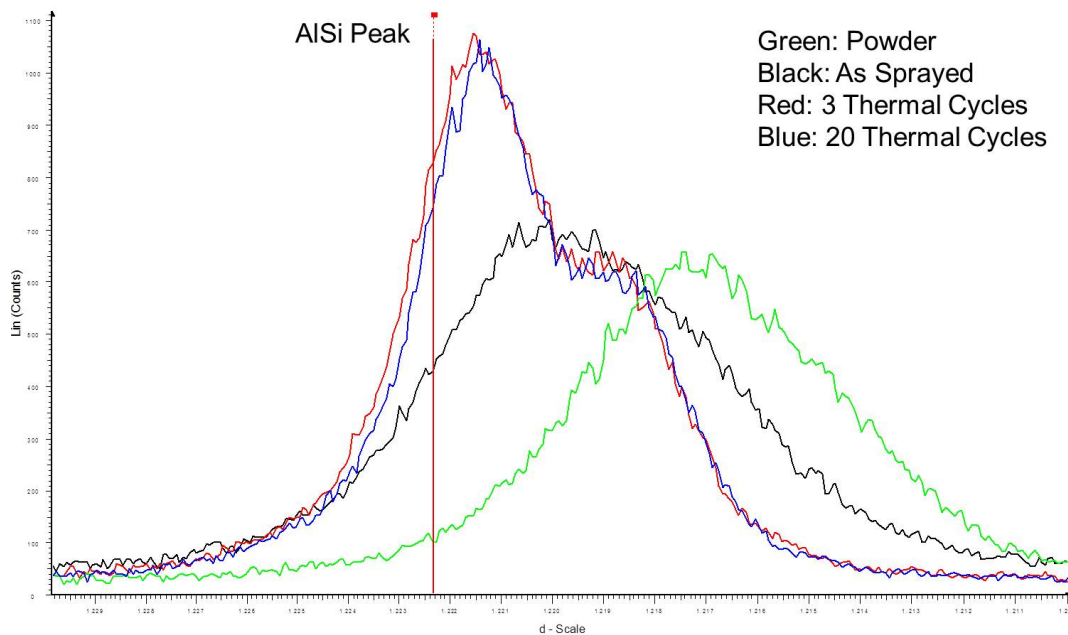


Figure 9.2: M320 Comparison *AlSi*-peak at  $2\theta=38$

Furthermore, the scans for the powder and as-sprayed material are wider than the scans for the heat cycled samples. During the spraying process, the material cools rapidly, enabling the solution of up to 12% *Si* into the *AlSi* metal matrix. This metastable phase is dominated by dislocations, substitutions and inclusions in its lattice structure. These intra-granular micro-stresses can be picked up during XRD analysis and show in a broadening of the peak.

A reduction in peak width, as can be traced for the heat cycled M320 abrasible seal material, indicates the reduction of micro-stresses. Allowing the material to creep relax at temperature and *Si* to precipitate out of the *AlSi* metal matrix, allows the lattice structure to form more regular, less stressed grains.

## 9.3 Resonance Frequency Damping Analysis

### 9.3.1 Theory

The RFDA uses a ballistic impactor to induce vibration into the abrasible material. The damping following the impact can be characterised as the energy absorption of the material investigated. The elastic properties of the abrasible seal can be assessed from the resonant frequencies exhibited by the sample. The material properties are assessed by recording the decay of the vibration [126].



The vibration of the sample, induced by the impactor, has a characteristic frequency for any material. The measured frequency is related to the elastic modulus, as well as the sample's geometry and density [127]. The damping effect originates from microstructural interactions, internal friction and other mechanical losses of the vibration applied. The relationship between the measured frequency ( $f_f$ ) and Young's modulus ( $E$ ) is given by the following equation:

$$E = 0.9465 * \left(\frac{m * f_f^2}{b}\right) * \left(\frac{L^3}{t^3}\right) * T_1 ,$$

where  $E$  - Young's Modulus,  $m$  - mass of the bar (g),  $b$  - width (mm),  $L$  - length (mm),  $t$  - thickness (mm),  $f_f$  - Fundamental flexural resonance frequency of the bar (Hz) and  $T_1$  - Correction factor for flexural mode.

The test set-up used at Cranfield University allows the sample to 'ring' after the impactor induced the vibration. This method is also called the natural frequency method. During testing, different frequencies can be picked up from the sample, which need to be sorted into the characteristic and higher mode frequencies.

### 9.3.2 Experimental Analysis

M320 is designed to work at temperatures of up to  $450^\circ C$  and elevated pressures. The material properties changes over the temperature interval. In order to investigate those changes, as-sprayed, freestanding samples were analysed in the RFDA. The machine holds the specimen in a furnace and increases temperature by  $1^\circ C$  every minute. An impactor hit the abradable every  $5 \text{ min}$  and the resulting frequencies the sample emits during its vibration are recorded with the help of a microphone.

When plotting the frequencies over the temperature, a graph like the one shown in Figure 9.3 can be produced; it shows the characteristic frequency of  $2368 \text{ Hz}$  and the first higher order frequency of  $7174 \text{ Hz}$ . This specific plot resulted from the analysis of a free-standing sample, which delaminated after 8 cycles of water-quenching.

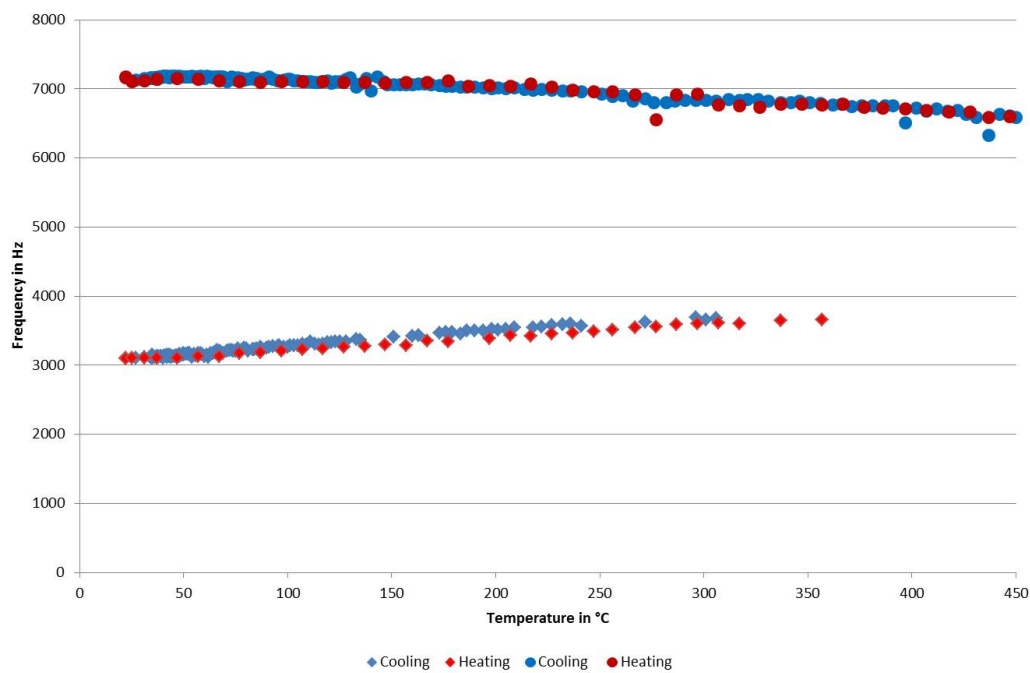


Figure 9.3: Measured Frequencies in the RFDA

Several samples, which delaminated due to heat-cycling were tested in the RFDA. Looking at the graphs of the experiments, it can be seen, that some frequencies disappear at elevated temperatures and reappear around the same temperatures during cooling down. This indicated, that changes in the material are not of permanent nature, but rather due to softening or grain boundary sliding. If chemical reactions or crystallisation were responsible for the changes in response, those frequencies would not be picked up again during cooling.

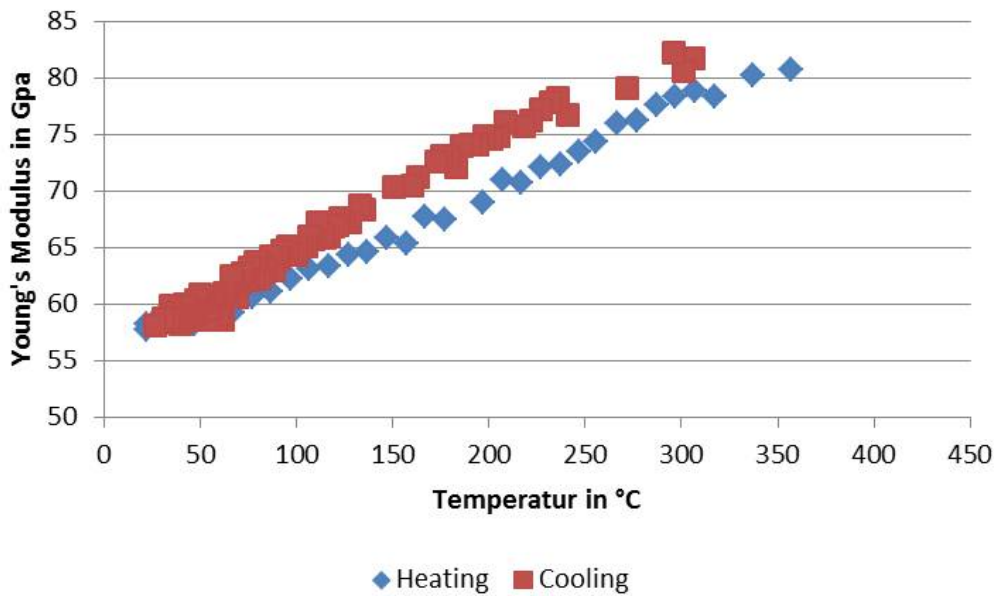


Figure 9.4: Young's Modulus relating to the measured Frequencies between 3000 – 4000 Hz

Figure 9.4 show the calculated Young's Modulus for the recorded frequency of 2368 Hz. The Young's modulus calculated for the samples tested after water-quenching is very high, which is unlike previous measurements made for M320. A Young's modulus between 9 – 25 GPa had been reported and is more reasonable for this friable seal coating. The high readings can be explained with the condition of the tested samples.

Due to the fact that delaminated material was used for the analysis, the samples had actually cracked during water-quenching. These cracks acted as barriers for the vibration and the waves traveling through the material were bounced off the crack rather than the edge of the sample. This shortened the distance the waves had to travel and falsified the readings.

## 9.4 Finite Element Modelling

Finite Element Analysis was used to simulate the stresses arising in the abrasible - substrate combination due to water-quenching. PATRAN 2008 was used to define geometry, create the mesh and apply the boundary conditions, as well as material properties. Following that, PATRAN Marc was used to run a thermal analysis to develop a temperature profile and subsequently PARTAN Marc delivered a thermo-mechanical profile.

As expected from material behaviour in the laboratory, temperature differences show at

the substrate - abrasable interface. The stress analysis reveals high stresses in that area, which confirms the area of failure witnessed during heat cycling experiments.

Since material data for M320 are rare, the thermal conductivity was calculated following the Maxwell-Euken Model, presented in [128].

$$K' = \frac{k_1 v_1 + k_2 v_2 \frac{3k_1}{2k_1 + k_2}}{v_1 + v_2 \frac{3k_1}{2k_1 + k_2}},$$

where  $K'$ -effective thermal conductivity,  $k$ -thermal conductivity of individual phases and  $v$ -volume fraction component. Index 1 refers to the continuous phase and index 2 to the dispersed phase. This calculation delivered a value of  $143 \text{ W/mK}$  for the sprayed M320 abrasable liner.

The density was approximated using the densities of  $AlSi$  ( $2.6 \text{ g/cm}^3$ ) and  $hBN$  ( $2.1 \text{ g/cm}^3$ ) and the distribution of 70% $AlSi$ , 20% $hBN$  and 10% porosity, resulting in  $\rho = 2.24 \text{ g/cm}^3$  for M320.

With the calculated material values, the convection rate needed to be adjusted, to meet measurements undertaken in the laboratory. It was measured, that the surface of a M320 - 316 stainless steel specimen reached  $50^\circ\text{C}$  on the abrasable's surface after 5s of swiveling in the quenching bath. After several simulations and a gradual increase of the convection value,  $10000 \text{ W/m}^2\text{K}$  could be established as the coefficient describing the set-up in the laboratory. This convection coefficient has been used for quenching stainless steel in water before [129].

The material properties used during FEA modelling are listed in Table 9.1.

Table 9.1: Material Data used for the Modelling Stage

	Abrasable	Substrate
Young's Modulus $E[\text{GPa}]$	55 – 70	200
Poisson's Ratio $\nu$	0.27 – 0.33	0.3
Density $\rho[\text{kg/m}^3]$	2510	8000
Specific Heat Capacity $c[\text{J/kgK}]$	910	500
Thermal Conductivity $K'[\text{W/mK}]$	147	18
Thermal Expansion $[\text{m/K}]$	$23 * e^{-6}$	$17 * e^{-6}$

Modelling was carried out for a 2D cross section of the abrasable samples, where the water-quenching was applied to the 4 outer edges and the evolving temperature and

strain profile would represent what is happening in the material during heat cycling. Figure 9.5 shows a cross section of a sample and represents the 2D model.

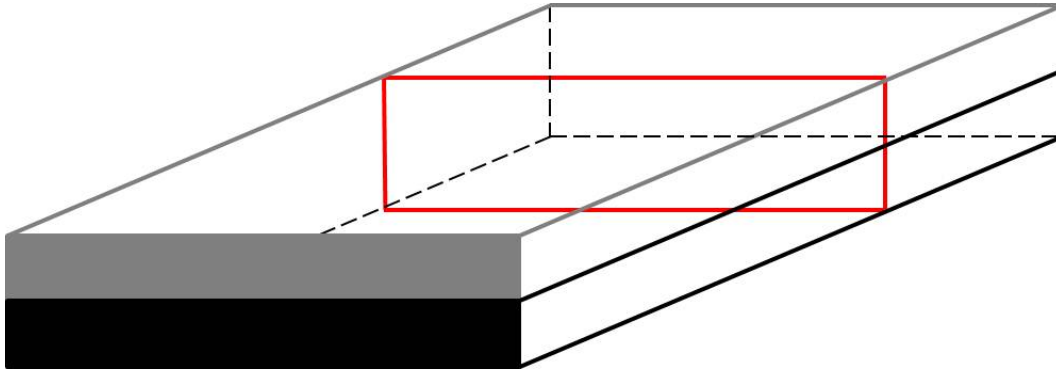
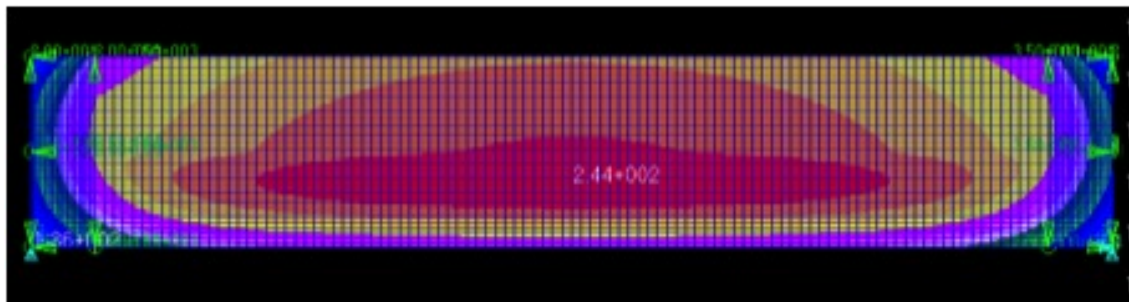
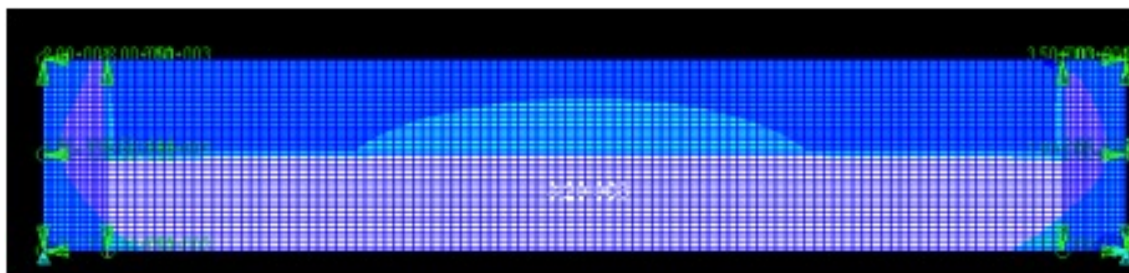


Figure 9.5: Schematic of the 2D model



(a) Temperature Profile of a Water-quenched sample after 2 Seconds in the Water



(b) Strain Profile of a Water-quenched sample after 2 Seconds in the Water

Figure 9.6: FEA Modelling of the Water-quenching Process

Figures 9.6 a and b show the profiles of temperature and strain in the system after 2 seconds of water-quenching. It can be seen, how the strain profile matches the temperature one and how the strain at the interfaces between the abrasible and the substrate give rise to material delamination. These confirm the areas of crack initiation during service and that, even though the tested samples in the laboratory were flat, the edge effect will also affect the service material. The abrasible will detach from the encasing substrate

and cracking will commence as a delamination crack. Surface cracking, which initiates at the edge after they have detached from the substrate, will grow towards the centre of the sample, where further cracks may have opened during cycling.

During modelling the material data for the abradable were varied, as this very heterogeneous material does not deliver constant properties. The thermal conductivity was varied between  $140 - 170 \text{ W/m} \cdot \text{K}$  and the Young's modulus was varied between  $9 - 25 \text{ GPa}$ . It was found that the temperature in the plume was consistent at  $211^\circ\text{C}$  after  $2 \text{ s}$  and surface temperature was  $133^\circ\text{C}$  for every model.

## Chapter 10

# Discussion

The use of abradable seal coatings in gas turbines is designed to enhance the engine's performance and thereby improving the specific fuel consumption. In order for these savings to occur, it is necessary for the material to last its design life time, so the engine does not need unscheduled overhauls. At this point in time, the performance of Metco 320, used as an abradable seal in the high pressure compressor, does not guarantee unplanned inspections.

During service the material experiences different kinds of mechanical and physical loads, such as elevated temperatures, harsh working environments,  $\Delta\alpha\Delta T$  mismatches and the high-speed blade incursion. These conditions make the coating prone to failure, which it has been designed to do, in order to protect the blade. The failure mechanisms of Metco 320 abradable compressor coating had been investigated prior to the start of this research project. Casings which were returned from service were investigated [93, 94, 96, 100] and their premature abradable liner loss was evaluated. Some material does not even make it into service, but fails straight after manufacturing, others erode, delaminate, spall, oxidise or corrode during their service life and / or storage.

Carrying on the research work initiated by Noel Hopkins [80], this project focused on the abradable performance drivers and ways to provide better understanding of the material behaviour, degradation and failure modes. Special importance was given to the microstructural changes during heat cycling and potential testing methods to assess the material's condition, without destroying the material.

Due to the lack of literature and the limited amount of previous work with that material, data produced by Noel Hopkins were used to identify the main parameters influencing the material removal during the abrasion process. Multiple regression analysis was used to identify interrelationships between individual parameters (see figure 5.12 on page 73). It was found, that blade material loss, blade pick up as well as temperature and blade tip

velocity were statistically important parameters during the abrasion process. Since the material operates at its maximum temperature capability, the influence of high temperature exposure over extended periods of time is a crucial parameter in the lifing process of M320 abradable seal coating.

Another point of interest was the failure mechanisms of the material. Cracking was high up on the list, alongside erosion and delamination failure. One of the crack driving parameters had been identified previously as the  $\Delta\alpha\Delta T$  mismatch between the abradable and the casing but other than that not a lot was known about the failure process itself. One of the questions arising continuously was about the changes in the material due to heat cycling and the effect those changes had on the abrasion process and failure mechanism. In order to evaluate the abradable's microstructure at different stages of its lifetime, samples had to be produced and heat cycled to various stages through part life.

Heat cycling was meant to show the degradation, as well as the cracking of the abradable material. In a first attempt to induce cracking, samples were cycled in an automated furnace, heating the material to  $450^{\circ}\text{C}$  for  $90\text{ min}$  and subsequent cooling via compressed air nozzles for  $3\text{ min}$ . It took those samples approximately 750 cycles to start cracking on a micro scale. Since the furnace could only take 3 samples at one time, this set up was superseded with more severe test procedure, as the air blast cooling led to tests taking too long.

To introduce cracking more quickly, water-quenching was chosen to be a better option to apply higher cooling rates and thus promote material failure. The differences in cooling rates applied to the material can be seen in Figure 6.2 on page 80. In a first attempt a box furnace was used to heat the samples, providing enough space for eight specimen. Unfortunately, the manufactured sample holder damaged the surface of the material and was therefore deemed unsuitable.

Finally, it was decided to use a standard baking furnace with a maximum constant temperature of  $500^{\circ}\text{C}$ . Since the samples needed heating to  $450^{\circ}\text{C}$ , the use of a high temperature oven was not necessary. The oven can be seen in Figure 6.3a on page 81, along with the water bath used for quenching (Figure 6.3b).

Comparing the two cooling methods, it was evident, that cooling rates have an effect upon the lifetime of M320 liner material. Maximum cooling rates of  $10\text{ K/s}$  during compressed air cooling was milder on the substrate-abradable combination, than maximum cooling rates of  $110\text{ K/s}$  during water-quenching. Visible cracking occurred on the water-quenching samples after only 3 – 5 cycles and micro-cracking was documented after the first and second cycle. It can therefore be concluded that 1 – 2 cycles of water-quenching equate to 700 – 750 cycles of compressed air cooling.



## 10.1 Cracking Behaviour

M320 abradable samples were tested for their cracking and delamination behaviour, focusing upon gaining an understanding the parameters influencing the decay of the material. In order to evaluate the material performance, the production process was observed and individual changes into the manufacturing were introduced to investigate their affect upon the abradable's failure modes.

Stresses in the system are influenced by grit blasting, the application process of the bond coat and surface machining of the top coat. In order to assess the level of stresses introduced at each stage of the manufacturing process, experiments were carried out, looking at different sample preparation and manufacturing techniques.

### 10.1.1 Grit Blasting

The first step of the manufacturing process is the surface preparation via grit blasting, to prepare the surface for the plasma spraying process and for the coating to adhere properly. In a design of experiment (see section 6.4.1 on page 96), the grit blasting direction was alternated between preparation parallel to the long axis (h - horizontal) of the substrate and parallel to the short axis (v - vertical).

The resulting crack patterns can be seen in Table 6.8 on page 98. The overall crack length on the individual substrates was tracked over the material's lifetime and plotted against the number of cycles (see Figure 10.1).

Indicated by the lines on the graph is the crack propagation for the samples, prepared with different grit blasting directions. After approximately 15 *cycles* of water quenching, the samples grit blasted parallel to the long axis stabilised and crack growth continued at a slower pace, when compared to the initial speed of crack propagation. Those samples grit blasted in parallel to the short axis carried on cracking rapidly until 20 *cycles* until the speed of crack propagation reduced.

The investigation into the grit-blasting process (see Section 6.4.1 on page 96) revealed that the direction plays an important role in the abradable's cracking behaviour in later stages. Since the samples had a dimension of 40x100 *mm*, it was possible to vary the

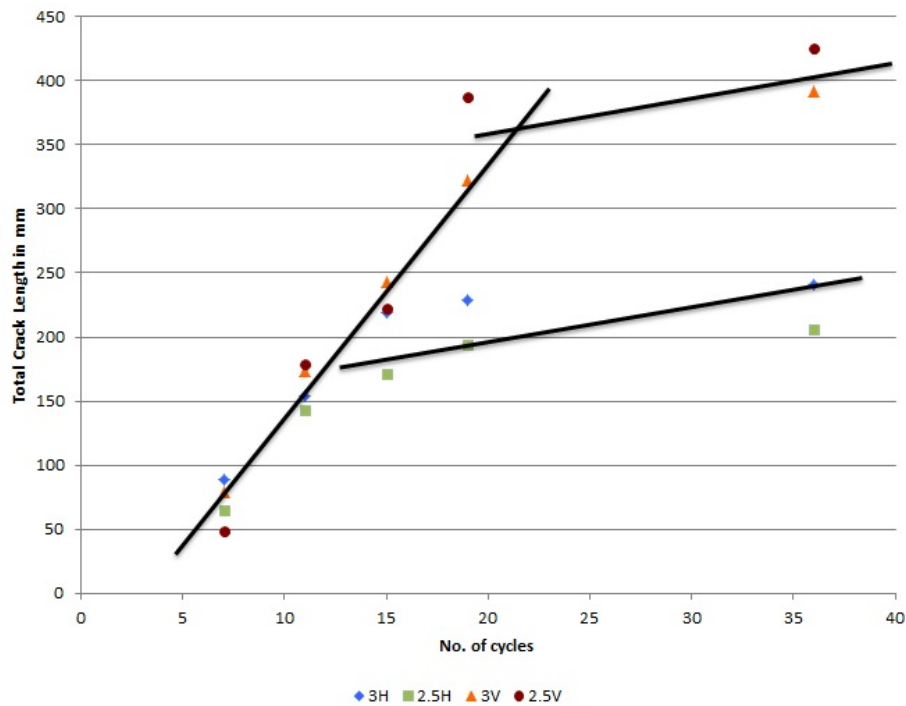


Figure 10.1: Total Crack Length on Samples with different Grit Blasting Direction

grit blasting process so that specimen were produced using different grit blasting directions during the preparation process.

Grit blasting parallel to the short axis resulted in higher stresses in the substrate and subsequently more intense cracking and an earlier failure due to delamination and spallation of the top coat. The differences in residual stresses after grit blasting are listed in Table 6.7 on page 97.

Grit blasting, parallel to the long axis of the sample, showed reduced cracking and deformation of the substrate, which is in line with less stresses being introduced into the system. For crack patterns observed during testing see table 6.8 on page 98.

The observations made during the substrate preparation for the grit blasting trial, along with the results during heat cycling, led to an immediate application in new sample manufacture and any abradable specimen sprayed from now on, is grit blasted parallel to the long axis, in order to reduce the stresses introduced into the substrate.

The thickness of the substrate affects the deformation of the material during the grit-blasting process (see Figure 10.2). Thin specimens deform quickly and heavily, whereas thicker ones remain in their original shape. The grit-blasting process does not change, which implies a constant thickness of the material affected by the procedure.

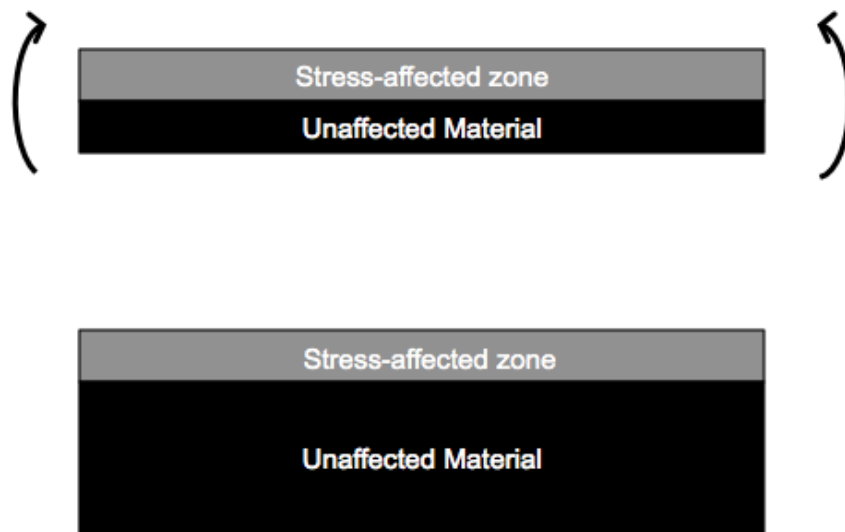


Figure 10.2: Schematic of Surface Stresses and its Effect on the Sample's Deformation

The deformation of the grit-blasted specimen and the dependency upon the direction of preparation, raises questions as to how the substrates were manufactured and if there might be pre-existing stresses in the material. Since no annealing took place before the grit-blasting and spraying of the coating, these can influence the substrate's response to the manufacturing process. Also, the forces needed to bend a rectangular sample when prepared vertically are less than the forces required to bend the material prepared horizontally.

To investigate the required forces to deform the substrates, the material properties for a  $40 \times 100 \text{ mm}$  stainless steel substrate were investigated. The Young's modulus is given as  $200 \text{ GPa}$ . The schematic in Figure 10.3 shows the plume size of the grit-blasting gun in relation to the substrate. Each blue bar represents one pass with the grit blasting gun. The gun is passed over the specimen from side to side, ensuring an overlap of the passes.

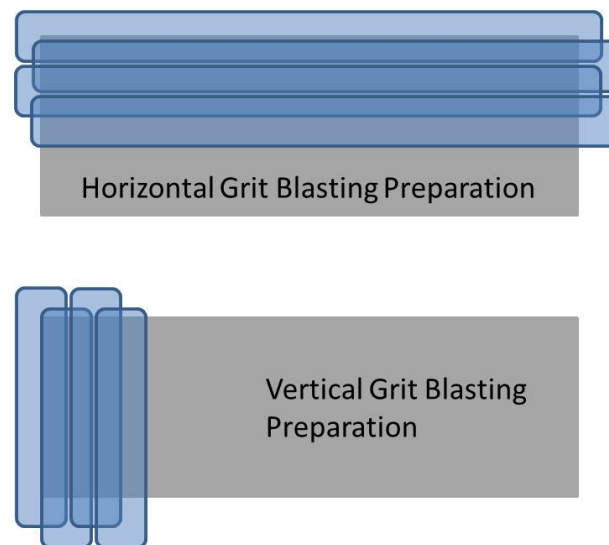


Figure 10.3: Schematic of Plume Size during Grit Blasting in Relation to the Substrate

The forces needed to bend a substrate were calculated using beam theory:

$$F = \frac{6dEI_y}{2x^3},$$

where  $d$  is the deflection of the sample ( $d = x \sin(\alpha)$ ),  $E$  is the Young's modulus,  $I_y$  is the moment of inertia ( $I_y = \frac{w \cdot t^3}{12}$ ) and  $x$  is the length of the deflected area. The schematics in Figure 10.4 show how the sample was assessed for the analysis. A deflection length ( $x$ ) for a single grit blasting pass of  $15 \text{ mm}$  and a deflection angle ( $\alpha$ ) of  $5 \text{ degree}$  were assumed. The sample thickness ( $t$ ) was varied and the sample width ( $w$ ) was  $40 \text{ mm}$  for vertical preparation and  $100 \text{ mm}$  for horizontal preparation.

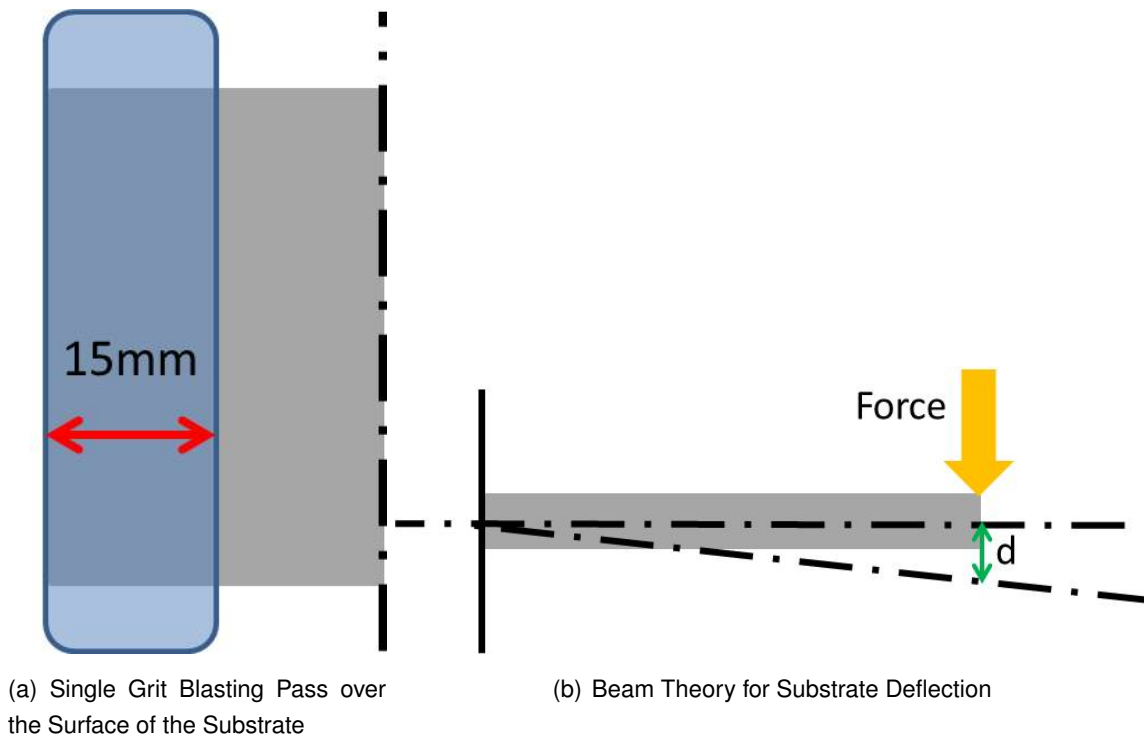


Figure 10.4: Beam Theory for the Deflection of the Substrate and the needed Forces

A 2D model for each preparation direction was assumed in order to calculate the forces acting upon the substrate with one pass of the grit blasting gun. For the vertical preparation a varying thickness  $a$  and beam length  $l$  of 40 mm was applied. For the horizontal preparation the same varying thickness  $a$ , but a beam length of 100 mm was used. Figure 10.5 shows the forces needed to deform a substrate when grit-blasted in a vertical and horizontal direction. It can be see that much higher forces are required to deform a substrate horizontally than vertically.

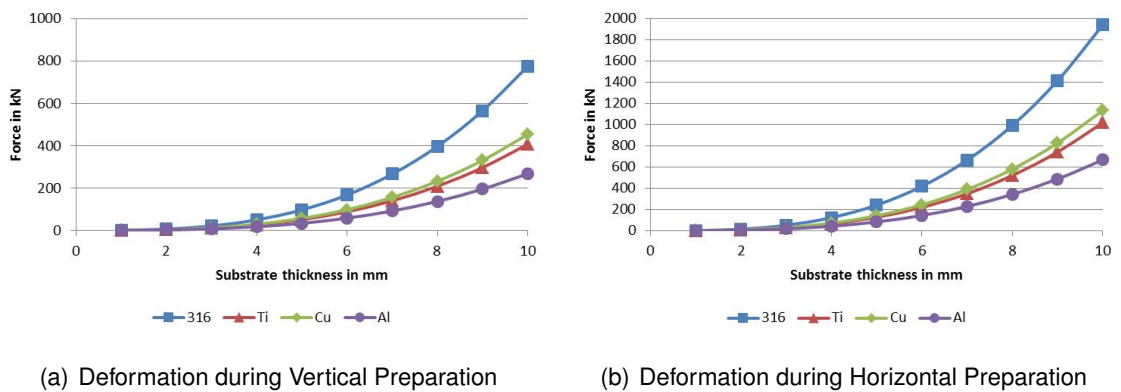


Figure 10.5: Forces needed to deform a Substrate depending upon its Thickness and Preparation Direction

During testing it was observed, that specimen of 316 stainless steel with a thickness of 1.5 mm deformed, when treated in a vertical manner, but not, when grit blasted horizontally. From experiences in the laboratory and the sample manufacturing processes, it can be concluded, that the grit-blasting process damages the surface layers of the substrate and generates deformations in the microstructure. These deformations cause plastic deformation and stresses, which relieve during heat cycling. These stress relieve mechanisms happen underneath the bond coat and can cause microstructural re-arrangements, which in turn lead to stresses in the bond coat.

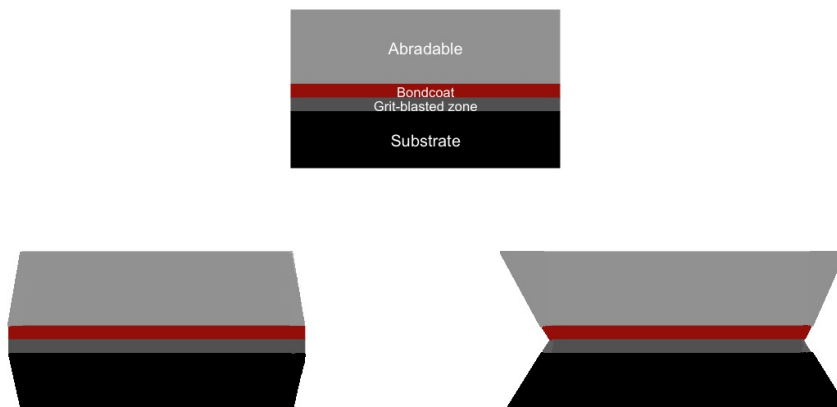


Figure 10.6: Schematic of Surface Stresses in the Substrate after Grit-Blasting and their relief Mechanisms

Figure 10.6 shows a schematic of the stress relief in the grit-blasted area of the substrate, resulting in stresses in the bond coat, which can affect the abradable as well, since a deformation of the bond-coat can cause a deformation of the top coat.

Due to the fact that the grit-blasting effect upon the substrate's microstructure is hard to assess, the stress relief mechanisms are difficult to predict. Shrinkage, as well as expansion is possible and therefore, a forecast of the potential deformation of the substrate/bond-coat interface and the resulting stresses in the abradable is unlikely.

A potential annealing stage after the grit-blasting process might relieve the stresses in the substrate and could improve the abradable's life-time. This annealing stage would have to be carried out in a vacuum, since the grit-blasted area could oxidise, destroying the prepared surface and adhesion of the bond-coat might fail.

### 10.1.2 Plasma Spraying

Sample manufacturing used to be carried out by plasma spraying the substrates from the outside inwards, as explained in section 6.4.4 on page 103. This set up left the substrates to experience intense thermal cycles during the deposition process, because no insulation was provided for the substrate's backside.

Investigating the potential of changing the manufacturing set-up to mimic the production of a casing revealed that an inside-outward spray process (see Figure 6.13 on page 89) reduced the thermal cycles the substrates were subjected to. Analysing samples of different preparation set-ups showed an increased number of material failures due to delamination of the abrasible top coat of the samples manufactured with an outside-inward set up (see Figure 6.4 on page 82).

The heating and cooling of the substrate during deposition is an important factor, when assessing the stress state of the final abrasible material. Intense thermal changes during the manufacturing process, lead to higher stresses building up in each layer of the coating, compared to insulated samples.

The times to failure were different for the samples produced in the different set-ups. For the outside-inward process, samples lasted for about 20 cycles before the top coat delaminated, whereas the samples produced with inside-outward spraying survived 40 cycles and more.

The stresses within the individual layers of the abrasible are different for the two spray set-ups, which is in line with the model explained by Asghari et. al. [59] and illustrated in figure 3.10 on page 43. The cooling of the deposited material during outside-inward spraying is higher than during inside-outward and therefore stresses arising in the individual layers are higher.

The abrasible creep relieves in each splat of the individually deposited layer of the material and higher stresses result in more microstructural changes. These changes of the material lead to crack initiation and propagation, where higher stresses cause quicker failure. Therefore, those samples produced with an outside-inward set-up fail at an increased speed.

### 10.1.3 Surface Machining

After the manufacturing stage the sprayed and cooled coating has to go through a machining process before the casing can be placed into the engine. Machining describes the grinding of the abrasible from an application thickness of 6 mm down to 3 → 4.5 mm for use in service. This introduces machining stresses into the surface of the abrasible liner, which may contribute to an accelerated material degradation, as well as the introduction of a surface layer of increased residual stresses, which will alter the material's properties relative to subsurface layers.

Experiments with machined surfaces, polished to different surface finishings, showed that abrasibles left with a rough surface after polishing were more prone to cracking than those polished to a smooth finish. The results of that test series can be seen in Figure 6.9 on page 100 in section 6.4.2.

Against expectations during testing, all the samples ground with a 120 grit paper, failed due to delamination within 7 – 15 cycles of heat cycling. Samples ground with a 240 grit paper lasted 18 – 25 cycles and those samples left with a rougher finish cracked more severely, but survived longer; with one sample delaminating after 18 cycles, but the others remained intact after 40 cycles of water-quenching.

These results of the machining trial, however, raise the question as to why the rougher finish increased cracking resistance. This led to the assumption that the cracking on the fine finished specimen was hidden from view and initiated underneath the surface and that the polished and compressed surface layer of the abrasible liner may act as a transient barrier due to its denser micro-structure.

The samples were cut up and polished to be investigated under the optical microscope. It was hoped to find areas of crack initiation underneath the surface, which in turn would grow towards the top and bottom of the abrasible. A schematic of the crack initiation at the interface between the polished material on the surface and the subsurface sprayed abrasible is shown in Figure 10.7. Crack growth was expected to extend upwards to the surface and towards the substrate, but the crack shown in Figure 6.21 on page 102 indicates there are cracks initiating underneath the surface, only extending towards the substrate, never breaking through the surface layer.

A crack, initiated in subsurface layers can be seen in Figure 6.21 on page 102. It grew towards the substrate, but failed to extend and break through the surface. These cracks, hidden from view, are a great risk to the assessment of the abrasible during service, since a look at the surface does not reveal the real state of degradation of the material. They also reduce the lifetime of the coating, since the crack is now initiated closer to the



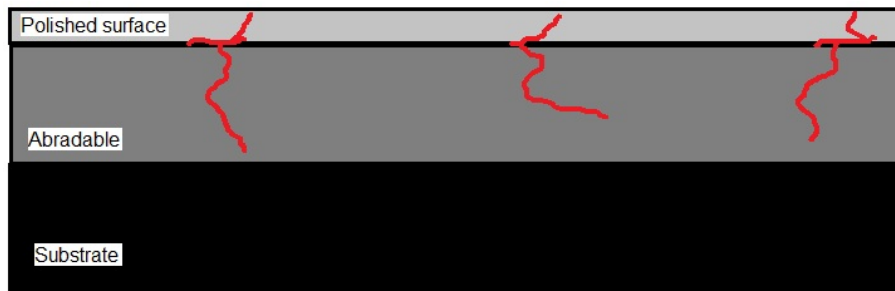


Figure 10.7: Crack Initiation on a Polished Abradable

substrate and needs less time to grow to the bond coat area, where they turn into delamination cracks.

#### 10.1.4 Abradable Hardness

The overall crack length on soft M320 (HR15Y 40) was observed to be much higher than the crack length measured for hard abrasives (HR15Y 70). The cracking in hard material (total length of 150 mm) was expected to be much deeper, than the cracking in soft material (crack length of 360 mm).

The mudflat size on the softer material was smaller than on the hard material, which suggested easier crack initiation during thermal cycling. Figure 10.8 shows a schematic of a cracking mechanism presented by [130]. It was suggested, that peak stresses occur in the center of each mudflat forming, which results in a new cracking generating in the middle of an existing mudflat.

In the case of an abradable coating, the model can be modified for a very defective surface structure, where crack initiation might not happen at the point of highest stresses, but rather in an area, where a defect exists and stresses at the point exceed  $\sigma_f$ . Figure 10.9 shows a schematic of the potential shifting of the point of crack initiation, when surface defects are present. In that case, the material in the center of the mudflat is able to withstand the existing surface stresses in material, but due to imperfections in the microstructure, the crack initiates, at a close-by *hBN* spot, where the metal matrix is intercepted and more prone to opening. These differences in crack initiation is due to the fact that  $\sigma_{max}(hBN) < \sigma_{max}(AlSi)$ .

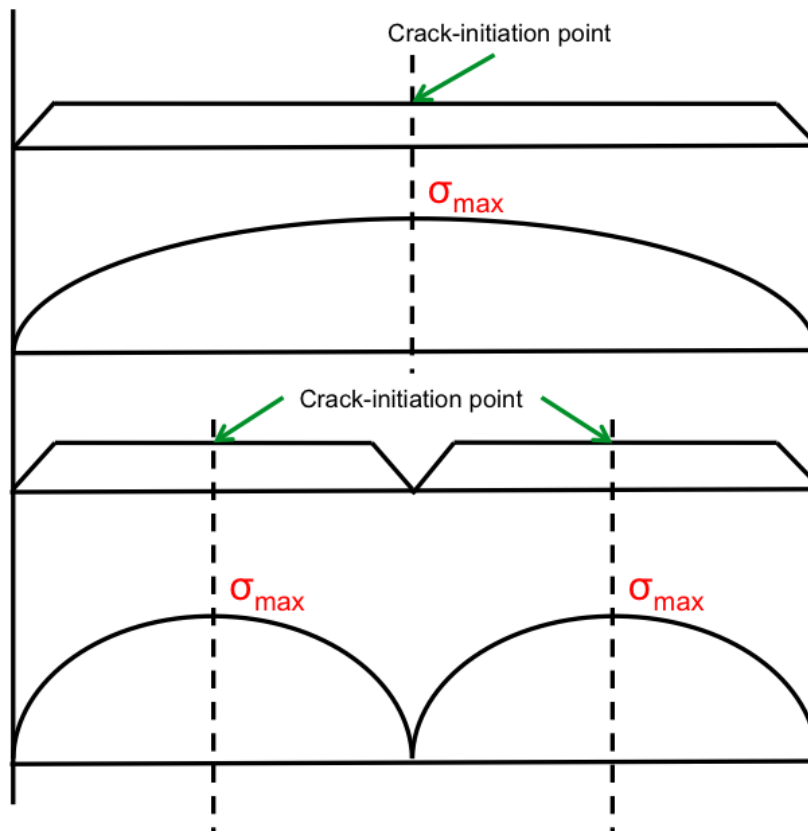


Figure 10.8: Crack Initiation Points according to Stress Distribution

### 10.1.5 Transient Analysis

Testing showed that the transient behaviour is crucial to the survival of the abrasible coating (see section 6.3 on page 89). The experiments showed how substrates with high Biot numbers resulted in coating delamination and cracking from the early stages of testing. Those substrates with lower Biot numbers revealed no cracking or delamination at all; they were documented to bend in a concave manner, due to tensile stress in the top surface of the abrasible.

Table 10.1 lists the substrate materials and their thicknesses, along with the variation in abrasible thickness, which were used to assess the cracking behaviour of M320, when exposed to different transients.

The listed materials were chosen because their transient behaviour being representative as the ones of the Jethete casing or the abrasible liner. The Biot number for different thicknesses of the selected materials was calculated and the graphs can be seen in Figure 6.15 on page 91. In Table 10.1 on page 152, material data for the substrates and the abrasible top coat are listed. In order to compare transient performances of the

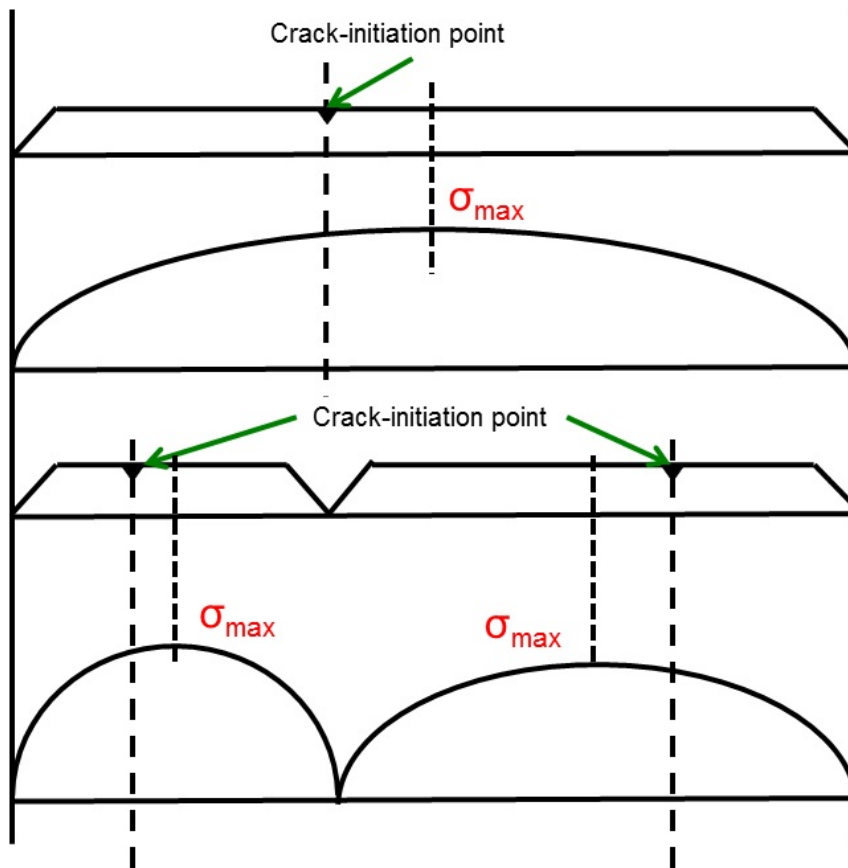


Figure 10.9: Crack Initiation Points in a defective Surface

different materials.

With increasing  $\Delta\alpha\Delta T$  mismatch, cracking progresses quicker and deeper, resulting in more crack growth over the abrasible's lifetime, rather than increased crack initiation, which can be seen on the thinner substrates. The aluminium and copper substrates bent upward, into the liners shrinkage during heat cycling, relieving the stresses in the abrasible without any cracking or delamination of the top coat.

The titanium and stainless steel samples delaminated along the interface with the bond coat and cracked on the top coat's surface. The abrasible creep relaxes at temperature and tries to shrink into its new, stress relieved state, but ends up cracking along its weak points on the surface, because it is held in place by the substrate. In parallel to the surface cracking, the abrasible material also tries to minimise tensile stresses during cooling via bending, which shows in the onset, and later progression, of delamination along the bond coat - abrasible interface, parallel to the substrate. This progresses during further heat cycling and quenching and ends with the liner material chipping off.

Table 10.1: Overview of Sample tested for Cracking and Delamination

Material	Substrate thickness	Abradable thickness	$\Delta\alpha$ coefficient	Young's Modulus	Biot Number for 3mm thickness
Aluminium	5 → 8mm	3mm	23	69	$8.18 * 10^{-5}$
Copper	5 → 8mm	3mm	17	117	$1.7 * 10^{-4}$
Titanium	3 → 6mm	3mm	8.3	110	$1.62 * 10^{-3}$
316 stainless steel	3 → 6mm	3mm	16	180	$3.19 * 10^{-3}$
316 stainless steel	1.5 → 3mm	3mm	16	180	$3.19 * 10^{-3}$
316 stainless steel	3mm	1 → 3mm	16	180	$3.19 * 10^{-3}$
M320 Abradable		3mm	26	18	$1.1 * 10^{-4}$

316 stainless steel substrates of 1.5 → 2.5 mm revealed a combination of bending and surface cracking. With increasing substrate thickness the amount of cracking increased, while the degree of bending decreased, until no bending could be observed for substrates of 3 mm and thicker .

Furthermore, a more defined mudflat area was expected to form on thicker substrates, when compared to thin material. But instead of more defined mudflats, the edge effect became dominant and took over increasing parts of the crack network 10.10. The edge effect was not expected to take over the crack propagation over the entire sample and therefore influence the total crack length, but analysis of the samples established two different crack drivers, mudflat- and edge driven propagation.

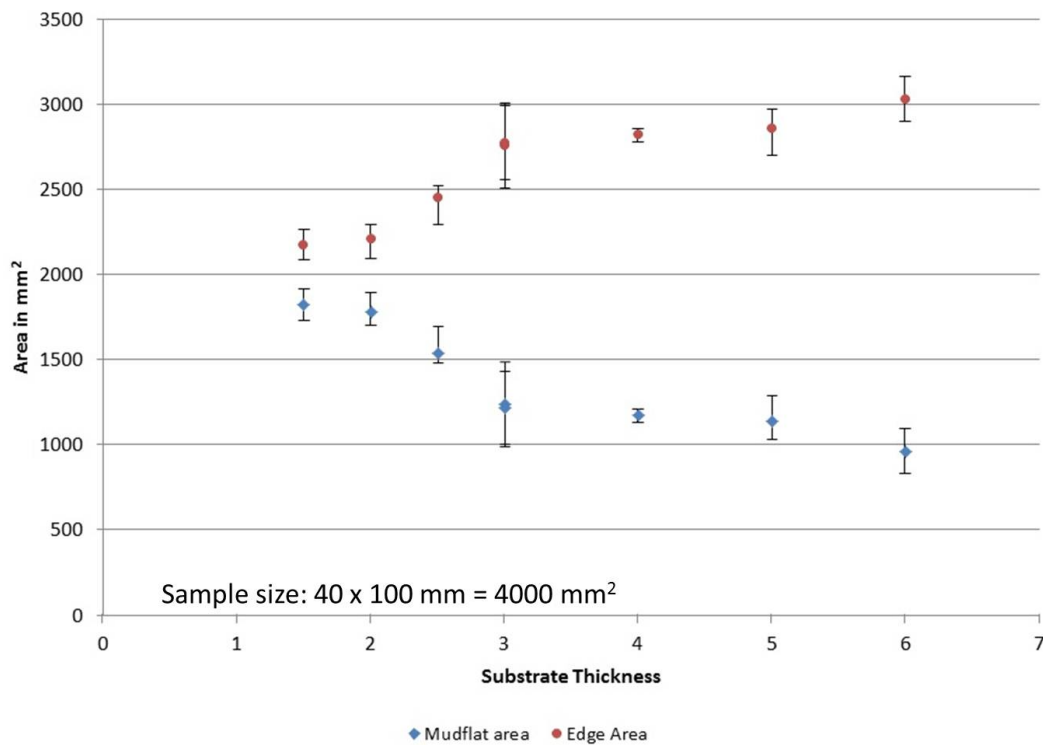


Figure 10.10: Area of Mudflat- and Edge Cracking as a Function of the Substrate's Thickness

Figure 10.11 shows the progression of cracking on the surface of the abrasible deposited onto stainless steel and titanium substrates. For the 1.5 – 2.5 mm substrates only stainless steel samples were available, but the thicker samples showed a surprising linearity of the crack growth for 316 and *Ti* substrates. Having calculated higher Biot numbers for stainless steel, it was expected to find higher levels of overall crack length, when compared to the titanium samples. But no considerable difference in overall crack length could be established. The *Ti* and 316 substrates showed almost the same length in cracking on the surface.

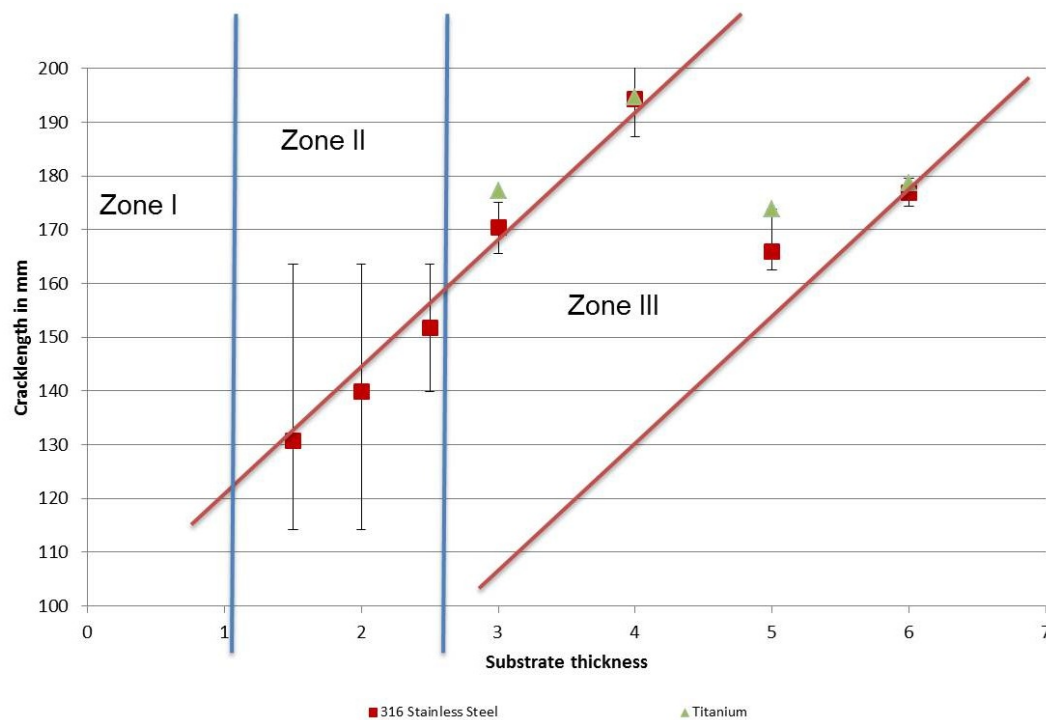


Figure 10.11: Total Crack Length on Substrates of Different Thicknesses and Materials

The graph in Figure 10.11 is separated into 3 zones by the blue lines. These zones describe the bending and delamination behaviour of different substrate materials with varying thicknesses. These zones were identified during testing and can be characterised as follows:

- Zone I - Substrate bends with the abrasible, but no cracking can be observed in the abrasible,
- Zone II - Bending of the substrate plus some crack initiation,
- Zone III - No bending, but cracking due to extensive crack growth rather than initiation.

The two red lines describe the mudflat- and edge driven crack processes which could be documented during testing. Those samples with a substrate of up to 4 mm thickness are placed on the mudflat driven cracking line, whereas those specimen with a 6 mm substrate are located on the edge driven cracking line. The 5 mm samples represent a transition phase between mudflat- and edge driven cracking.

The emerging crack patterns of the different samples can be seen in Table 6.6 on page 95. As described, on thin substrates the edge effect was minimal and a very random pattern of mudflat cracking in the center of the sample dominated the crack growth and propagation (indicated by the red square). With increasing thickness the edge effect became more dominant and the mudflat area in the center shrank.

Figures 10.12 and 10.13 show the total crack length as a function of the substrate thickness and the number of cycles. It shows the increase of crack length over the number of cycles and the dip in the total length when looking at the substrate's thickness. These graphs can be linked to Figure 10.11, where the total crack length is plotted over the substrate thickness; here the number of cycles are included in the graph, which shows how the crack grow over time. The dip at 5 mm thick substrates can be seen in this presentation as well.

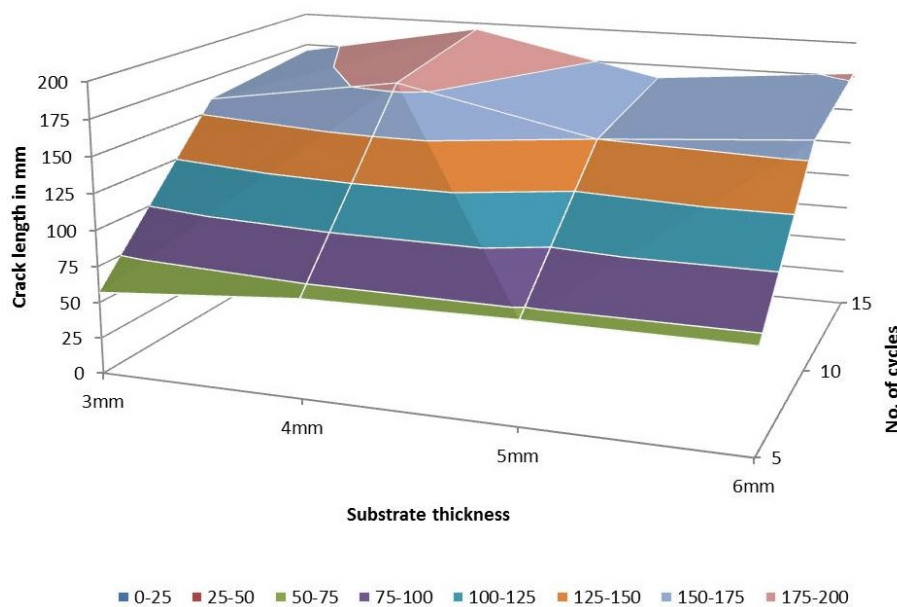


Figure 10.12: Crack Growth on a 316 Stainless Steel Substrate

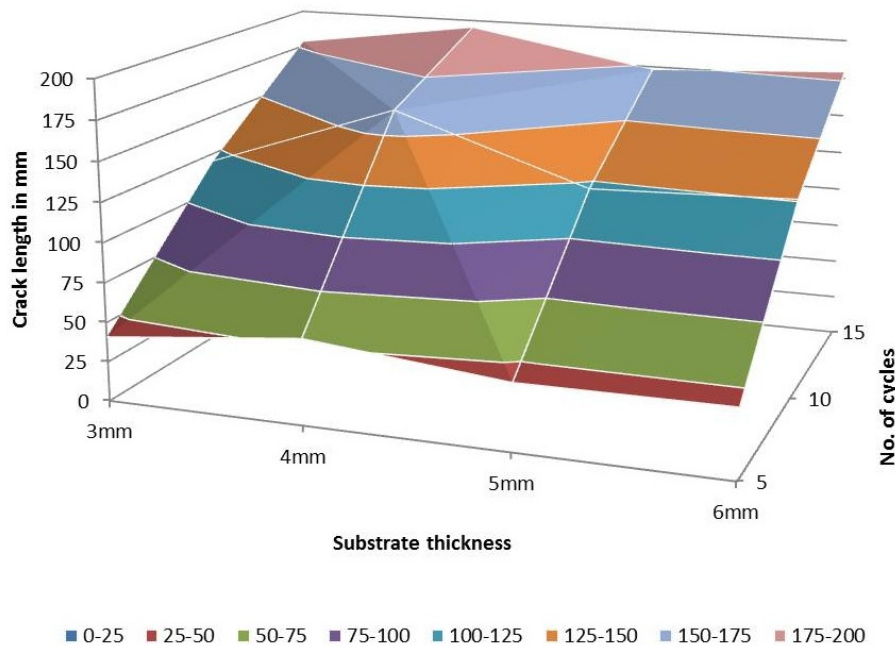


Figure 10.13: Crack Growth on a Titanium Substrate

Since the same thickness of abrasible coating is sprayed onto the substrates, the contraction of the liner does not vary, but the limitations of its shrinkage do. Therefore, the thicker substrates increase tensile stresses forming in the abrasible and following that more intense cracking.

Analysing the material deposited onto *Al* and *Cu* substrates, the abrasible showed no cracking during testing. Instead of cracking and delaminating, like the material on *Ti* and stainless steel substrates, the samples bend upwards, due the shrinkage of the liner. The bending was first observed on the *Al* substrates of 5 and 6 mm thickness, which bend from the first water-quenching cycle. Also the *Cu* substrates of 5 and 6 mm thickness were observed to deform early during testing. After 15 cycles of water-quenching, all substrates were documented to bend upwards and no cracking or delamination occurred.

Table 10.2: Biot Numbers of *Al* and *Cu* Substrates

Substrate	<i>Al</i> – 5mm	<i>Al</i> –6mm	<i>Cu</i> – 5mm	<i>Cu</i> – 6mm	<i>Al</i> –7mm	<i>Al</i> –8mm	<i>Cu</i> – 7mm	<i>Cu</i> – 8mm
Biot No.	$2 * 10^{-4}$	$2.7 * 10^{-4}$	$4.1 * 10^{-4}$	$5.6 * 10^{-4}$	$3.4 * 10^{-4}$	$4.2 * 10^{-4}$	$7.1 * 10^{-4}$	$8.7 * 10^{-4}$

Looking at the Biot number of for the *Al* and *Cu* substrates (see Table 10.2), it can be concluded, that the degree of bending is related to the transient properties of the substrate material. This is encouraged further by the observations made during testing of thin stainless steel substrates, where 2 mm deformed, but 2.5 mm survived thermal cycling of up to 40 cycles without bending.



Table 10.3: Biot Numbers of thin Stainless Steel Samples

Substrate Thickness	1.5	2	2.5	3
Biot No.	$8.8 * 10^{-4}$	$15.2 * 10^{-4}$	$22.9 * 10^{-4}$	$31.9 * 10^{-4}$

*Ti* samples, which were only tested from 3 → 6 mm of thickness, never revealed any bending. This is due to the fact that 3 mm of *Ti* started with a Biot number of  $16.2 * 10^{-4}$ , which is above the value for 2 mm stainless steel, which was the thickest substrate to deform during testing of the stainless steel specimen (see Table 10.3). Specimen with higher Biot numbers did not show bending during thermal cycling, but any samples with a Biot number below  $16.2 * 10^{-4}$  deformed.

From the transient analysis it can be concluded, that its influence upon the cracking behaviour is greater than previously appreciated. It has to be pointed out though, that the grit blasting process introduces stresses into the substrate's surface, which might not be sufficient to deform the sample during preparation, but might have an effect upon the sample's performance during heat exposure. Should the surface stresses in the substrate/abradable system be relieved it could result in substrate deformation, which is not caused by the shrinkage of the liner.

### 10.1.6 Abradable Thickness Variation

Testing samples with a different abradable thickness showed that increasing thickness resulted in more residual stresses after manufacturing; and more cracking during heat cycling. This was observed, whilst heat cycling samples of 1, 2 and 3 mm abradable thickness. The 3 mm samples cracked and delaminated within 40 cycles; 2 mm of abradable started cracking around 30 cycles and the 1 mm samples showed no signs of cracking or delamination after 40 cycles.

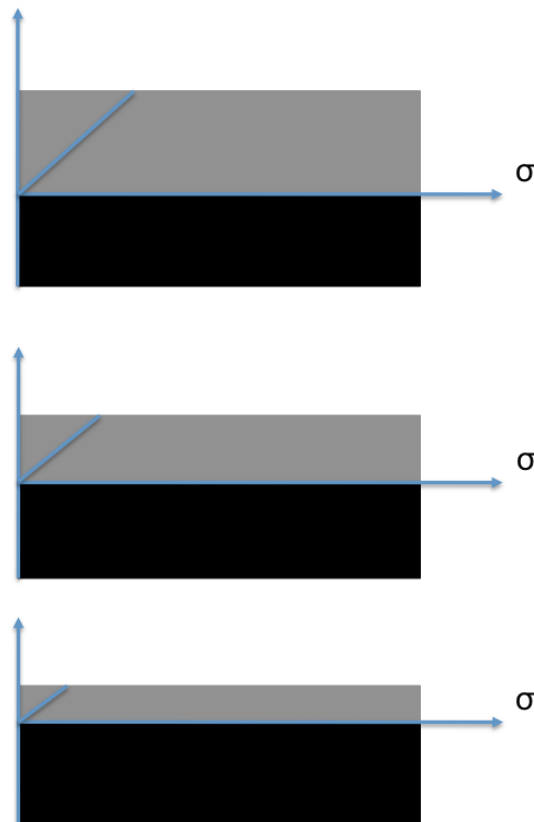


Figure 10.14: Schematic of the resulting Surface Stresses due to Abradable Thickness Variation

Figure 10.14 shows the influence of the abradable thickness upon the surface stresses. In the schematic, a linear increase of stresses in the surface is indicated. This is not the case for the heterogeneous, porous abradable material, but as an indication of the stress variation over thickness, it can be said that an increasing thickness leads to higher stresses in the top surface. This shows, how cracking on  $3mm$  samples progresses much quicker than on the thinner samples. Higher stresses in the material result in crack initiation and propagation in earlier cycles.

## 10.2 Material Changes/Degradation

Metco 320 abradable coating is subject to intense thermal cycling during service and due to its harsh working environment, the interaction with the blade tip, as well as mechanical stresses applied to the material, the abradable liner degrades. This degradation is planned for the sacrificial coating, as the alternative would be failure of the blades or casing.

Since the abrasible is plasma sprayed from an *AlSi-hBN*-polyester powder, the microstructure and physical properties change, depending upon spray process parameters and subsequent surface treatments. Even though material properties potentially change with every spray-run, constant performance is expected during flight service. This implies that the abrasible has to last the service interval, whilst protecting blade tip and casing.

At temperature, the abrasible liner material

(a) creep relaxes,

(b) *Si* precipitates out of the *AlSi* matrix and

(c) the metal matrix builds up a network, isolating the *hBN* particles, which can potentially be removed from the metal matrix, resulting in the formation of layers  $X_1$  and  $X_2$ . These Layers describe the *hBN* deprived surface layer ( $X_1$ ) and the remaining as deposited material underneath ( $X_2$ ).

### (a) - Creep Relaxing

In order to measure stresses in the abrasible coating, X-Ray diffraction was used to analyse the material. A top coat in the as sprayed condition, meaning not machined or heat cycled, shows a shift of its aluminium-silicon peak at  $\Theta = 78 - 78.5$ . This shift indicates tensile stresses in the surface of the abrasible. Since X-Ray analysis only penetrates the material to a depth of  $50\mu m$ , only surface and near-surface stresses can be measured. These tensile stresses disappear after the first cycle of water quenching, showing as a realigned XRD peak in subsequent analyses.

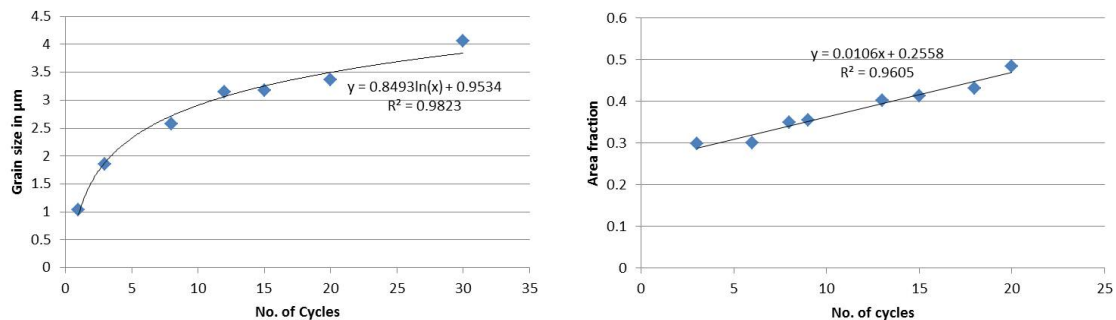
To evaluate the level of stresses in the material, detailed stress runs over several angles of  $\Psi$  was carried out. Samples of the as-sprayed material, as well as heat cycled and the loose powder were tested. The as-sprayed coating shows a higher level of tensile stresses, than the heat cycled top coat. Those results indicate a constant level of tension in the top surface, but not high enough to fracture the material, since crack opening would be observed otherwise.

Once heat cycling started and the material started to creep relax during heat exposure, cracking begins at the points of high tensile stress concentration, developed in the cooling cycle. Stress relieve cracking only releases the those stresses above the Yield stress of

the abrasable; stresses under this threshold will remain and can be picked up by the XRD.

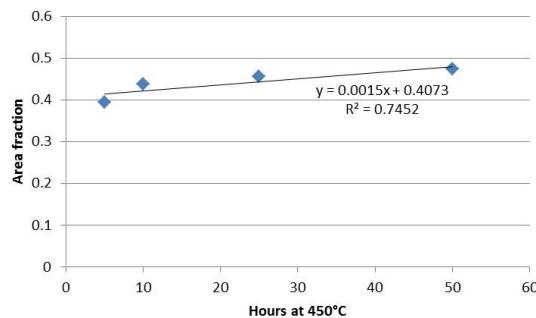
### (b) - *Si*-Precipitation

Precipitation (section 6.4.5) allows the metal matrix to harden due to two stable phases being present rather than one supersaturated and unstable *AlSi* metal matrix material. The increase in hardness from *Si* precipitating out of the matrix is offset by the loss of polymer binder during heat exposure, resulting in a reduction of the hardness of the overall system. In Figure 10.15 the measured precipitation and agglomeration of *Si* in documented.



(a) Grain-size as a Function of Cycles

(b) Area Fraction as a Function of Cycles



(c) Area Fraction as a Function of Time at 450°C

Figure 10.15: Precipitation and Agglomeration of *Si* in the *AlSi* matrix

The binder burn out is believed to be responsible for the observed hardness loss at the beginning of an abrasable's lifetime (see Figure 6.28 on page 109). Further time at temperature allows for a hardness increase from precipitation to take effect. Hence the initial rapid drop in hardness is followed by a slight increase. The changes in mechanical properties, along with stress relaxation and blade interaction can result in coating cracking, spallation and complete liner loss at any time during service. Potential corrosion and oxidation during storage can also contribute to premature abrasable failure.

### (c) - Layering Effect

During heat cycling the formation of a lighter layer on the surface was observed (referred to as  $X_1$ -layer, see Figure 10.16). Analysis of that layer revealed that the metal matrix of the abrasives sinters together, initiating from the surface, growing towards the substrate with increasing numbers of thermal cycles (see Figure 7.2). The material builds up a network between the individual particles of  $AlSi$ , which solidified during plasma spraying. The progression of  $X_1$  growth shows in the clearly defined layer on the surface, with a visible distinction from the bottom layer (referred to as  $X_2$ -layer).

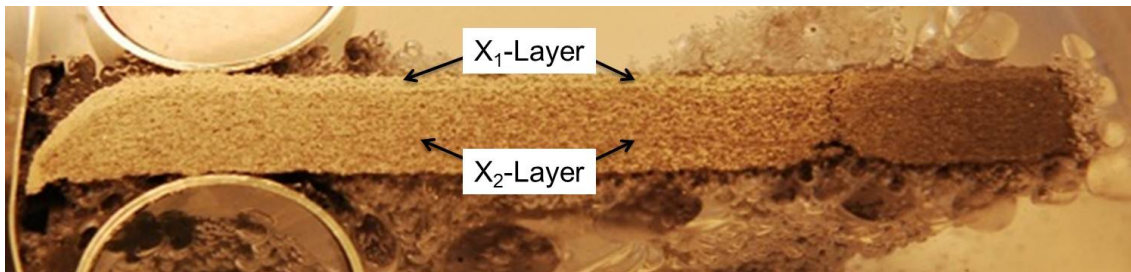


Figure 10.16:  $X_1$ -Layer Forming on the Surface, with the  $X_2$ -Layer underneath

In order to characterise the different layers forming within the material, XRD and EDX analyses were used to assess the material composition of the abrasives'  $X_1$  and  $X_2$  layer. It was shown, that the counts per second, during XRD analysis, for  $hBN$  had reduced, when comparing the  $X_1$  scan to the  $X_2$  readings. This implied that less  $hBN$  can be detected in the surface, compared to the bottom. For  $AlSi$  the counts per second increase, when comparing  $X_1$  and  $X_2$ . This shows, that  $hBN$  comes out of the surface layer, but remains in the lower regions of the abrasible.

EDX analyses were carried out in order to determine the elemental compounds of the two different layers. It was hoped to see variations in  $hBN$  and  $AlSi$  reading for the material, when analysing a cross section, looking at the interface between  $X_1$  and  $X_2$ . Unfortunately, due to the nature of boron and nitride, it is hard to detect those materials using dispersive X-rays.

During EDX analysis, it was found that  $20kV$  beam, which is required for a good material response, was too intense for M320 abrasible material. The beam penetrated the material too deeply for a clear image to be produced, since responses from deeper layers get picked up and blurred the picture.

To generate a good picture, the beam was turned down to 10kV, which resulted on less penetration depth, but also less responses for the mapping process. The penetration depth ( $R$ ) can be calculated using the following formula:

$$R = \frac{0.0276 * A * BE^{1.67}}{Z^{0.89} * \rho} \quad [\mu m],$$

where  $A$ -Atomic Weight [ $g/mole$ ],  $BE$ -Beam Energy [ $kV$ ],  $Z$ -Atomic Number and  $\rho$ -Density [ $g/cm^3$ ].

Table 10.4: Penetration Depths for EDX Analysis

Phase	Atomic Weight	Atomic Number	Density	Beam Energy	Activation Depth
<i>AlSi</i>	55g/mole	13, 14	2.67g/cm <sup>3</sup>	10kV	2.5μm
<i>hBN</i>	24.8g/mole	5, 7	2.1g/cm <sup>3</sup>	10kV	0.24μm

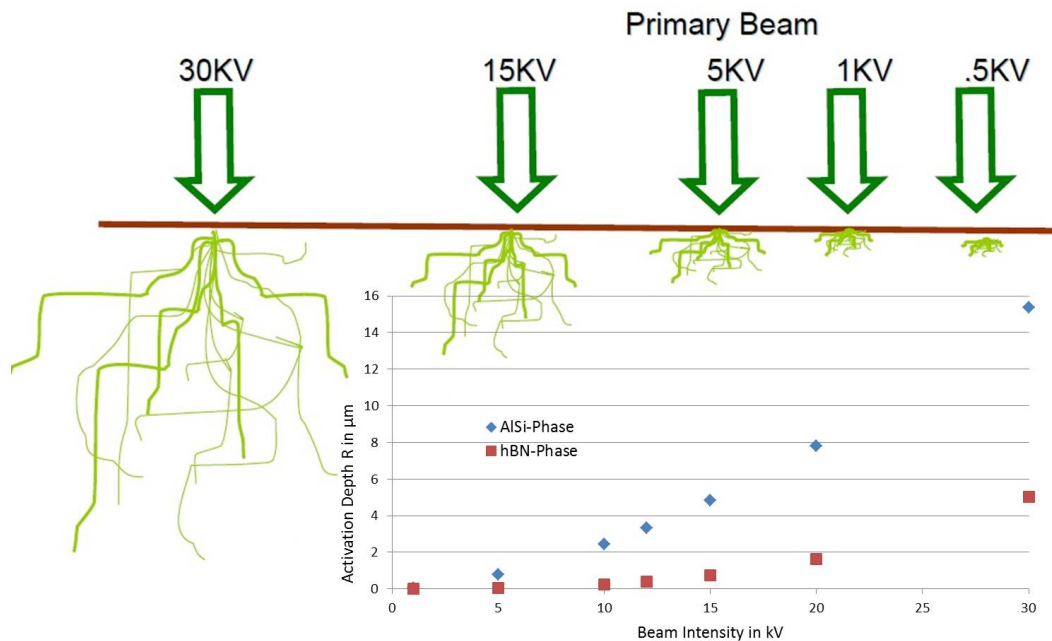


Figure 10.17: Penetration Depths of varying Beam Intensities - adapted from [131] for M320

Figure 10.17 shows the Depth of activation during EDX analysis, depending upon beam intensity. A similar scenario can be calculated for M320 abrasadable seal coating, which is documented in Table 10.4.

It shows, that higher beam intensities activate more material, but due to the light phases and the porous structure of the abrasible, the resulting images are poor. Reducing the beam, results in better picture quality, but the amount of electrons released from the material are not sufficient to generate a material map.

Figure 10.18 shows the main *hBN* and *AlSi* peak. The red line resulted from the scan over the  $X_1$  layer and the black line shows the  $X_2$  results. It can be seen, how the *hBN* peak increases from  $X_1$  to  $X_2$  and the *AlSi* peak decreases. Comparing the counts per second for the *hBN* and *AlSi* peaks, the  $X_1$ -layer only contains about 50% of the *hBN* the  $X_2$ -layer does.

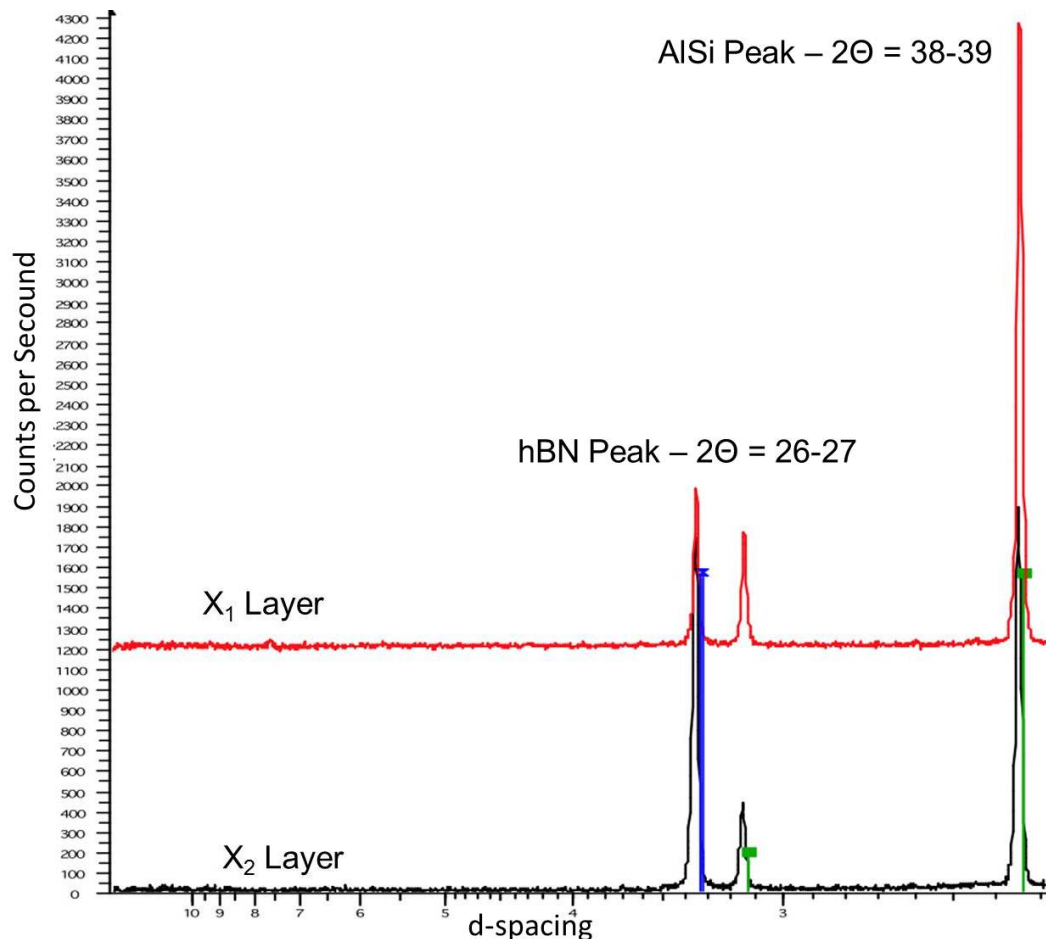


Figure 10.18: XRD Scan of an Abradable Chip: Top ( $X_1$ ) and Bottom ( $X_2$ )

Due to the fact that abradable material had to delaminate and chip off the substrate for the XRD analysis to be carried out, the available material was limited. The samples to be tested needed to be of at least  $15 \times 15$  mm, which left only a few specimens for the

analysis. Those that were available, were not generated in the same spray runs or at the same time, which made a comparison between samples impossible.

Depletion profiles, characterising the slow-growing surface layer of aluminium or chromium on oxidation resistant alloys, were documented by Pragnell et. al. [132]. The profiles resulting from the oxide growth, depriving the subsurface layers of aluminium and chromium respectively, can be compared to the *hBN* depletion of the surface layers of M320 abrasible material. The  $X_1$  surface layer formation can be described as a surface driven material loss of the *hBN*. Figure 10.19 shows the growth over time at temperature.

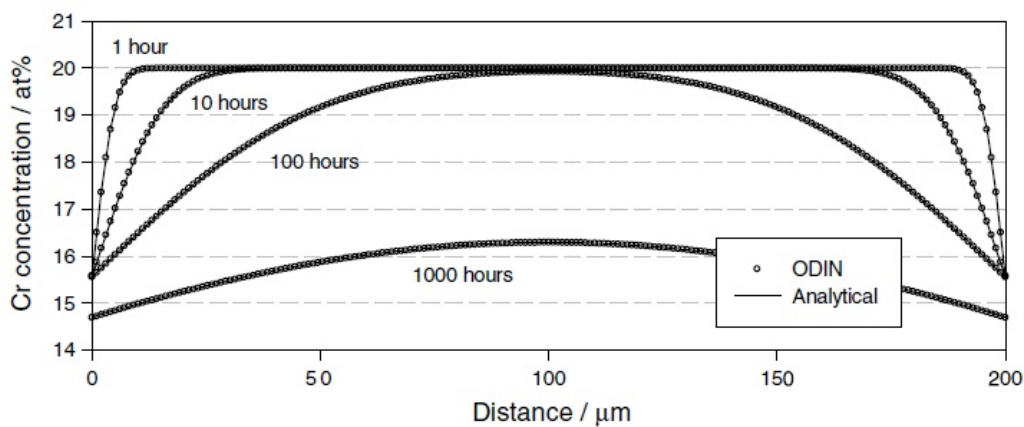


Figure 10.19: Depletion Profile of a Chromium deprived high temperature alloy [132]

### Theories for *hBN* Removal from the Metal Matrix

The top surface is subject to more intense thermal cycling than the subsurface layers, enabling quicker cooling and hardening of the top surface material, than the rest of the coating. Following the thermal cycling, the top surface splats grow together, building up a network of *AlSi* metal matrix. Due to the *hBN* particles being isolated and unable to form connections, they are not integrated into the material structure, promoting an environmentally assisted material removal from the abrasible structure during heat cycling, leaving behind a very porous and brittle metal matrix. Possible *hBN* removal possibilities were discussed with colleagues and are listed below.

- *AlSi* shrinkage during cycling/sintering forces *hBN* particles out of the structure, due to thermal expansion of the metal matrix being higher than the thermal expansion of *hBN*. The expansion of the metal matrix put pressure on the *hBN* and should the particle be close to the surface, it might be squeezed out of the structure (This is the preferred theory amongst colleagues at the surface engineering department at Rolls-Royce).



- Vaporisation has also been considered as a *hBN* removal tool during heat cycling, but with its temperature stability of up to  $1500^{\circ}\text{C}$  it is unlikely for the dislocator phase to vaporise.
- The decomposition of boron nitride (*BN*) has previously been observed, when air plasma sprayed thermal barrier coatings were heat cycled at  $1150^{\circ}\text{C}$ . Smith [133] investigated the cyclic life of APS TBCs exposed to *BN* during cleaning processes. It was found, that after the first heat cycle, *BN* breaks down and forms borates, which were thought to penetrate the porous APS coating and attack the oxides at the BC-TGO-TC interface. But borates only start to form around  $900^{\circ}\text{C}$  [133] and heat cycling M320 was carried out at only  $450^{\circ}\text{C}$ .

## 10.3 Material Testing

During material testing, it was found that the  $X_1$ -layer is less resistant to erosion, scratching and indentation, indicating decreased material performance. The samples produced during heat cycling were analysed using erosion, indentation and scratch testing to investigate, how the documented material changes affected its performance during service.

Specimens of the abradable were removed every 3 water-quenching cycles, in order to erode, scratch and indent the surface, so a performance profile could be established. Furthermore, samples were cut to shape, so they could be analysed using XRD, where a maximum sample size of  $15 \times 15 \times 8 \text{ mm}$  can be analysed.

It was chosen to investigate scratch and indentation performance of the abradable material over its lifetime, since a shopfloor assessment tool for the quality of the abradable liner could help avoid costly and unplanned engine overhauls. The two methods were chosen due to the limited damage they cause to the material, in comparison to erosion testing.

The aforementioned formation of a surface layer, was found to affect the abradable's resistance to erosion and scratching, as well as indentation and RFD analysis. The changed material eroded quicker, but indentation and scratch testing penetrated the material less with increasing age.

### 10.3.1 Erosion Testing

In the early stages of this research project, erosion was used in order to try and rank abradable samples, which were produced in different spray runs, under different spray

conditions. For these tests the samples were in the as-sprayed condition and a dependency of the erosion performance upon the hardness of the liner was established.

During erosion testing, samples of  $35\text{ mm} \times 40\text{ mm}$  were impacted at  $30^\circ$  and  $90^\circ$  angles. The failure modes were analysed and it was found that different impact angles resulted in different modes of failure of the abradable liner. Material, which was under attack from a  $30^\circ$  particle stream showed smearing and ductile erosion, when analysed under the microscope. In comparison, the samples eroded at  $90^\circ$  showed sharp edges and signs of brittle failure in their scars.

Analysing the samples under the optical microscope, it was expected to find underlying material damage in the subsurface layers, due to the harsh impact damage from the erodent. The analysis of cross-sections of erosion samples showed no subsurface damage for samples eroded at  $90^\circ$ , while some as-sprayed samples eroded at  $30^\circ$  showed a very thin layer of compressed material on the top surface, when examined under the optical microscope, with a maximum thickness of approximately  $50\ \mu\text{m}$ . The compressed layer was not continuous, but very patchy, only on some parts of the samples. Further investigation, with the microscope, could not determine whether this was the result of the erosion test or a feature of the original material microstructure.

Mathematical analysis of the erosion process showed that individual particles of alumina, impacting the surface at a speed of  $85 \rightarrow 110\ \text{m/s}$ , were not forceful enough to plastically deform the abradable top coat. Assuming spherical particles and standard distribution of the  $75 \rightarrow 150\ \mu\text{m}$  particles, the force applied by a single particle was calculated as  $8 * 10^{-9} \rightarrow 70 * 10^{-9}\ \text{N}$ . With no observable plasticity, these particles will interact with the abradable elastically.

The number of particles within a single gram of erodent was about  $3 * 10^5$ , assuming a standard distribution of the particle sizes ( $75 \rightarrow 150\ \mu\text{m}$ ), which results in a cyclic fatigue type of failure of the top coat. The constant impact of particles on the surface of the abradable causes minimal plastic and cyclic elastic deformation in the top surface. This leads to fatigue in the areas which absorb the impact and need to recover, resulting in material loss due to cyclic fatigue, similar to high cyclic fatigue if there is little observable plastic damage. These numbers and analysis explained why no subsurface damage could be found in the cross-sections of the eroded abradable material.

The erosion rate of the abradable (defined as 'g of mass loss / kg of erodent'), is influenced by the  $X_1$ -layer that is formed on the surface. The effects of ageing upon erosion rate can be seen in Figures 10.20 and 10.21. Throughout the ageing stages, the initial erosion rate is high, showing as a peak in erosion rate, and then drops off, once the  $X_1$ -layer has been removed.

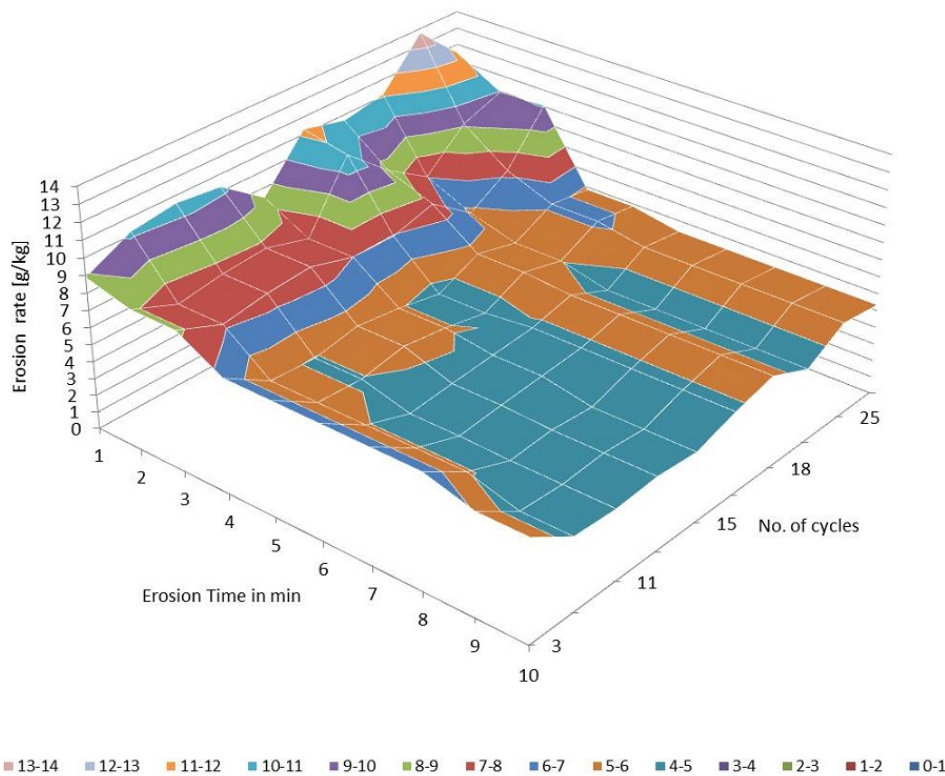


Figure 10.20: Erosion-rate over Time for 30° Erosion Testing

Since erosion testing was carried out on as-sprayed and cycled material, using two different granulates as erodent, it was established that the erosion rate depended upon the impact angle, the particle size and kind of the erodent, as well as the age of the abradable. Table 10.5 gives an overview of the tests undertaken during this research project. The results of aged testing and the variation of hardness in as-sprayed material have been discussed earlier in this discussion.

Comparing the results of eroding samples after the binder burn-out, using two different erodents revealed a dependency of the erosion rate upon the granulate used during the test.  $Al_2O_3$  caused a more intense material removal than  $SiO_2$ . The established, steady-state erosion rate, showed an increase from around 1 g/kg for 30° and 1.3 g/kg for 90° testing using *Si*-sand, to 2.9 g/kg for 30° and 4.5 g/kg for 90° testing using  $Al_2O_3$ .

One possible explanation for the difference in erosion performance under different material attacks, could be the density of the erodent.  $Al_2O_3$  is with  $3.95\text{ g/cm}^3$  heavier than  $SiO_2$  with  $2.65\text{ g/cm}^3$  and may cause more severe impacts on the surface of the abradable.

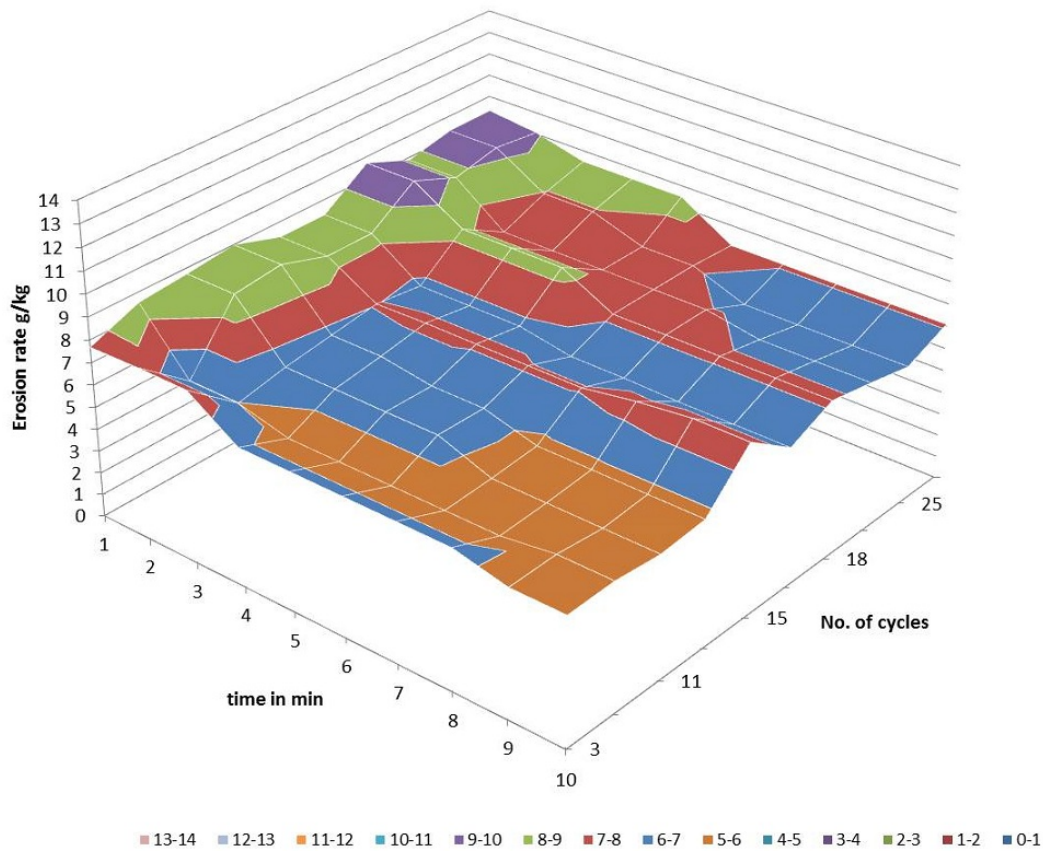


Figure 10.21: Erosion-rate over Time for 90° Erosion Testing

### 10.3.2 Scratch Testing

The use of the scratch tester as a tool to determine material age and degradation was intensely studied, since this tool would be of great help on the shop-floor as a material quality assessment tool. Abradable material was heat cycled and scratched every 3 – 5 cycles, using a 20 N load, with a 5 mm tungsten carbide ball indenter. Since it was established that the machine could not be used to directly compare coatings, it was thought possible to find differences in the scratching behaviour with increasing material age.

Table 10.5: Erosion Testing Experiments

Material Condition	Erodent	Particle-size	Particle speed	Steady state erosion rate 30°	Steady state erosion rate 90°
Binder burnt out	$SiO_2$	76 → 212 $\mu m$	80 – 120 $m * s^{-1}$	1g/kg	1.3g/kg
Binder burnt out	$Al_2O_3$	74 → 150 $\mu m$	85 – 110 $m * s^{-1}$	2.9g/kg	4.5g/kg
Aged	$Al_2O_3$	74 → 150 $\mu m$	85 – 110 $m * s^{-1}$	5.6g/kg	7g/kg

Unfortunately, 4 years into the project, a service engineer determined that the loading sensor of the tester did not work properly and any recorded z-displacement measurements were inaccurate. After further investigation into the matter, it was established that friction occurred in the loading sequence, which was interpreted as putting load onto the surface of the sample. This falsified the recordings for the actual applied load and the z-displacement.

The friction in the load-sensor was not constant, so no continuous error could be implemented and taken into consideration during the analysis. It was decided to ignore the first 30 s of each scratch, since this was assumed to be the time and distance for the loading and friction in the sensor to stabilise. In an attempt to evaluate the scratch-data recorded by the machine, it was chosen to look at the depth of displacement for each scratch, in order to compare the ageing stages.

Peak displacements were plotted over the duration of the 30 scratches. These peak scratches reduced in number with increasing number of water-quenching cycles. Figure 10.22 shows a plot recorded during scratch testing and the increased readings for the z-displacement peak out. It could be established that with increasing age the number of peaks reduced and after their disappearance the abrasable failed due to delamination. Further scratch testing of aged material should be carried out in the future, in order to verify these findings over the full length of scratches.

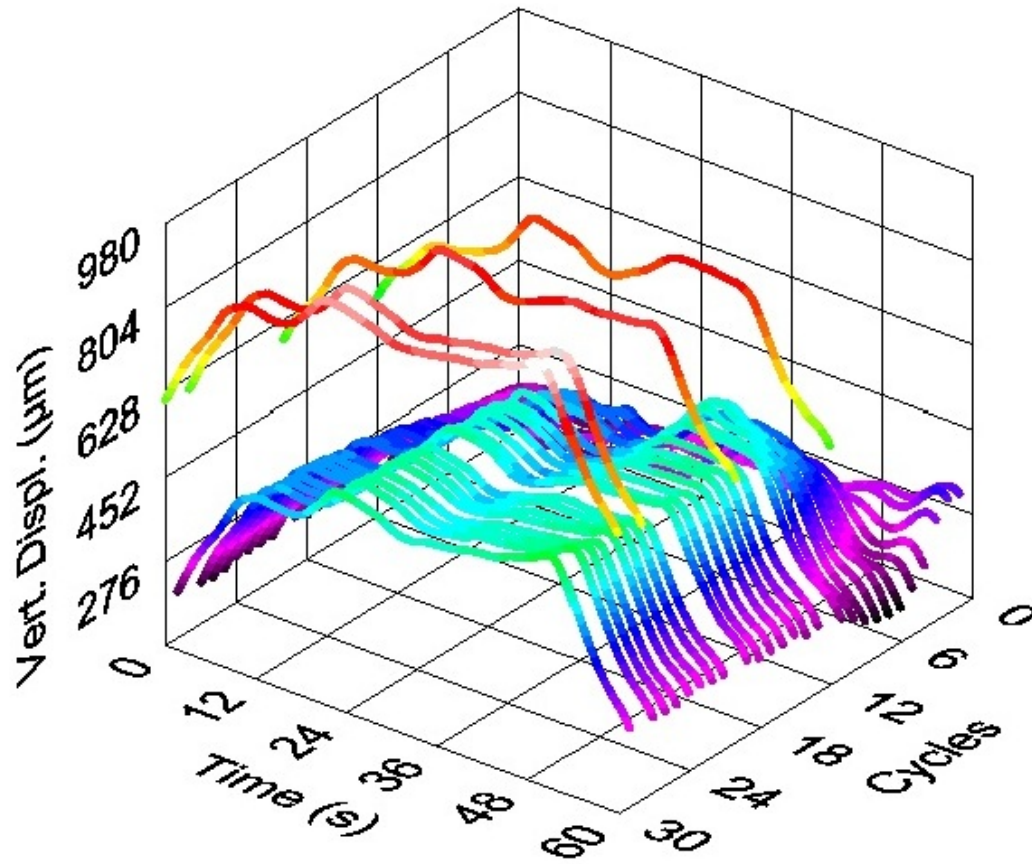
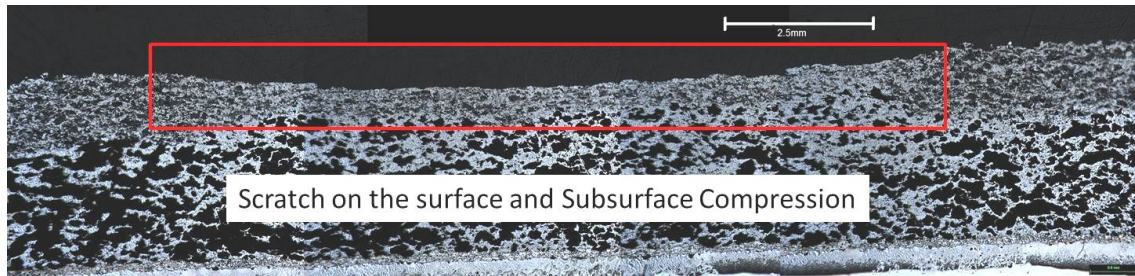
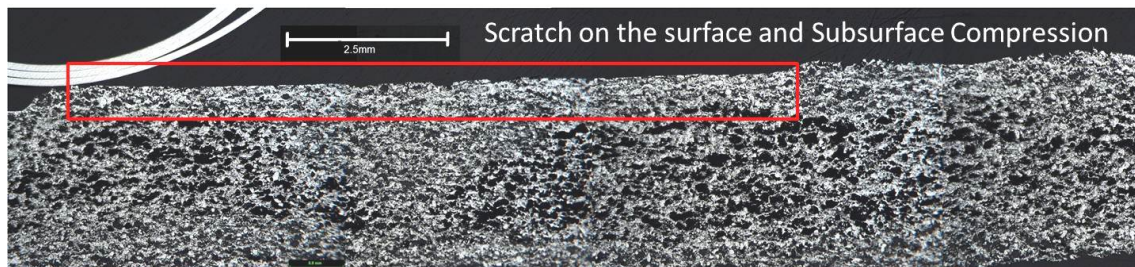


Figure 10.22: Scratch Testing Plot of z-displacement for 30 Scratches

With the quantitative data questionable, it was hoped the analysis of the material under the microscope could show differences in compression of subsurface damage for the cycled samples. It became clear, that with increasing age and  $X_1$ -layer thickness on the surface, the damage under the indenter was more severe.



(a) Scratch Cross Section of an As-sprayed Sample



(b) Scratch Cross Section of a Sample after 9 Cycles

Figure 10.23: Cross Section of Scratch Scars before and after Heat Cycling

To contrast the high cycle fatigue problem exhibited during erosion testing, cyclic scratch testing can be described as a low cycle fatigue type process, which does affect the subsurface layers, as can be seen under the microscope (see Figure 8.3 on page 124). A 20  $N$  load is sufficient to plastically deform the abrasible, resulting in crushed material underneath the scar.

After testing had finished and the material was to be examined under the optical microscope, it was found that those samples sprayed with the outside-in set-up had a very porous structure (see Figure 10.24). This left limited numbers of samples to investigate and measure scratch scars in the  $X_1$  layer.

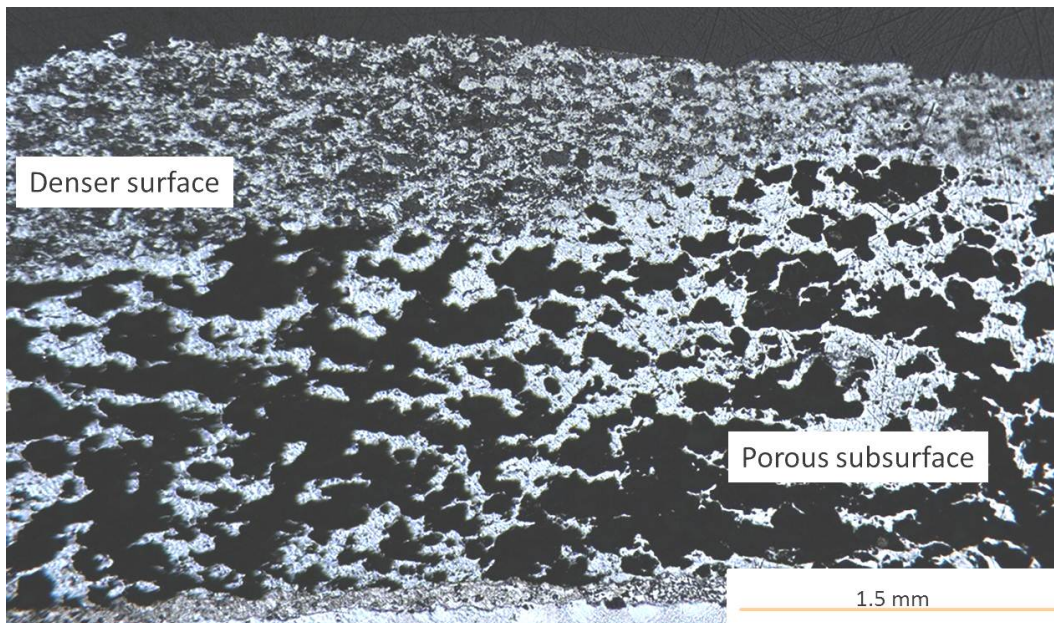


Figure 10.24: Porous Microstructure of Scratch Tested Samples

This structure made the assessment of layers very difficult, since the thickness of the  $X_1$ -layer could not be measured. Because scratching and indenting was carried out at the same time, the surface damage on one line was excessive and the areas of potential  $X_1$  assessment was limited. Figure 10.25 shows how much space was taken up for testing, compared to the areas left untouched on the surface.



Figure 10.25: Surface of an Abradable Sample after Scratch and Indentation Testing

This very difficult assessment of the layers left only a few samples for the analysis and those data points which could be established were plotted in Figure 10.26. Results prove



a change in the microstructure on the top surface, which penetrates the abrasible over its lifetime.

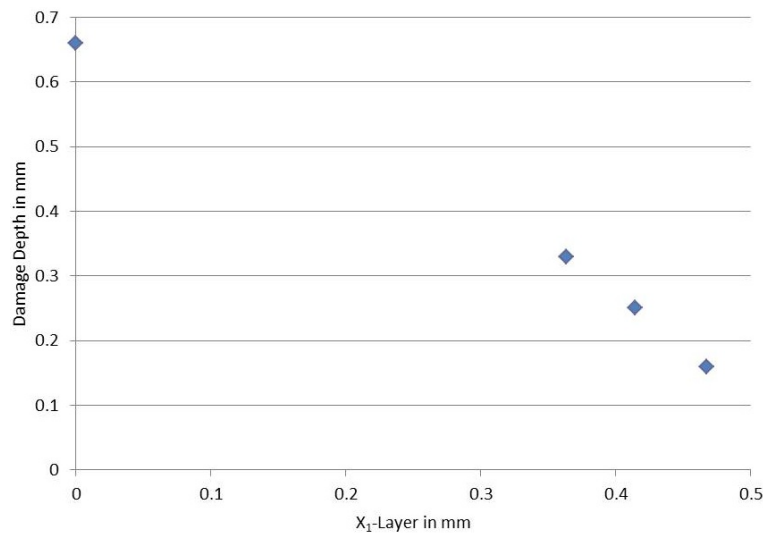


Figure 10.26: Scratching Subsurface Damage as a Function of  $X_1$ -Layer Thickness

The degradation of the material during thermal cycling might be traceable with the scratch tester. The increasing brittle structure resists the scratching better than the as sprayed material, since the damage depth decreases with increasing  $X_1$  thickness.

### 10.3.3 Indentation Testing

Indentation testing was investigated regarding its capabilities of delivering a lifetime assessment of the abrasible material. It was established, that the indentation results are of a cyclic nature and depend upon the stress state of the surface of the abrasible. Figure 10.27 shows the graphs of the two sample sets which were tested and the increase and decrease of plastic deformation can be seen.

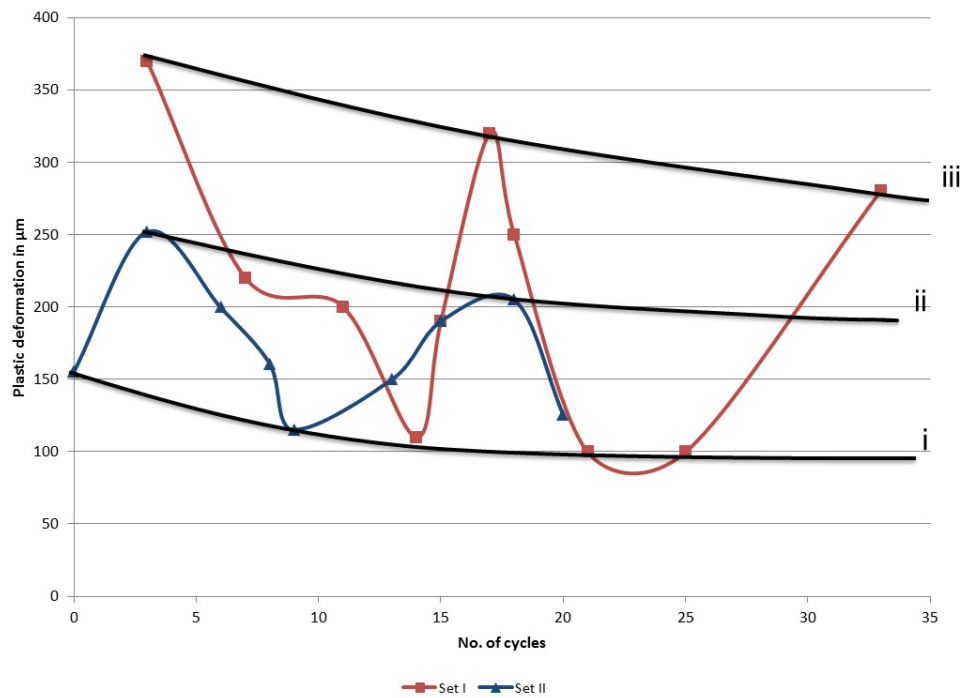


Figure 10.27: Plastic Deformation as a Function of the Number of Cycles, showing Cyclic Nature of Indentation Performance

Thermal cycling of samples results in surface stress building up which leads to subsequent cracking of the top coat. If the material is indented when the surface stresses are high, but cracking did not occur, the plastic deformation is low, since the deformation of a strained material requires more work than the deformation of an unstrained material. Once the cracks opened, the strain reduces and plastic deformation increases for the same load applied to the surface.

This cyclic build-up and relieving of stresses causes the appearance of the graphs in Figure 10.27. The black lines, labeled i, ii and iii indicate cyclic maximum and minimum stress states. Line i runs through the lowest plastic deformations recorded and therefore the highest stress-levels achieved during thermal cycling. The slightly downwards sloping nature of the line indicates a decreasing maximum strain the material is able to withstand with every cycle of stress built-up and crack opening.

Line ii runs through the peaks of the sample set II. These points indicate the material performance in a stress relieved state, which is also of decreasing nature, like line i. Line iii connects the peaks of sample set I, which describes the stress relieved state of the samples in that set. Comparing lines ii and iii, both describing stress relieved material states, it can be said that the sets of abradable material behave differently during thermal cycling.

The level of stresses introduced into the surface before cracking is similar for both sets (line i), but the stress relief due to cracking is less for set II. The relaxed state of set II is capable to retain more strain than the samples of set I.

With the help of indentation testing, the decay of the abradable properties can be traced in the laboratory, but for material assessment on the shop-floor indentation testing is not useful, because only one indent can not be placed on a specific slope. This way a state of the material can not be assessed.

Figure 8.6 on page 127 shows the indentation records for aged abradables. The sudden displacements in the loading curve show the brittle nature of the coating, giving way to the load applied to the surface by fracturing.

### 10.3.4 High Temperature Testing

#### RFDA

Analysing the material in the RFDA gave an insight into the changes to the Young's modulus over temperature and material age. For the experiments carried out with water-quenched material, the following material response to elevated temperature could be recorded (see Table 10.6).

Table 10.6: RFDA Results of Heat Cycled Material

8 Cycles			12 Cycles		
Frequency (+/ - 10%)	max. recorded	Temp.	Frequency (+/ - 10%)	max. recorded	Temp.
11000	380		12500	280	
7900	330				
7100	450		7100	450	
3100	320 / 430		3100	320 / 410	
2300	360		2300	350	

Testing water-quenched material resulted in the detection of Young's moduli between 50 – 85 *GPa*. These results are questionable, since the delicate material was had been investigated using the RFDA before and delivered Young's moduli between 9 – 25 *GPa*, which is more reasonable.

Recording these high readings, it was assumed that the cracking behaviour of the material influenced the results by shortening the length a vibration wave had the travel before

arriving at an 'edge'. The RFDA records frequencies and how quickly they travel through a specimen. For this purpose, the dimensions and the mass of the sample were entered into the software, which used the data to calculate the damping and speed of the waves. Should the distance be shortened due a crack in the material, this can not be attributed by the software when recording the frequencies.

Due to the deterioration and cracking of the material, using the RFDA as a measure for material lifing will be difficult. Free-standing material could be used, but water-quenching these samples does not have the same effect as it has on abradable material deposited onto a substrate.

### Hot Hardness

The hot hardness tester was thought to deliver valuable data concerning the softening of the abradable during heat cycling and a full testing plan was drafted out, in order to characterise the material at temperature. Furthermore, it was expected to see differences of the hardness measurements depending upon the material's age. The increasing thickness of the  $X_1$  layer was thought to influence the hardness of the abradable.

Unfortunately, the machine broke and the testing could not be carried out, except for the initial indents conducted to see whether testing was possible at all. These initial measurements showed however, that material softening changes the response to indentation testing and much larger indents were recorded for the same load. Carrying out a full design of experiments, investigating the temperature response of *AlSi* and *hBN* separately would be beneficial for future material development.

## 10.4 Failure Model

To visualise the cracking behaviour of Metco 320 during heat cycling, the following figures show a schematic approach to show crack initiation and growth. Figure 10.28 shows the temperature over the flight cycle, the material is subjected to. During start-up and climb the temperature rises to  $450^{\circ}C$ , resulting in an expansion of the casing and the abradable coating. Once the cruise level is reached, the casing is fully expanded and remains that way until the engine starts to cool down after landing.

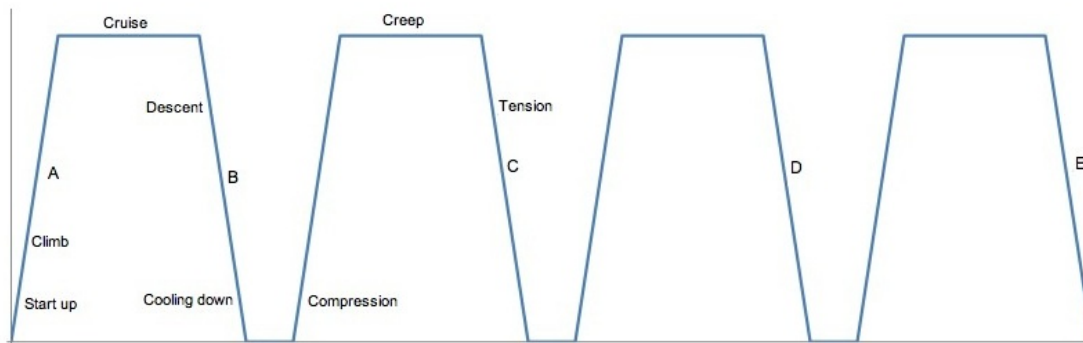


Figure 10.28: Temperature Profile of an Engine and Material Response

The *AlSi* abrasible wants to expand more and quicker than the casing during heating up, resulting in compressive stresses, which creep relax during the cruise period. As soon as the engine reduces temperature after touch down, the liner contracts, again quicker than the casing material. This time resulting in tensile stresses throughout the abrasible. These stresses cause the abrasible to crack on the surface in order to relief the tension. On the next cycle, compressive stresses result in creep relaxing during cruise and further crack opening and initiation during cooling down because of tensile stresses (see figure 10.29).

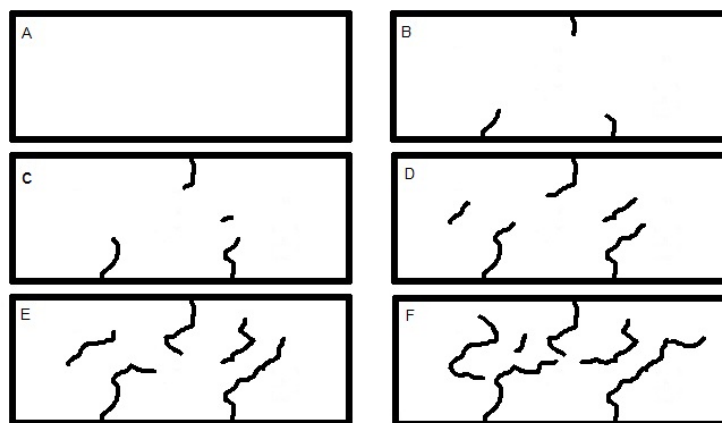


Figure 10.29: Schematic of Crack Initiation and Growth

Finite Element Analysis has confirmed what was observed in the laboratory, concerning stress distribution in the abrasible material and resulting delamination behaviour. Even though the casing delivers and enclosed substrate on three sides (see Figure 10.30), the abrasible was shown, using a 2D FEA model, to detach from the walls and the separation cracks will grow into delamination cracks during heat cycling (see Figure 9.6b on page 137).

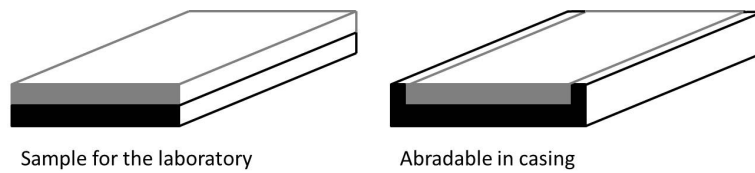


Figure 10.30: Schematic of Samples for Laboratory Testing and Casing Geometry

Furthermore, a temperature profile (see Figure 9.6a on page 137) of the material cooling was created and the changing material properties will alter the cooling behaviour, resulting in more areas of high strain and potential crack initiation.

Finite Element Analysis was carried out for water-quenching, but can be transferred to air cycling, since creep relaxation during heat exposure will result in equal strain field building up within the material over time. Finally, a material response similar to the water-quenching investigation will be observed during air cooling.

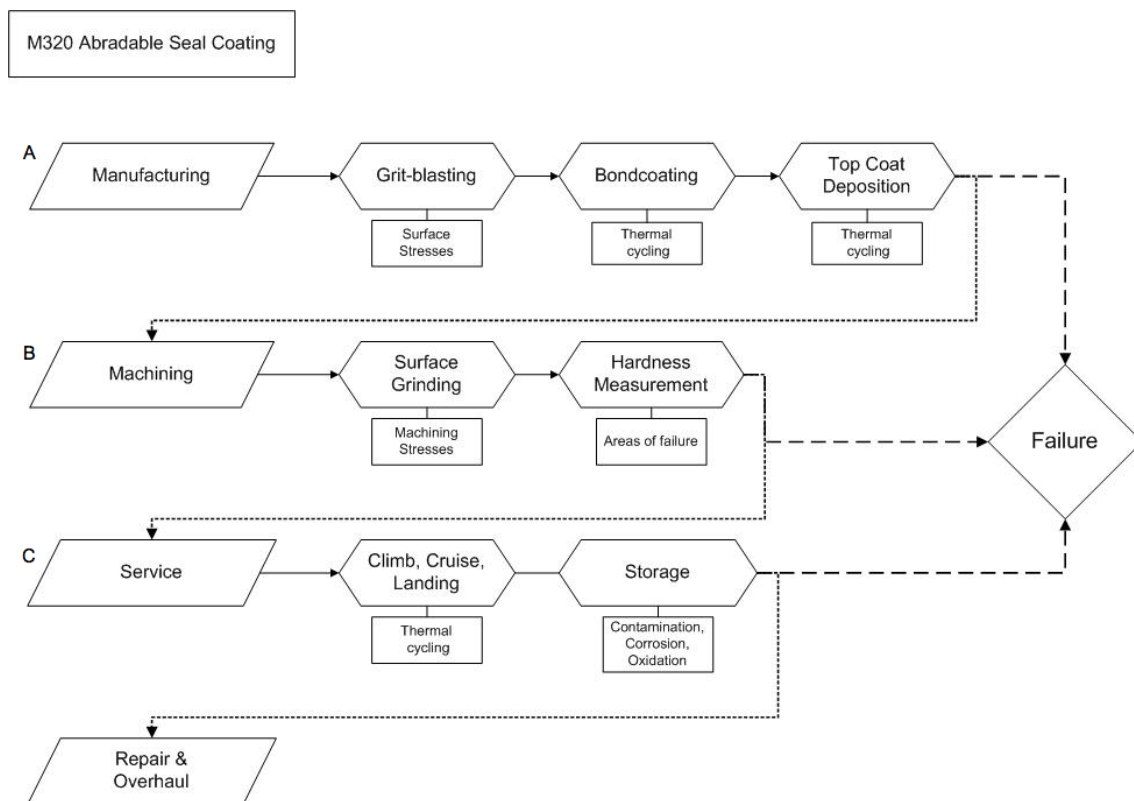


Figure 10.31: Lifetime Model of a M320 Abradable Seal Coating

The material changes documented in this thesis affect the abradable’s properties, which in turn influence the thermal cycling behaviour. Figure 10.31 illustrates the life time of a M320 abradable seal coating, which starts with the grit-blasting process of the cas-

ing, followed by the application of the bond coat and afterwards the abradable top coat. This causes stresses to be introduced into the material. Following surface machining increases the stress state of the surface material further.

Once thermal cycling has been started, the liner is subject to abrasion from the blade tip, which can cause plastic deformation and work-hardening of the material. Cyclic heat exposure initiates material decay through thermal fatigue, which can result in material loss, should cracking and delamination commence quickly.

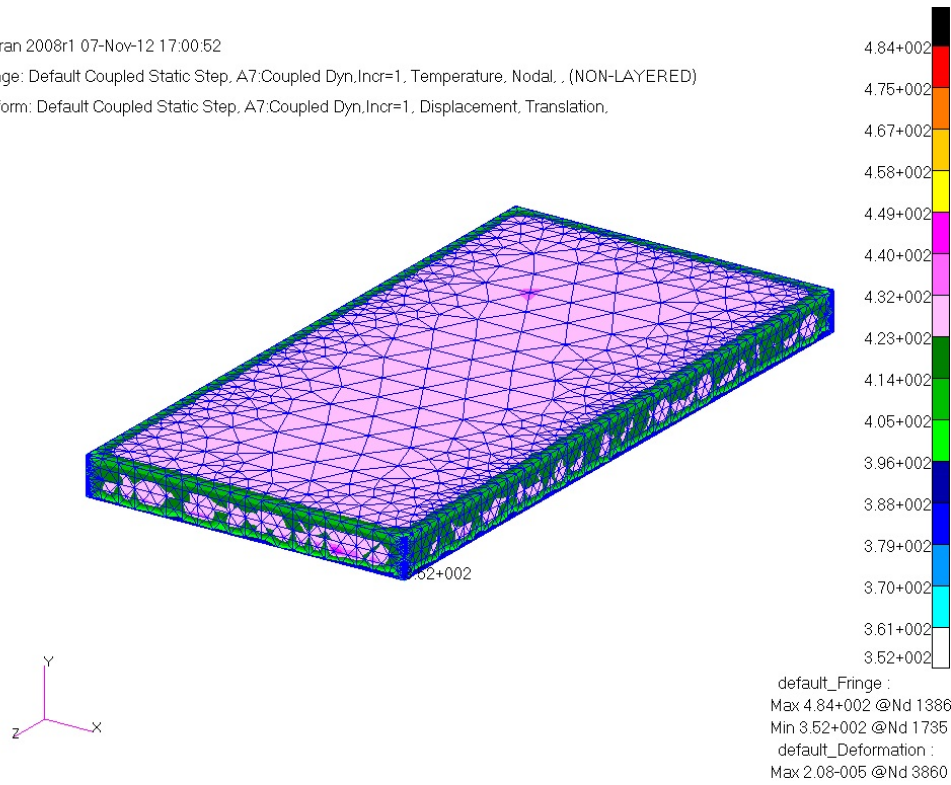
Material parameters, like substrate preparation, abradable hardness and surface machining (see chapter 6), influence the speed of degradation. More  $AlSi$  in the structure, stress relieving the substrate after grit-blasting, back-plate heating during spraying and, if necessary, gentle surface machining have been shown to improve material behaviour. Furthermore, the liner thickness should not exceed  $3\text{ mm}$ . Reducing its thickness would improve the thermal cycling response of M320 further.

3D modelling of the water-quenching process showed the areas of high strain, which were in line with cracking observations made during testing. Highest strain first develop at the edges, where the abradable starts to open and cracking propagates towards the centre of the sample. The peak in strain is documented at  $650\text{ ms}$  after the initial drop of the sample into the quenching bath. These strains decreased once the substrate starts to cool and shrink, therefore relieving the strains applied to the top coat's edges.

Patran 2008r1 07-Nov-12 17:00:52

Fringe: Default Coupled Static Step, A7:Coupled Dyn,Incr=1, Temperature, Nodal, (NON-LAYERED)

Deform: Default Coupled Static Step, A7:Coupled Dyn,Incr=1, Displacement, Translation,

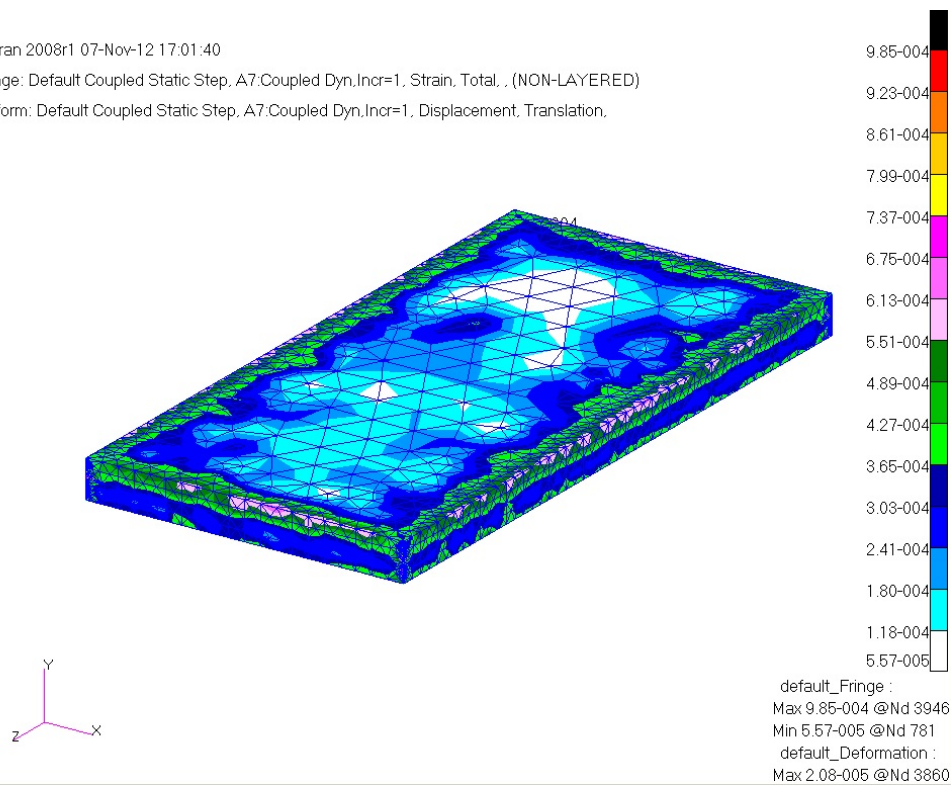


(a) Thermal Profile

Patran 2008r1 07-Nov-12 17:01:40

Fringe: Default Coupled Static Step, A7:Coupled Dyn,Incr=1, Strain, Total, (NON-LAYERED)

Deform: Default Coupled Static Step, A7:Coupled Dyn,Incr=1, Displacement, Translation,



(b) Strain Profile

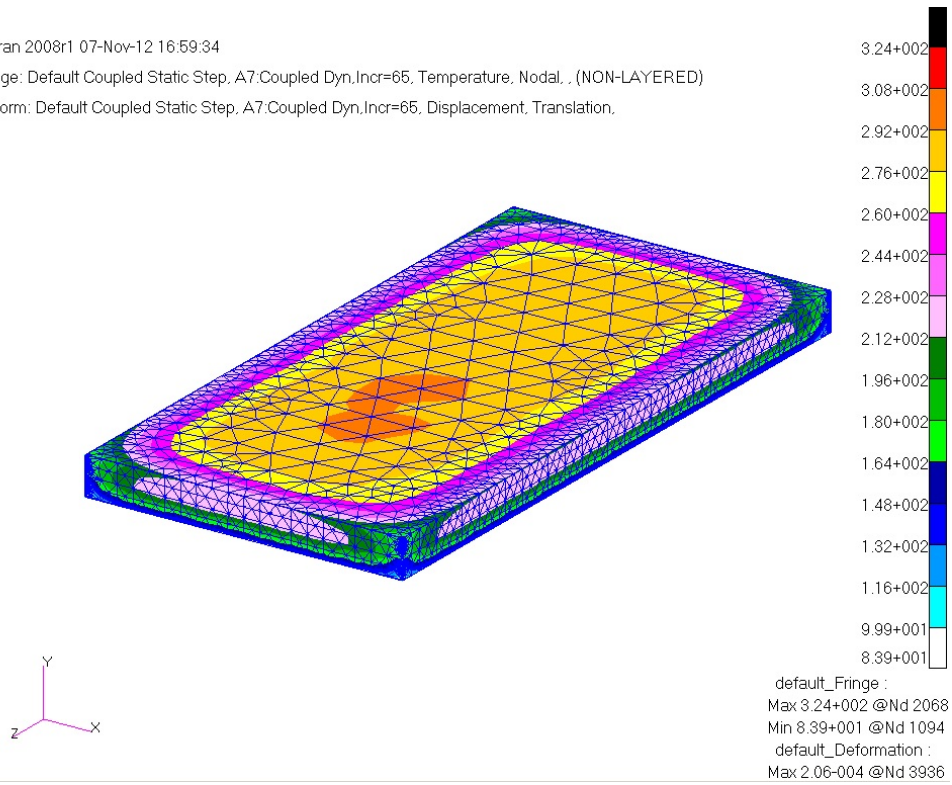
Figure 10.32: Initial Drop of the Sample into the Water Quenching Bath



Patran 2008r1 07-Nov-12 16:59:34

Fringe: Default Coupled Static Step, A7:Coupled Dyn,Incr=65, Temperature, Nodal, . (NON-LAYERED)

Deform: Default Coupled Static Step, A7:Coupled Dyn,Incr=65, Displacement, Translation,

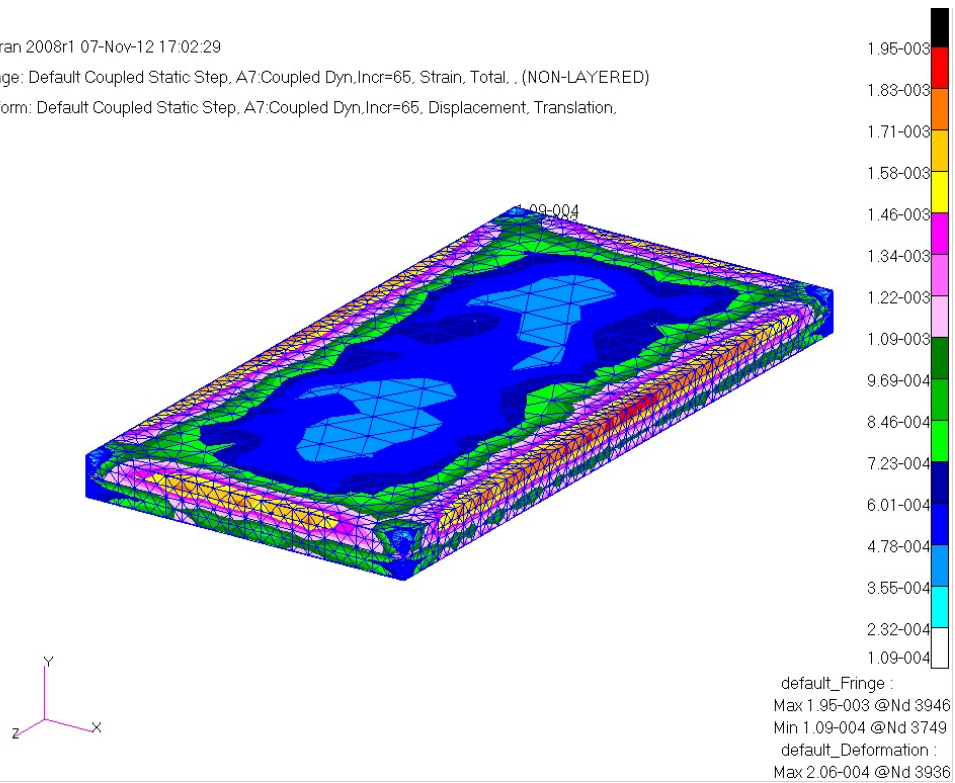


(a) Thermal Profile

Patran 2008r1 07-Nov-12 17:02:29

Fringe: Default Coupled Static Step, A7:Coupled Dyn,Incr=65, Strain, Total, . (NON-LAYERED)

Deform: Default Coupled Static Step, A7:Coupled Dyn,Incr=65, Displacement, Translation,



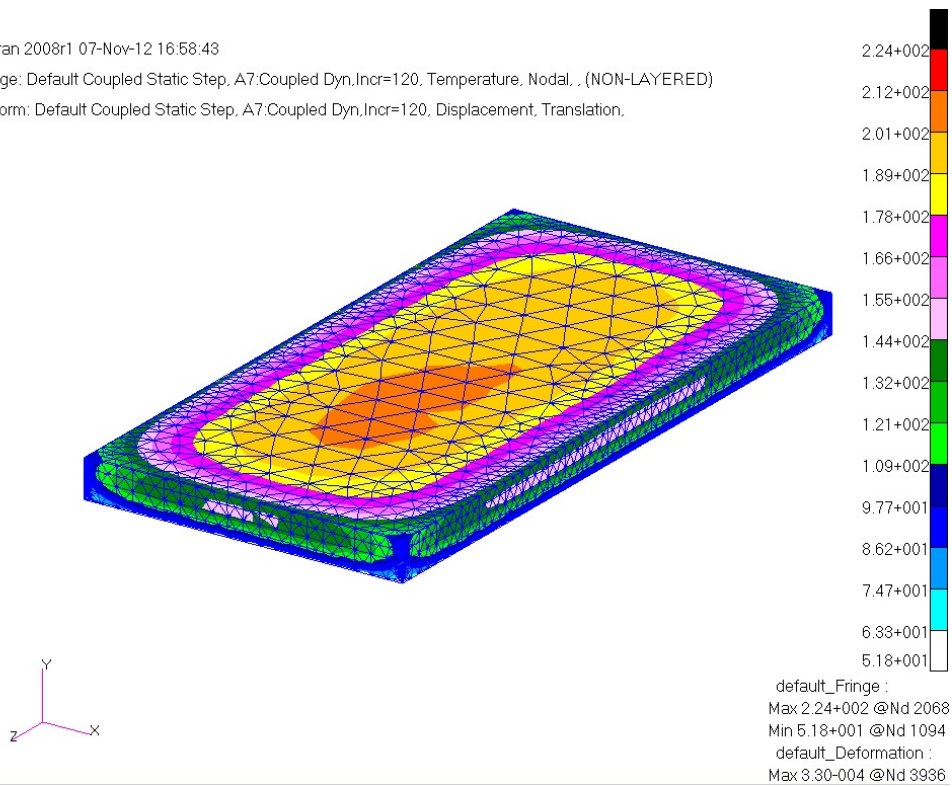
(b) Strain Profile

Figure 10.33: 650ms after the Drop into Water

Patran 2008r1 07-Nov-12 16:58:43

Fringe: Default Coupled Static Step, A7:Coupled Dyn,Incr=120, Temperature, Nodal, . (NON-LAYERED)

Deform: Default Coupled Static Step, A7:Coupled Dyn,Incr=120, Displacement, Translation,

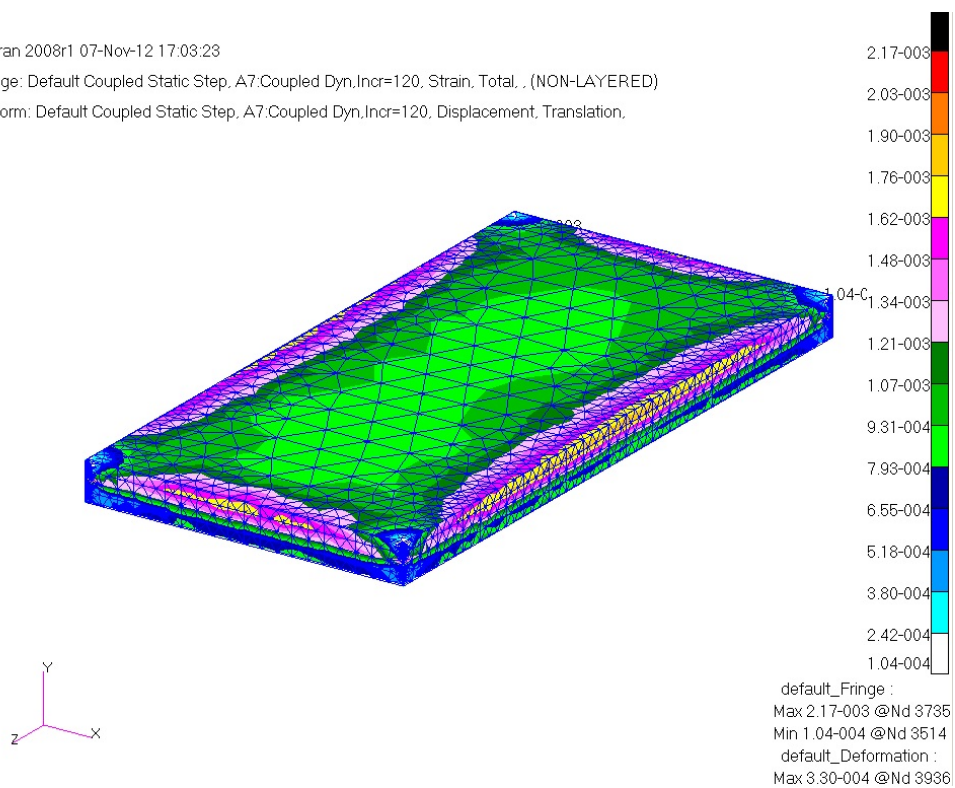


(a) Thermal Profile

Patran 2008r1 07-Nov-12 17:03:23

Fringe: Default Coupled Static Step, A7:Coupled Dyn,Incr=120, Strain, Total, . (NON-LAYERED)

Deform: Default Coupled Static Step, A7:Coupled Dyn,Incr=120, Displacement, Translation,



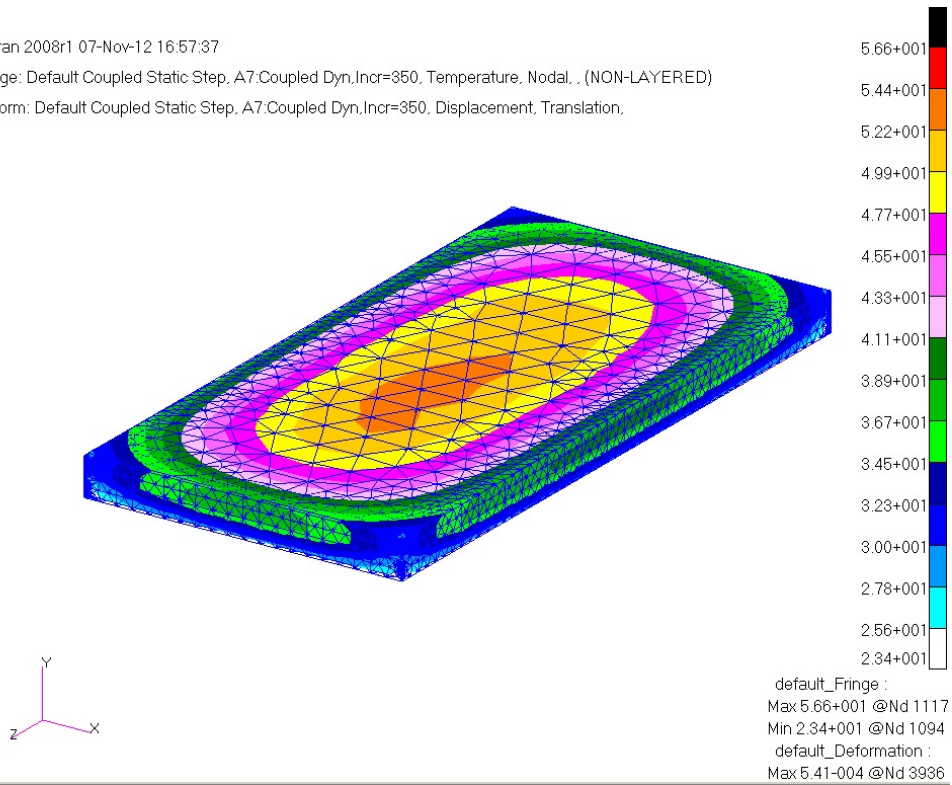
(b) Strain Profile

Figure 10.34: 1.2s after the Drop into Water

Patran 2008r1 07-Nov-12 16:57:37

Fringe: Default Coupled Static Step, A7:Coupled Dyn,Incr=350, Temperature, Nodal, . (NON-LAYERED)

Deform: Default Coupled Static Step, A7:Coupled Dyn,Incr=350, Displacement, Translation,

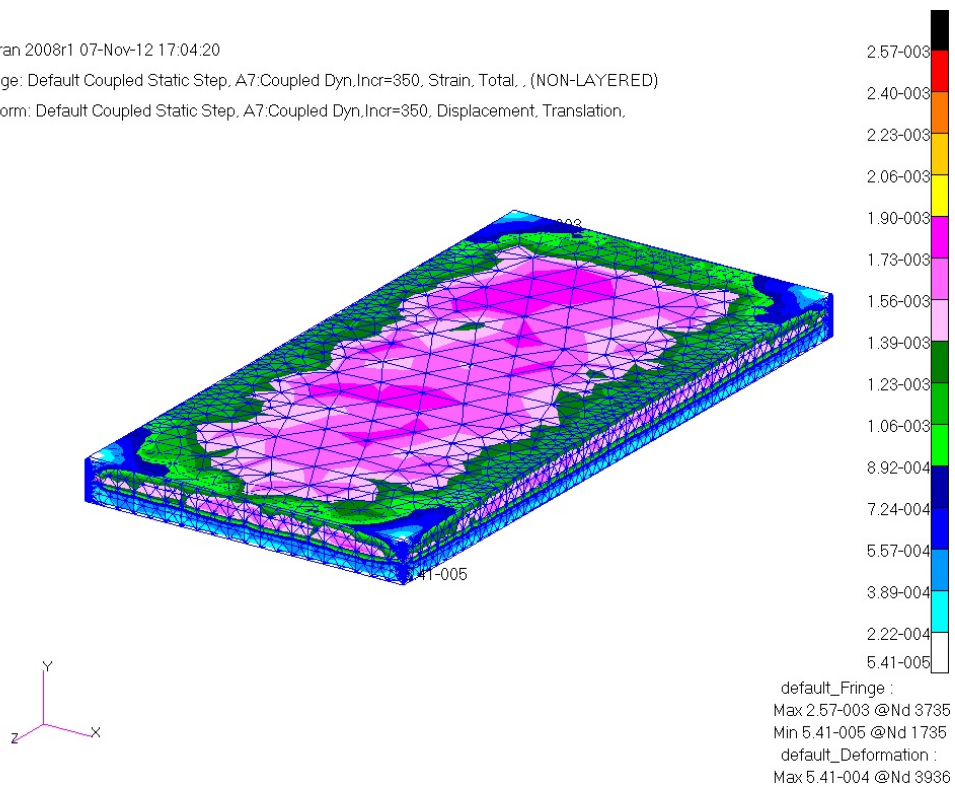


(a) Thermal Profile

Patran 2008r1 07-Nov-12 17:04:20

Fringe: Default Coupled Static Step, A7:Coupled Dyn,Incr=350, Strain, Total, . (NON-LAYERED)

Deform: Default Coupled Static Step, A7:Coupled Dyn,Incr=350, Displacement, Translation,



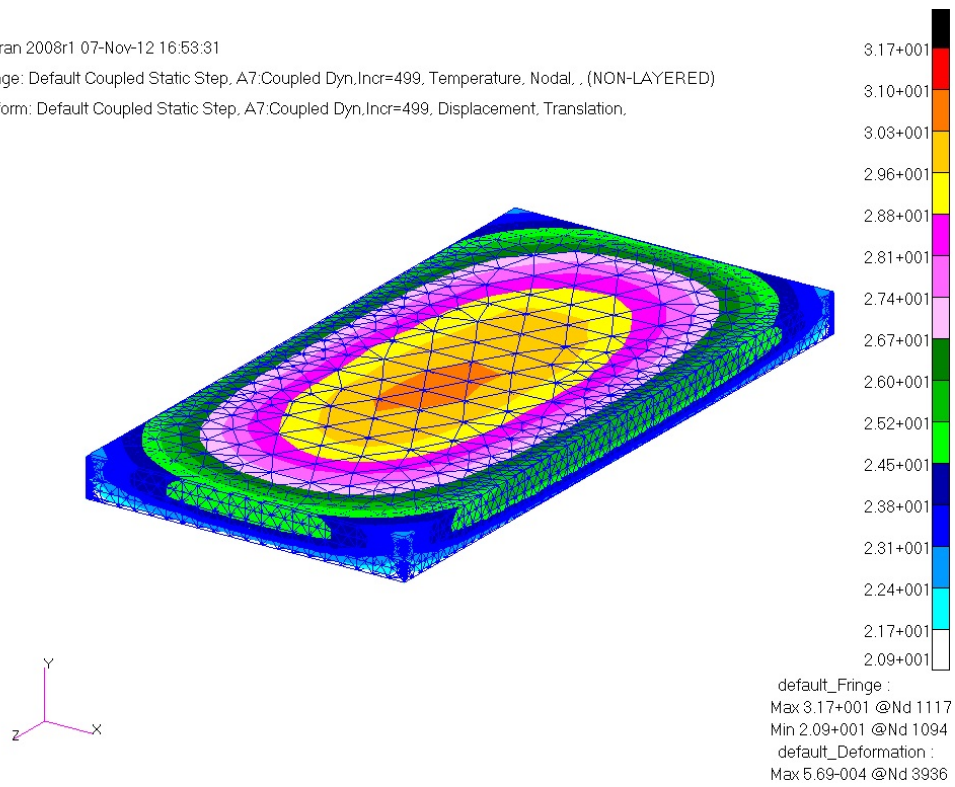
(b) Strain Profile

Figure 10.35: 3.5s after the Drop into Water

Patran 2008r1 07-Nov-12 16:53:31

Fringe: Default Coupled Static Step, A7:Coupled Dyn,Incr=499, Temperature, Nodal, . (NON-LAYERED)

Deform: Default Coupled Static Step, A7:Coupled Dyn,Incr=499, Displacement, Translation,

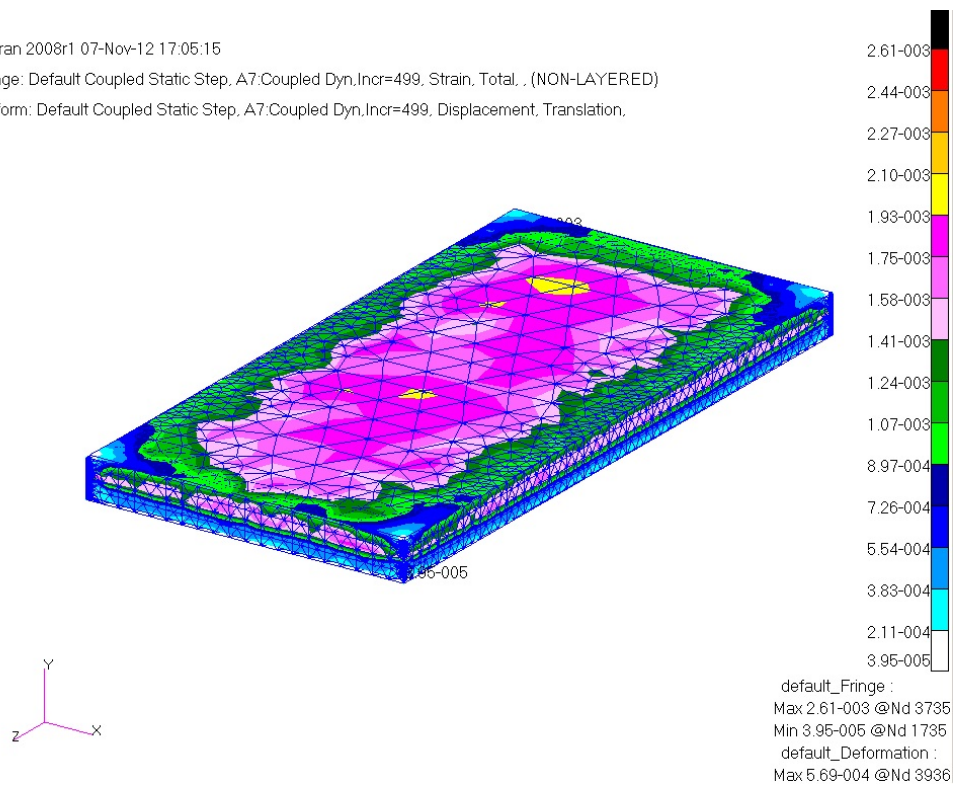


(a) Thermal Profile

Patran 2008r1 07-Nov-12 17:05:15

Fringe: Default Coupled Static Step, A7:Coupled Dyn,Incr=499, Strain, Total, . (NON-LAYERED)

Deform: Default Coupled Static Step, A7:Coupled Dyn,Incr=499, Displacement, Translation,



(b) Strain Profile

Figure 10.36: 5s after the Drop into Water

## Chapter 11

# Conclusion

Metco 320 abradable seal coating is used extensively in the high pressure compressor in commercial gas turbines. The  $\Delta\alpha\Delta T$  mismatch between the casing and the liner material leads to stresses building up in the abradable, which leads to cracking, delamination and material loss.

Test methods to simulate the failure modes of abradable seal material Metco 320 have been established during this research project. The cyclic water-quenching process has been used to re-produce the dominant failure mode - mudflat cracking - in the laboratory for the first time.

Alongside the mechanical challenge the material is subjected to, the liner degrades, as a result of the working temperature and environment. Heat cycling the abradable between  $-40 \rightarrow 450^\circ C$  allows for material softening and sintering of the individual *AlSi* particles deposited during spraying. The sintering process enables the liner to built up a network of metal matrix.

Analysing the heat-cycled material, shows the formation of two layers,  $X_1$  on the top and  $X_2$  on the bottom, which reveal a different microstructure. The  $X_1$ -layer describes those parts of the coating where a network of metal matrix has been formed and the *hBN* is isolated in individual particles. The  $X_2$ -layer are those subsurface layers, which still show the as sprayed microstructure.

With increasing number of cycles, the metal network grows and the *hBN* phase is removed from the abradable material, leaving behind a very brittle, very porous structure of *AlSi*. This remaining skeleton metal matrix is extremely sensitive to erosion with  $X_1$  eroding at approximately twice the rate of the lower  $X_2$  material.

During scratch testing, the performance of the growing surface layer was assessed, by

analysing the cross sections of the scratch scars. With increasing thickness of  $X_1$  during scratch testing, a shallower scar is left on the surface of the material.

Over the duration of this project, it was established, that hard coatings perform better than soft abrasives. With more metal matrix material, a thicker, more resilient structure can form during the sintering process, ensuring better performance of the abrasible during service.

Too much metal matrix, on the other hand, makes the abrasible too hard and blade damage occurs due to the rub interaction between the blade and the seal. The current specification for M320 states a HR15Y hardness between  $50 \rightarrow 70$ ; following the results from this research project, aiming at the higher end of that hardness range would be beneficial for the material's performance.

To minimise cracking and material loss during service, the residual stresses in the casing-bondcoat-abrasible system need to be kept as low as possible. The grit-blasting process introduces mechanical stresses into the surface of the substrate; these could be reduced by heating the casing to annealing temperature before the bondcoat is applied. Also, it was previously found that higher pressure and shorter times are to be preferred over long lasting low pressure grit blasting. So fast, hard grit blasting, with a subsequent annealing stage is recommended.

The analysis of the transient influence upon the failure of the abrasible top coat revealed a great change in the material response to thermal cycling. Substrate materials with Biot numbers close to the abrasible's end up bending concavely, whereas substrates with higher Biot numbers show cracking and delamination. Also, the substrate thickness showed influence upon the thermal cycling failures. Thinner substrates showed fine cracking with total crack lengths of up to  $130 \text{ mm}$  and thick substrates measure a total crack length of up to  $200 \text{ mm}$ .

RFDA analysis showed variability in the Young's Modulus over the material's temperature range. With increasing temperature the Young's modulus reduces, but increases again when cooling down. The cracked free standing samples were cracked, which delivered unreliable data for heat treated material, but as-sprayed samples showed the variability in Young's modulus.

Modelling has shown that, even though the abrasible is sprayed into an enclosed casing, the material will start to delaminate off the walls and the bottom, along with the surface cracking. The difference in thermal expansion between the substrate and the abrasible, as well as the creep relaxing of the abrasible during cruise, enables the opening of the interface between the liner and the casing. Also, with increasing  $\Delta\alpha\Delta T$  mismatch cracking

commences quicker.

## Chapter 12

# Further Work

After the investigations carried out during this research project, many questions are still unanswered. Further efforts should be made to understand the effects of grit-blasting onto the failure behaviour of the abradable material. Annealing substrates before and after grit-blasting should be analysed in order to see, whether crack patterns will change.

Furthermore, the substrates grit-blasted in the preparation should be investigated as a function of the thickness of the material affected by the process. The dependency of that thickness upon the force of the grit-blasting process, its time and speed, should be evaluated.

The effect of the grit-blasting stage of the sample manufacturing is also important during thermal cycling of different substrate materials. The transient analysis carried out showed a crucial dependency of the failure mechanisms upon the Biot number. This will have to be verified in further tests, in which the substrates are stress-free, when the abradable top coat is applied. This will show, if the deformations witnessed during testing is due to stresses in the abradable, in the substrate or in both.

The thermal stresses introduced into the material during plasma spraying need to be analysed. Since each layer of deposited material generates stresses during the cooling of the splats, it needs to be analysed, how these stresses will change should back-plate heating be applied.

The machining process of the surface introduces a layer of compacted material and causes crack initiation in subsurface layers. Ways of surface treatment, avoiding material compaction should be investigated, in order for the cracks to initiate at the surface and grow through the coating.

Heat cycling the substrate/abradable combination causes creep relaxing and cracking



of the top coat. Samples for analysis are flat squares, which can deform and have free edges. Both parameters affect the material failure and vary the laboratory set-up from the service conditions. Rings of abradable material should be tested for all the stages of the material preparation process, as well as heat cycling closed and coated rings.

After grit-blasting of a ring, one should be cut open to see how it deforms, indicating the stresses in the material, which can not be relieved and are present in the substrate, once the abradable is deposited. Also, a possible crack pattern during heat cycling should be documented and compared to cracking of the material in an annealed ring.

The formation of  $X_1$  and  $X_2$  layers and the removal of  $hBN$  needs to be investigated. Theories of the material changes have been presented, but they need to be proved or dismissed during further testing. Since the  $hBN$  removal was established as cause of the formation of  $X_1$  and  $X_2$  only towards the end of the project, further analysis into the mechanisms was impossible.

Material testing showed, that the material changes greatly during heat exposure. RFDA and hot hardness was applied during this project, which delivered good results for an initial assessment of the changes taking place and how that might affect service. The research into the RFDA and hot hardness should be intensified and more detailed test plans with changing material age is needed.

Indentation testing was investigated and delivered interesting insights into the cyclic nature of the abradable's deterioration. Since the machine used for the indents was the scratch tester, no proper data were recorded to calculate Plasticity Indices. These would give another insight into the material behaviour during heat cycling.

The scratch testing carried out during this project was subject to faulty measurements being recorded due to a misalignment of the displacement sensor. This was discovered only weeks before the project finished and attempts to reassess some material failed. It could be established that the loading of the sample was interfered by friction occurring in the z-displacement sensor, which was interpreted as load on the surface. A new testing plan needs to be established to prove or dismiss the theories stated in this report.

## References

- [1] Robert C. Bill and Lawrence P. Ludwig. Wear of seal materials used in aircraft propulsion systems. *Wear*, 59(1):165–189, 3/1 1980.
- [2] R. K. Schmid, F. Ghasripor, M. Dorfman, and X. Wei. An overview of compressor abrasives. In C.C.Berndt, editor, *Thermal Spray Surface Engineering via Applied Research, Proceedings, 1st International Thermal Spray Conference (ITSC 2000), Montreal, Quebec, Canada; 8-11 May 2000*, pages 1087–1093, OH 44073-0002, USA; ASM International, 2000. SULZER INNOTECH LTD, Materials Park.
- [3] Sulzer Metco. Solution flash - cause and effect of metco 320ns spray parameters for optimisation of coating hardness and service life, Sulzer Metco, April 2008.
- [4] Maozhong Yi, Jiawen He, Baiyun Huang, and Huijiu Zhou. Friction and wear behaviour and abrasibility of abrasible seal coating. *Wear*, 231(1):47–53, 6 1999/6//.
- [5] Hougong Wang. Criteria for analysis of abrasible coatings. *Surface and Coatings Technology*, 79(1-3):71–75, 2 1996.
- [6] M. Bounazef, S. Guessasma, and B. Ait Saadi. The wear, deterioration and transformation phenomena of abrasible coating on-sial-bonding organic element, caused by the friction between the blades and the turbine casing. *Materials Letters*, 58(27-28):3375–3380, 11 2004.
- [7] G. Sutter, S. Philippon, and F. Garcin. Dynamic analysis of the interaction between an abrasible material and a titanium alloy. *Wear*, 261(5-6):686–692, 9 2006.
- [8] M. O. Borel, A. R. Nicoll, H. W. Schläpfer, and R. K. Schmid. The wear mechanisms occurring in abrasible seals of gas turbines. *Surface and Coatings Technology*, 39-40:117–126, 12/1 1989.
- [9] W. F. Laverty. Rub energetics of compressor blade tip seals. *Wear*, 75(1):1–20, 1/1 1982.
- [10] F. Ghasripor, R. K. Schmid, M. R. Dorfman, and L. Russo. A review of clearance control wear mechanisms for low temperature aluminium silicon alloys. In C.Coddet, editor, *Thermal Spray - Meeting the Challenges of the 21st Century*,

- Proceedings, 15th International Thermal Spray Conference, Nice, France, Vol.1; 25-29 May 1998, pages 139–144, OH 44073-0002, USA; ASM International, 1998. SULZER INNOTECH LTD, Materials Park.*
- [11] R. Zenas, T. Archbold, J. Wolak, A. F. Emery, and S. Etemad. Metallurgical and mechanical phenomena due to rubbing of titanium against sintered powder nichrome. *Annual Meeting; Chicago, Ill ; U.S.A ; 7-10 May 1984. 7 pp. 1984 1984. NU: Preprint No. 84-AM-8A-1; ML: Ti-6Al-4V; Nichrome.*
- [12]
- [13] Mitchell Dorfman, Ulrich Erning, and James Mallon. Gas turbines use ‘abradable’ coatings for clearance-control seals. *Sealing Technology,, 2002(1):7–8, 1 2002.*
- [14] Jeanine T. DeMasi-Marcin and Dinesh K. Gupta. Protective coatings in the gas turbine engine. *Surface and Coatings Technology, 68-69:1–9, 12 1994.*
- [15] R. E. Chupp, F. Ghasripoor, G. D. Moore, L. S. Kalv, and J. R. Johnston. Applying abradable seals to industrial gas turbines. In *38th Joint Propulsion Conference and Exhibition. General Electric, July 7-10 2002.*
- [16] Alternative methods for determination of composition and porosity in abradable materials. *Materials Characterization, 57(1):17–29, 7 2006.*
- [17] H. I. Faraoun, T. Grosdidier, J. L. Seichepine, D. Goran, H. Aourag, C. Coddet, J. Zwick, and N. Hopkins. Improvement of thermally sprayed abradable coating by microstructure control. *Surface and Coatings Technology,, 201(6):2303–2312, 12/4 2006.*
- [18] M. J. Pomeroy. Coatings for gas turbine materials and long term stability issues. *Materials and Design,, 26(3):223–231, 5 2005.*
- [19] Gottfried Laschet, Stephan Rex, Dieter Bohn, and Norbert Moritz. *3-D conjunction analysis of cooled coated plates and homogenization of their thermal properties, volume 42, pages 91–106. 2002.*
- [20] Richard Karl Schmid. *New High temperature Abradables for Gas Turbines. PhD thesis, 1997.*
- [21] H. I. Faraoun, J. L. Seichepine, C. Coddet, H. Aourag, J. Zwick, N. Hopkins, D. Sporer, and M. Hertter. Modelling route for abradable coatings. *Surface and Coatings Technology,, 200(22-23):6578–6582, 6/20 2006.*
- [22] Mokhtar Bounazef, Sofiane Guessasma, Ghislain Montavon, and Christian Coddet. Effect of aps process parameters on wear behaviour of alumina–titania coatings. *Materials Letters, 58(20):2451–2455, 8 2004.*

- [23] C. Sellars, D. Sansom, T. Rose, and R. E. Johnston. Mace d1-1 understanding and quantification of abradable performance drivers. Technical Report STC30185, Rolls-Royce, Materials, 2006.
- [24] A. F. Emery, J. Wolak, S. Etemad, and S. R. Choi. An experimental investigation of temperatures due to rubbing at the blade-seal interface in an aircraft compressor. *Wear*, 91(2):117–130, 11/1 1983.
- [25] M. A. Clegg and M. H. Mehta. Nicral/bentonite thermal spray powder for high temperature abradable seals. *Surface and Coatings Technology*, 34(1):69–77, 1 1988.
- [26] Ed F. Rejda, Darrell F. Socie, and Takamoto Itoh. Deformation behavior of plasma-sprayed thick thermal barrier coatings. *Surface and Coatings Technology*, 113(3):218–226, 3 1999.
- [27] S. C. Lim, M. F. Ashby, and J. H. Brunton. Wear-rate transitions and their relationship to wear mechanisms. *Acta Metallurgica*, 35(6):1343–1348, 6 1987.
- [28] O. Trunova, T. Beck, R. Herzog, R. W. Steinbrech, and L. Singheiser. Damage mechanisms and lifetime behavior of plasma sprayed thermal barrier coating systems for gas turbines—part i: Experiments. *Surface and Coatings Technology*, 202(20):5027–5032, 7 2008.
- [29] Dieter Sporer, Arno Refke, Marian Dratwinski, Mitch Dorfman, Sulzer Metco, Iacopo Giovannetti, Massimo Giannozzi, and Manuele Bigi. New high-temperature seal system for increased efficiency of gas turbines. *Sealing Technology*, 2008(10):9–11, 10 2008.
- [30] Roy McIntyre. Plasma sprayed coatings versus high velocity oxy fuel processes. *Materials World*, 4(8):455–457, 1996.
- [31] E. Lugscheider and T. Weber. Plasma spraying - an innovative coating technique: Process variants and applications. *IEEE Transactions on Plasma Science*, 18(6):968–973, December 1990 1990.
- [32] E. Lugscheider, J. Zwick, H. Hertter, and D. Sporer. Control of coating properties of abradable seals by on-line process diagnostics. In *Thermal Spray Connects: Explore its Surfacing Potential. Proceedings, International Thermal Spray Conference and Exposition (ITSC 2005), Basel, Switzerland, 2-4 May 2005*. MTU AERO ENGINES GMBH. GERMANY, 40010 Düsseldorf, Germany; DVS-Verlag, for Deutscher Verband für Schweißen und verwandte Verfahren; 2005. ISBN 3-87155-793-5, 2005.
- [33] *Introduction to Thermal Spray Processing*. ASM International # 06994G, www.asminternational.org, 2004.

- [34] Sanjay Sampath. Microstructural characteristics of plasma spray consolidated amorphous powders. *Materials Science and Engineering: A*, 167(1-2):1–10, 8 1993.
- [35] U. Bardi, C. Giolli, A. Scrivani, G. Rizzi, F. Borgioli, A. Fossati, K. Partes, T. Seefeld, D. Sporer, and A. Refke. Development and investigation on new composite and ceramic coatings as possible abradable seals. *Journal of Thermal Spray Technology*, 17:805–811, 2008. 10.1007/s11666-008-9246-5.
- [36] E. Novinski, J. Harrington, and J. Klein. Modified zirconia abradable seal coating for high temperature gas turbine applications. volume San Diego, CA, 1982.
- [37] W. Smarsly, N. Zheng, D. Sporer, M. Tuffs, K. Schreiber, H. Goehler, N. Simms, and G. McColvin. Advanced high temperature turbine seals materials and designs. *Materials Science Forum*, 492-493(Trans Tech Publications, Switzerland 2005):21–26, 2005.
- [38] P. Fauchais. Understanding plasma spraying. *Journal of Physics D*, 37:R86–R108, 2004.
- [39] S. J. Bull, D. S. Rickerby, A. Matthews, A. Leyland, A. R. Pace, and J. Valli. The use of scratch adhesion testing for the determination of interfacial adhesion: The importance of frictional drag. *Surface and Coatings Technology*, 36(1-2):503–517, 12 1988/12/1/.
- [40] Jan Wigren. Technical note: Grit blasting as surface preparation before plasma spraying. *Surface and Coatings Technology*, 34(1):101–108, 1 1988.
- [41] K. Poorna Chander, M. Vashista, Kazi Sabiruddin, S. Paul, and P. P. Bandyopadhyay. Effects of grit blasting on surface properties of steel substrates. *Materials & Design*, 30(8):2895–2902, 9 2009.
- [42] M. H. Staia, E. Ramos, A. Carrasquero, A. Roman, J. Lesage, D. Chicot, and G. Mesmacque. Effect of substrate roughness induced by grit blasting upon adhesion of wc-17% co thermal sprayed coatings. *Thin Solid Films*, 377-378:657–664, 12 2000.
- [43] A. Nusair Khan, J. Lu, and H. Liao. Effect of residual stresses on air plasma sprayed thermal barrier coatings. *Surface and Coatings Technology*, 168(2-3):291–299, 5 2003.
- [44] Shigeyasu Amada and Tohru Hirose. Influence of grit blasting pre-treatment on the adhesion strength of plasma sprayed coatings: fractal analysis of roughness. *Surface and Coatings Technology*, 102(1-2):132–137, 4 1998.

- [45] M. Mellali, P. Fauchais, and A. Grimaud. Influence of substrate roughness and temperature on the adhesion/cohesion of alumina coatings. *Surface and Coatings Technology*, 81(2-3):275–286, 6 1996.
- [46] tset advanced equipment refurbishment services. <http://www.tsetinc.com/ceramicoat.htm>, August 2012.
- [47] R. Johnston. The sensitivity of abradable coating residual stresses to varying material properties. *Journal of Thermal Spray Technology*, 18:1004–1013, 2009. 10.1007/s11666-009-9378-2.
- [48] P. Fauchais, M. Fukumoto, A. Vardelle, and M. Verdelle. Knowledge concerning splat formation: An invited review. *Journal of Thermal Spray Technology*, 13(3):337–360, 2004.
- [49] Yi Maozhong, Huang Baiyun, and He Jiawen. Erosion wear behaviour and model of abradable seal coating. *Wear*, 252(1-2):9–15, 1 2002.
- [50] D. L. Clingman, B. Schechter, K. R. Cross, and J. R. Cavanagh. Material removal considerations for metal/ceramic abradable turbine seal systems. *Lubr.Eng*, 39(11):712–716, Nov. 1983.
- [51] Y. Nava, Z. Mutasim, and M. Coe. Abradable coatings for low-temperature applications. In K. A. Khor and E. F. Lugscheider C.C.Berndt, editors, *Thermal Spray 2001. New Surfaces for a New Millennium, Proceedings, International Thermal Spray Conference (ITSC 2001), Singapore; 28-30 May 2001*, pages 263–268, OH 44073-0002, USA; ASM International, 2001. SOLAR TURBINES INC. USA, Materials Park.
- [52] M. Borri-Brunetto, A. Carpinteri, and S. Invernizzi. Characterization and mechanical modeling of the abrasion properties of sintered tools with embedded hard particles. *Wear*, 254(7-8):635–644, 4 2003.
- [53] N. X. Zheng, M. A. Daeubler, K. K. Schweitzer, W. Hensle, and H. Schlegel. Development of air seal systems for modern jet engines. *MTU Aero Engines GmbH, Dachauer Str. 665, 80995 Muenchen*.
- [54] J. M. Guilemany, J. Navarro, C. Lorenzana, S. Vizcaino, and J. M. Miguel. Tribological behaviour of abradable coatings obtained by atmospheric plasma spraying (aps). In K. A. Khor and E. F. Lugscheider C.C.Berndt, editors, *Thermal Spray 2001. New Surfaces for a New Millennium, Proceedings, International Thermal Spray Conference (ITSC 2001), Singapore; 28-30 May 2001*, pages 1115–1118, OH 44073-0002, USA; ASM International, 2001. UNIVERSITY OF BARCELONA. SPAIN, Materials Park.

- [55] J. W. H. Price, B. Kerezsi, and M. Chang. Thermal shock cracking guidelines for acceptance in service. *Engineering Failure Analysis*, 11(2):267–277, 4 2004.
- [56] Jie-Cai Han and Bao-Lin Wang. Thermal shock resistance enhancement of functionally graded materials by multiple cracking. *Acta Materialia*, 54(4):963–973, 2 2006.
- [57] Wangang Xie, Eric Jordan, and Maurice Gell. Stress and cracking behavior of plasma sprayed thermal barrier coatings using an advanced constitutive model. *Materials Science and Engineering: A*, 419(1-2):50–58, 3 2006.
- [58] T. E. Strangman. Thermal strain-tolerant abradable thermal barrier coatings. *Journal of Engineering for Gas Turbines and Power*, 114(April 1992):264–267, 1992.
- [59] S. Asghari and M. Salimi. Finite element simulation of thermal barrier coating performance under thermal cycling. *Surface and Coatings Technology*, In Press, Corrected Proof:–.
- [60] H. B. Guo, R. Vassen, and D. Stoeber. Atmospheric plasma sprayed thick thermal barrier coatings with high segmentation crack density. *Surface and Coatings Technology*, 186(3):353–363, 9 2004.
- [61] L. Fu, K. A. Khor, H. W. Ng, and T. N. Teo. Non-destructive evaluation of plasma sprayed functionally graded thermal barrier coatings. *Surface and Coatings Technology*, 130(2-3):233–239, 8 2000.
- [62] K. W. Schlichting, N. P. Padture, E. H. Jordan, and M. Gell. Failure modes in plasma-sprayed thermal barrier coatings. *Materials Science and Engineering A*, 342(1-2):120–130, 2 2003.
- [63] M. Y. He, J. W. Hutchinson, and A. G. Evans. Simulation of stresses and delamination in a plasma-sprayed thermal barrier system upon thermal cycling. *Materials Science and Engineering A*, 345(1-2):172–178, 3 2003.
- [64] Zhenghao Gan, Heong Wah Ng, and Appuswamy Devasenapathi. Deposition-induced residual stresses in plasma-sprayed coatings. *Surface and Coatings Technology*, 187(2-3):307–319, 10 2004/10/22/.
- [65] S. Takeuchi, M. Ito, and K. Takeda. Modelling of residual stress in plasma-sprayed coatings: Effect of substrate temperature. *Surface and Coatings Technology*, 43-44(Part 1):426–435, 12 1990.
- [66] R. Elsing, O. Knotek, and U. Balting. Calculation of residual thermal stress in plasma-sprayed coatings. *Surface and Coatings Technology*, 43-44(Part 1):416–425, 12 1990.

- [67] S. Kuroda and T. W. Clyne. The quenching stress in thermally sprayed coatings. *Thin Solid Films*, 200(1):49–66, 5 1991.
- [68] H. W. Ng and Z. Gan. A finite element analysis technique for predicting as-sprayed residual stresses generated by the plasma spray coating process. *Finite Elements in Analysis and Design*, 41(13):1235–1254, 7 2005.
- [69] D. S. Rickerby, G. Eckold, K. T. Scott, and I. M. Buckley-Golder. The interrelationship between internal stress, processing parameters and microstructure of physically vapour deposited and thermally sprayed coatings. *Thin Solid Films*, 154(1-2):125–141, 11 1987.
- [70] M. Lugovy, V. Slyunyayev, and V. Teixeira. Residual stress relaxation processes in thermal barrier coatings under tension at high temperature. *Surface and Coatings Technology*, 184(2-3):331–337, 6 2004.
- [71] G. Qian, T. Nakamura, and C. C. Berndt. Effects of thermal gradient and residual stresses on thermal barrier coating fracture. *Mechanics of Materials*, 27(2):91–110, 2 1998.
- [72] W. G. Mao, Y. C. Zhou, L. Yang, and X. H. Yu. Modeling of residual stresses variation with thermal cycling in thermal barrier coatings. *Mechanics of Materials*, 38(12):1118–1127, 12 2006.
- [73] Takashi Wakui, Jrgen Malzbender, and Rolf W. Steinbrech. Mechanical testing of thermally stressed materials with rough interfaces: Mechanically induced delamination cracking in thermal barrier composites. *Surface and Coatings Technology*, 200(18-19):5419–5426, 5 2006.
- [74] A. Portinha, V. Teixeira, J. Carneiro, M. G. Beghi, C. E. Bottani, N. Franco, R. Vassen, D. Stoeber, and A. D. Sequeira. Residual stresses and elastic modulus of thermal barrier coatings graded in porosity. *Surface and Coatings Technology*, 188-189:120–128, 2004.
- [75] T.L. Alford J.R. Tucker, B. Abbott. Residual stress reduction for air plasma sprayed al-si abrasable coatings. *TMS - The Minerals, Metals and Materials Society*, Supplemental Proceedings, Vol. 3:General Paper Selection, 249–255, 2009.
- [76] Y.C. Tsui and T.W. Clyne. An analytical model for predicting residual stresses in progressively deposited coatings part 1: Planar geometry. *Thin Solid Films*, 306(1):23 – 33, 1997.
- [77] P.S. Prevey. Current application of x-ray diffraction residual stress measurement. *Lambda Technologies, ASM International*, Development in Materials Characterization Technologies:103–110, 1996.



- [78] P.S. Prevey. X-ray diffraction residual stress techniques. *Lambda Technologies, Metals Handbook*, American Society for Metals:380–392, 1986.
- [79] P. Prevey. Thermal residual stress relaxation and distortion in surface enhanced gas turbine engine components. *Lambda Technologies, 1st International Induction Heat Treating Symposium*, ASM, Materials Park:3–12, 1998.
- [80] Noel P. Hopkins. *Abradable Coatings - From Black Art, To Materials Science*. PhD thesis, Birmingham University, 2007.
- [81] R. E. Johnston and W. J. Evans. Freestanding abrasible coating manufacture and tensile test development. *Surface and Coatings Technology*, 202(4-7):725–729, 12 2007.
- [82] R. E. Johnston. Mechanical characterisation of alsi-hbn, nicral-bentonite, and nicral-bentonite-hbn freestanding abrasible coatings. *Surface and Coatings Technology*, 205, Iss. 10:3268–3273, 2011.
- [83] Xiao Ma and Allan Matthews. Investigation of abrasible seal coating performance using scratch testing. *Surface and Coatings Technology*, 202(4-7):1214–1220, 12 2007.
- [84] K. Venkateswarlu, Gautam Das, A.K. Pramanik, Cheng Xu, and Terence G. Langdon. Using ball-indentation to evaluate the properties of an ultrafine-grained al-2 *Materials Science and Engineering: A*, 427(1-2):188 – 194, 2006.
- [85] P. Agee. *Instrumented Indentation Testing with the Agilent Nano Indenter G200*. Agilent Technology, 5990-4905en edition, 2009. [aglient.com/find/nanoindenter](http://aglient.com/find/nanoindenter).
- [86] M.R. VanLandingham. Review of instrumented indentation. *Journal of Research of the National Institute of Standards and Technology*, 108:249–265, 2003.
- [87] P. Leroux. *Breakthrough Indentation Yield Strength Testing*. NANOVEA, 6 Morgan, Ste156, Irvine CA 92618, 2011. [nanovea.com](http://nanovea.com).
- [88] B.D. Beake, G.S. Fox-Rabinovich, S.C. Veldhuis, and S.R. Goodes. Coating optimisation for high speed machining with advanced nanomechanical test methods. *Surface and Coatings Technology*, 203(13):1919 – 1925, 2009.
- [89] P. Morel. Introduction to instrumented indentation testing. Presentation - MTS Nano Instruments Innovation Center Oak Ridge, TN.
- [90] G.M. Hay, J.L.; Pharr. *Instrumented Indentation Testing*. ASM Handbook Nanoin-dentation.
- [91] Jin Yan, Thorsten Leist, Marion Bartsch, and Anette M. Karlsson. On cracks and delaminations of thermal barrier coatings due to indentation testing: Experimental investigations. *Acta Materialia*, 56(15):4080 – 4090, 2008.

- [92] J. Yan, A.M. Karlsson, and X. Chen. Determining plastic properties of a material with residual stress by using conical indentation. *International Journal of Solids and Structures*, 44(11-12):3720 – 3737, 2007.
- [93] G. Pattinson. Assessment of abradable liner from trent 500 - 71089, hpc1 and 2 casing, part number fk13818. Technical Report STC30077, Rolls-Royce, Surface Engineering, 2006.
- [94] G. Pattinson. Assessment of abradable liners from trent 500 engine number 70005/5 hpc 1 and 2 casing. Technical Report STC30095, Rolls-Royce, Surface Engineering, 2006.
- [95] C Sellars. Abradable process excellence - blueprint of understanding update. Technical Report STC30745, Rolls-Royce, Materials, 2009.
- [96] G. Pattinson. Assessment of abradable lining loss from trent 500 71374 exhibiting hpc2 lining loss. Technical Report STC30208, Rolls-Royce, 2007.
- [97] N. Hopkins and C. Sellars. Blueprint of current abradable understanding. Technical report, Rolls-Royce, Surface Engineering, 2005.
- [98] N. Hopkins and D. Sansom. Mace m1-2 definition of the principle mechanics of abradability. Technical Report STC30183, Rolls-Royce, Materials, 2006.
- [99] C. Sellars, J. Leggett, and D. Roth-Ragaraseanu. Compressor coating strategy. Technical Report DNS69565, Rolls-Royce, Materials, 2004.
- [100] G. Pattinson. Assessment of casing section following abradable liner loss from trent 500 71374. Technical Report STC30282, Rolls-Royce, Materials, 2007.
- [101] N. Hopkins. Development of a thermal shock test method for abradable coatings. Technical Report DHC138972, Rolls-Royce plc, 2003.
- [102] S. Purdie, M. Dorfman, K. Harrison, and C. Britton. An aluminium - silicon / boron nitride material for aerospace applications. Technical Report PNR92900, Rolls-Royce plc, 2002.
- [103] RJ Hallifax. Ageing of abradable materials: Metco 601, 313 and 320. Technical Report MFR40690, Rolls-Royce, Materials, 2000.
- [104] PW Voorhees. The theory of ostwald ripening. *Journal of Statistical Physics*, 38:231–252, 1985.
- [105] D. Sansom. Test specification for cyclic life evaluation fo various abradable lining materials. Technical Report STC30411, Rolls-Royce, Materials, 2008.

- [106] R. E. Johnston and W. J. Evans. In-service thermally-induced abradable coating stress/strain prediction: Thermal step model. Technical Report EGR143, MACE, Rolls-Royce, Materials, 2006.
- [107] D. Sansom. Evaluation of scratch testing for use as a process control tool for abradable coatings. Technical Report STC30305, Rolls-Royce plc, 2007.
- [108] AJ Sparks. On the determination of a parameter to predict the thermal shock/fatigue resistance of compressor abradables. Technical Report DNS18674, Rolls-Royce, Materials, 1995.
- [109] Sealcoat Project. Final report - abradable seal coatings and claddings for compressor applications. Contract: G4RD-CT-2002-00707 Project: GRD1-2001-40124-Sealcoat, Rolls-Royce, MTU, Engineering Surfaces International, Institute of plasma physics, Neomet Ltd., Rilla Alvarez y Lopez sa, RWTH Aachen, 2006.
- [110] C. Sellars, J. Nichols, and T. Rose. Mace work package 1 final report (tp/2/et/6/i/10037) - d1-4. Technical Report STC30465, Rolls-Royce, Surface Engineering, 2008.
- [111] D. Sansom. M1-3 mace - establish optimum cutting envelope for current abradable systems. Technical Report STC30184, Rolls-Royce, Materials, 2006.
- [112] WJ Evans RE Johnston. Dti deliverable d1-1: Understanding and quantification of abradable performance drivers. Technical Report MACE Programme, Rolls-Royce, Materials, 2006.
- [113] Mathias Legrand, Alain Batailly, Benoît Magnain, Patrice Cartraud, and Christophe Pierre. Full three-dimensional investigation of structural contact interactions in turbomachines. *Journal of Sound and Vibration*, 331(11):2578 – 2601, 2012.
- [114] Xiao Ma and Allan Matthews. Evaluation of abradable seal coating mechanical properties. *Wear*, 267(9-10):1501–1510, 9 2009.
- [115] Tanja Steinke, Georg Mauer, Robert Vaßen, Detlev Stöver, Dan Roth-Fagaraseanu, and Matthew Hancock. Process design and monitoring for plasma sprayed abradable coatings. *Journal of Thermal Spray Technology*, 19:756–764, 2010. 10.1007/s11666-010-9468-1.
- [116] Yukio Kuroda, Makoto Tadano, Masahiro Sato, Masayuki Niino, Yoichiro Miki, and Akira Konno. Performance and damage evaluation of a regeneratively cooled thrust engine coated with zro2 / ni functionanlity graded materials. 42(3):532–538, 08/1999.
- [117] D.P. Incropera, F.P.; Witt. *Fundamentals of heat and gas transfer*. John Wiley and Sons, 3 edition, 1990.

- [118] J. R. Johnston. Abradable mechanical integrity module: Grit blasting stress approximation methodology. Technical report, Swansea University, Rolls-Royce, 2006.
- [119] Wolfgang Bergmann. *Werkstofftechnik Teil1: Grundlagen*, volume 3. Carl Hanser Verlag, 2000.
- [120] A.J. Murray, J.L.; McAlister. The al-si (aluminium-silicon) system. *Bulletin of Alloy Phase Diagrams*, 5(1):74–84, 1984. National Bureau of Standards.
- [121] J.F. Shackelford. *Introduction to materials science for engineers*, volume 6. Pearson, Prentice Hall, 2005.
- [122] Wolfgang Seidel. *Werkstofftechnik*, volume 5. Carl Hanser Verlag, 2001.
- [123] A. Greatholder. An internship investigating metco 320's response to elevated temperatures. Technical report, Rolls-Royce, 2011.
- [124] Y.N. Liang, S.Z. Li, and S. Li. Evaluation of abrasability of porous seal materials in a single-pendulum scratch device. *Wear*, 177(2):167 – 173, 1994.
- [125] F. E. Kennedy. Single-pass rub phenomena- analysis and experiment. *ASME Journal of Lubrication Technology*, 104:582–588, 1982.
- [126] J. Banhart, J. Baumeister, and M. Weber. Damping properties of aluminium foams. *Materials Science and Engineering A*, 205(1-2):221 – 228, 1996.
- [127] A K Swanakar, S Gimenez, S Salehi, J Vleugels, and O Van der Biest. Recent advances in materials characterization using impulse excitation technique (iet). *Key Engineering Materials*, 333:235–238, 2007.
- [128] Jianfeng Wang, James K. Carson, Mike F. North, and Donald J. Cleland. A new approach to modelling the effective thermal conductivity of heterogeneous materials. *International Journal of Heat and Mass Transfer*, 49(17-18):3075–3083, 8 2006.
- [129] J. M.Jalil H. K. D. H. Bhadeshia H.S. Hasan, M.J.Peet. Heat transfer coefficients during quenching of steels. <http://www.msm.cam.ac.uk/phase-trans/2011/transferHasan2011.pdf>, 2011.
- [130] Michael Schuetze. *Protective Oxide Scales and Their Breakdown*. ISBN: 0471959049. Wiley, 1 edition, February 1997.
- [131] David Muller. Scanning electron microscopy. Presentation, 2008.
- [132] H.E. Pragnell, W.M.; Evans. A finite-difference model to predict 2d depletion profiles arising from high temperature oxidation of alloys. *Modelling and Simulation in Materials Science and Engineering*, 14:733–740, 2006.

- 
- [133] P.J.R. Smith. *The Effect of Cooling Holes on the Cyclic Life of Air Plasma Sprayed Thermal Barrier Coatings*. PhD thesis, Cranfield University, School of Applied Sciences, 2010.